



University  
of Glasgow

Tang, Song (2019) *InP-based semiconductor lasers with novel sampled Bragg gratings and applications*. PhD thesis.

<https://theses.gla.ac.uk/72468/>

Copyright and moral rights for this work are retained by the author

A copy can be downloaded for personal non-commercial research or study, without prior permission or charge

This work cannot be reproduced or quoted extensively from without first obtaining permission in writing from the author

The content must not be changed in any way or sold commercially in any format or medium without the formal permission of the author

When referring to this work, full bibliographic details including the author, title, awarding institution and date of the thesis must be given

Enlighten: Theses

<https://theses.gla.ac.uk/>  
[research-enlighten@glasgow.ac.uk](mailto:research-enlighten@glasgow.ac.uk)



University  
of Glasgow

**InP-based Semiconductor Lasers with Novel  
Sampled Bragg Gratings and Applications**

**Song Tang**

A Thesis submitted to  
School of Engineering  
University of Glasgow

In fulfilment of the requirements for the degree of  
Doctor of Philosophy (Ph.D.)

May 2019

## Abstract

Semiconductor diode lasers have a wide variety of applications in optical communications, spectroscopy and imaging. This thesis reports on work to produce novel semiconductor diode lasers, and expand their application areas. Semiconductor lasers designed and fabricated in this work are based on quantum well structures operating at 1550 nm.

Three main findings are reported in this thesis. The first finding is about distributed feedback semiconductor lasers and laser arrays based on novel sampled Bragg grating structures. These semiconductor lasers have enhanced effective coupling coefficients compared to distributed feedback lasers based on the conventional sampled Bragg grating structure. The effective coupling coefficient of the conventional sampled Bragg grating is only about 0.32 times of a uniform Bragg grating. However, based on novel sampled Bragg grating structures, the effective coupling coefficients can be up to 0.9 times of a uniform Bragg grating. An eight-wavelength distributed feedback semiconductor laser array is reported, which has a precise wavelength separation of 100 GHz at 1550 nm. 10 mW of output optical power was achieved by a single diode laser. The second finding regards a novel dual-mode semiconductor diode laser based on a single cavity. The dual wavelengths of this laser are lasing stably with a wavelength separation of 4.45 nm. Based on this dual-mode diode laser, a THz frequency of 560 GHz is generated based on the photomixing technique. The third finding of this thesis is about THz repetition frequency mode-locked semiconductor lasers. The mode-locked semiconductor lasers are based on novel sampled grating distributed Bragg reflector structures. Compared to the mode-locked laser based on the conventional sampled grating distributed Bragg reflector structure, the effective coupling coefficient is increased by more than a factor of three in the new mode-locked laser. Optical pulses at repetition frequencies of 620 GHz and 1 THz are generated based on the mode-locked diode laser. Design, fabrication and characterisation of these semiconductor lasers are introduced in detail in this thesis.

## **Declaration**

I declare that the thesis does not include work forming part of a thesis presented successfully for another degree.

I declare that the thesis represents my own work except where acknowledged to others.

## List of Publications

### Journal Papers

L. Hou, **S. Tang**, B. Hou, S. Liang, and J. H. Marsh, "1.55- $\mu\text{m}$  AlGaInAs/InP Sampled Grating Laser Diodes for Mode Locking at Terahertz Frequencies," *IEEE Journal of Selected Topics in Quantum Electronics*, vol. 24, pp. 1-8, 2018.

**S. Tang**, L. Hou, X. Chen, and J. H. Marsh, "Multiple-wavelength distributed-feedback laser arrays with high coupling coefficients and precise channel spacing," *Optics Letters*, vol. 42, pp. 1800-1803, 2017.

### Conference Papers

**S. Tang**, B. Hou, S. Liang, D. Chen, L. Hou, and J. H. Marsh, "Terahertz Signal Generation Based on a Dual-Mode 1.5  $\mu\text{m}$  DFB Semiconductor Laser," in *CLEO Pacific Rim*, Hong Kong, China, 2018.

L. Hou, **S. Tang**, B. Hou, and J. H. Marsh, "Mode Locking at THz Repetition Frequencies using Lasers with Phase Shifted Sampled Gratings," in *CLEO: Science and Innovations*, p. SW4Q. 7, 2018.

L. Hou, **S. Tang**, and J. H. Marsh, "Integrated phase-locked laser diodes at 1.55  $\mu\text{m}$ ," in *IEEE High Power Diode Lasers and Systems Conference (HPD)*, pp. 27-28, 2017.

L. Hou, **S. Tang**, and J. H. Marsh, "THz repetition frequency mode-locked laser using novel sampled gratings," in *The European Conference on Lasers and Electro-Optics*, p. CB\_8\_5, 2017.

**S. Tang**, L. Hou, X. Chen, and J. H. Marsh, "DFB laser arrays with precise channel separation and high coupling coefficient," in *The European Conference on Lasers and Electro-Optics*, p. CB\_6\_5, 2017.

**S. Tang**, L. Hou, I. Eddie, X. Chen, and J. H. Marsh, "Novel Sampled Grating Design for High Precision, Multiple Wavelength DFB Laser Arrays," in *European Conference on Integrated Optics (ECIO)*, 2017.

L. Hou, **S. Tang**, M. Sorel, and J. H. Marsh, "Phased locked laser diode by using passive array of multi-mode interference couplers," in *IEEE Photonics Conference (IPC)*, pp. 325-326, 2016.

## Acknowledgements

To finish the adventure of this PhD, I would like to thank all the people who gave me support during the study. I appreciate all of you, all of your contributions and encouragements. I will remember all the happy and bitter moments during the PhD, which are already part of my life.

Firstly, I would like to thank my supervisor, Prof. John Marsh, for his invaluable support throughout my PhD. I am grateful to have this opportunity of perusing the PhD study at the University of Glasgow. I also would like to thank my second supervisor, Dr. Lianping Hou, for his selflessness to teach me laser design, fabrication and characterisation. When I have a problem with the research, he will always give his valuable advice.

I sincerely appreciate the contributions from all the staff in the James Watt Nanofabrication Centre. Without their dedications in operating and maintaining the facilities, my research is not possible to be completed.

In particular, I would like to mention some friends for their kind help with my research. I would like to thank Thomas Reilly for his patience on fixing and operating the old sputtering machine. I would like to thank Eugenio for sharing his experience of optimizing the ICP dry etch recipe. I also would like to thank Vincenzo for his valuable suggestions on my research and resume.

Finally, thank all of my friends. I will remember the life spent with you in Glasgow.

To my family.

# Contents

<b>Abstract</b> .....	<b>I</b>
<b>Declaration</b> .....	<b>II</b>
<b>List of Publications</b> .....	<b>III</b>
<b>Acknowledgements</b> .....	<b>V</b>
<b>List of Figures</b> .....	<b>XII</b>
<b>List of Tables</b> .....	<b>XXI</b>
<b>Acronyms</b> .....	<b>XXII</b>
<b>Chapter 1</b> .....	<b>1</b>
<b>Introduction</b> .....	<b>1</b>
1.1 Motivation .....	1
1.2 DFB Semiconductor Laser Diodes for Optical Communications.....	2
1.2.1 Light Sources for the Internet .....	2
1.2.2 Wavelength Division Multiplexing.....	5
1.2.3 Photonic Integrated Circuits.....	5
1.2.3.1 InP-based Photonic Integration .....	6
1.2.3.2 Hybrid Integration.....	7
1.2.3.3 Silicon Photonics.....	8
1.2.4 The Aim of This Research .....	9

1.3 Terahertz Signals Generation .....	10
1.3.1 Introduction of Terahertz Waves .....	10
1.3.2 Terahertz Sources.....	12
1.3.2.1 Terahertz Time-domain Spectroscopy .....	12
1.3.2.2 Terahertz Quantum Cascade Lasers.....	14
1.3.2.3 Resonant Tunnelling Diodes .....	15
1.3.2.4 Photomixing Based on Two Wavelengths .....	16
1.3.3 The Aim of This Research .....	17
1.4 Mode-locked Semiconductor Lasers.....	18
1.4.1 Theory of Mode-locking .....	18
1.4.2 Structure of A Simple semiconductor mode-locked laser.....	22
1.4.3 Autocorrelator .....	23
1.4.4 The Aim of This Research .....	25
1.5 Thesis Overview.....	25
<b>Chapter 2 .....</b>	<b>27</b>
<b>Theory and Design .....</b>	<b>27</b>
2.1 Theory of Bragg Grating Reflection .....	28
2.2 Transfer Matrix Method.....	29

2.3 Sampled Bragg Gratings .....	32
2.3.1 Basic Theory .....	32
2.3.2 Sampled Bragg Gratings with Equivalent Phase Shift.....	35
2.4 Sampled Bragg Gratings with Phase-shifted Sections.....	38
2.4.1 Structures for High Coupling Coefficients .....	39
2.4.2 Structures for Dual-mode Lasers .....	41
2.4.3 Structures for Mode-locked Lasers .....	43
2.5 Chapter Summary.....	46
<b>Chapter 3 .....</b>	<b>48</b>
<b>Materials and Fabrication.....</b>	<b>48</b>
3.1 MQW Wafer Structures .....	48
3.2 Ridge Waveguides .....	51
3.2.1 Waveguide Design .....	51
3.2.2 Optical Modes .....	53
3.2.3 Curved Ridge Waveguides.....	54
3.3 Electron Beam Lithography .....	55
3.4 Fabrication Steps.....	58
3.4.1 Pattern Design .....	59

3.4.2 Sample Preparation .....	60
3.4.3 Marker Definition.....	61
3.4.4 Waveguide Isolation.....	64
3.4.4.1 Reactive Ion Etching .....	64
3.4.4.2 Etching Process .....	66
3.4.5 Waveguide Definition .....	69
3.4.5.1 Side-wall Gratings.....	69
3.4.5.2 Dose Test.....	69
3.4.5.3 Undercut and RIE Lag Effects .....	72
3.4.6 Contact Window Opening.....	76
3.4.7 Metallisation for P-contact.....	77
3.4.8 Thinning and Cleaving.....	78
3.5 Chapter Summary.....	80
<b>Chapter 4 .....</b>	<b>81</b>
<b>Novel DFB Semiconductor Lasers and Laser Arrays.....</b>	<b>81</b>
4.1 Introduction .....	81
4.2 Device Design and Fabrication .....	82
4.3 Set-up for Measurements .....	86

4.4 Enhancement of Effective Coupling Coefficients Based on SBGs with Phase-shifted Sections .....	89
4.4.1 Comparison of Stopbands .....	89
4.4.2 Single-mode Lasers with Equivalent $\pi$ -phase shift.....	92
4.5 An Eight-wavelength DFB Laser Array .....	94
4.6 Measurements of Far-field Patterns .....	98
4.7 Chapter Summary.....	104
<b>Chapter 5 .....</b>	<b>105</b>
<b>Terahertz Frequency Generation Based on Dual-mode Semiconductor Lasers.....</b>	<b>105</b>
5.1 Introduction .....	105
5.2 Design of Dual-mode Lasers.....	106
5.3 Characteristics of Dual-mode Lasers .....	108
5.3.1 Optical Power and Spectra .....	108
5.3.2 Autocorrelation Traces.....	110
5.4 Measurement of THz Frequency Generation .....	112
5.5 Chapter Summary.....	118
<b>Chapter 6 .....</b>	<b>120</b>
<b>Mode-locked Semiconductor Lasers Based on SGDBR Structures .....</b>	<b>120</b>
6.1 Introduction .....	120

6.2 Device Design .....123

    6.2.1 Mode-locked Laser Diodes based on C-SGDBR.....123

    6.2.2 Mode-locked Laser Diodes based on PPS-SGDBR.....125

6.3 Characteristics of Mode-locked Lasers .....128

    6.3.1 640 GHz MLLDs Based on PPS-SGDBR .....128

    6.3.2 1 THz MLLDs Based on PPS-SGDBR.....133

6.4 Chapter Summary.....136

**Chapter 7 .....138**

**Conclusions and Future Work.....138**

    7.1 Research Summary.....138

    7.2 Main Achievements .....139

    7.3 Future Work .....140

**Bibliography .....143**

## List of Figures

Figure 1.1: A typical structure of optical fibre communication system.....	2
Figure 1.2: Bandgap energy versus lattice constant of various III-V alloys at room temperature [7]......	3
Figure 1.3: The diagram of a typical WDM link [13]......	4
Figure 1.4: Schematic of a typical 100 Gb/s DWDM PIC transmitter [23]......	6
Figure 1.5: Schematic of coupling the laser array in a PLC. ....	8
Figure 1.6: The fundamental optical mode of the silicon waveguide. ....	9
Figure 1.7: The THz spectrum region in the whole electromagnetic frequency spectrum [45]......	10
Figure 1.8: Atmospheric attenuation calculated due to rain rates of 25 and 5 mm/h, with water content of 7.5 g/m <sup>3</sup> and atmospheric temperature of 20 °C [69]. ....	12
Figure 1.9: Schematic of a typical THz-TDS imaging system [76]......	13
Figure 1.10: THz signal generation based on photomixing of two wavelengths.....	17
Figure 1.11: Schematic of an FP cavity laser and its output spectrum. ....	19
Figure 1.12: Schematic of (a) active mode-locking, and (b) passive mode-locking.....	20
Figure 1.13: Time-dependent loss in a saturable absorber.....	21
Figure 1.14: Micrograph of a semiconductor mode-locked laser based on the FP cavity structure integrated with an SA.....	23

Figure 1.15: Schematic of an intensity autocorrelator. ....	24
Figure 2.1: Schematic of (a) DFB diode laser, and (b) DBR diode laser. ....	27
Figure 2.2: Schematic of a Bragg grating with coupling of forward and backward optical propagating modes. ....	28
Figure 2.3: Cascaded transfer matrices. ....	31
Figure 2.4: Schematics of (a) a uniform Bragg grating, with the grating period $\Lambda_0$ , and (b) a uniformly-sampled Bragg grating, with the sampling period $P$ . ....	32
Figure 2.5: The reflectivity spectrum of (a) a uniform Bragg grating, and (b) a uniformly-sampled Bragg grating. ....	34
Figure 2.6: Schematic of the uniform Bragg grating with a $\pi$ -phase shift in the centre. ....	35
Figure 2.7: The reflectivity spectra of a uniform Bragg grating and a $\pi$ -phase shift Bragg grating with the same grating period. ....	36
Figure 2.8: The reflectivity spectra of the uniformly-sampled Bragg gratings with/without an equivalent $\pi$ -phase shift. ....	38
Figure 2.9: Grating structures of (a) C-SBG, (b) 2PS-SBG, (c) 3PS-SBG and (d) 4PS-SBG. $P$ is the sampling period [160]. ....	39
Figure 2.10: Reflectivity spectra of (a) C-SBG, (b) 2PS-SBG, (c) 3PS-SBG and (d) 4PS-SBG. ....	40
Figure 2.11: Combined reflectivity spectra of C-SBG, 2PS-SBG, 3PS-SBG and 4PS-SBG. ....	41
Figure 2.12: The reflectivity spectrum of 8 nm wavelength spacing between $\pm 1$ st-order channels. ....	42

Figure 2.13: The reflectivity spectrum of 8 nm wavelength spacing between $\pm 1$ st-order channels with EPS.....	43
Figure 2.14: The sampling structure of a C-SGDBR. $P$ is the sampling period and $r$ is the duty cycle. ....	44
Figure 2.15: The reflectivity spectrum of a C-SGDBR, with a duty cycle $r$ of 0.15. ....	44
Figure 2.16: The sampling structure of a PPS-SGDBR.....	45
Figure 2.17: The reflectivity spectra of a PPS-SGDBR, with the duty cycle $r$ of (a) 0.1, (b) 0.2, (c) 0.3 and (d) 0.4. ....	45
Figure 2.18: The reflectivity spectrum of a PPS-SGDBR, with the duty cycle $r$ of 0.25....	46
Figure 3.1: Band offsets between InP lattice-matched materials [167]. ....	49
Figure 3.2: IQE five quantum well wafer structure. ....	50
Figure 3.3: Energy band diagram for the conduction bands of the layers. ....	51
Figure 3.4: Schematic of the cross-section of a (a) shallow-etched ridge waveguide and (b) deep-etched ridge waveguide, where $n_{eff}$ is the effective refractive index of the optical mode and $n_c$ is the refractive index of “cladding” layer. ....	52
Figure 3.5: Waveguide modal effective index versus ridge width for the fundamental, 1 <sup>st</sup> - and 2 <sup>nd</sup> -order TE modes at 1550 nm. ....	53
Figure 3.6: Simulated fundamental optical mode for a shallow-etched ridge waveguide for the 2 $\mu$ m wide, 1920 nm deep ridge. ....	54
Figure 3.7: Schematic of the curved ridge waveguide.....	55
Figure 3.8: The overall e-beam lithography process flow. ....	55

Figure 3.9: Patterning with positive or negative tone resists. ....	57
Figure 3.10: The exposure dose distribution for a 20 $\mu\text{m}$ square (a) before and (b) after proximity correction. ....	58
Figure 3.11: The user interface of L-Edit. ....	59
Figure 3.12: A single sample cleaved. ....	60
Figure 3.13: The process flow of lift-off technique. ....	61
Figure 3.14: The micrograph of the sample after development. ....	62
Figure 3.15: A micrograph of the markers after lift-off process. ....	63
Figure 3.16: A diagram of a common RIE set-up. A RIE consists of two electrodes (1 and 4) that create an electric field (3) that accelerates ions (2) toward the sample surface (5) [172]. ....	65
Figure 3.17: (a) Schematic of anisotropic etch, and (b) resist loss and etch depth during the process of dry etching. ....	66
Figure 3.18: (a) A reflectivity trace from the interferometer for waveguide isolation etch, and (b) a micrograph of waveguide isolation patterns after dry etch. ....	68
Figure 3.19: SEM images of patterned HSQ for ridge waveguides with gratings, (a) under exposure, (b) right exposure, and (c) over exposure. ....	71
Figure 3.20: The reflectivity trace for ridge waveguides dry etch. ....	72
Figure 3.21: The side view of a laterally-coupled grating, etched by $\text{CH}_4/\text{H}_2/\text{O}_2$ . ....	73
Figure 3.22: The cross-section view of (a) a ridge waveguide, and (b) a laterally-coupled grating. ....	73

Figure 3.23: The side view of a laterally-coupled grating etched by the same recipe with a 2-inch InP wafer underneath the sample. ....	74
Figure 3.24: The side view of a laterally-coupled ridge waveguide with gratings based on two-step etching. ....	75
Figure 3.25: The micrograph of a ridge waveguide (a) before and (b) after RIE etching for contact window opening. ....	77
Figure 3.26: The micrograph of Ti/Pt/Au p-contact layer. ....	78
Figure 3.27: Annealing temperature changing with time.....	78
Figure 3.28: Design of the cleave sign.....	79
Figure 3.29: An image of cleaved laser bars.....	79
Figure 4.1: The micrograph of a single DFB semiconductor laser diode. ....	82
Figure 4.2: The <i>LI</i> curve of the DFB laser diode. ....	82
Figure 4.3: The output optical spectrum of the DFB laser diode @ 60 mA. ....	83
Figure 4.4: (a) The design of a DFB laser diode with bend ridge waveguides on both sides, and (b) the micrograph of the fabricated DFB laser diode [160]. ....	84
Figure 4.5: The SEM image of the bend waveguides of fabricated DFB laser diodes. ....	84
Figure 4.6: The micrograph of the equivalent $\pi$ -phase shift introduced in the middle of ridge waveguides of (a) C-SBG, and (b) 2PS-SBG. ....	85
Figure 4.7: The SEM image of a C-SBG with an equivalent $\pi$ -phase shift. ....	85

Figure 4.8: The SEM image of 2PS-SBG, 3PS-SBG and 4PS-SBG structures with equivalent $\pi$ -phase shifts. ....	86
Figure 4.9: Schematic of the set-up to measure a DFB laser diode integrated with an SOA. ....	87
Figure 4.10: (a) The photograph of the set-up, and (b) the micrograph of the two touched probes and the lensed fibre.....	88
Figure 4.11: Model 8000 from <i>Newport Company</i> .....	88
Figure 4.12: (a) The optical spectrum of a laser diode just below threshold (50 mA) with uniform seed grating, and (b) the reflectivity spectrum of a passive waveguide of the corresponding uniform seed grating [160]. ....	89
Figure 4.13: Optical spectra measured just below threshold (50 mA) of (a) C-SBG, (b) 2PS-SBG, (c) 3PS-SBG and (d) 4PS-SBG [160]. ....	90
Figure 4.14: Simulated reflectivity spectra of passive waveguides with different values of $\kappa$ (smaller $\kappa$ having narrower stopband) [160]. ....	91
Figure 4.15: <i>LI</i> curves of the fabricated DFB laser diodes for the four SBGs, at the SOA's injection currents of 20 mA.....	92
Figure 4.16: SMSRs of the lasers at different DFB injection currents when the SOA injection current was 20 mA [160]. ....	93
Figure 4.17: Optical spectra of the four SBGs at 100 mA [160]. ....	94
Figure 4.18: The micrograph of the fabricated eight-wavelength DFB laser array. ....	95
Figure 4.19: (a) Optical spectra of the laser array at injection currents of 100 mA (channels 1 to 8, left to right), and (b) linear fitting of the wavelengths [160]. ....	95

Figure 4.20: <i>LIV</i> characteristics of the fabricated eight-wavelength laser array with SOA drive currents set at 40 mA [160].....	96
Figure 4.21: The 2D optical spectrum mapping of one of the DFB laser diodes. ....	97
Figure 4.22: The SMSR changing with the DFB injection current.....	97
Figure 4.23: The lasing wavelength changing with DFB injection currents.....	98
Figure 4.24: Schematic of the set-up to measure far-field patterns. ....	99
Figure 4.25: The photograph of the set-up to measure far-field patterns of diode lasers. ....	99
Figure 4.26: (a) 3D and (b) 2D light beam intensity profiles for a diode laser based on the straight ridge waveguide. ....	100
Figure 4.27: Vertical and horizontal profiles of light intensity for a diode laser based on the straight ridge waveguide. ....	101
Figure 4.28: (a) 3D and (b) 2D light beam intensity profiles for a diode laser based on a bend ridge waveguide. ....	102
Figure 4.29: The horizontal profile of light intensity for a diode laser based on a bend ridge waveguide. ....	103
Figure 4.30: Vertical and horizontal profiles of light intensity based on the bend ridge waveguide centered at the peak of intensity. ....	103
Figure 5.1: The grating structure of 2PS-SBG.....	106
Figure 5.2: <i>LI</i> curves of a dual-mode laser. ....	108
Figure 5.3: The optical spectrum at an SOA current of 40 mA and DFB current of 120 mA [198].....	109

Figure 5.4: A 2D-wavelength mapping at an SOA current of 40 mA [198].	110
Figure 5.5: Schematic of the set-up to measure autocorrelation traces.	111
Figure 5.6: Equipment used for measuring autocorrelation traces.	111
Figure 5.7: A measured autocorrelation trace [198].	112
Figure 5.8: Schematic of the set-up for generating and detecting THz waves.	112
Figure 5.9: (a) The front view and (b) the back view of the PCA.	114
Figure 5.10: The Golay cell optoacoustic detector from <i>TYDEX</i> Company.	115
Figure 5.11: 2D power intensity mapping of THz signals.	116
Figure 5.12: Schematic of the set-up for generating and detecting THz waves transmitted through a piece of paper.	117
Figure 5.13: 2D power intensity mapping of THz signals transmitted through a piece of paper.	118
Figure 6.1: Schematic of a typical CPM laser: two optical pulses colliding in the SA, which is placed in the cavity centre.	121
Figure 6.2: Schematic of a monolithic CCM device with an etched slot reflector.	122
Figure 6.3: (a) Schematic of the MLLD based on C-SGDBR, (b) configuration of the sidewall C-SGDBR [216].	123
Figure 6.4: Schematic of round trips generated in C-SGDBR.	124
Figure 6.5: Sampled Bragg grating structures of (a) C-SGDBR, and (b) PPS-SGDBR; (c) simulated reflectivity spectra for the two grating structures [217].	126

- Figure 6.6: (a) Device structures based on C-SGDBR and PPS-SGDBR, (b) SEM images of the sidewall gratings of both of SGDBRs [217]. ..... 127
- Figure 6.7: Micrograph of the fabricated MLLDs. .... 127
- Figure 6.8: Typical output power from the SOA side of the 640 GHz (a) C-SGDBR, and (b) PPS-SGDBR laser versus the gain current with different SOA currents, when the  $V_{SA} = -3.0$  V and  $I_{SGDBR} = 10$  mA. .... 128
- Figure 6.9: (a) The optical spectra of 640 GHz C-SGDBR and PPS-SGDBR MLLDs measured at  $V_{SA} = -3.0$  V,  $I_{Gain} = 144$  mA,  $I_{SGDBR} = 10$  mA and  $I_{SOA} = 150$  mA, (b) the corresponding autocorrelation trace for PPS-SGDBR [217]. .... 129
- Figure 6.10: 2D optical spectrum mapping of a 640 GHz PPS-SGDBR MLLD measured at  $V_{SA} = -3.0$  V,  $I_{SGDBR} = 10$  mA and (a)  $I_{SOA} = 0$  mA, (b)  $I_{SOA} = 100$  mA, (c)  $I_{SOA} = 200$  mA, (d)  $I_{SOA} = 300$  mA. .... 131
- Figure 6.11: 2D optical spectrum mapping of a 640 GHz PPS-SGDBR MLLD at  $I_{SOA} = 100$  mA,  $I_{SGDBR} = 10$  mA and (a)  $V_{SA} = -2.4$  V, (b)  $V_{SA} = -2.6$  V, (c)  $V_{SA} = -2.8$  V, (d)  $V_{SA} = -3.0$  V. .... 132
- Figure 6.12: (a) Simulated reflectivity spectra of the 1THz PPS-SGDBR and its counterpart C-SGDBR, (b) typical output power from the SOA side for 1THz PPS-SGDBR MLLD when the  $V_{SA} = -3.0$  V and  $I_{PPS-SGDBR} = 10$  mA [217]. .... 133
- Figure 6.13: (a) The optical spectrum and FFT of AC trace (inset) measured at  $V_{SA} = -3.0$  V,  $I_{Gain} = 232$  mA,  $I_{PPS-SGDBR} = 10$  mA, and  $I_{SOA} = 100$  mA, (b) corresponding AC trace for the 1 THz PPS-SGDBR MLLD [217]. .... 135
- Figure 6.14: 2D optical spectrum mapping of a 1 THz PPS-SGDBR MLLD measured at  $V_{SA} = -3.0$  V,  $I_{SGDBR} = 10$  mA, and  $I_{SOA} = 100$  mA. .... 136

## List of Tables

Table 4.1 Properties of modelled and measured gratings [160].....91

## Acronyms

2PS-SBG	An SBG with Two Phase-shifted Sections
3D	Three Dimensional
3PS-SBG	An SBG with Three Phase-shifted Sections
4PS-SBG	An SBG with Four Phase-shifted Sections
AC	Autocorrelation
ASE	Amplified Spontaneous Emission
Au	Gold
AWG	Arrayed-waveguide Grating
CAD	Computer-aided Design
CCM	Compound-cavity Mode-locking
CD	Compact Disc
CHF <sub>3</sub>	Fluoroform
Cl <sub>2</sub>	Chlorine
CMOS	Complementary Metal Oxide Semiconductor
CMP	Chemical Mechanical Polishing
CPM	Colliding Pulse Mode-locking
C-SBG	Conventional SBG
C-SGDBR	Conventional SGDBR
CW	Continuous-wave
DBR	Distributed Bragg Reflector
DFB	Distributed Feedback
DNA	Deoxyribonucleic Acid
DVD	Digital Versatile Disc
DWDM	Dense Wavelength Division Multiplexing
EAM	Electro-absorption Modulator
EBL	Electron Beam Lithography
EDFA	Erbium-doped Fibre Amplifier
EPS	Equivalent Phase Shift
FFP	Far-field Pattern
FFT	Fast Fourier Transform

FP	Fabry-Perot
GaAs	Gallium Arsenide
GPIB	General-Purpose Interface Bus
GRINSCH	Graded Index Separate Confinement Heterostructure
HSQ	Hydrogen Silsesquioxane
ICP	Inductively Coupled Plasma
InP	Indium phosphide
IPA	Isopropyl Alcohol
ITU-T	International Telecommunications Union
JWNC	James Watt Nanofabrication Centre
LI	Light-current
LIDAR	Light Detecting and Ranging
LiIO <sub>3</sub>	Lithium Iodate
LiNbO <sub>3</sub>	Lithium Niobate
LIV	Light-current-voltage
MBE	Molecular Beam Epitaxy
MIBK	Methyl Isobutyl Ketone
MLLD	Ultrafast Mode-locked Laser Diode
MMI	Multimode Interference
MOCVD	Metal Organic Chemical Vapour Deposition
MQW	Multiple Quantum Well
MZM	Mach-Zehnder Modulator
NiCr	Nichrome
OPM	Optical Power Monitoring
PCA	Photoconductive Antenna
PECVD	Plasma-Enhanced Chemical Vapour Deposition
PIC	Photonic Integrated Circuits
PLC	Planar Lightwave Circuit
PMMA	Polymethyl Methacrylate
PON	Passive Optical Network
PPS-SGDBR	$\pi$ phase-shifted SGDBR
QCL	Quantum Cascade Laser

QW	Quantum Well
QWI	Quantum-well Intermixing
REC	Reconstruction-equivalent-chirp
RF	Radio Frequency
RIE	Reactive Ion Etching
RO	Reverse Osmosis
RTA	Rapid Thermal Annealing
RTD	Resonant Tunnelling Diode
SA	Saturable Absorber
SBG	Sampled Bragg Grating
SEM	Scanning Electron Microscope
SGDBR	Sampled Grating Distributed Bragg Reflector
SH	Second Harmonic
SiO <sub>2</sub>	Silicon Dioxide
SLM	Single Longitudinal Mode
SMSR	Side Mode Suppression Ratio
SOA	Semiconductor Optical Amplifier
SOI	Silicon on Insulator
TE	Transverse Electric
TEC	Thermo Electric Cooler
THz	Terahertz
THz-TDS	Terahertz Time-domain Spectroscopy
TM	Transverse Magnetic
TMAH	Tetramethylammonium Hydroxide
TMM	Transfer Matrix Method
TW-PD	Traveling-Wave Photodiode
UTC-PD	Uni-Traveling Carrier Photodiode
VOA	Variable Optical Attenuator
VR	Virtual Reality
WDM	Wavelength Division Multiplexing

# Chapter 1

## Introduction

### 1.1 Motivation

Since the first semiconductor laser diodes were reported in 1962 [1], they have undergone an enormous development, which has had great influence in the world. Various kinds of applications have been developed, from the readout sources in CD/DVD, laser printers, mice and pointers to the multiwavelength transmitters used in optical fibre communication systems [2]. In addition to these “classic” applications, new applications are continuously being developed based on semiconductor laser diodes. For example, lasers diodes can be used in gas monitor systems in manufacturing plants for safety and pollution control purposes [3]; many new patents have been applied for 3D cameras for virtual reality (VR) environments [4, 5]; semiconductor laser arrays are expected to be used in high-definition light detecting and ranging (LIDAR) systems [6], which can be used for driverless cars in the near future, etc. Many of the applications are popular around the world and are expected to change the world in the future. Indeed, expanding the application areas of semiconductor laser diodes is really an exciting research area.

The applications of semiconductor lasers in the optical fibre communication systems are very important. Fibre links are the foundation of the Internet, which is the basis of the modern world, the so-called “information era”. Nowadays, we can hardly live without the Internet. We surf on the Internet, communicate with each other through instant messaging software, play online games, make payments online and even order meals through the Internet. As the light sources for optical fibre communication systems, semiconductor laser diodes are of the key importance. These laser diodes are usually InP-based devices with high efficiency. Since light stimulated from InP-based semiconductor laser diodes can be transmitted through silica fibres, information has been transferred worldwide through the optical fibre networks. New semiconductor lasers are expected to be developed for novel applications.

## 1.2 DFB Semiconductor Laser Diodes for Optical Communications

A typical structure of an optical fibre communication system is illustrated in Fig. 1.1. Usually, the system consists of an optical transmitter, the optical channels, one or more optical amplifiers and optical receivers. Modulated by electric signals, light is generated from the optical transmitter and is transmitted through the optical channels, which are based on silica optical fibres. Because there is optical loss, an optical amplifier is needed. At last, after transmission through optical channels, light is detected by optical receivers, where electric signals will be demodulated. Semiconductor laser diodes are used as the light source in the optical transmitter.

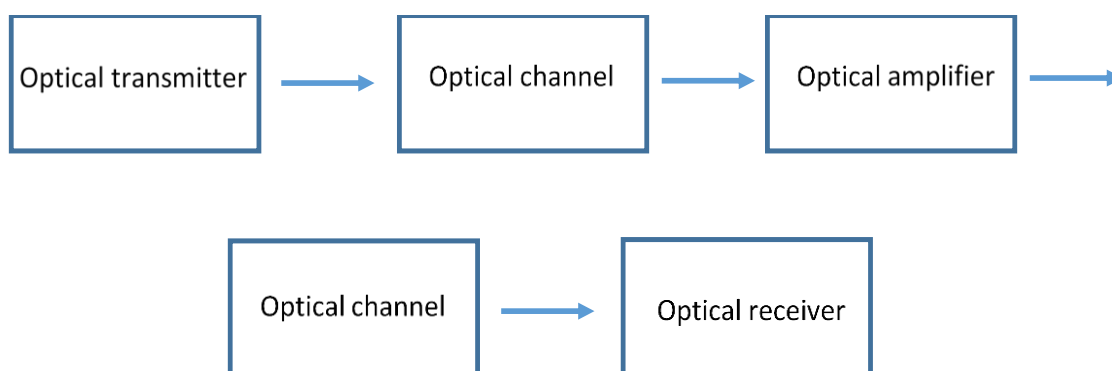
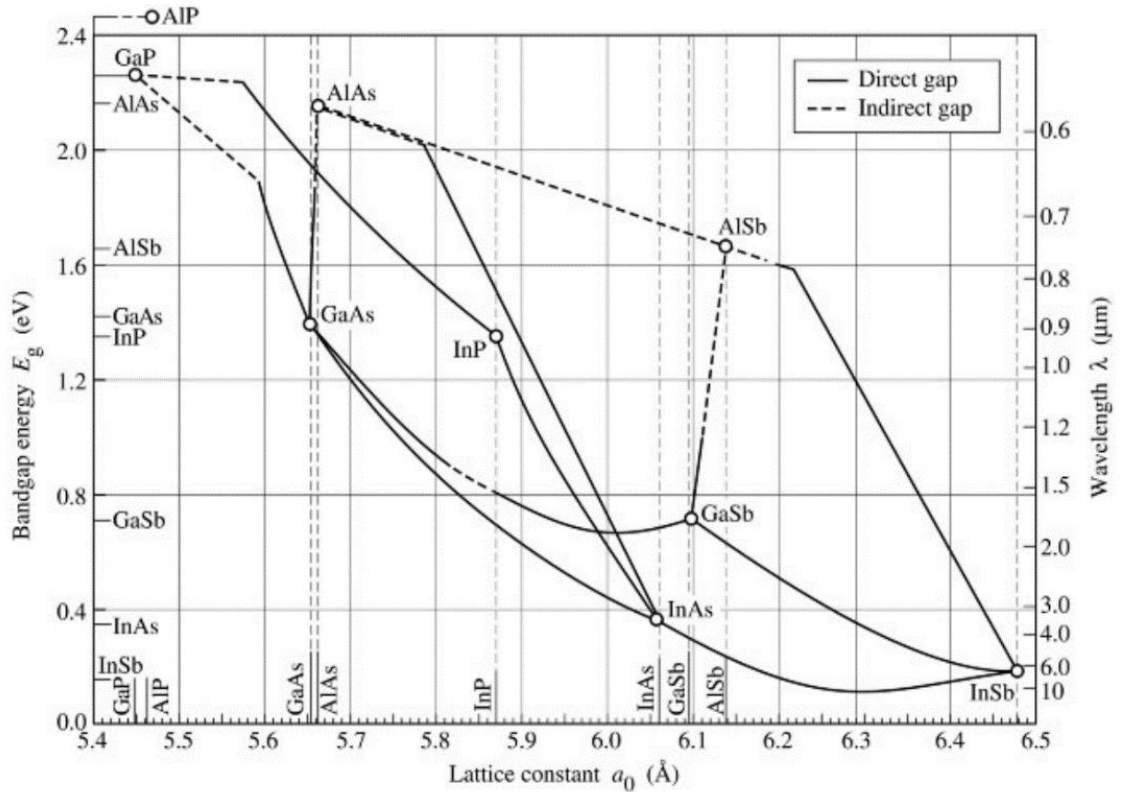


Figure 1.1: A typical structure of optical fibre communication system.

### 1.2.1 Light Sources for the Internet

III-V alloys with direct gaps are adopted for semiconductor laser diodes, which are in small sizes, have high efficiency and can be electrically pumped. Figure 1.2 shows the bandgap energy versus lattice constant diagram of some commonly-used III-V alloys, covering a wide wavelength range from red to the far infra-red (about 0.63-10  $\mu\text{m}$ ) [7]. From this figure, we can see that GaAs- and InP-based materials and their alloys can be used at telecom wavelengths ranging from 0.8 to 1.6  $\mu\text{m}$ . Because of the invention of the Erbium-doped fibre amplifier (EDFA), wavelengths around 1.5  $\mu\text{m}$  can be amplified in the optical transmission systems, which experiences the lowest loss transmitted through the optical fibre. This is the

reason that semiconductor laser diodes operating at 1.5  $\mu\text{m}$  are adopted for the long-haul optical communication systems. In this thesis, the semiconductor lasers all work at the wavelengths around 1.55  $\mu\text{m}$ .



**Figure 1.2: Bandgap energy versus lattice constant of various III-V alloys at room temperature [7].**

To fabricate semiconductor lasers operating in a wide wavelength range, alloys of III-V quaternary material systems (AlGaInAs/InP or InGaAsP/InP) are well developed for telecommunications [8]. By tuning the composition of the quaternary materials, lattice-matched materials are grown on the substrates (N-type InP or GaAs). To increase the energy conversion efficiency, quantum wells (QWs) are introduced to fabricate semiconductor lasers [9]. QWs are formed in semiconductors by having a material sandwiched between two layers of a material with a wider bandgap. A potential well is then formed that supports only discrete energy values. Electrons in semiconductors will concentrate in the lowest energy levels and the energy conversion efficiency is enhanced. By introducing a small percentage of lattice-mismatch, compressive strain and tensile strain can also be introduced into QWs

to adjust the bandgap of the materials. The small percentage of lattice-mismatch would not lead to dislocations in the materials, because the strained layers are only a few nanometres. What is more, the Transverse Electric (TE) mode will have much larger gain than the Transverse Magnetic (TM) mode if the compressive strain is introduced. However, if sufficient tensile strain is introduced, the TM mode can have much larger gain profiles [10]. The introduced strain is beneficial to single-mode lasing of semiconductor lasers. Semiconductor laser diodes in this thesis are all based on 5QW wafer structures. The detailed material structure will be introduced in Chapter 3.

To stimulate lasing in semiconductor lasers, optical feedback is essential. The most basic structure is the Fabry-Perot (FP) laser, which has optical reflections from both output facets. A vast number of wavelength modes are supported by the FP laser and mode competition can be severe especially if the laser is modulated. To avoid mode dispersion, single-mode lasers are required for efficient data transmission in the telecom networks and weakly-coupled gratings are used to guide single longitudinal mode (SLM) operation. Distributed feedback (DFB) [11] and distributed Bragg reflector (DBR) [12] semiconductor lasers are the two types of diode lasers with integrated gratings. In this thesis, QW semiconductor lasers with novel sampled Bragg gratings (SBGs) are introduced. Novel optoelectronic devices have been designed and fabricated successfully, broadening the application areas of semiconductor lasers.

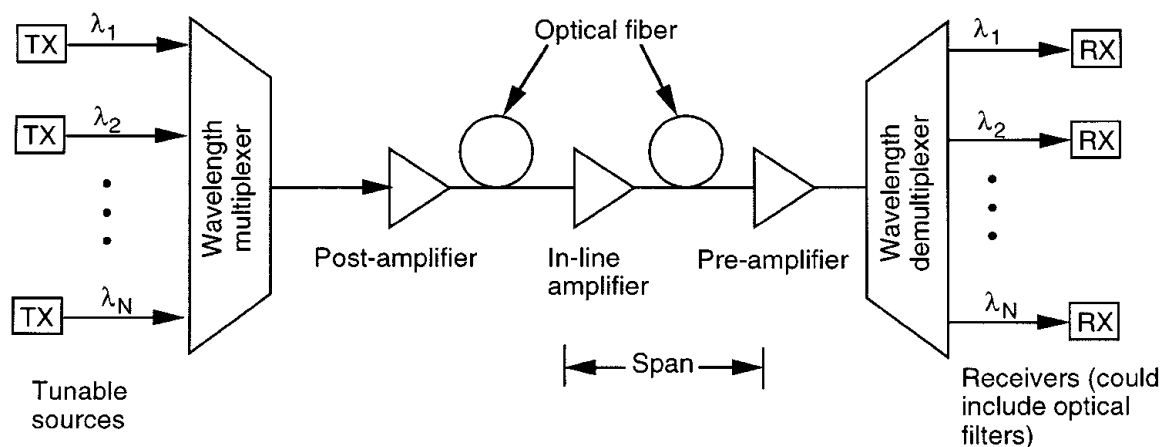


Figure 1.3: The diagram of a typical WDM link [13].

## 1.2.2 Wavelength Division Multiplexing

The demand for data capacity is continuously increasing with the development of the Internet. One way to increase data capacity in optical communication systems is to add more channels with different wavelengths in a single fibre, an approach which is named as Wavelength Division Multiplexing (WDM). Figure 1.3 shows a typical WDM link for telecoms [13]. For the optical transmitter, multiple independent wavelengths are generated by the semiconductor lasers. Each wavelength is modulated by an electrical signal, then all the wavelengths are combined by a wavelength multiplexer and launched into a single mode fibre. After transmission through the optical fibre (optical amplifiers may be needed), the wavelengths are demultiplexed by a wavelength demultiplexer, then each wavelength is sent to an individual receiver. WDM is widely used both in short-reach interconnects [14] and long-haul optical communication systems [15]. In 1997, the era of WDM systems began in terms of significant commercial deployments with promoted WDM systems featuring 10 channels at 2.5 Gb/s [16]. In modern dense wavelength division multiplexing (DWDM) systems, commercial optical communication systems carry up to 192 channels at up to 250 Gb/s on a 50 GHz grid, supporting a long-haul capacity of  $\sim 48$  Tb/s, and for short-reach applications up to 400 Gb/s per channel, reaching a total capacity of  $\sim 76$  Tb/s [17, 18]. For the research records today, a data rate in excess of 1 Tb/s has been achieved on per-carrier wavelength and the WDM capacity in a single-mode fibre can reach a data rate of up to 115 Tb/s [19-21].

## 1.2.3 Photonic Integrated Circuits

Modern optical communication systems based on a massive number of individual devices are raising concerns about form factor and energy consumption [22]. Photonic integration is a promising way to solve the problems [23-25], in which different functional devices are integrated on a single chip, so that more compact size and better energy efficiency will be achieved. Figure 1.4 shows a typical 100 Gb/s DWDM optical transmitter based on a photonic integrated circuit (PIC), which includes an optical power monitoring (OPM) array, a DFB laser array, an electro-absorption modulator (EAM) array, a variable optical attenuator (VOA) array and an arrayed-waveguide grating (AWG) multiplexer. As the main

optical sources used in optical communication systems and in PICs, making DFB and DBR laser arrays with high yields as well as high performance is always a challenge.

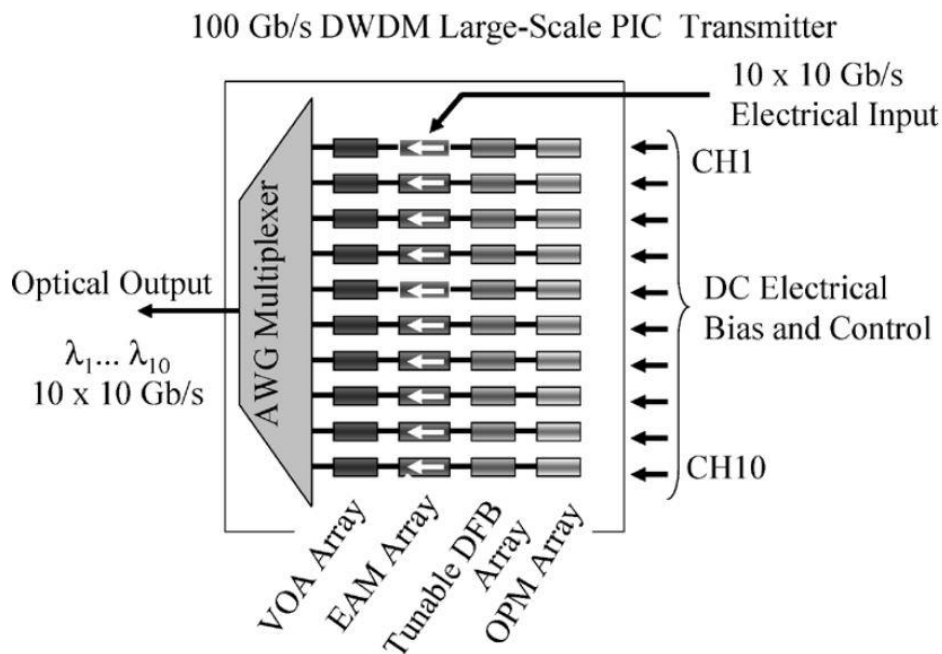


**Figure 1.4: Schematic of a typical 100 Gb/s DWDM PIC transmitter [23].**

There are three main approaches to realize PICs: InP-based photonic integration, hybrid integration, and silicon photonics. The three types of PICs will be introduced as follows.

### 1.2.3.1 InP-based Photonic Integration

Since we can make semiconductor laser diodes directly based on InP, it is very natural to come up with the idea to fabricate PICs with the same material. The key point here is how to make passive devices based on InP, such as optical waveguides, multimode interference (MMI) couplers, AWG multiplexers, Mach-Zehnder modulators (MZMs), etc. [26]. Researchers have developed several methods for active/passive integration on the InP platform: offset quantum-well waveguides [27], butt-joint regrowth [28], selective area growth [29] and quantum-well intermixing (QWI) [30]. Different methods have their advantages and limitations and, for practical applications, different methods may be used in combination.

The first commercial success for PICs is the photonic integration based on InP, which is produced by *Infinera*. In 2012, terabit/s class InP PICs were realized by this company and more than 450 functions were integrated on a single chip [31]. However, because of the optical diffraction limit and the difficulty of achieving optical isolation, photonic integration on a single chip cannot scale in the same way as electronic devices, which makes it difficult to increase the capacity on a single chip. At the same time, the processes to make InP-based PICs are complex and, as a result, the price of these chips is high. Hence, researchers are trying to make PICs in other ways.

### 1.2.3.2 Hybrid Integration

Another way to make PICs is to couple laser diodes with passive devices in different materials, which is called hybrid integration. Passive devices can be made of various kinds of materials, like silica, LiNbO<sub>3</sub>, silicon nitride, polymer and silicon on insulator (SOI) [32-35]. In this case, the passive devices can be optimized separately to obtain the best performance. For example, the silica-based AWG is really a success because of its low loss and low cost; MZMs based on LiNbO<sub>3</sub> can achieve very high modulation performance and passive devices based on polymers can have very low cost. These passive devices are typically classed as planar lightwave circuits (PLCs). Figure 1.5 shows the simplified schematic for hybrid integration, where the laser array and the multiplexer (made in a PLC) are coupled together.

The problem with hybrid integration is the coupling loss. Because of different materials used, the refractive indices are very different, which means that the optical modes are different. To reduce the coupling loss between different materials, a spot-size converter is usually introduced [36]. Packaging is therefore a big challenge for hybrid integration.

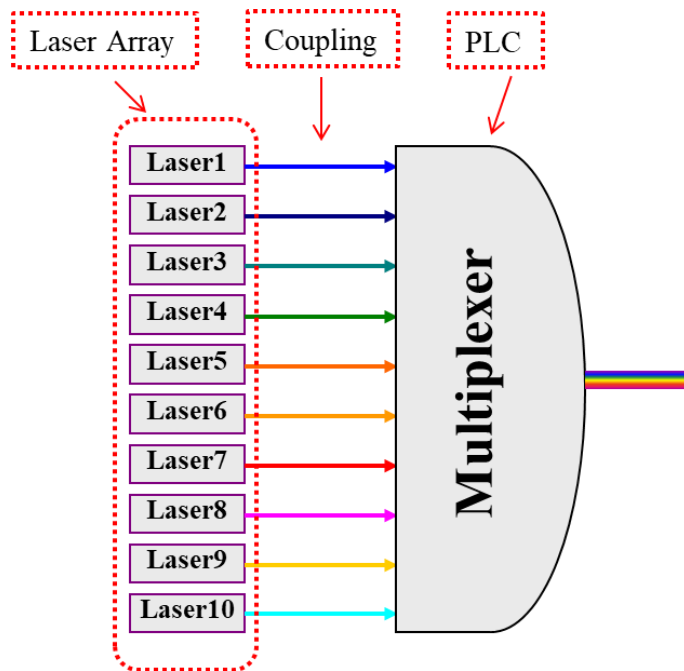
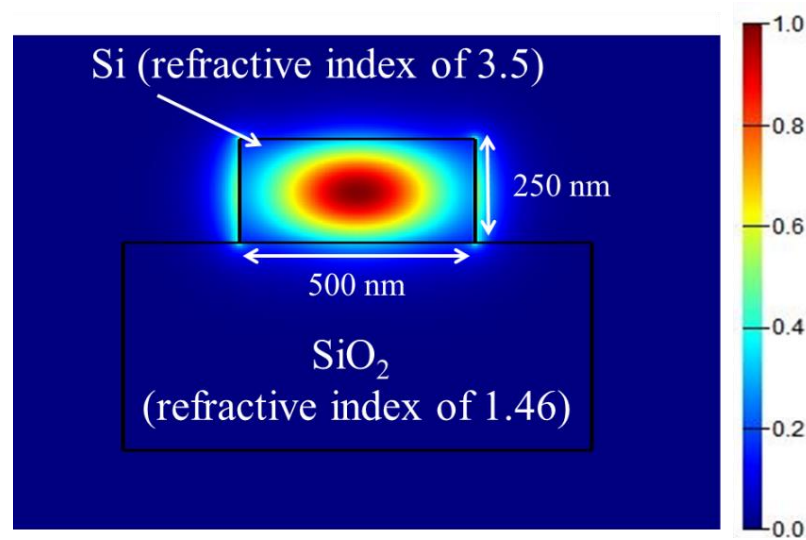


Figure 1.5: Schematic of coupling the laser array in a PLC.

### 1.2.3.3 Silicon Photonics

Silicon photonics is considered to be a key technology for the next generation of PICs. This technology is based on the silicon-on-insulator (SOI) platform, which has silicon grown on *Silicon Dioxide* ( $\text{SiO}_2$ ) based on a silicon substrate. The SOI fabrication could be compatible with Complementary Metal Oxide Semiconductor (CMOS) technology, leading to a robust and high yield technology with reliability and performance [37]. At the same time, because the refractive index difference between silicon and  $\text{SiO}_2$  is much higher, it has better optical confinement than InP/GaAs, which means the feature sizes of the devices can be much smaller and the device integration can be much more compact. Figure 1.6 shows the fundamental optical mode of a silicon waveguide based on the SOI platform, simulated by *Lumerical MODE Solutions*. With the refractive index of Si and  $\text{SiO}_2$  being 3.5 and 1.46 at 1550 nm respectively, the vertical refractive index contrast is rather high. As a result, a width of the silicon waveguide as small as several hundred nanometres can be achieved. By contrast, the width of an optical waveguide based on InP is typically 2  $\mu\text{m}$  when a shallow-etched ridge waveguide is introduced. The vertical refractive index contrast of InP devices cannot be designed high because of material properties.



**Figure 1.6: The fundamental optical mode of the silicon waveguide.**

As is well known, silicon is an indirect-gap material. Although various kinds of passive devices have been realised on SOI platform, such as grating-coupler, low-loss optical waveguide, AWG, spot-size converter, etc. [38, 39], a practical silicon based laser is still not available. The problem is then how to integrate laser diodes with silicon photonics devices. There are mainly three techniques for integration. One way is to transfer an InP-based epitaxial structure to the SOI substrate through a direct wafer-bonding process [40]. Another way is to grow III-V materials directly on silicon to make semiconductor lasers [41]. The third is “pick and place” of lasers into an SOI PLC [42]. One company, called *Luxtera*, has been founded to apply the wafer-bonding technique, and their products based on silicon photonics have been promoted to the market.

### 1.2.4 The Aim of This Research

As we can see, DFB semiconductor laser diodes are key optoelectronic devices for optical communications. For photonic integration, DFB semiconductor lasers will still play an important role. In this work, DFB semiconductor lasers and laser arrays with novel SBGs will be designed and fabricated. We will show that the wavelength spacing can be precisely controlled. DFB semiconductor laser arrays with precisely-controlled wavelengths can meet the requirements for the Telecommunication Standardization Sector of the International Telecommunications Union (ITU-T), which means less tuning (by temperature or by

current) will be required. Novel SBGs are therefore promising structures to be applied to the laser sources for PICs.

## 1.3 Terahertz Signals Generation

### 1.3.1 Introduction of Terahertz Waves

The research of terahertz (THz) electromagnetic radiation has attracted more and more attentions in recent years [43]. The THz spectrum region lies in the gap between radio waves and light, which is roughly defined by the frequency range from 0.1 to 10 THz, as shown in Fig. 1.7. Historically, this spectral region was called the “terahertz gap” because of the lack of inexpensive and convenient sources, detectors and systems for terahertz waves. At longer wavelengths, applications such as radar, microwaves and radio communications have been developed for a long time and have had a great impact on humanity. At shorter wavelengths, we have the applications of optical communications, medical imaging, astrophysics, etc. The “terahertz gap” is waiting to be explored. The good news is that, after so many years of development, many new terahertz techniques have been proposed and realized, with great potential applications in terahertz spectroscopy, imaging, sensing and wireless communications [44].

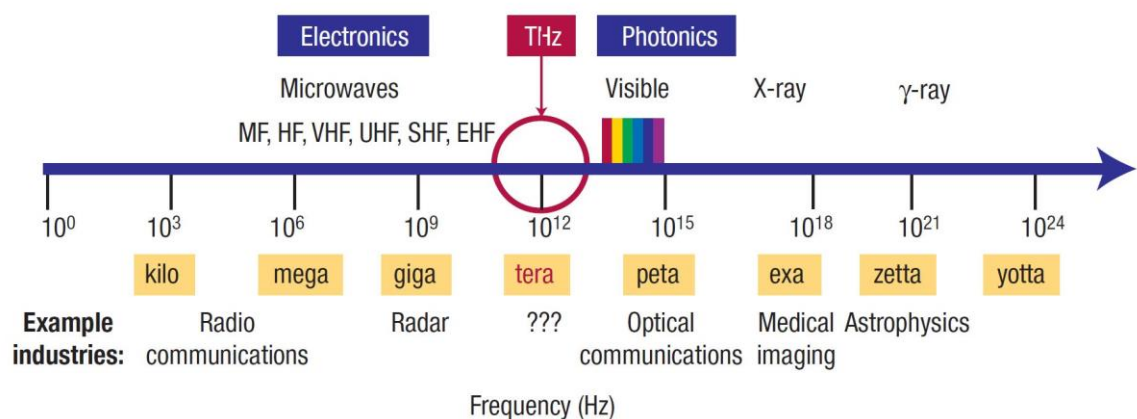


Figure 1.7: The THz spectrum region in the whole electromagnetic frequency spectrum [45].

Although research has already been carried out in the THz spectrum region for several decades, the main drive came from radio astronomy [46-48], which is the last largely-unexplored wavelength frontier for astronomical observations [49]. Terahertz spectroscopy could be used to study the evolution of matter in our galaxy and the formation history of stars. For example, since many atoms, ions, and molecules have emission lines at THz frequencies [50, 51], these emission lines can be used to probe the conditions in Giant Molecular Clouds through our galaxy [52].

THz radiation can also be potentially used for imaging and sensing, in the areas of biological and medical sciences, pharmacology and security [53, 54], which results from various characteristics of THz waves. For dielectrics, the absorption of THz radiation depends on the polarity and optical phonon resonances of the material [55]. For most dry, non-metallic and nonpolar objects like paper, plastics and nonpolar organic substances, THz waves are transmitted with very little loss [56]. On the other hand, for polar liquids such as water, strong absorption occurs in the THz frequency region [57, 58]. By utilizing these features, terahertz techniques have been applied for transillumination of biological tissues [59], recognition of protein structural states [60], performing label-free DNA sequencing [61], security screening and counterterrorism [62], etc.

It is known that higher frequencies will provide higher bandwidth for wireless communications. With more and more people relying on wireless networks, there is an explosive increase in mobile traffic [63]. The commercially-utilized radio frequency has increased from 2.4 to 5 GHz for wireless communications and 60 GHz wireless communication systems are on the way [64, 65]. To go further, with much higher frequencies, THz waves are expected to achieve 10 Gb/s data rates or even higher in the near future [66-68]. For indoor applications of THz wireless communications, there is no major problem of transmission, but for long-distance transmission, strong attenuation of THz signals needs to be taken into consideration because of absorption by water in the atmosphere. Figure 1.8 illustrates the atmospheric attenuation calculated due to rain rates of 25 and 5 mm/h, where the red lines show the base attenuation with the rain. We can see that, with the increase of frequency, the attenuation increases dramatically, which will lead to very short transmission distances in the THz frequency region. This will be an obstacle for

the application of THz wireless communications. However, several transmission windows may be utilized.

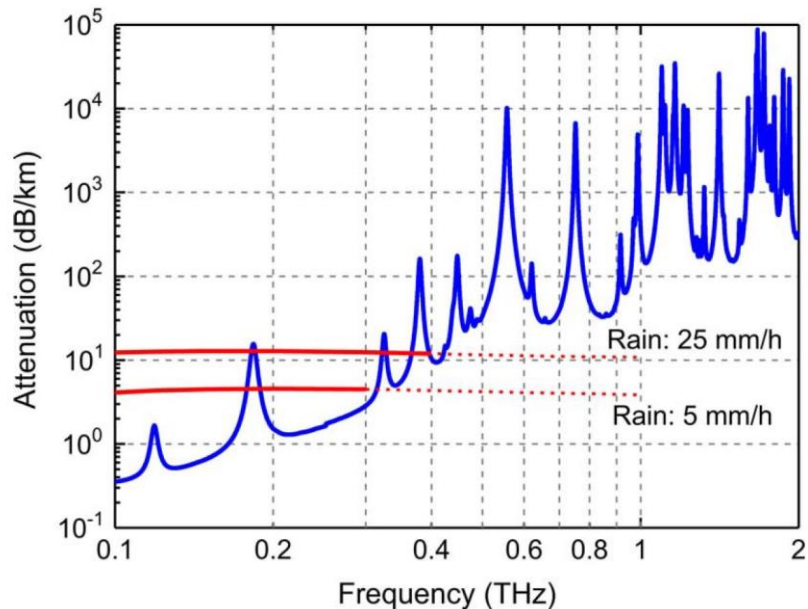


**Figure 1.8: Atmospheric attenuation calculated due to rain rates of 25 and 5 mm/h, with water content of  $7.5 \text{ g/m}^3$  and atmospheric temperature of  $20 \text{ }^\circ\text{C}$  [69].**

Terahertz techniques provide various possible applications to make people's life better and are expected to achieve huge development in the near future. Here, we will focus on the techniques for terahertz sources.

## 1.3.2 Terahertz Sources

Terahertz sources are considered to be the most difficult components among all the elements in terahertz technology [53]. Several main techniques for terahertz sources will be introduced as follows.

### 1.3.2.1 Terahertz Time-domain Spectroscopy

Terahertz time-domain spectroscopy (THz-TDS) is a technique to generate broadband THz radiation in the form of short pulses, which was firstly studied in the 1980s at the IBM T.J. Watson Research Centre and AT&T Bell Labs [70, 71]. Since many materials have their

own typical absorption bands in THz spectrum region, called fingerprints, broadband THz radiation can be used to find the fingerprint spectra of target materials in security and/or biological uses for materials analysis [43]. For example, THz-TDS has been successfully used for gas sensing and inspection of DNA components and biological tissues [72-75].

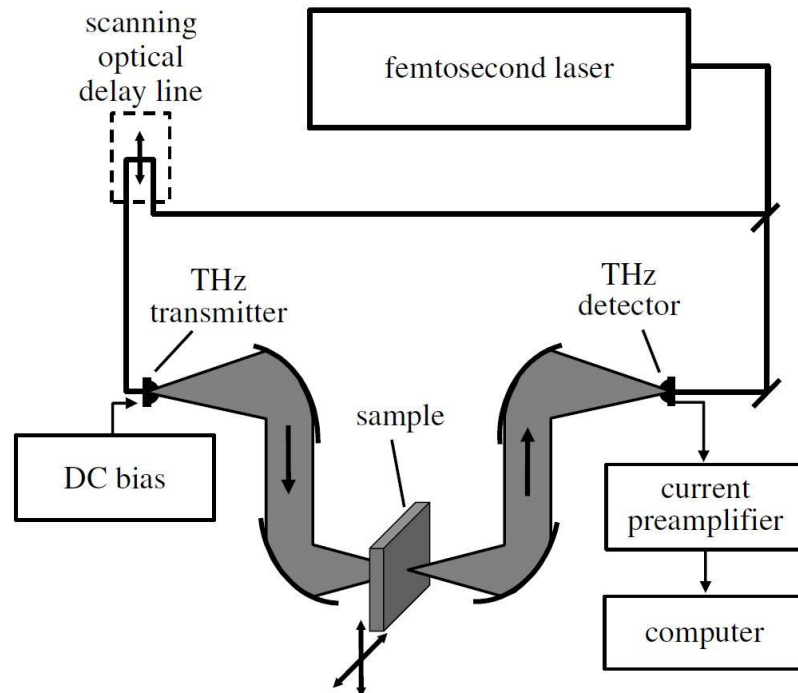


**Figure 1.9: Schematic of a typical THz-TDS imaging system [76].**

Figure 1.9 illustrates a schematic of a typical THz-TDS imaging system, which starts from a femtosecond laser. The femtosecond laser can be a femtosecond Ti:Sapphire laser or a diode-pumped Cr:LiSAF laser [56], which is able to produce trains of pulses with duration of about 100 fs. The femtosecond laser beam is split into two beams. One beam is incident on a THz transmitter to generate THz pulses, while another beam is used to gate the THz detector and measure the THz signals, after being amplified by a current preamplifier. The data is collected by a computer. Before the beam is incident on the THz transmitter, a scanning optical delay line is used to offset the two beams and allow the THz temporal profile to be iteratively sampled. For the THz transmitter, a number of different mechanisms can be applied to generate THz pulses, including photoconductive antennas (PCA), second-order non-linear effects in electro-optic crystals, optical rectification, electronic non-linear transmission lines and plasma oscillations [45, 77-79]. THz pulses are then collimated and

focused on the sample by several parabolic mirrors. After transmitting through the sample, the THz signals are collimated and focused onto the THz detector. Such a THz-TDS system is widely used for imaging and spectroscopy. However, this kind of system is usually expensive and large. Cheap and portable THz-TDS systems are the future.

### **1.3.2.2 Terahertz Quantum Cascade Lasers**

Quantum Cascade Lasers (QCLs) are semiconductor lasers first developed in the mid infrared region [80]. QCLs in the terahertz region were first realized in 2002 [81]. They are compact THz sources for narrowband THz radiation, and frequencies in the region of about 1 to 5 THz have already been realized [82-85].

For conventional semiconductor lasers, photons are generated according to the bandgap of the active material by radiative recombination between electrons in the conduction bands and holes in the valence bands, which is called an interband transition. However, for QCLs, light emission is realized through intersub-band transitions in a potential staircase of coupled quantum wells, the conduction band of which is split into a series of distinct sub-bands by quantum confinement effects [81]. The quantum well design of THz QCLs (bandgap engineering) can be realized by growing thin layers (several few-nm-thick) of different semiconductor materials, such as GaAs/AlGaAs layers. By applying an electric field, electron population inversion will be obtained between two sub-bands in a series of identical repeating units, with THz photons being emitted during each transition. A point of interest is that the emission wavelength is determined by the thickness of semiconductor layers, not the physical properties of the materials [43]. Therefore, arbitrary emission frequencies can be controlled through the thickness of different layers, with the advantage that different wavelengths can be achieved with the same material. QCLs can operate in both pulsed and continuous-wave (CW) modes.

At first, QCLs could only work at liquid nitrogen temperature (77 K). However, with researchers' efforts, the working temperature has been increased [86]. Based on intracavity difference-frequency generation from mid-infrared dual-wavelength quantum cascade lasers, THz sources have been realized at 4 THz at room temperature [87]. This is an indirect way

to generate THz signals at room temperature rather than using a QCL standard THz laser. It is still challenging to take QCLs from the laboratory to industry.

### 1.3.2.3 Resonant Tunnelling Diodes

Since THz radiation is located between light and radio waves, both optical and electronic devices can be investigated to extend their frequency range to act as THz sources. For semiconductor lasers, as mentioned above, QCLs for THz radiation have been realized from the optical device side. On the electronic device side, oscillators with hetero-bipolar transistors, high electron mobility transistors and Si-based transistors are being studied for THz signal generation [88-92]. Among these devices, the resonant tunnelling diode (RTD) is a promising candidate for THz sources. Previously, RTDs with high frequencies could only operate at low temperature. For example, frequencies up to 2.5 THz were achieved at 25 K [93]. However, RTDs with oscillation frequencies up to 1.92 THz working at room temperature have been realized recently [94], which shows great potential for future applications.

The structure of a RTD is simple, consisting of a single quantum well for confinement of carriers. The single quantum well comprises three thin layers of material, each of thickness of only several nanometres, with one of the layers confined between two other layers of a different material with a larger band gap, called barriers. If the barriers are sufficiently thin, carriers can tunnel through them by quantum effects. With parameters optimized for the quantum well, resonant tunnelling can occur at THz frequencies. A THz oscillator then can be realized by integrating the RTD with a slot antenna to generate THz waves [94]. Most RTDs are based on the InGaAs/AlAs material system [95-97], while other material systems like InAs/AlSb can also be used [98]. The thin layers of the quantum well are generally grown by Molecular Beam Epitaxy (MBE), while Metal Organic Chemical Vapour Deposition (MOCVD) can also be used if the process is well controlled. A slot antenna has a length of 10-50  $\mu\text{m}$ , which determines the oscillation frequency [99]. To achieve high output power, the RTD and the antenna need to be impedance-matched.

The THz oscillation frequency is determined by the  $LC$  resonance, where the inductance  $L$  is from the antenna and the capacitance  $C$  is from both the structures of the RTD and the

antenna. To achieve higher THz oscillation frequencies, the  $LC$  value needs to be reduced. On one hand, the length of the antenna can be reduced to reduce both the inductance and the capacitance [100]. However, this results in a reduction of the radiation conductance, which leads to a decrease of the output power. On the other hand, thin layers can be employed to reduce the resonant tunnelling time [101, 102]. In this circumstance, thin wells and barriers can be used with the barriers of as thin as 1 nm [103], which places very high requirements on the growth technique for MBE or MOCVD. To achieve a higher output power, an array of RTDs can be designed and fabricated [104, 105], because the output power is currently very low. For example, an output power of 60  $\mu\text{W}$  at 1 THz was achieved for a typical RTD [99]. The output power needs to be improved for future applications.

#### **1.3.2.4 Photomixing Based on Two Wavelengths**

To generate narrow THz linewidth spectra with good stability and reliability, a continuous-wave (CW) system is a suitable option, which could offer a better resolution on a pre-selected linewidth [106]. THz CW systems are generally based on photomixing of two different wavelengths and the schematic of the system is shown in Fig. 1.10. Two wavelengths with a frequency difference in the THz frequency range are generated by two CW lasers and combined through a beam splitter. The combined beam is then focused on the THz photomixer antenna to generate THz waves coupled to the air. Two CW Ti:sapphire lasers were first used in a CW THz system by Verghese *et al.* [107]. To detect the THz signals, a THz photomixer antenna, a bolometer or a Golay cell can be used [108-110]. Detectors are expected to be integrated with the transmitters to build an integrated transceiver containing both THz transmitting and receiving elements.

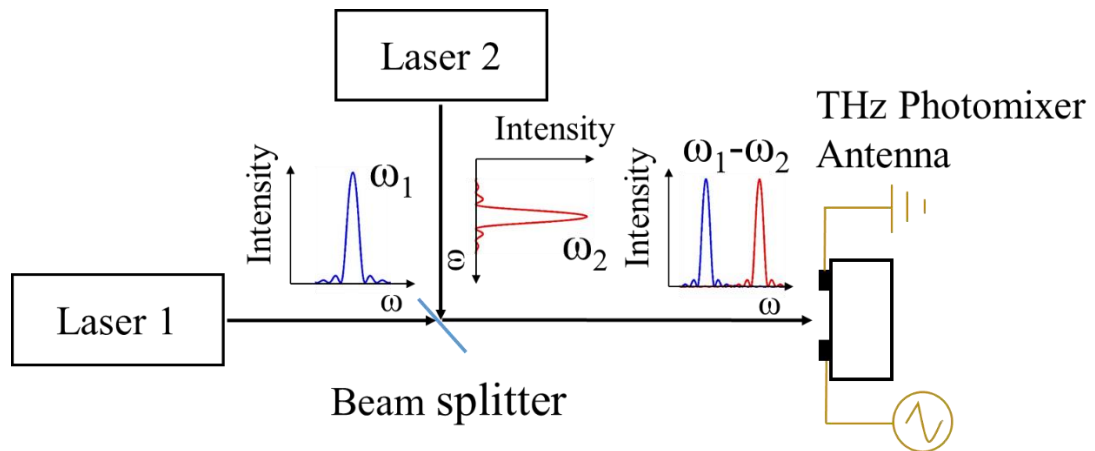


**Figure 1.10: THz signal generation based on photomixing of two wavelengths.**

A THz photomixer antenna generally consists of two metallic (usually gold) electrodes on a photoconductive substrate. Typical photoconductors include high-resistivity GaAs, InP, InGaAs and radiation-damaged silicon wafers [45]. Metallic electrodes are used for current bias and to form an antenna. The antenna's structure and dimensions need to be designed carefully to achieve the designed resonant frequency [111], which should match the frequency difference of the two wavelengths.

As well as photoconductors, ultra-fast photodetectors with high-frequency responses can also be utilised in THz antennas [112, 113]. These photodetectors have p-i-n structures modified to give a shorter carrier transit time, lower load resistance and smaller intrinsic and parasitic capacitances. Two typical structures have been demonstrated, which are the Traveling-Wave Photodiode (TW-PD) [114] and the Uni-Traveling Carrier Photodiode (UTC-PD) [115]. 24  $\mu\text{W}$  output power at 914 GHz has already been demonstrated by adopting the UTC-PD by the research group at University College London [116].

THz photomixer antennas with compact sizes are expected to achieve higher efficiencies. These antennas could be used in compact THz systems with good portability.

### 1.3.3 The Aim of This Research

THz waves have a diverse range of applications in terahertz spectroscopy, imaging, sensing and wireless communications. As the key components of the THz systems, compact and

low-cost THz sources are needed. In this work, novel dual-mode semiconductor lasers based on SBGs will be presented. We will show that two wavelengths with stable stimulation can be achieved in a single diode laser. Using the dual-mode lasers, THz signal generation has been observed based on photomixing when laser output light is focused on a THz photomixer antenna. Additionally, these compact dual-mode lasers have the potential for mass production. Integrated with THz photomixer antennas, it is possible to encourage compact and low-cost continuous-wave THz systems in the future.

## 1.4 Mode-locked Semiconductor Lasers

### 1.4.1 Theory of Mode-locking

Mode-locking is a technique in optics to generate ultrashort pulses from lasers, which are then called *mode-locked lasers* [117]. Generally, the resulting pulses of light have extremely short durations, on the order of picoseconds ( $10^{-12}$  s) or femtoseconds ( $10^{-15}$  s). According to the Fourier transform, to generate pulses of light, multiple wavelengths with the same frequency separation are required. Limited by the Fourier transform, to achieve a shorter pulse duration, a wider spectrum is needed. The width of spectrum over which a laser may operate is limited by its gain bandwidth and the gain bandwidth varies with different types of lasers. For a typical helium-neon laser, the gain bandwidth is about 1.5 GHz, with a wavelength range of about 0.002 nm at the central wavelength of 633 nm. However, for a titanium-doped sapphire (Ti:sapphire) laser, its gain bandwidth can be as wide as 300 nm wavelength range centred at 800 nm. For semiconductor lasers, the gain bandwidth is normally dozens of nanometres, which is sufficient to produce femtosecond mode-locked pulses [118-120].

In the simplest situation, an FP cavity is applied to generate multiple longitudinal modes with different wavelengths to make a mode-locked laser. An FP cavity laser consists of two plane mirrors facing each other with the laser gain medium between the two mirrors. Bouncing between the two mirrors, light will interfere with itself and multiple longitudinal modes will be generated within the gain spectrum. For an FP cavity length  $L$  and free space wavelength  $\lambda$ , the generated longitudinal modes satisfy the condition:

$$L = m\lambda/2n_{eff}, \quad (1.1)$$

where  $m$  is an integer (around  $10^3$  to  $10^4$  approximately) and  $n_{eff}$  is the effective refractive index. The frequency separation between adjacent longitudinal modes is given by  $\Delta\nu$ :

$$\Delta\nu = \frac{c}{2n_g L}, \quad (1.2)$$

where  $c$  is the speed of light in the vacuum and  $n_g$  is the group index of the gain medium.

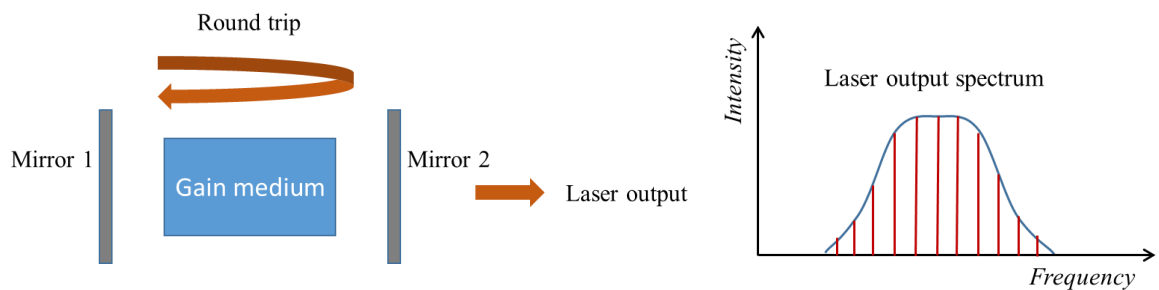


**Figure 1.11: Schematic of an FP cavity laser and its output spectrum.**

Figure 1.11 illustrates the schematic of an FP cavity laser and its output spectrum. The output optical spectrum is limited by the bandwidth of the gain medium. For a simple FP laser, operating in continuous-wave condition, each of the stimulated wavelengths oscillates independently. In this case, the phase between different modes is not fixed and the output light intensity is constant. When the phase between different modes is fixed, the laser is said to be “mode-locked” and pulses of light will be emitted periodically. Considering a light pulse travelling inside the cavity, part of the light pulse will be emitted when the pulse hits the output mirror. Hence, the pulse separation time equals the laser cavity’s round trip time  $\tau$ , which is given as:

$$\tau = \frac{2n_g L}{c}. \quad (1.3)$$

Comparing with equation (1.2), the round trip time and the mode spacing of the laser have the relation of:

$$\Delta\nu = 1/\tau. \quad (1.4)$$

The pulse duration time is much shorter than the round-trip time and it is determined by the number of modes with fixed phase.

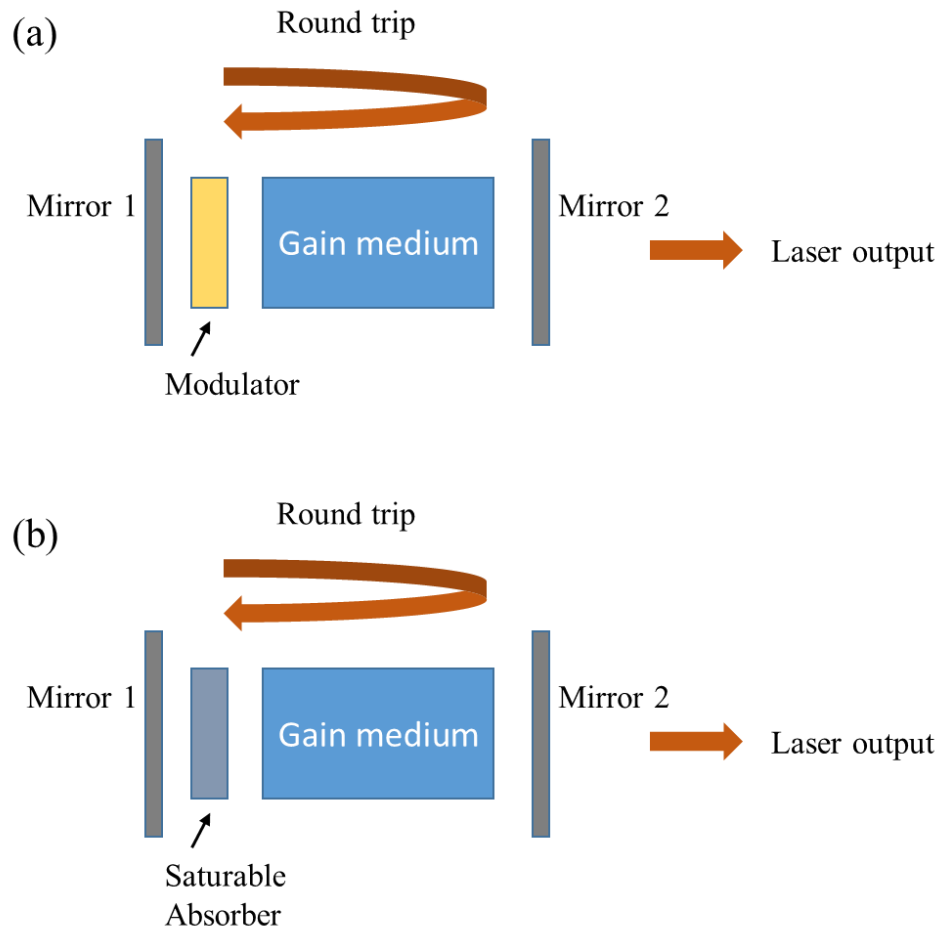


**Figure 1.12: Schematic of (a) active mode-locking, and (b) passive mode-locking.**

There are two basic methods to produce mode-locking in a laser, named as either “active mode-locking” or “passive mode-locking”. A modulator is introduced into the laser cavity to achieve active mode-locking, as shown in Fig. 1.12(a). To introduce modulation of the resonator losses or of the cavity phase change, the modulator can be either an acousto-optic modulator, electro-optic modulator or electroabsorption modulator [121, 122]. When the modulation is synchronized with the resonator round trip time, ultrashort pulses with

picosecond pulse durations can be generated. This technique requires accurately matching the modulation frequency and the round trip time.

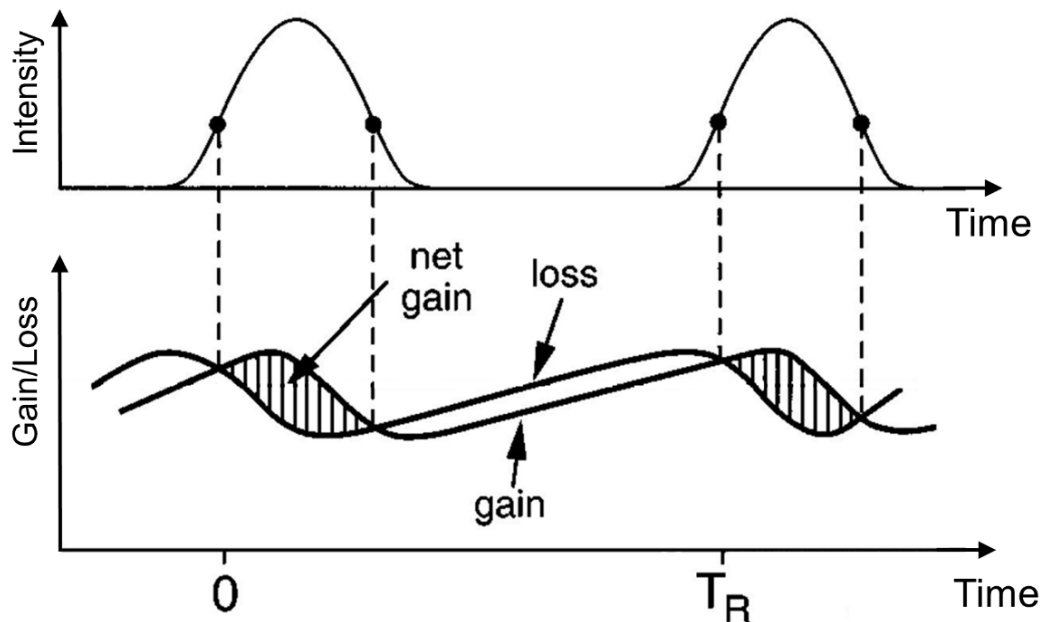


**Figure 1.13: Time-dependent loss in a saturable absorber.**

As the name indicates, passive mode-locking does not require an external signal modulation, and it allows the generation of pulses with much shorter pulse duration time (on the order of femtosecond), compared with active mode-locking. A saturable absorber (SA) is generally used to achieve passive mode-locking [123, 124], as shown in Fig. 1.12(b). The mechanism of optical pulse generation will be explained as follows [125]. In the pumped laser cavity, noise is present and the electric field intensity fluctuates with time incoherently. Figure 1.13 shows the time-dependent gain and loss when an optical pulse passes through an SA. Because of the nonlinear absorption characteristics of the SA, at higher intensities the loss is reduced, while the low intensity components are strongly attenuated. When the loss reaches saturation before the gain in a total cavity, a net gain window will be formed in the time domain according to the intensity fluctuation. In the net gain window, the pulse intensity is amplified. At the end of the net gain window, the energy of the optical pulse is high enough to deplete the gain, and losses are high again. By this time, the SA begins to

recover and an optical pulse is output. This pulse formation process will be repeated and an optical pulse train will be generated, reaching a steady state in the laser cavity.

In this thesis, a semiconductor SA will be integrated to fabricate semiconductor mode-locked lasers at THz repetition frequencies based on passive mode-locking technique.

### **1.4.2 Structure of A Simple semiconductor mode-locked laser**

Here, a simple semiconductor mode-locked laser structure based on passive mode-locking will be introduced, which is the basis to understand the complex structures of other semiconductor mode-locked lasers. Figure 1.14 shows the micrograph of a simple semiconductor mode-locked laser. This diode laser was as-cleaved to form an FP cavity, and an SA was integrated to introduce passive mode-locking. To achieve better mode-locking performance, the SA needs to be optimised to have non-saturable loss, low saturation fluence, etc. as low as possible, when saturated [126]. This may require a different QW structure in the gain and SA sections which requires relatively complex processes. However, it has been shown that provided the length of the SA and gain sections are optimal, an identical QW structure can be used in both sections with good performance. Furthermore, this optimal structure simplifies the fabrication process. The gain section was biased to achieve enough gain for lasing, while the SA was inversely biased with a voltage of  $-2\text{ V} \sim -3\text{ V}$ . The inverse-bias may remove the photogenerated carriers in the range of subpicosecond, which corresponds to THz frequency range [127]. The related mechanisms were reported, such as spectral hole burning and carrier heating by the electric field in the SA [128]. According to equation (1.2), the frequency separation of adjacent longitudinal modes introduced by the FP cavity is determined by the cavity length and the group index of the material. The cavity length is typically several hundred microns, while the length of the SA is generally dozens of microns. For a typical cavity length of  $500\ \mu\text{m}$ , the repetition frequencies of generated light pulses are generally tens of gigahertz [129, 130]. The cavity length cannot be too short, otherwise it will not lase efficiently and so it is difficult for mode-locked lasers based on this approach to achieve repetition frequencies higher than 100 GHz. What is more, the repetition frequency is sensitive to the cavity length, so the precision of the repetition frequencies is limited by the resolution of conventional scribing tools.



**Figure 1.14: Micrograph of a semiconductor mode-locked laser based on the FP cavity structure integrated with an SA.**

To overcome the above limitations and achieve much higher repetition frequencies, novel semiconductor mode-locked lasers based on sampled grating distributed Bragg reflectors (SGDBR) will be introduced in this thesis, with the SA section also applied to achieve passive mode-locking. Instead of the FP cavity, these types of mode-locked lasers will use SGDBR structures to achieve multiple longitudinal modes. Compared with FP cavity mode-locked lasers, these new mode-locked lasers can achieve much higher repetition frequencies, even in the terahertz frequency range.

### 1.4.3 Autocorrelator

Being on the order of femtoseconds, ultrashort pulse duration times cannot be measured by conventional optoelectronic devices directly. To break the limitation of conventional optoelectronic devices, a nonlinear interaction is used to measure the signal indirectly. The nonlinear interaction is often based on a nonlinear crystal, such as lithium iodate ( $\text{LiIO}_3$ ). An intensity autocorrelator was used to measure the ultrashort pulse duration in this work, and autocorrelation (AC) traces could be measured. This method does not require a fast photodetector and only a slow photodetector is essential. A second-harmonic (SH) signal is generated by the nonlinear process in the autocorrelator. After the SH signal is detected, the pulse duration time can be calculated.

Figure 1.15 shows the schematic of the intensity autocorrelator. After the light is coupled into the autocorrelator, a beam splitter is used to create two copies of the input optical pulses. One of the copies is transmitted through a delay line to achieve a relative time delay, then the two copies of pulses are focused on a nonlinear crystal by an optical lens. Because of the nonlinear process, these copies interact in a nonlinear medium if they are overlapped temporally, and the SH signal is then generated. Transmitted through an aperture, the SH

signal is detected by a slow photodetector, while the original signals are blocked by the aperture to reduce the noise. Autocorrelation traces can be derived from the detected signal, and the pulse duration can then be calculated.

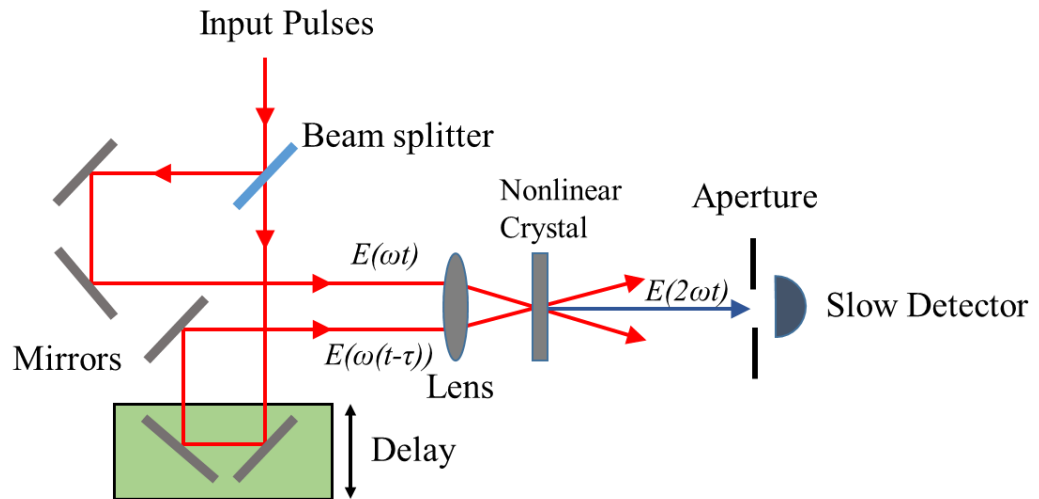


**Figure 1.15: Schematic of an intensity autocorrelator.**

In the time domain, if  $I(t)$  describes the optical intensity of half of the input pulses and  $I(t-\tau)$  describes that of the delayed pulses, the generated autocorrelation signal  $I_{ac}(\tau)$  is given by:

$$I_{ac}(\tau) = \int I(t)I(t - \tau) dt. \quad (1.5)$$

The shorter the pulses are, the faster the autocorrelation signal will decay with the increase of  $\tau$ . For a known pulse shape, the pulse duration is some factor times the duration of the autocorrelation signal according to theoretical calculation. For Gaussian-shaped pulses, the factor is about 0.707, while the factor is about 0.65 for  $\text{sech}^2$ -shaped pulses. We cannot determine the exact shape of ultrafast optical pulses using autocorrelation trace, and it is determined by various parameters, including the number of modes, the group velocity dispersion, etc. In this work, at the very high frequencies reported (560 GHz to 1 THz), AC traces are more like sinusoidal signals, because only two or three lasing modes participated. We therefore assume the pulses here sinusoidal shapes. The pulse duration time is half of the period time of pulses in this circumstance.

#### **1.4.4 The Aim of This Research**

Mode-locked semiconductor lasers are able to generate ultrashort pulses on the order of femtoseconds. These lasers have promising applications in various areas such as femtochemistry, medical imaging and optical spectroscopy. In this work, THz repetition frequency mode-locked lasers based on novel SGDBR structures will be introduced. These diode lasers have higher coupling coefficients than mode-locked lasers based on conventional SGDBR structures, as well as stable multiple-wavelength lasing performance. Using a THz photomixer antenna, generation of THz pulses is realized based on these diode lasers. These mode-locked lasers are compact and can be readily mass produced. When integrated with THz photomixer antennas, it will be possible to manufacture compact and low-cost THz pulse systems in the future.

### **1.5 Thesis Overview**

The thesis is organized as follows. Chapter 2 is aimed at the basic theory and design for novel sampled Bragg gratings (SBGs). The theories of Bragg grating reflection and the transfer matrix method for simulation are reviewed first. Then key highlights of novel SBGs are introduced for DFB lasers and laser arrays, dual-mode lasers, and mode-locked lasers separately. Corresponding simulation results are presented as well.

The materials and fabrication steps for semiconductor diode lasers are introduced in Chapter 3. Wafer structures based on quantum wells and ridge waveguides of DFB lasers are described first. The main fabrication steps carried out for DFB lasers are introduced in detail in this chapter.

In the next three chapters, three types of novel semiconductor lasers will be presented respectively, which are the highlights for the thesis. The fourth chapter describes novel DFB laser diodes and laser arrays. Starting from the principles of design, fabrication results are presented. In this chapter, measurements of novel DFB laser diodes and laser arrays with precisely-controlled wavelengths are presented, including the output optical power, the optical spectra and the far-field patterns. The fifth chapter introduces the realization of novel dual-mode semiconductor lasers, which are used to generate continuous-wave THz

radiation. Meanwhile, mode-locked lasers with THz repetition frequency based on novel SGDBR structures are introduced in the sixth chapter. Characterisation of both the dual-mode lasers and mode-locked lasers is carried out and results are presented. Based on these diode lasers, THz signal generation is expected to be realized.

The last chapter is about conclusions and future work. The main innovation points and achievements are reviewed and highlighted. Furthermore, challenges and suggestions for future work are presented.

## Chapter 2

### Theory and Design

Conventional DFB and DBR semiconductor lasers use Bragg gratings as optical filters to select the lasing wavelengths. Typical optical wavelengths will strongly couple with the Bragg gratings, leading to single frequency operation of the DFB and DBR diode lasers. Figure 2.1 shows schematics of the DFB and DBR lasers fabricated in this thesis. Multi-wavelength lasing was also realized with the same schematic.

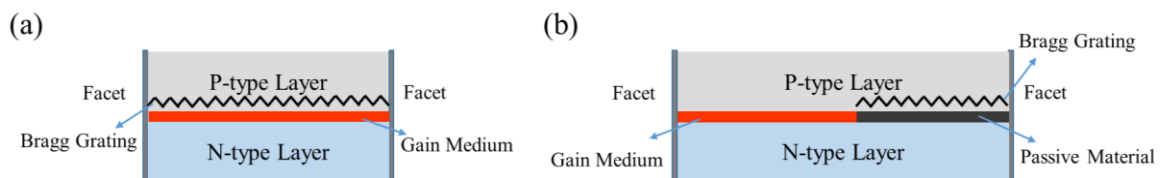


**Figure 2.1: Schematic of (a) DFB diode laser, and (b) DBR diode laser.**

Figure 2.1(a) shows the schematic of a typical DFB diode laser in this thesis. The gain medium, consisting of quantum wells, is placed between the N-type and P-type materials. In the DFB diode laser, the Bragg grating is distributed along the gain medium. As a comparison, Fig. 2.1(b) illustrates the structure of a DBR diode laser. In the DBR diode laser, there are gain sections and passive sections with the Bragg grating distributed along the passive section. The passive section has a wider bandgap than the gain section. The Bragg gratings are important to both of the DFB and DBR lasers. The theory and design of sampled Bragg gratings will be introduced in this chapter. The lasing wavelengths of DFB semiconductor lasers are affected by many factors, including the Bragg gratings, optical gain and loss, nonlinear effects, etc. These factors will lead to the detuning of lasing wavelengths from the Bragg gratings. However, we will focus on the reflectivity spectra of Bragg gratings here. The reflectivity spectra can give a clear picture of single-mode lasing as well as multiple wavelength lasing in semiconductor lasers. They can also be used to effectively explain the precise position of lasing wavelengths and effective coupling coefficients.

## 2.1 Theory of Bragg Grating Reflection

The basic theory of Bragg gratings will be introduced first. Optical coupling between propagating modes is induced when a refractive index perturbation is present in optical waveguides. The refractive index perturbation is generally formed by two different kinds of materials, with refractive index of  $n_1$  and  $n_2$  separately (say  $n_2 > n_1$ , and  $n_2 - n_1 \ll n_1$ ). According to the Fresnel equations, light reflection will occur at the interface of the two materials. For normal incidence light, the reflection coefficient,  $r$ , is described as:

$$r = \frac{n_2 - n_1}{n_2 + n_1} = \frac{\Delta n}{n_2 + n_1}. \quad (2.1)$$

And the transmission coefficient,  $t$ , is

$$t = \frac{2n_1}{n_2 + n_1}. \quad (2.2)$$

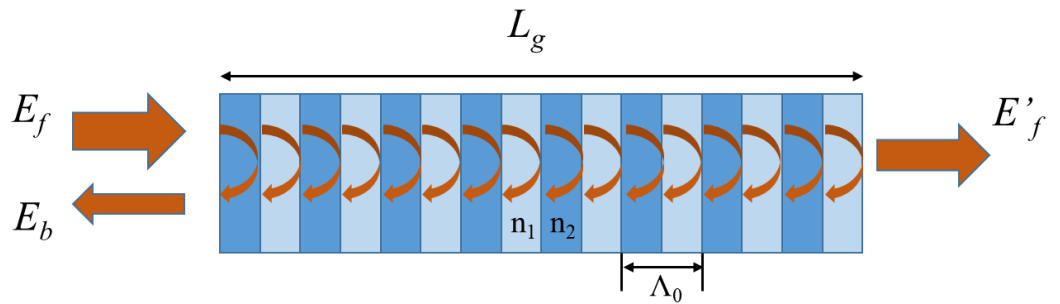


**Figure 2.2: Schematic of a Bragg grating with coupling of forward and backward optical propagating modes.**

As shown in Fig. 2.2, by introducing a periodic perturbation in the propagating direction along the optical waveguide, Bragg gratings are formed. The forward propagating mode ( $E_f$ ) and backward propagating mode ( $E_b$ ) will be strongly coupled with each other at certain values of wavelengths. The resonant wavelengths are given by the Bragg condition:

$$m\lambda_b = 2n_{eff}\Lambda_0, \quad (2.3)$$

where  $m$  is the order of the grating response ( $m$  is an integer,  $m > 0$ ),  $\lambda_b$  is the free space wavelength of the propagating mode satisfying the Bragg condition,  $n_{eff}$  is the effective refractive index of the corresponding waveguide mode and  $\Lambda_0$  is the Bragg grating period. For DFB and DBR semiconductor lasers, the first-order grating ( $m = 1$ ) for wavelength resonance is often adopted, because it has the largest coupling efficiency.

## 2.2 Transfer Matrix Method

The transfer matrix method (TMM) is widely used for Bragg grating analysis, which is based on coupled-mode theory. The coupled-mode theory has been studied in several papers and books [2, 131-134], and it can be derived from the general electromagnetic wave equation for the electric field propagating:

$$\frac{d^2 E}{dz^2} + \beta_0^2 E = 0, \quad (2.4)$$

where  $E$  is the sum of the forward and backward propagating electric fields. For a free space wavelength  $\lambda_b$ , the free space propagation constant  $k_0$  (only considering the first order grating,  $m = 1$ ) can be described as:

$$k_0 = \frac{2\pi}{\lambda_b}. \quad (2.5)$$

If we use  $n(z)$  as the refractive index changing along the propagating direction ( $z$ ), the Bragg propagation constant  $\beta_0$  can be written as:

$$\beta_0 = n(z)k_0. \quad (2.6)$$

And if we use  $R(z)$  and  $S(z)$  representing forward and backward propagating electric fields magnitudes, the general solution of the electric field  $E(z)$  can be given as:

$$E(z) = R(z)e^{-j\beta_0 z} + S(z)e^{j\beta_0 z}. \quad (2.7)$$

For DFB and DBR semiconductor lasers, the difference between  $n_1$  and  $n_2$  is relatively small, which means that  $n(z)$  varies slowly with  $z$ . Hence, the functions  $R(z)$ ,  $S(z)$  and  $E(z)$  all vary slowly along the propagating direction. Therefore, it is reasonable to make the approximation that  $n(z)$  and  $E(z)$  are constant in a small region of the Bragg gratings, which is the basis of the TMM. One key parameter, called the *coupling coefficient*, is used to represent the coupling strength between Bragg gratings and propagating modes. When the gratings have a duty cycle of 0.5, the *coupling coefficient*  $\kappa$  can be expressed as:

$$\kappa = \frac{(n_2^2 - n_1^2)\Gamma_{x,y}}{2n_{ef}^2\Lambda_0}, \quad (2.8)$$

where  $\Gamma_{x,y}$  is the optical confinement factor of the mode to the grating area [134].

Based on the coupled-mode theory, there is a set of equations known as the *coupled-wave equations*:

$$\frac{dR}{dz} + j\Delta\beta R = -j\kappa S \quad (2.9)$$

$$\frac{dS}{dz} + j\Delta\beta S = -j\kappa R, \quad (2.10)$$

where  $\Delta\beta$  is the detuning around  $\beta_0$ , with  $\Delta\beta \ll \beta_0$ . From the equations, when  $\kappa$  equals 0, the two equations are independent. In this circumstance, the forward and backward propagating modes are not coupled with each other. Further, for uniform Bragg gratings with a length of  $L$  (starting from the point of  $z = 0$ ), the coupled-wave equations can be described as:

$$R(L) = \left[ \cosh(\gamma z) - \frac{j\Delta\beta}{\gamma} \sinh(\gamma z) \right] R(0) - \frac{j\kappa}{\gamma} \sinh(\gamma z) S(0) \quad (2.11)$$

$$S(L) = \frac{j\kappa}{\gamma} \sinh(\gamma z) R(0) + \left[ \cosh(\gamma z) + \frac{j\Delta\beta}{\gamma} \sinh(\gamma z) \right] S(0), \quad (2.12)$$

where  $\gamma^2 = \kappa^2 - \Delta\beta^2$  [133]. These equations can be written into a matrix form:

$$\begin{bmatrix} R(L) \\ S(L) \end{bmatrix} = T \begin{bmatrix} R(0) \\ S(0) \end{bmatrix}, \quad (2.13)$$

where  $T$  is

$$T = \begin{bmatrix} \cosh(\gamma z) - \frac{j\Delta\beta}{\gamma} \sinh(\gamma z) & -\frac{j\kappa}{\gamma} \sinh(\gamma z) \\ \frac{j\kappa}{\gamma} \sinh(\gamma z) & \cosh(\gamma z) + \frac{j\Delta\beta}{\gamma} \sinh(\gamma z) \end{bmatrix}. \quad (2.14)$$

$T$  is called the *transfer matrix* [131].

For phase-shifted gratings, the Bragg gratings are not continuous and there is a phase shift  $\varphi$ . In reference [131], the phase-shift matrix is given as:

$$T_\varphi = \begin{bmatrix} \exp\left(\frac{-j\varphi}{2}\right) & 0 \\ 0 & \exp\left(\frac{j\varphi}{2}\right) \end{bmatrix}. \quad (2.15)$$

In general, Bragg gratings can be either phase-shifted, chirped (grating periods vary) or apodized (coupling coefficients vary). Since the chirp and apodization vary slowly along the propagating direction and the gratings are weakly coupled, as an approximation, the Bragg gratings can be divided into many sections. Then, in each section, the gratings are seen as uniform and can be represented by a typical transfer matrix.

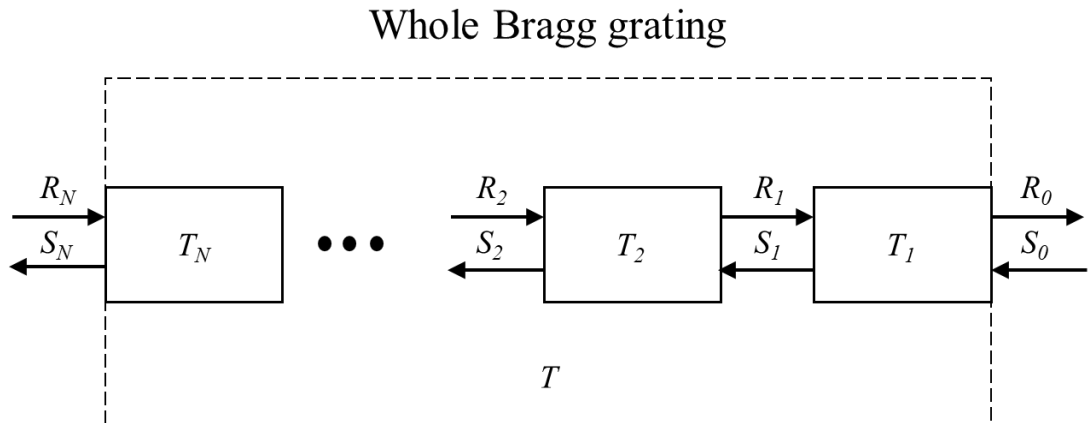


Figure 2.3: Cascaded transfer matrices.

Figure 2.3 shows that the whole Bragg grating is divided into  $N$  sections. Each of the sections is quasi-uniform and can be represented by a transfer matrix. For every individual section  $i$ , we have

$$\begin{bmatrix} R_i \\ S_i \end{bmatrix} = T_i \begin{bmatrix} R_{i-1} \\ S_{i-1} \end{bmatrix} \quad (i = 1, 2 \dots N). \quad (2.16)$$

Then, we can obtain

$$\begin{bmatrix} R_N \\ S_N \end{bmatrix} = T_N * \dots * T_2 * T_1 \begin{bmatrix} R_0 \\ S_0 \end{bmatrix} = T \begin{bmatrix} R_0 \\ S_0 \end{bmatrix}, \quad (2.17)$$

where the net transfer matrix  $T = T_N * \dots * T_2 * T_1$ . The above is a description of how the TMM works.

The TMM is a powerful method to simulate Bragg gratings. In this thesis, the TMM is used to calculate the reflectivity spectra of various kinds of Bragg gratings.

## 2.3 Sampled Bragg Gratings

### 2.3.1 Basic Theory

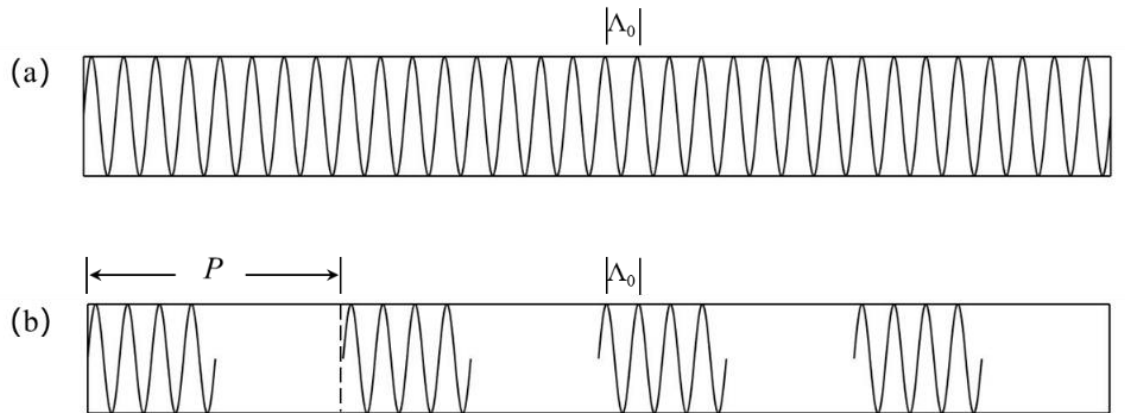


Figure 2.4: Schematics of (a) a uniform Bragg grating, with the grating period  $\Lambda_0$ , and (b) a uniformly-sampled Bragg grating, with the sampling period  $P$ .

For DFB and DBR semiconductor lasers, the first-order Bragg grating periods are only of the order of several hundred nanometres, which means it is not easy to produce complex Bragg gratings by changing the first-order grating periods directly. To overcome this problem, sampled Bragg gratings are used to realize complex grating designs [135, 136]. Figure 2.4(a) shows a uniform first-order Bragg grating with the grating period  $\Lambda_0$ , while Figure 2.4(b) shows a uniformly-sampled Bragg grating, with the sampling period  $P$ . The duty cycle of 0.5 is chosen to achieve the largest coupling coefficients.

Hence, the total refractive index change  $\Delta n_s(z)$  along the propagating direction can be described as:

$$\Delta n_s(z) = \frac{1}{2} s(z) \Delta n \exp\left(j \frac{2\pi z}{\Lambda_0}\right) + c. c., \quad (2.18)$$

where  $\Delta n$  is the refractive index difference and  $s(z)$  represents the sampling structure. Since the sampling structure has a sampling period of  $P$ ,  $s(z)$  can be expanded as a Fourier series:

$$s(z) = \sum_m F_m \exp\left(j \frac{2m\pi z}{P}\right), \quad (2.19)$$

where  $m$  is the order of the Fourier series and  $F_m$  is the corresponding Fourier coefficient. Therefore,  $\Delta n_s(z)$  can be rewritten as:

$$\Delta n_s(z) = \sum_m \frac{1}{2} \Delta n F_m \exp\left(j \frac{2m\pi z}{P} + j \frac{2\pi z}{\Lambda_0}\right) + c. c., \quad (2.20)$$

which can be transformed to a Fourier series:

$$\Delta n_s(z) = \sum_m \frac{1}{2} \Delta n F_m \exp\left(j \frac{2\pi z}{\Lambda_m}\right) + c. c.. \quad (2.21)$$

$\Lambda_m$ , named as the  $m^{\text{th}}$ -order Fourier subgrating, is expressed as:

$$\frac{1}{\Lambda_m} = \frac{m}{P} + \frac{1}{\Lambda_0}. \quad (2.22)$$

In this case,  $\Lambda_0$  can be named as the ‘‘seed grating’’.

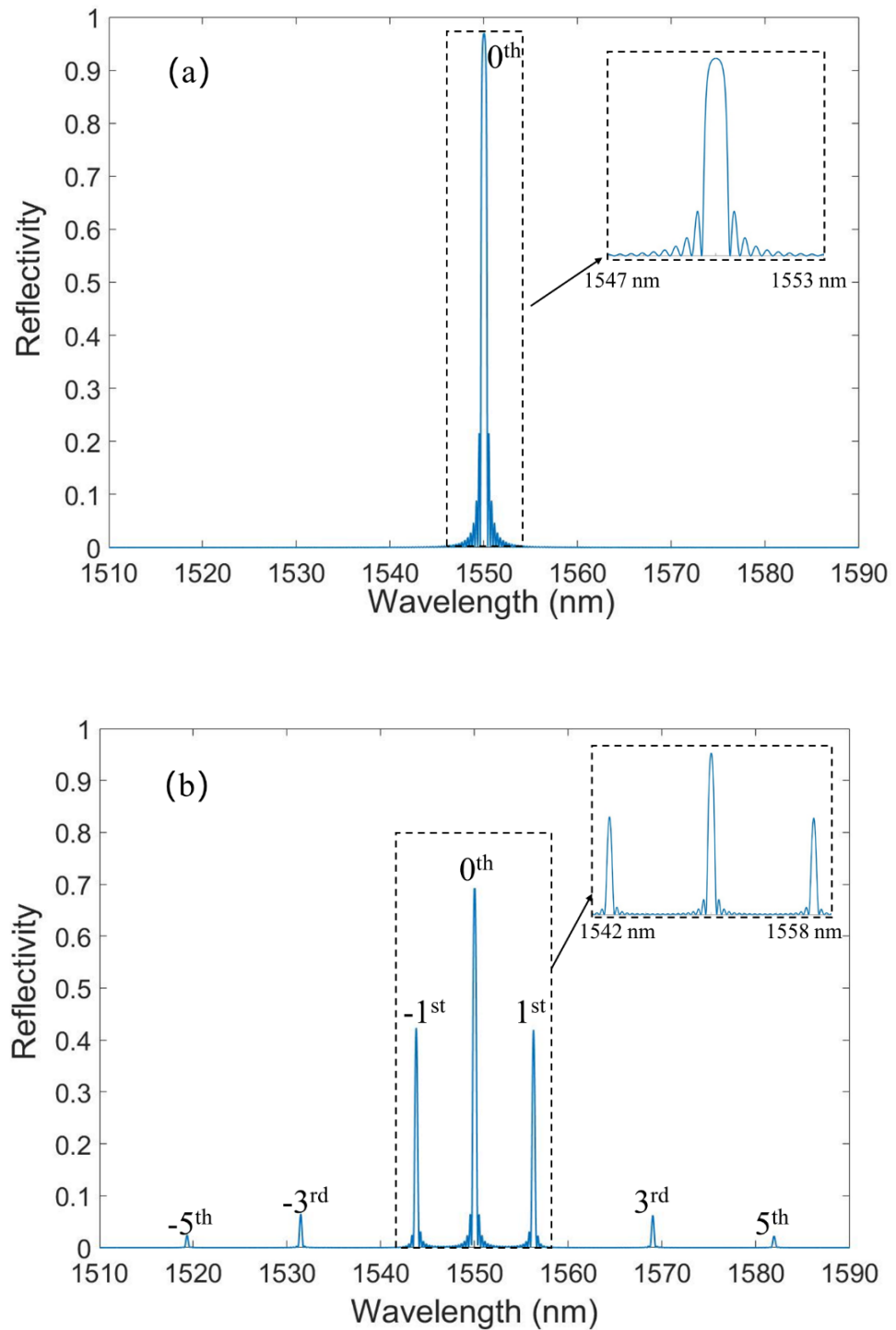


**Figure 2.5: The reflectivity spectrum of (a) a uniform Bragg grating, and (b) a uniformly-sampled Bragg grating.**

By using the TMM, we can calculate the optical reflectivity spectra of uniform Bragg gratings and sampled Bragg gratings by *Matlab* codes. Figure 2.5(a) shows the typical

reflectivity spectrum of a uniform Bragg grating, which has a main reflectivity peak at the Bragg wavelength ( $0^{\text{th}}$ -order reflectivity peak). However, a uniformly-sampled Bragg grating has higher-order reflectivity peaks, as shown in Fig. 2.5(b). The  $\pm 1^{\text{st}}$ -order reflectivity peaks are chosen as working channels for DFB and DBR lasers. Other higher-order reflectivity peaks are relatively weak, and can be neglected in practical applications.

### 2.3.2 Sampled Bragg Gratings with Equivalent Phase Shift

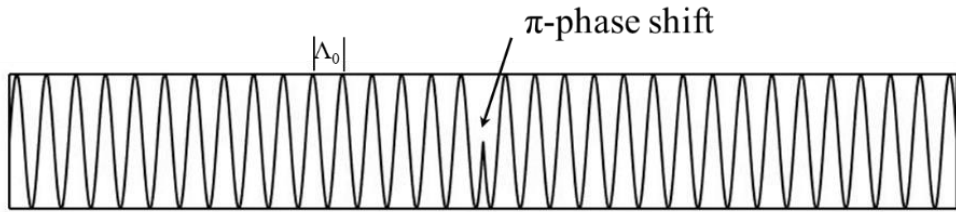


Figure 2.6: Schematic of the uniform Bragg grating with a  $\pi$ -phase shift in the centre.

It is known that DFB semiconductor lasers based on uniform Bragg gratings have the problem of two-mode lasing because of the mode degeneracy [132, 137]. To achieve single-mode lasing, the solution is to introduce a  $\pi$ -phase shift (also called a “quarter-wavelength phase shift”) in the centre, as shown in Fig. 2.6. The  $\pi$ -phase shift can be achieved by shifting the right half of the uniform Bragg grating by half of the grating period. The phase-shifted Bragg grating can be described by the equations:

$$\Delta n(z) = \frac{1}{2} \Delta n \begin{cases} \exp\left(j \frac{2\pi z}{\lambda_0}\right) + c.c & (0 \leq z < z_0) \\ \exp\left(j \frac{2\pi(z+\lambda_0/2)}{\lambda_0}\right) + c.c & (z > z_0) \end{cases}, \quad (2.23)$$

which is

$$\Delta n(z) = \frac{1}{2} \Delta n \begin{cases} \exp\left(j \frac{2\pi z}{\lambda_0}\right) + c.c & (0 \leq z < z_0) \\ \exp\left(j \frac{2\pi z}{\lambda_0} + j\pi\right) + c.c & (z > z_0) \end{cases}. \quad (2.24)$$

$z_0$  is the centre position of the uniform Bragg grating. Figure 2.7 shows the reflectivity spectra of a uniform Bragg grating and a  $\pi$ -phase shift Bragg grating with the same grating period. For a  $\pi$ -phase shift Bragg grating, we can see that the reflectivity is zero at the Bragg wavelength, in the centre of the reflectivity spectrum. By introducing the  $\pi$ -phase shift, single-mode lasing will occur at the Bragg wavelength.

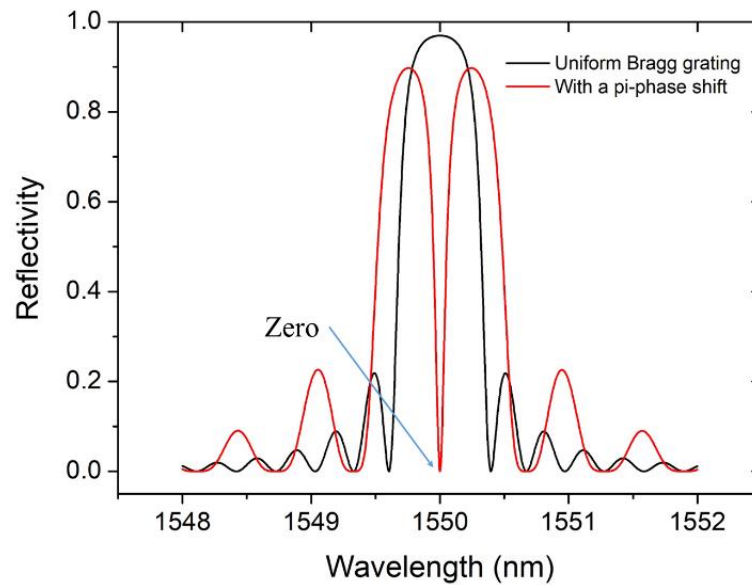


**Figure 2.7: The reflectivity spectra of a uniform Bragg grating and a  $\pi$ -phase shift Bragg grating with the same grating period.**

To achieve various types of functionalities, superstructure gratings have been well developed for a long time, examples of which are multiple grating sections with different grating periods, apodization, chirps, phase shifts, or sampling structures [138]. These specially-designed gratings have been used in many applications, including fibre Bragg gratings for sensing [139, 140], tunable semiconductor lasers with a broad tuning range [141-143], etc. A further technique, called the “equivalent phase shift” (EPS) technique, was developed by Prof. Xiangfei Chen group [144, 145]. The EPS technique was based on the reconstruction-equivalent-chirp (REC) technique. The REC technique is powerful and can realize complex gratings with either phase shifts, chirps or apodization by designing sampled structures without changing the seed Bragg grating period. The REC technique was first applied to fibre Bragg gratings for passive devices, including dispersion compensation [146-149], optical code division multiple access encoders-decoders [150, 151], high channel-count

comb filters [152], etc. Then, the EPS technique was successfully applied to make novel distributed feedback fibre lasers and high quality of single-mode lasing was obtained [153-155]. Further, this technique was applied to fabricate DFB semiconductor lasers [156, 157], and a wide variety of DFB diode lasers have been produced.

Here, the basic theory of the EPS technique will be introduced. If we shift the sampling periods at  $z_0$  in the sampling structure of sampled Bragg gratings by  $\Delta P$ , according to equation (2.20) and (2.23), the sampling structure can be expressed as:

$$\Delta n_s(z) = \frac{1}{2} \Delta n \begin{cases} \sum_m F_m \exp\left(j \frac{2m\pi z}{P} + j \frac{2\pi z}{\Lambda_0}\right) + c. c & (0 \leq z < z_0) \\ \sum_m F_m \exp\left(j \frac{2m\pi z}{P} + j \frac{2\pi z}{\Lambda_0} + j\theta\right) + c. c & (z > z_0) \end{cases}, \quad (2.25)$$

where  $\theta$  is the “equivalent phase” and has the value of

$$\theta = \frac{2m\pi\Delta P}{P}. \quad (2.26)$$

The equivalent phase has the same effect as the “real phase”. That is why we call it the equivalent phase shift technique. When the shift of the sampling periods is half of the sampling period ( $\Delta P = P/2$ ), we get  $\theta = m\pi$ . Apparently, the equivalent phase  $\theta$  is related to the order of the Fourier series  $m$ . The duty cycle of the sampling periods is chosen as 0.5 to obtain the largest coupling efficiency for the  $\pm 1^{\text{st}}$ -order reflection peaks [158]. In this circumstance, when  $m$  is odd, we can obtain an equivalent  $\pi$ -phase shift, however, when  $m$  is even, there is no phase shift at all. Figure 2.8 shows the reflectivity spectra of a uniformly-sampled Bragg gratings with/without an equivalent  $\pi$ -phase shift. Transmission windows indeed appear in the centre of the  $\pm 1^{\text{st}}$ -order reflectivity spectra. Comparing with the transmission window in the reflectivity spectrum of a  $\pi$ -phase shift Bragg grating, as shown in Fig. 2.6, single-mode lasing of DFB semiconductor lasers are expected to be achieved by introducing equivalent  $\pi$ -phase shifts.

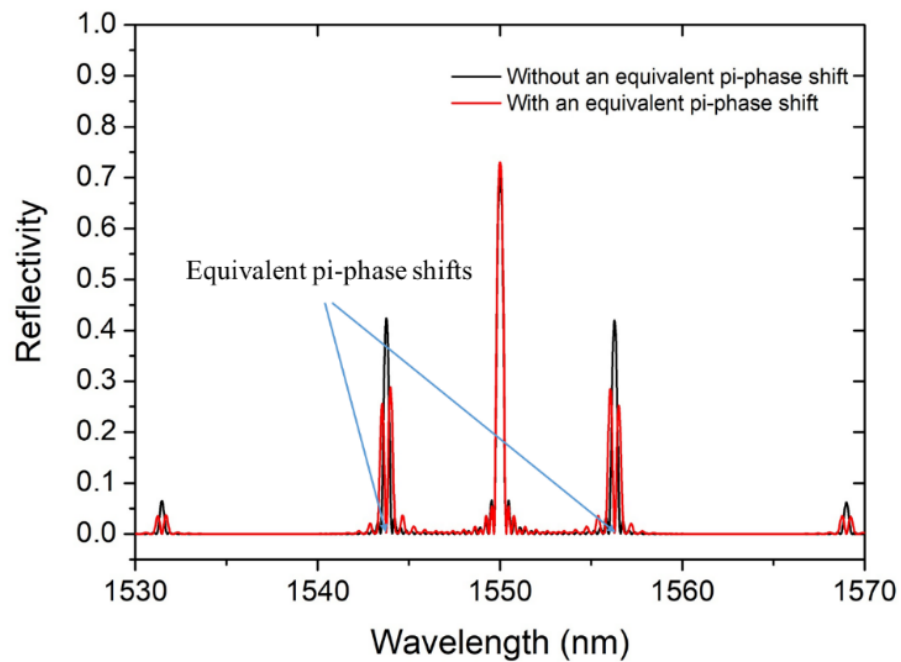


**Figure 2.8:** The reflectivity spectra of the uniformly-sampled Bragg gratings with/without an equivalent  $\pi$ -phase shift.

## 2.4 Sampled Bragg Gratings with Phase-shifted Sections

Firstly, let us consider the sampled Bragg gratings shown in Fig. 2.4(b). From Fig. 2.5, we can see that the reflectivity of the  $\pm 1^{\text{st}}$ -order subgratings of the sampled Bragg gratings decreases significantly compared to a uniform grating. If we want to use the  $\pm 1^{\text{st}}$ -order subgratings as working channels, there will be a related decrease of coupling coefficient,  $\kappa$ , which will influence single-mode lasing of DFB semiconductor lasers. Specifically, by calculating the Fourier coefficients, we can draw the conclusion that the  $\kappa$  associated with the  $\pm 1^{\text{st}}$ -order subgratings are only  $1/\pi$  ( $\sim 0.32$ ) times that of uniform Bragg gratings, which may be not sufficient for a DFB or DBR semiconductor laser to lase. Such a large reduction in  $\kappa$  is not desirable; either the cavity length of the laser ( $L$ ) has to be increased to maintain an optimum  $\kappa L$  product at the expense of an increase in threshold current, or  $\kappa L$  is reduced which will affect the stability of SLM operation. Furthermore, although in this sampling structure the 0th-order reflection strength is reduced to half of that of a uniform grating (no sampling), it remains the strongest reflection and its presence may affect the operation of the working channels.

Designs of SBGs that incorporate phase-shifted sections can overcome these defects, by simultaneously enhancing the effective  $\kappa$  of the  $\pm 1^{\text{st}}$ -order channels and eliminating the  $0^{\text{th}}$ -order reflection. A technique called the “Multiexposure Technique” has successfully been used to make distributed feedback fibre lasers [159]. The general idea for this technique is to fill the blank parts of the sampling structures (as shown in Fig. 2.4(b)) with phase-shifted sections. For distributed feedback fibre lasers, the multiexposure technique can be realized by several steps’ exposure for different sections of gratings in every sampling period. The phase shifts between different sections were achieved by simply moving the position of the fibre longitudinally. However, to achieve  $\pi$ -phase shifts for DFB/DBR semiconductor lasers, a shift of half of the grating period is only about one hundred nanometres, which can hardly be realized mechanically. In this thesis, we apply this technique to DFB and DBR semiconductor lasers by using electron beam lithography (EBL) for the first time. New designs of sampled Bragg grating structures will be introduced for novel semiconductor lasers.

### 2.4.1 Structures for High Coupling Coefficients

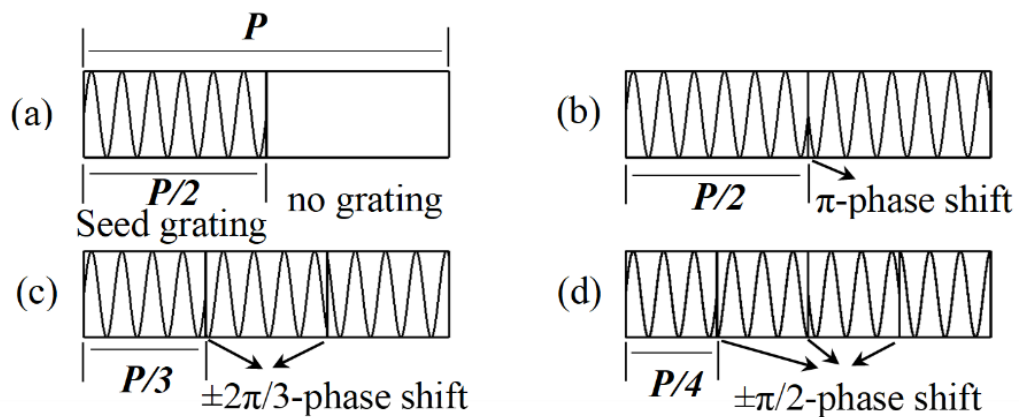


**Figure 2.9: Grating structures of (a) C-SBG, (b) 2PS-SBG, (c) 3PS-SBG and (d) 4PS-SBG.  $P$  is the sampling period [160].**

The principle of introducing phase-shifted sections into SBGs is illustrated in Fig. 2.9, where various designs are shown. Figure 2.10 shows the corresponding reflectivity spectra of these structures. Figure 2.9(a) shows the design of a conventional SBG (C-SBG), which is the same as the structure shown in Fig. 2.4(b). With a duty cycle of 0.5, the reflectivity spectrum

of a C-SBG is illustrated in Fig. 2.10(a). The theoretical analysis and simulation results were already presented in Reference [159]. Figure 2.9(b) illustrates an SBG with two phase-shifted sections in a single sampling period (2PS-SBG), in which a  $\pi$  phase-shifted seed grating fills a half of the sampling period where the grating would be absent in a C-SBG. In a 2PS-SBG structure, the 0<sup>th</sup>-order reflection disappears and the effective  $\kappa$  of the  $\pm 1^{\text{st}}$ -order channels is doubled compared to the C-SBG, with a value of  $2/\pi$  ( $\sim 0.64$ ) times that of a uniform grating, as shown in Fig. 2.10(b). We can further divide the sampling period into more equal sections to obtain progressively higher effective  $\kappa$ . If we divide one sampling period  $P$  into  $m$  equal sections ( $m > 2$ ), with length of  $P/m$  in every section, the phase shift between adjacent sections can be set as  $\pm 2\pi/m$ . When the phase shift is  $-2\pi/m$ , simulation shows the  $\kappa$  of the  $-1^{\text{st}}$ -order channel will be enhanced, with both the 0<sup>th</sup>-order and 1<sup>st</sup>-order channels suppressed, and vice versa. Figure 2.9(c) shows an SBG with three phase-shifted sections (3PS-SBG) and Fig. 2.9(d) illustrates an SBG with four phase-shifted sections (4PS-SBG), the effective  $\kappa$  of which are calculated to be about 0.83 and 0.90 times that of a uniform Bragg grating respectively. The reflectivity spectra of 3PS-SBG and 4PS-SBG are shown in Fig. 2.10(c) and Fig. 2.10(d) respectively, with the respective phase shift of  $-2\pi/3$  and  $-2\pi/4$ .

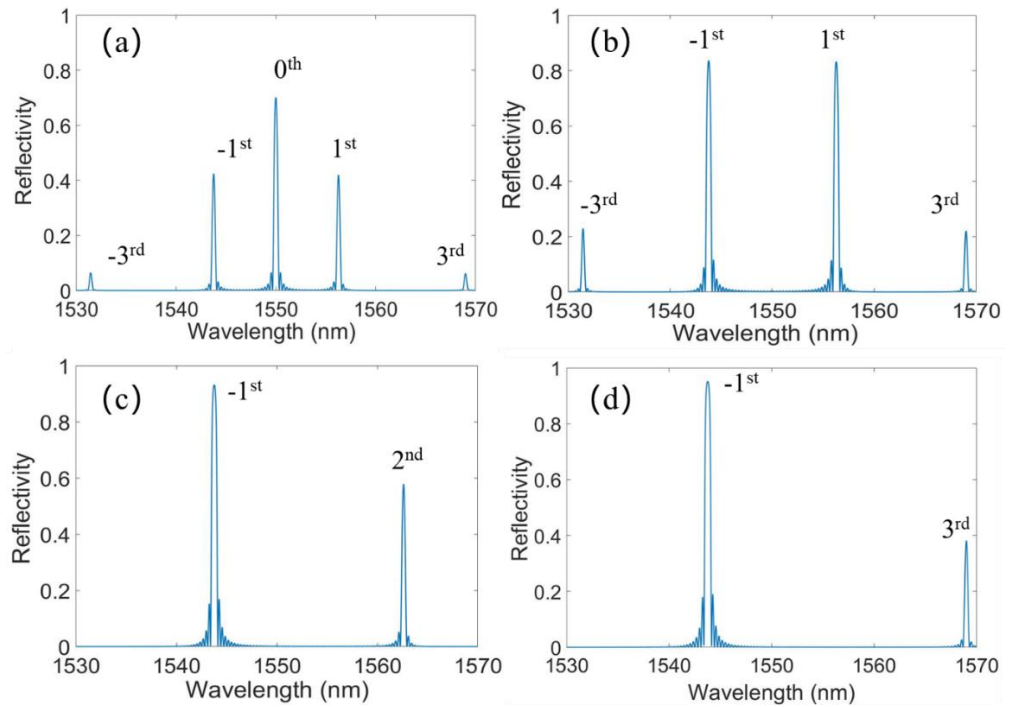


**Figure 2.10: Reflectivity spectra of (a) C-SBG, (b) 2PS-SBG, (c) 3PS-SBG and (d) 4PS-SBG.**

Combined reflectivity spectra of the four sampling structures with phase-shifted sections are illustrated in Fig. 2.11. Focusing on the  $-1^{\text{st}}$ -order reflectivity peaks, the reflection peak becomes higher with an increasing number of divided sections, which means higher effective  $\kappa$  is achieved. For 3PS-SBG and 4PS-SBG, the effective  $\kappa$  is very close to that of the uniform grating. To obtain single-mode lasing, it is straightforward to introduce equivalent  $\pi$ -phase shifts into the sampling structures by shifting the sampling periods by half of the sampling period in the centre of the sampling structures. By applying the EPS principles, DFB diode lasers with different lasing wavelengths can be realized with high precision by only changing the sampling periods.

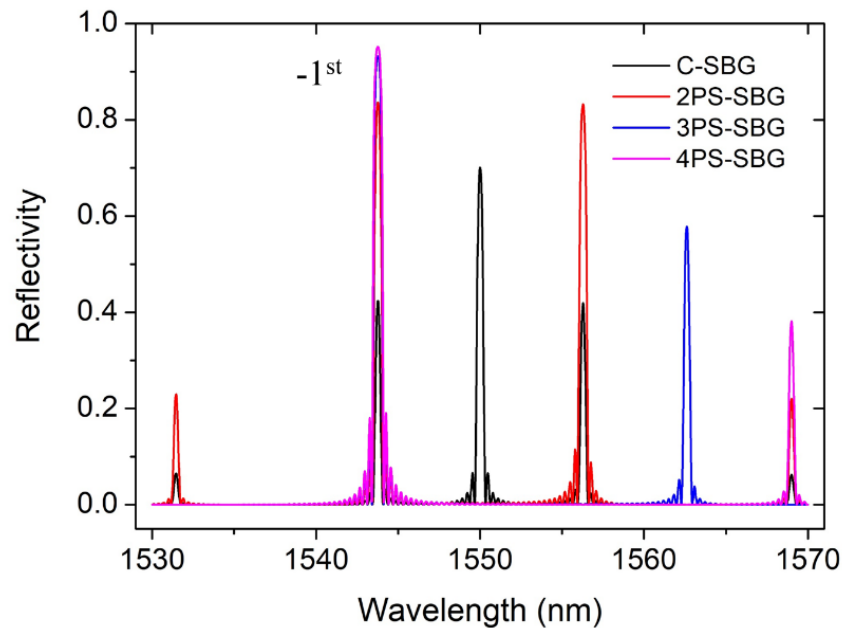


Figure 2.11: Combined reflectivity spectra of C-SBG, 2PS-SBG, 3PS-SBG and 4PS-SBG.

## 2.4.2 Structures for Dual-mode Lasers

If we take a look at Fig. 2.10(b), the reflectivity spectrum of 2PS-SBG, it is natural to come up with the idea to make dual-mode lasers based on this structure. In this structure, if the  $\pm 1^{\text{st}}$ -order channels move closer, the laser may obtain stable lasing at two wavelengths at the same time. Hence, dual wavelength lasing in a single cavity could be achieved. By designing the wavelength spacing to be several nanometres, THz signals can be generated by photomixing with the two lasing wavelengths.

From equation (2.22), we can obtain the grating periods  $\Lambda_{\pm 1}$  for the  $\pm 1^{\text{st}}$ -order subgratings as:

$$\frac{1}{\Lambda_{\pm 1}} = \frac{1}{\Lambda_0} \mp \frac{1}{P}, \quad (2.27)$$

which is

$$\Lambda_{\pm 1} = \frac{P\Lambda_0}{P \mp \Lambda_0} \approx \Lambda_0 \pm \frac{\Lambda_0^2}{P}. \quad (2.28)$$

Generally, the sampling period  $P$  is much larger than  $\Lambda_0$ . According to equation (2.3), we can calculate the wavelength spacing  $\Delta\lambda_{\pm 1}$  between the  $\pm 1^{\text{st}}$ -order reflectivity peaks:

$$\Delta\lambda_{\pm 1} \approx 4n_{eff} \frac{\Lambda_0^2}{P}. \quad (2.29)$$

By simply adjusting the sampling period  $P$ , different wavelength spacings can be achieved.

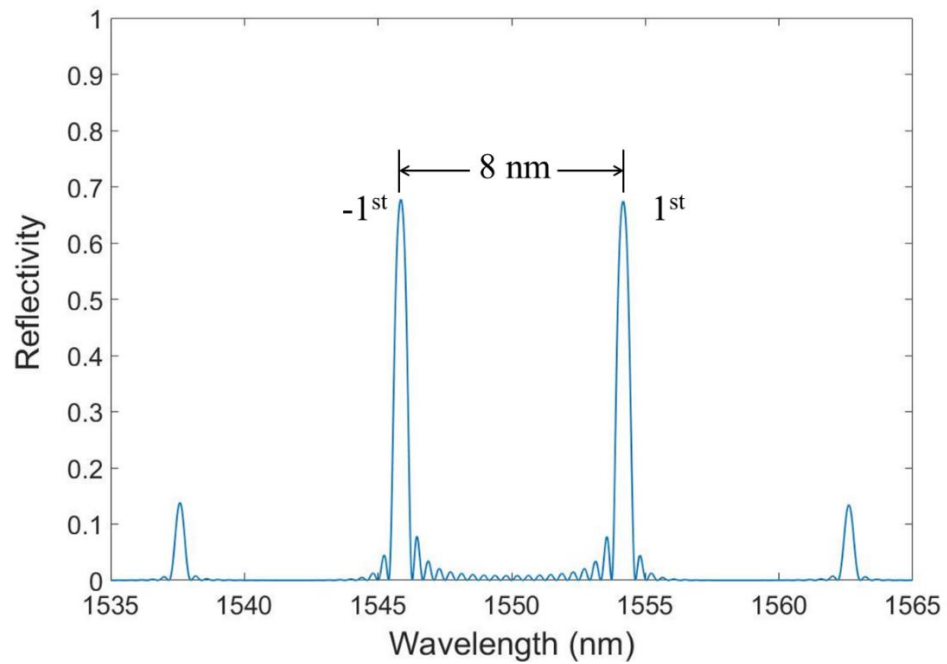


**Figure 2.12: The reflectivity spectrum of 8 nm wavelength spacing between  $\pm 1^{\text{st}}$ -order channels.**

For example, Figure 2.12 shows the reflectivity spectrum of an 8 nm wavelength spacing, which corresponds to 1 THz in frequency.

To achieve single-mode lasing for each channel, an EPS can be introduced in the centre of the sampling structure. Figure 2.13 shows the corresponding reflectivity spectrum with an EPS where transmission windows appear in the centre of the  $\pm 1^{\text{st}}$ -order channels at the same time. Hence, two wavelengths of the  $\pm 1^{\text{st}}$ -order channels lasing at the same time could be achieved.

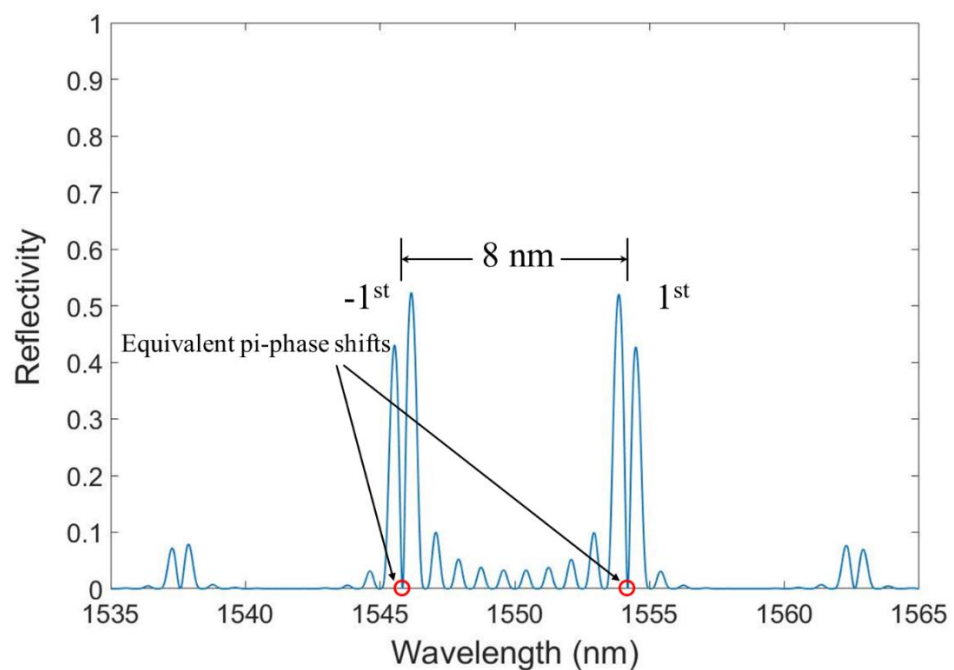


**Figure 2.13: The reflectivity spectrum of 8 nm wavelength spacing between  $\pm 1^{\text{st}}$ -order channels with EPS.**

### 2.4.3 Structures for Mode-locked Lasers

Sampling structures of sampled-grating distributed Bragg reflector (SGDBR) are widely used in tunable semiconductor lasers, since a comb-like optical filter can be generated [161, 162]. By supporting multiple wavelength lasing, SGDBR structures can also be applied to make mode-locked lasers. The conventional SGDBR (C-SGDBR) structure is similar to the

C-SBG structure, only with the difference of the duty cycle. To support multiple wavelength lasing, the duty cycle  $r$  (defined as the length of the gratings in each sampling period divided by the length of the sampling period) needs to be low enough to make the optical reflectivity spectrum as uniform as possible. However, the duty cycle  $r$  cannot be too small, or the effective  $\kappa$  will not be large enough to support multiple wavelength lasing. Figure 2.14 shows the sampling structure for a C-SGDBR.

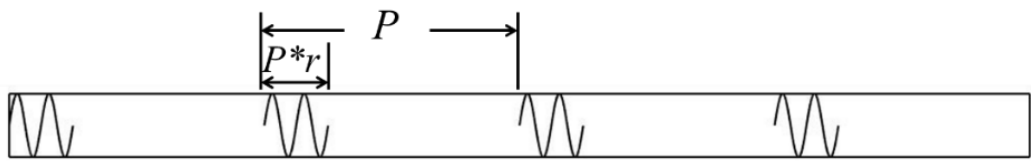


**Figure 2.14:** The sampling structure of a C-SGDBR.  $P$  is the sampling period and  $r$  is the duty cycle.

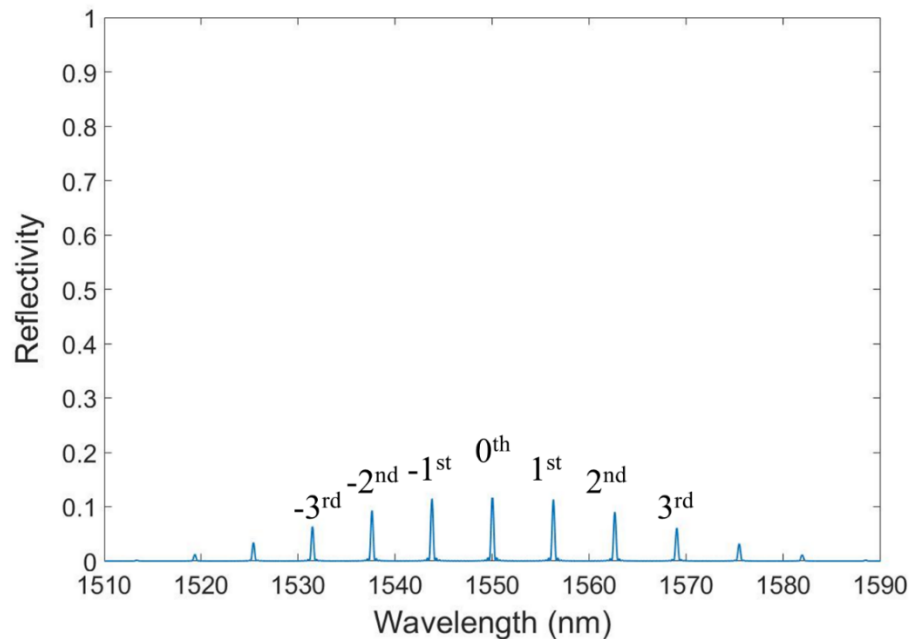


**Figure 2.15:** The reflectivity spectrum of a C-SGDBR, with a duty cycle  $r$  of 0.15.

Using the same parameters as in Fig. 2.5, Figure 2.15 shows the simulated reflectivity spectrum of a C-SGDBR, with the duty cycle  $r$  of 0.15. Compared with Fig. 2.5 (b), the reflectivity peaks drop by a factor of 0.3, which means that the effective  $\kappa$  is much lower and is not suitable for making a high-performance mode-locked semiconductor laser. To

overcome this problem, phase-shifted sections could be introduced into the sampling structures. The new structure is named as a  $\pi$  phase-shifted SGDBR (PPS-SGDBR) structure. Figure 2.16 shows the sampling structure of a PPS-SGDBR with the duty cycle of  $r$  ( $0 < r \leq 0.5$ ) in a sampling period. Here, the duty cycle,  $r$ , is defined as the length of the uniform gratings in each sampling period divided by the length of the sampling period. Hence, the percentage of the length of the  $\pi$  phase-shifted gratings in each sampling period is  $1 - r$ .

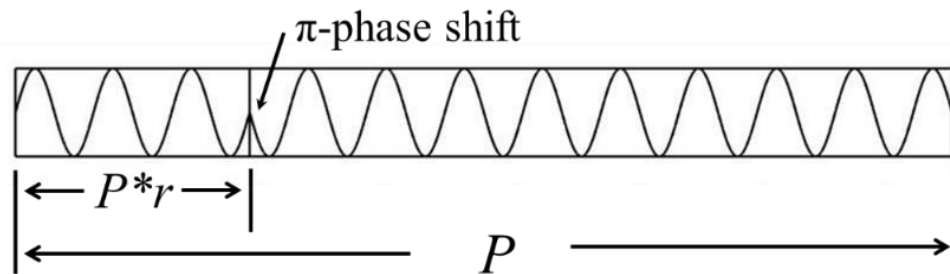


Figure 2.16: The sampling structure of a PPS-SGDBR.

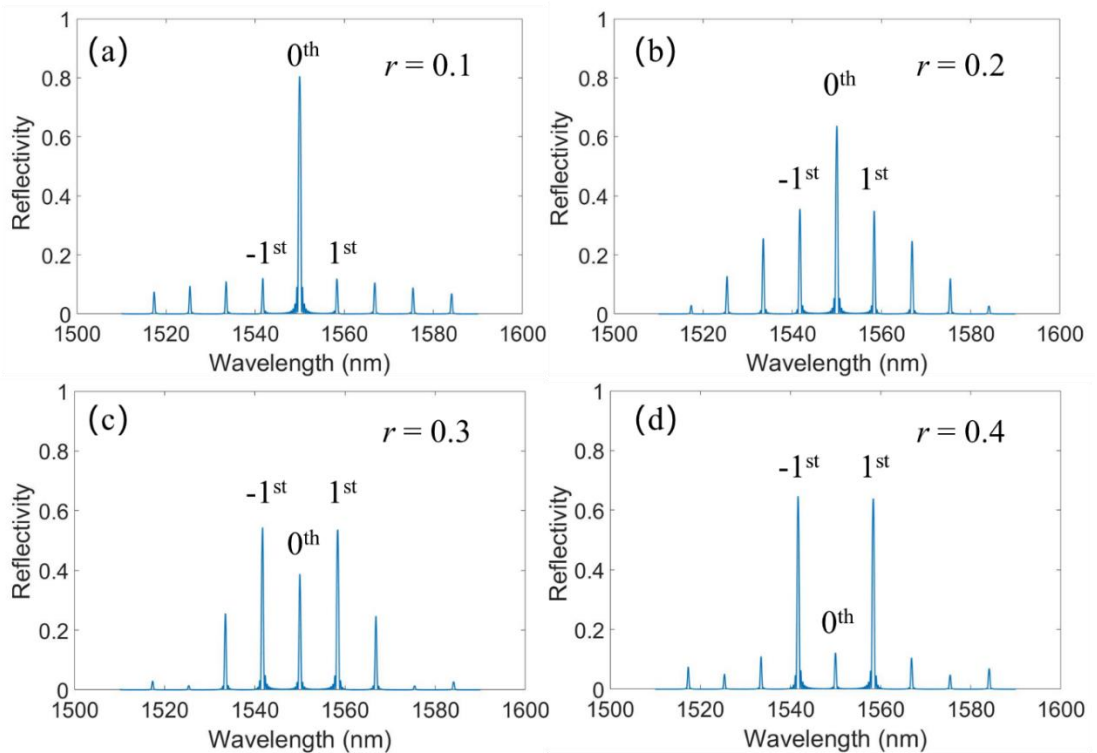


Figure 2.17: The reflectivity spectra of a PPS-SGDBR, with the duty cycle  $r$  of (a) 0.1, (b) 0.2, (c) 0.3 and (d) 0.4.

Using the TMM, simulated by *Matlab* codes, Figure 2.17 illustrates the reflectivity spectra of a PPS-SGDBR, with duty cycles of 0.1, 0.2, 0.3 and 0.4 respectively. With the increase of the duty cycle, the reflectivity peak of the 0<sup>th</sup>-order channel drops while these of the  $\pm 1^{\text{st}}$ -order channels rise. To make the reflectivity spectrum as uniform as possible, the duty cycle is chosen as 0.25 and the corresponding reflectivity spectrum is shown in Fig. 2.18. The reflectivity spectrum is uniform enough to make a mode-locked laser with a THz repetition frequency. The coupling coefficient increases as expected, with the effective  $\kappa$  about 3 times as large as that of the spectrum shown in Fig. 2.15. The same as for the design of dual-mode semiconductor lasers, different wavelength spacings can be achieved by simply changing the sampling periods for mode-locked lasers based on SGDBR structures.

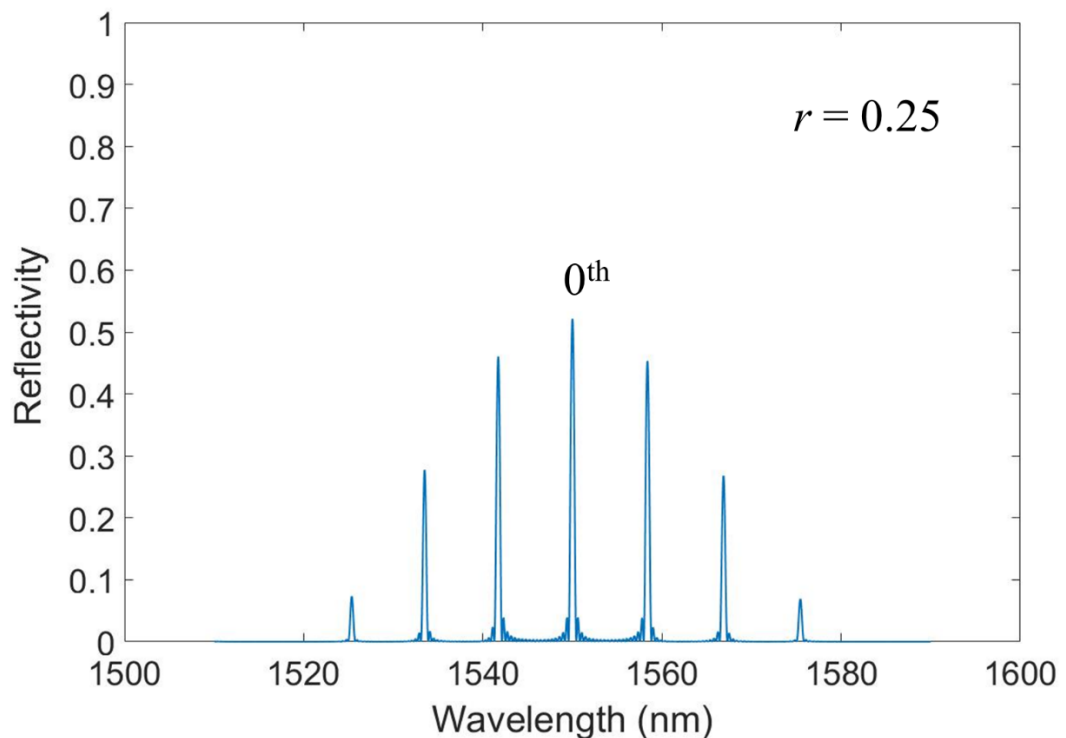


Figure 2.18: The reflectivity spectrum of a PPS-SGDBR, with the duty cycle  $r$  of 0.25.

## 2.5 Chapter Summary

In this chapter, the theory and design of the SBGs were introduced including novel SBG structures with phase-shifted sections. The theory of the uniform Bragg grating was introduced first, which is the basis for complex Bragg gratings. Then the transfer matrix

method was described in detail and it was shown to be a powerful tool for the simulation of various kinds of Bragg gratings. The transfer matrix for the phase shift in the grating structures was also identified. For complex gratings, the gratings were divided into many sub-sections and each section could be described by a transfer matrix. Then the basic theory of SBGs was introduced. Higher orders of reflectivity peaks appear on both sides of the seed grating's reflectivity peak by introducing sampling structures. An equivalent phase shift can easily be introduced in the sampling structure for single-mode lasing of DFB lasers and it has the same effect as a "real" phase shift. However, the coupling coefficient decreases significantly for the C-SBG. To overcome this problem, novel SBGs with phase-shifted sections were introduced. This is an effective way to increase the coupling coefficient, which is beneficial for single-mode lasing of DFB semiconductor lasers. New SBG structures for dual-mode lasers were also introduced based on the 2PS-SBG structure. These dual-mode lasers can be used as the laser sources for continuous-wave THz signals generated by photomixing. Additionally, new SBG structures for mode-locked lasers were designed. Through simulation with the TMM, an optimized duty cycle of 0.25 was identified to gain a reasonably uniform reflectivity spectrum. The new sampled Bragg grating designs introduced here are expected to be used to make novel mode-locked semiconductor lasers to generate THz pulses.

## Chapter 3

### Materials and Fabrication

The semiconductor lasers fabricated in this thesis are all based on commercial multiple quantum well (MQW) epitaxial wafers and the wafers were bought from the IQE Company. The design concepts for DFB lasers are based on ridge waveguides with sidewall gratings, which are easy to fabricate and no regrowth is required. Ridge waveguides offer a versatile route to device integration that eliminates the oxidation and contamination problems associated with regrowth. Compared to buried heterostructure devices, the threshold current of ridge waveguides is higher because of the wider waveguide and current spreading. However, ridge waveguide devices generally deliver higher optical powers, which is an important consideration for transceivers in passive optical networks (PONs). The devices were fabricated in the James Watt Nanofabrication Centre (JWNC) at the University of Glasgow [163], which is a nanofabrication platform offering the necessary state-of-the-art facilities. The JWNC has a vast number of facilities and its staff are professional, which is beneficial for making devices with good performance.

#### 3.1 MQW Wafer Structures

The design of wafer structures has a strong relationship with the material, since different alloys have different electrical and optical characteristics, e.g. refractive index, bandgap, etc. Wafer structures need to be optimized according to the applications. For example, if high frequency modulation is the target, more quantum wells are expected to be used, while for narrow linewidth lasers, a low optical confinement factor is essential, which means that fewer quantum wells are the choice [164]. The different alloys chosen for different layer structures will also have an impact on the geometrical characteristics of the devices, which will largely affect the far-field patterns (FFPs) of the output optical modes. For telecommunications devices, we made the choice of a material with its wavelength peak of the gain spectrum in the C-band wavelength range (1530-1565 nm). After so many years of development, the growth techniques for semiconductor lasers based on InP are mature. The material systems of InGaAsP/InP and AlGaInAs/InP are two general choices. To let the two

quaternary alloys be epitaxially grown on InP, the following relations need to be fulfilled for lattice matching: for  $\text{In}_{1-x}\text{Ga}_x\text{As}_y\text{P}_{1-y}$ :  $x \approx 0.46 y$  and for  $\text{AlGaInAs} = (\text{Al}_{0.48}\text{In}_{0.52}\text{As})_z(\text{Ga}_{0.47}\text{In}_{0.53}\text{As})_{1-z}$  [165, 166]. Within the two quaternary alloy systems, for the same bandgap, the electron and hole effective masses, the refractive index and the room temperature Hall mobilities are very similar [167]. The major difference is the band offsets, as shown in Fig. 3.1. It can be calculated that the ratios between the conduction band offset and the bandgap difference are 0.40 for  $\text{In}_{0.53}\text{Ga}_{0.47}\text{As}/\text{InP}$  and 0.75 for  $\text{In}_{0.53}\text{Ga}_{0.47}\text{As}/\text{Al}_{0.48}\text{In}_{0.52}\text{As}$ . As a result, AlGaInAs/InP alloys have better confinement for electrons, and a consequence offer better high-temperature performance of lasers [168]. Here, AlGaInAs/InP alloys are chosen for the semiconductor diode lasers.

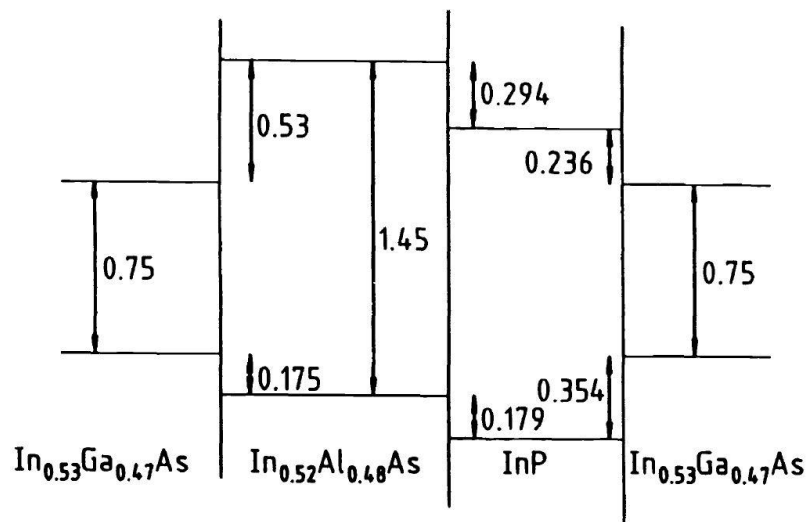


Figure 3.1: Band offsets between InP lattice-matched materials [167].

Figure 3.2 illustrates the wafer structure used, which uses the AlGaInAs/InP material system. The commercially available 2-inch IQE five quantum well (QW) wafer structure has a wavelength peak in the gain spectrum at around 1550 nm and is grown by MOCVD, consisting of five compressively strained (12000 ppm) 6 nm thick  $\text{Al}_{0.07}\text{Ga}_{0.22}\text{In}_{0.71}\text{As}$  wells with six tensilely strained ( $-3000$  ppm) 10 nm thick  $\text{Al}_{0.224}\text{Ga}_{0.28}\text{In}_{0.49}\text{As}$  barriers. The QWs and barriers are situated between two 60 nm AlGaInAs graded index separate confinement heterostructure (GRINSCH) layers, which prevent electrons and holes escaping from the QW region. A heavily-doped 800 nm N-type InP buffer layer is used as the lower cladding

and a 1600 nm P-type InP layer is used as the upper cladding, which is also heavily doped. Just below the InP upper cladding, a 20 nm wet etch stop layer of  $\text{In}_{0.85}\text{Ga}_{0.15}\text{As}_{0.33}\text{P}$  is introduced for better control of etching depth. On top of the structure, the material of the 200 nm contact layer is chosen as heavily doped ( $1.5 \times 10^{19} \text{ cm}^{-3}$ ) InGaAs for better ohmic contact. All layers (except the wells and barriers) are lattice-matched to the highly-doped N-type InP substrate and the wafer has a thickness of 360  $\mu\text{m}$ . Zn and Si are used as the P-type and N-type dopants respectively, and Figure 3.3 shows the energy band diagram for the conduction bands of all the layers.

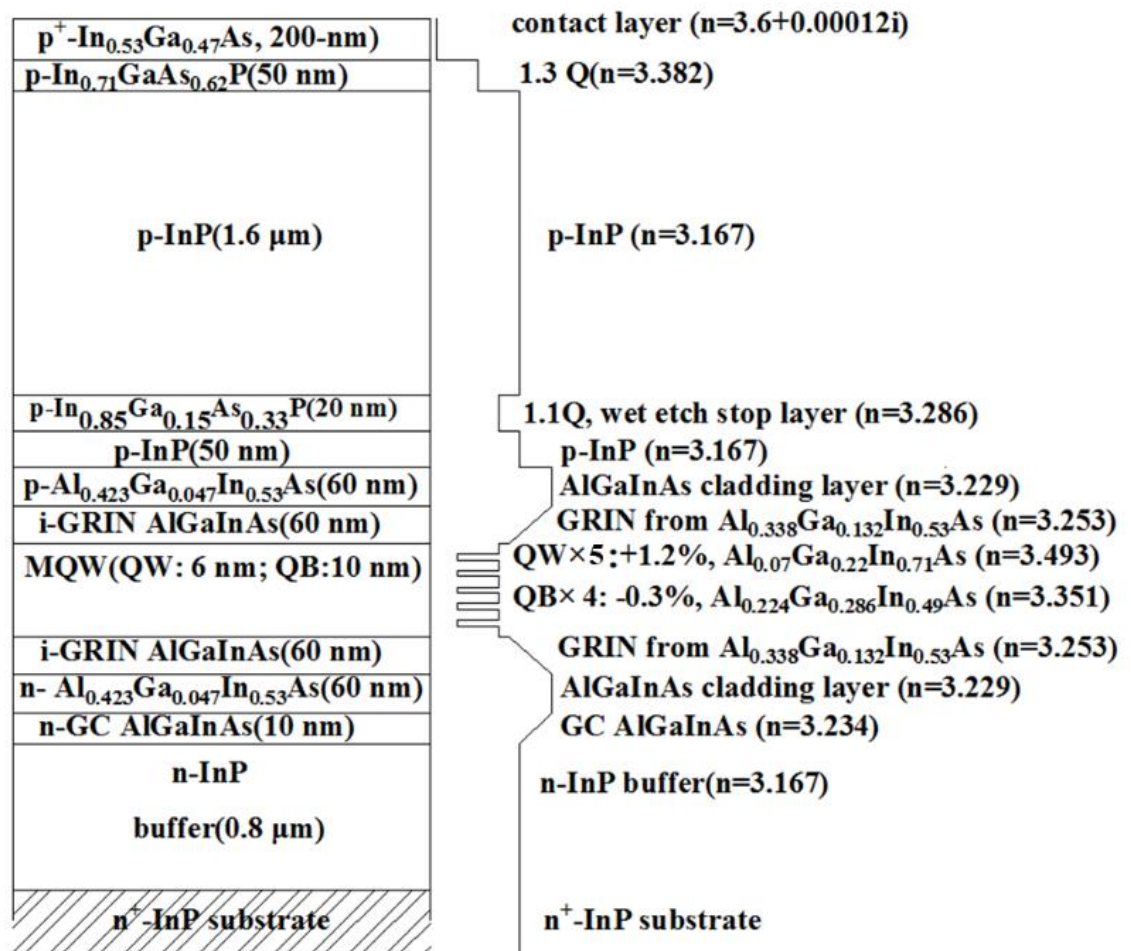


Figure 3.2: IQE five quantum well wafer structure.

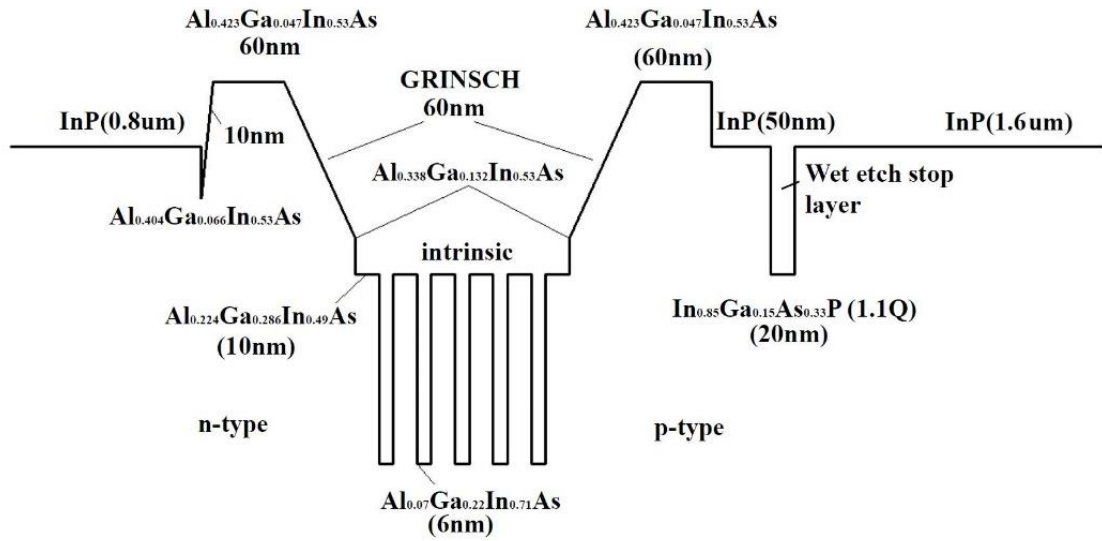


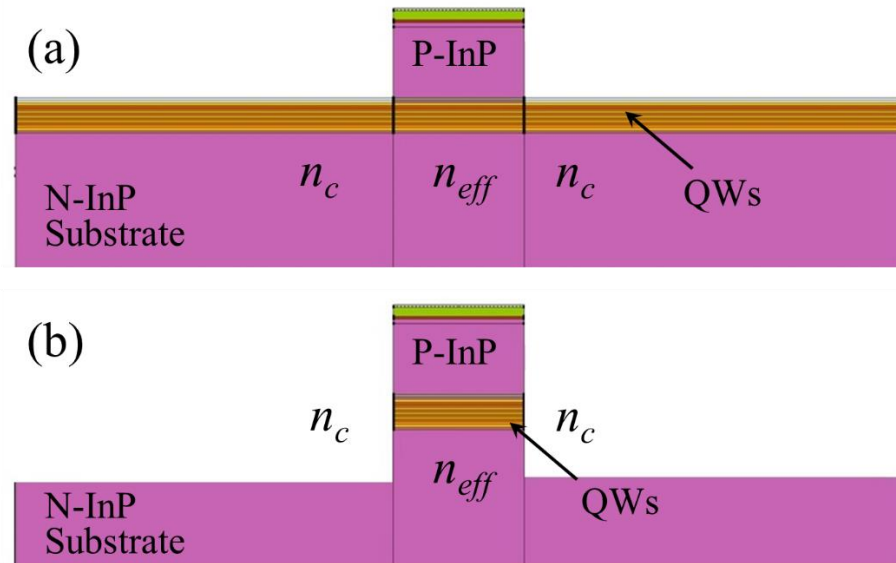
Figure 3.3: Energy band diagram for the conduction bands of the layers.

Figure 3.2 also shows the refractive index of each layer and the refractive index distribution is designed to be symmetric from top to bottom centred on the QW region. The refractive index of the QW region is the highest while InP has the lowest refractive index on the upper and lower side of the QWs, which leads to optical confinement vertically. To achieve optical confinement laterally, ridge waveguides need to be introduced.

## 3.2 Ridge Waveguides

### 3.2.1 Waveguide Design

Lateral optical confinement can be realized by introducing a shape-induced refractive index difference laterally. Shape-induced refractive index differences are achieved by introducing ridge waveguides. There are two main kinds of such index guiding: shallow-etched and deep-etched ridge waveguides, as shown in Fig. 3.4.



**Figure 3.4: Schematic of the cross-section of a (a) shallow-etched ridge waveguide and (b) deep-etched ridge waveguide, where  $n_{eff}$  is the effective refractive index of the optical mode and  $n_c$  is the refractive index of “cladding” layer.**

For shallow-etched waveguides, the material is etched to a depth between the original surface and the upper edge of the active region (etching down for 1920 nm in this circumstance based on the wafer structure, as shown in Fig. 3.2), while deep-etched waveguides are etched through the active region. After the ridge waveguides were etched, a SiO<sub>2</sub> layer was deposited and covered the ridge waveguides for protection and insulation. Deep-etched ridge waveguides have a stronger optical confinement than shallow-etched ridge waveguides. Deep-etched ridge waveguides are preferred for making passive devices, since better optical confinement leads to a smaller size of the devices [169], also reducing capacitance for modulators. However, semiconductor lasers are fabricated based on shallow-etched ridge waveguides because defects can be easily introduced into QWs when etching through the active region, which would make the diode lasers not reliable. On the other hand, as the etching does not penetrate into the active region, the shallow-etched waveguides have a reduced carrier recombination rate at the sidewalls and less optical scattering loss will be introduced by the sidewall roughness. In this thesis, all the fabricated semiconductor lasers are based on shallow-etch ridge waveguides.

### 3.2.2 Optical Modes

For a DFB laser with a compressively strained QW structure, only the TE modes will lase [10]. Moreover, the number of the guided TE modes depends on the width of the ridge waveguide. When the ridge waveguide is narrow enough, only the fundamental TE mode will lase, with higher-order optical modes suppressed. The simulation for optical modes was carried out by *Lumerical MODE Solutions*, based on the ridge waveguides etched to a depth of 1920 nm. In this software, the Finite Difference Eigenmode (FDE) solver is used to calculate the mode field profile and effective index by solving Maxwell's equations on a cross-sectional mesh of the waveguide. The waveguide modal effective index versus ridge width for the fundamental, 1<sup>st</sup> and 2<sup>nd</sup> TE modes was simulated at the wavelength of 1550 nm, as shown in Fig. 3.5. For a specific TE mode, the modal effective index increases with the increase of ridge width. For the same ridge width, high-order modes have a lower waveguide modal effective index. From this figure, we can see that only the fundamental mode is supported when the ridge width is 2  $\mu\text{m}$  and below. Considering the fabrication tolerance, the ridge width is chosen as 2.5  $\mu\text{m}$  in this work for semiconductor lasers. Only the fundamental TE mode was observed to lase and higher order TE modes were not supported, because they experience higher loss than that of the fundamental TE mode.

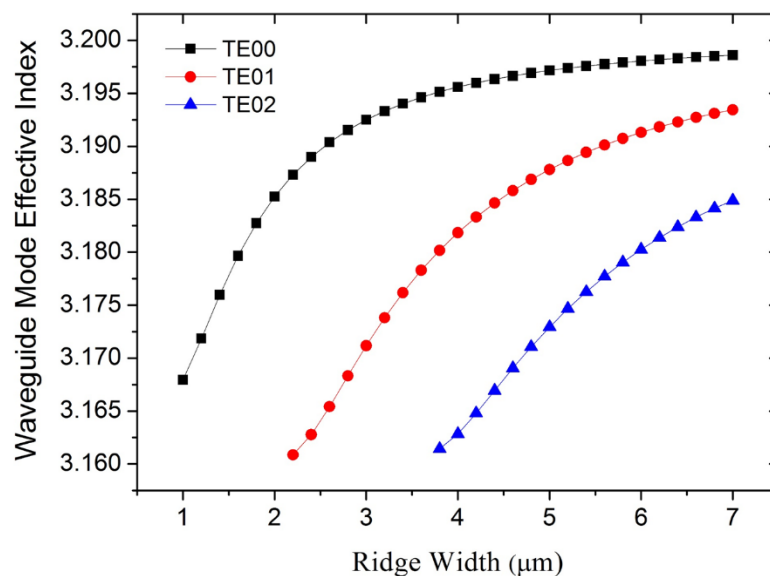


**Figure 3.5: Waveguide modal effective index versus ridge width for the fundamental, 1<sup>st</sup>- and 2<sup>nd</sup>-order TE modes at 1550 nm.**

Figure 3.6 shows the simulated fundamental optical mode for a shallow-etched ridge waveguide for the 2  $\mu\text{m}$  wide, 1920 nm deep ridge. The single optical mode is sufficiently confined by the shallow-etched ridge waveguide. The modal effective index is calculated to be 3.185 for this structure based on the wafer structure shown in Fig. 3.2.

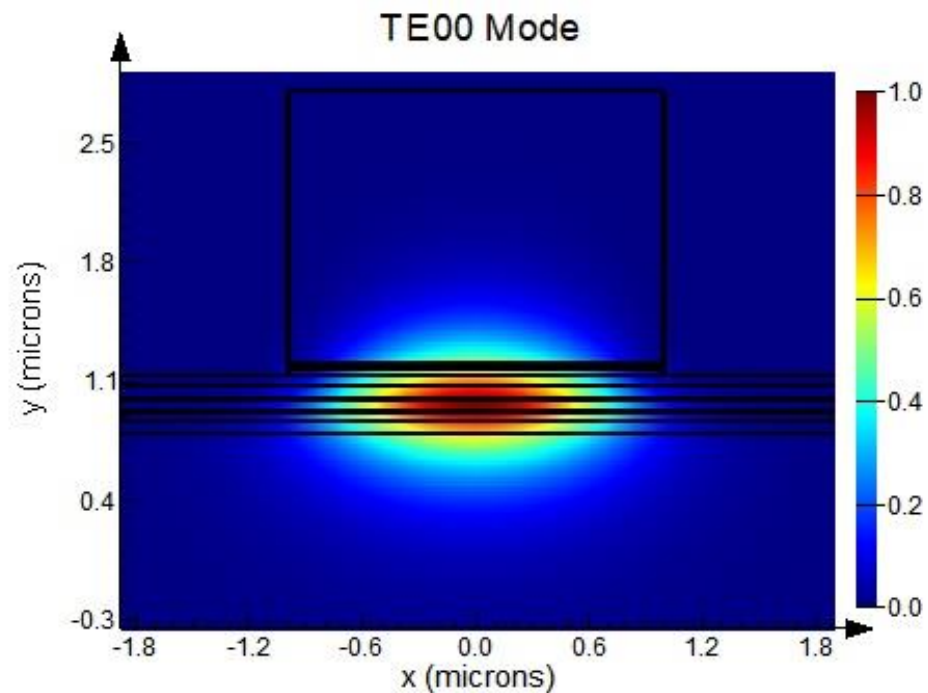


**Figure 3.6: Simulated fundamental optical mode for a shallow-etched ridge waveguide for the 2  $\mu\text{m}$  wide, 1920 nm deep ridge.**

### 3.2.3 Curved Ridge Waveguides

For as-cleaved DFB diode lasers, optical reflections occur at the cleaved facets (interfaces of the material and the air). FP modes will therefore be generated by the optical reflections, leading to undesirable effects on SLM operation for DFB lasers. Antireflection coatings can be used to reduce the optical reflections by depositing dielectric films. This method requires high-precision control of the refractive index and thickness of the layers of the dielectric layers. In this thesis, to make the fabrication easier, curved ridge waveguides are applied to eliminate facet reflections.



**Figure 3.7: Schematic of the curved ridge waveguide.**

For shallow-etched ridge waveguides, curved ridge waveguides with a small curvature can be applied to eliminate facet reflections, while maintaining sufficient optical confinement. Figure 3.7 shows the schematic of a curved ridge waveguide with a tilt angle of  $10^\circ$  at the output facet, which was used for the real design of the semiconductor diode lasers. The length of the ridge waveguide horizontally was  $300\ \mu\text{m}$  and the radius was designed as  $1730\ \mu\text{m}$ . The tilt angle of  $10^\circ$  produced an optical transmission angle of about  $33^\circ$  calculated by Fresnel equations [170]. In this circumstance, the optical reflections from the facets will not be reflected back into the ridge waveguide, reducing optical reflections at the facets dramatically. The small tilt angle is applied to avoid optical mode propagating loss in a bent ridge waveguide. The tilt angle can further to be designed as  $17.4^\circ$ , which is the Brewster's angle. By applying the Brewster's angle, the light is transmitted perfectly with a particular polarisation, with no reflection. A tilted lensed fibre is essential to achieve maximum output light coupling with bent ridge waveguides.

### 3.3 Electron Beam Lithography



**Figure 3.8: The overall e-beam lithography process flow.**

During the laser fabrication process, several lithography steps for pattern transfer are required. To achieve high precision of sub-micron pattern transfer, electron beam lithography (EBL) is preferred over photo lithography. EBL uses electron beams for exposure rather than the ultraviolet light used by photo lithography. EBL is widely used for researchers world-wide to realize nanostructures. The high precision EBL tool available in the JWNC is a Vistec VB6-UHR-EWF 100 keV machine. This machine can produce a minimum electron beam spot size of 4 nm, and the minimum pattern resolution is 0.5 nm, which has a writeable field size of 0.5 mm  $\times$  0.5 mm. Capable of producing sub 10 nm feature sizes, the electron beam is aligned by magnetic coils and e-beam scanning is controlled by a computer programmed with the designed pattern. The cavity length with gratings in this thesis can be as long as 1.2 mm. Because the writeable field size of the VB6 is only 0.5 mm  $\times$  0.5 mm, there will be stitch errors between adjacent writing fields. These stitch errors will introduce additional phase shifts in the gratings. However, the stitch error is normally less than 10 nm, which will not have a big influence on the single mode operation of diode lasers compared to the relatively large grating periods (about 240 nm). Later, from the experimental results, the high precision of lasing wavelengths will also show that the influence of the stitch errors on the lasing wavelengths was not observed. The gratings could also be realized by holography, where there are no stitch errors. However, holography can only generate the same grating periods on the whole sample, and grating periods cannot be changed independently at different positions. Here we choose the e-beam machine to write the gratings so that different grating periods could be achieved precisely at different positions on the sample.

The overall EBL process flow is shown in Fig. 3.8. Firstly, patterns are designed by using professional computer-aided design (CAD) software, e.g. L-Edit. After the pattern is sent to the e-beam machine, a highly focused electron beam writes the pattern on the sample surface, which was pre-coated with an electron sensitive resist. The sample is then dipped into a specific developer to reveal the pattern. The patterned resist can be used as a mask for etching (wet etch or dry etch) or lift off, and the pattern will then be transferred to the sample.

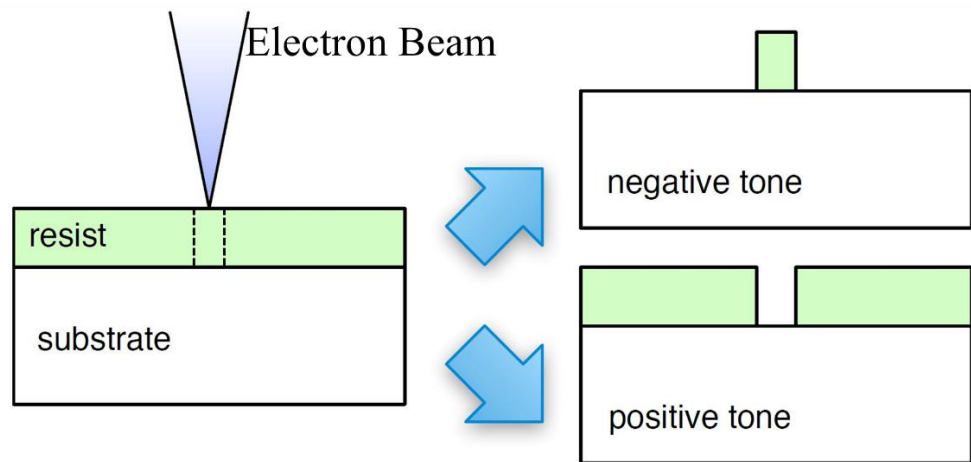


**Figure 3.9: Pattering with positive or negative tone resists.**

There are generally two types of e-beam resists: positive and negative tone. The positive tone resist that we use is polymethyl methacrylate (PMMA) and the negative tone resist used is hydrogen silsesquioxane (HSQ), both of which were coated on the surface of the sample by spinning the sample with the resist at a certain spinning speed according to the resist thickness. The difference between positive tone and negative tone resists is shown in Fig. 3.9. For the negative tone resist, the area exposed to electron beams will remain after development, while for the positive tone resist, such areas will be removed (dissolving in the developer). Whether positive tone or negative tone resist is chosen depends on feature sizes, as well as the cost, since e-beam writing is time-consuming. Although HSQ produces better precision, it is much more expensive than PMMA. In this work, HSQ is only used for ridge waveguide definition as grating periods of about 240 nm are defined in this step.

Throughout this work, an acceleration voltage of 100 kV was used for EBL. The exposure dose is an important parameter that describes the required charge per unit area to expose the resist and is measured in  $\mu\text{C}/\text{cm}^2$ . To determine the optimum exposure dose, electron scattering in the material needs to be taken into consideration. A modification of the exposure dose distribution on a sample is essential, which is called proximity correction. A commercial software called Beamer is used for the proximity correction calculation. Figure 3.10 shows the exposure dose distribution for a 20  $\mu\text{m}$  square before and after proximity correction respectively. Before proximity correction, the exposure dose is the same everywhere. After proximity correction, the square is divided into many small rectangles,

which have different values of exposure doses. In the middle of the square, the exposure dose decreases while the dose increases in the edge areas, because the middle areas are exposed to more scattering electrons than the edge areas. Proximity correction is very useful to achieve patterns with better shapes.

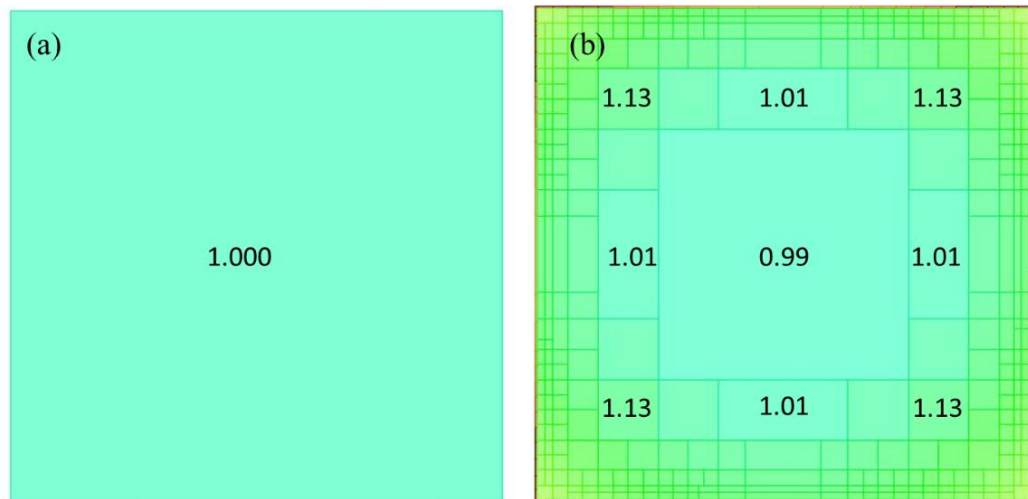


**Figure 3.10: The exposure dose distribution for a 20  $\mu\text{m}$  square (a) before and (b) after proximity correction.**

### 3.4 Fabrication Steps

Main fabrication steps will be introduced in this section. The fabrication process flow can be generally divided into 8 steps:

- 1) Pattern design
- 2) Sample preparation
- 3) Marker definition
- 4) Waveguide isolation
- 5) Waveguide definition

- 6) Contact Window Opening
- 7) Metallisation for P-contact
- 8) Thinning and cleaving

This process flow can be applied to most of the semiconductor lasers fabricated in the JWNC, based on ridge waveguides. However, the detailed process will be adjusted according to specific material, device design as well as the wafer structure. The 8 fabrication steps will be introduced in the following sections.

### 3.4.1 Pattern Design

Before carrying out the fabrication, designs of masks for each step of EBL need to be prepared. The commercial software, L-Edit, was used for pattern design in this thesis and Fig. 3.11 shows the user interface of this software. In this software, different layers are used for different steps of lithography. The grid resolution can be manually set and 0.5 nm was chosen for the patterns designed in this thesis.

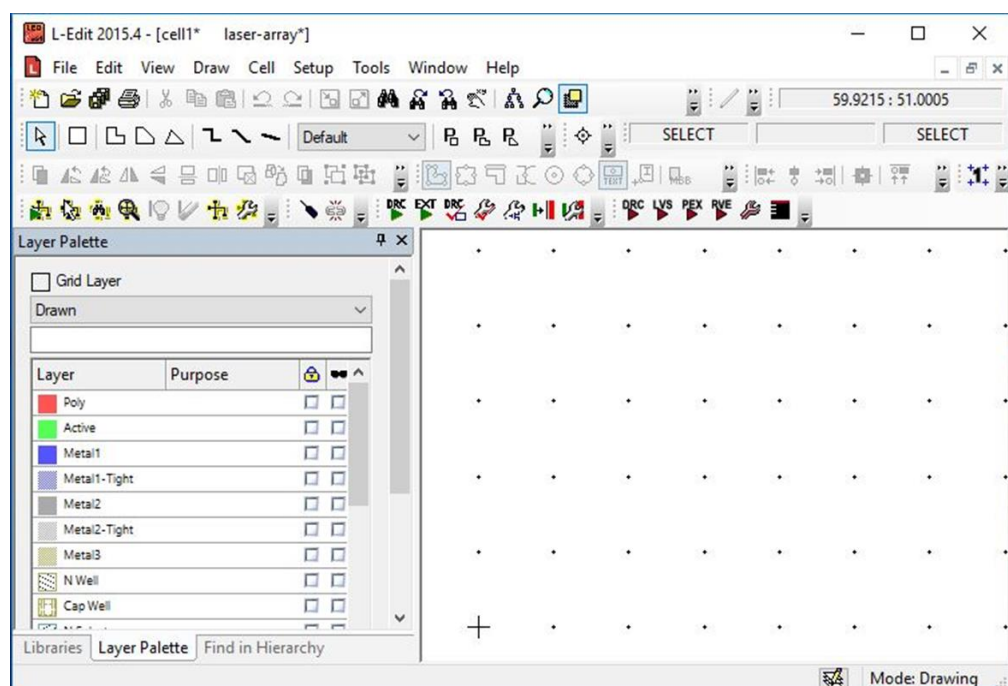
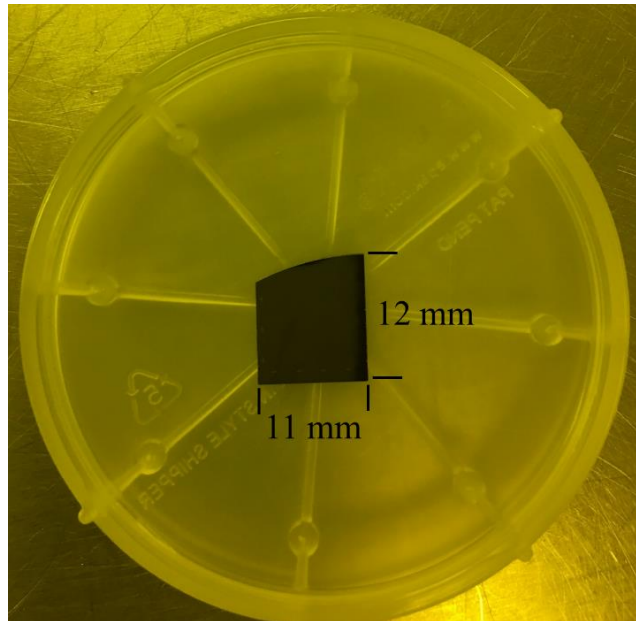


Figure 3.11: The user interface of L-Edit.



**Figure 3.12: A single sample cleaved.**

### 3.4.2 Sample Preparation

A 2-inch wafer was bought from the IQE Company, based on the wafer structure shown in Fig. 3.2. Before fabrication, the whole wafer was cleaved into small pieces for fabrication of different devices. A diamond tip was used for cleaving and Fig. 3.12 shows a single sample cleaved, with a dimension of about 11 mm  $\times$  12 mm. The upper edge of this sample is curved because this sample is close to the edge of the wafer. Samples were kept in small plastic boxes during the fabrication.

Cleaning is always essential before each step of the fabrication process. The aims are to remove all organic and inorganic contaminants. The standard recipe for cleaning is as follows. The sample was first dipped into *Acetone* ( $\text{CH}_3\text{COCH}_3$ ), then into *Isopropyl Alcohol* (IPA,  $\text{C}_3\text{H}_8\text{O}$ ) and finally into *Reverse Osmosis* (RO) water, five minutes for each solvent. All of these steps are carried out in a water bath at a temperature of 50 °C. During the cleaning, ultrasonic cleaning could be introduced for better cleaning effects at room temperature. After the final step of RO water cleaning, the sample was blown dry using a nitrogen gun. After the solvent-based cleaning, oxygen ashing could be applied to remove any remaining organic contaminant.

### 3.4.3 Marker Definition

Alignment markers were defined first for multiple-step lithography, which were used to guarantee the correct alignment between the subsequent lithography steps. Clearly-defined markers are particularly important for EBL, since the alignment process is automatic and requires well-defined markers with high contrast. Both etched markers and metallised markers can be used for EBL. Metallised markers were chosen here to achieve a higher contrast.

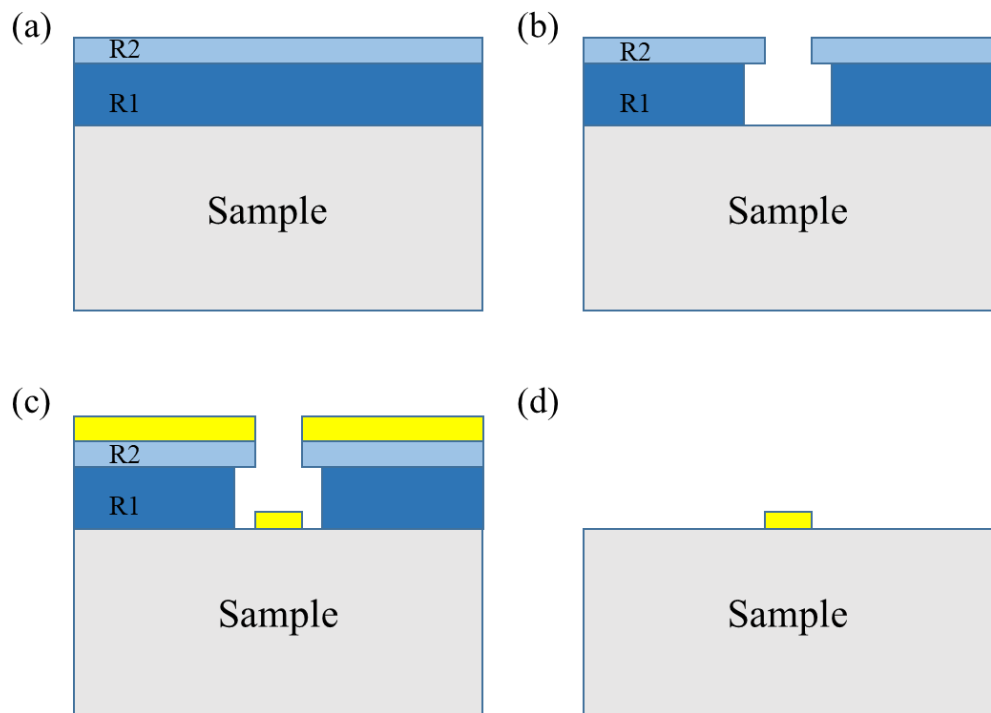


**Figure 3.13: The process flow of lift-off technique.**

The lift-off technique is widely used for metallisation. During the whole fabrication procedure, this method was carried out twice, including p-contact layer deposition. Figure 3.13 shows the process flow of the lift-off technique for EBL. Two different PMMA layers were spun on the sample, with the first (R1) and second (R2) layer thicknesses being 1.2  $\mu\text{m}$  and 110 nm respectively. After spinning the first layer of PMMA, the sample was baked at 180  $^{\circ}\text{C}$  for 30 minutes in an oven. Then the second layer of PMMA was spun and the sample was baked for another 90 minutes also at 180  $^{\circ}\text{C}$  in the oven to remove the solvents in the

resists, following which the sample was sent to the e-beam machine. The second layer's sensitivity to electron beams is lower than that of the first layer because of its higher molecular weight, which results in an undercut profile of the resist after development. After exposure by electron beams, development was carried out to unveil the pattern. The developer is a mixture of methyl isobutyl ketone (MIBK) and IPA, the ratio of which depends on the exposure dose, resist thickness and feature size. The ratio of MIBK: IPA chosen here was 1:1. The sample was dipped in MIBK: IPA (1:1) for 30 seconds at 23 °C and then rinsed in IPA at room temperature for 15 seconds. After blowing dry, the sample was sent to the metal deposition machine. The undercut profile will prevent the resist sidewalls from being coated by the highly-directional metal deposition, as shown in Fig. 3.13(c). The sample is then placed in hot acetone (water bath at 50 °C) for about 20 minutes, and the PMMA and the overlying metal layer are removed, leaving metal deposited in the areas where we wanted it to be, as shown in Fig. 3.13(d).



**Figure 3.14: The micrograph of the sample after development.**

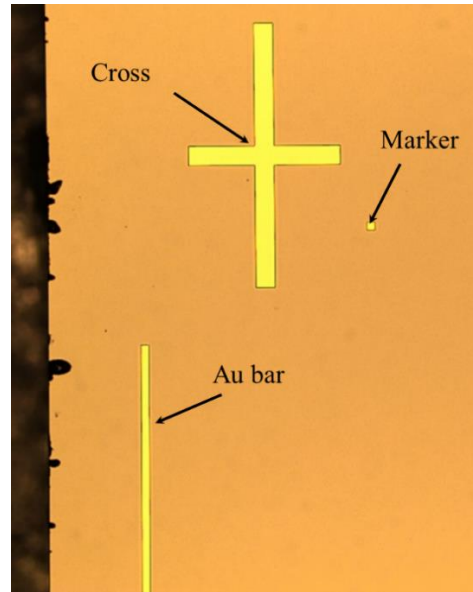


**Figure 3.15: A micrograph of the markers after lift-off process.**

Figure 3.14 shows a micrograph of a sample after development of markers with the resist layers removed at the places exposed to electron beams. Since markers were placed around the design patterns for DFB lasers, the markers were mostly close to the edge of the sample. It can be seen from this micrograph that the remaining resist is colourful, which comes from a light interference pattern, because the thickness of the resist is not uniform in the edge area of the sample.

The metal deposited for the markers contained two layers: the first layer of *Nichrome* (NiCr) and the second layer of *Gold* (Au), with thicknesses of 10 nm and 100 nm respectively. Metal deposition in the JWNC is performed by electron-beam evaporation. Metal targets are heated by electron beams and metal vapour is generated. When the metal vapour reaches the sample surface, metal deposition is realized. Figure 3.15 shows a micrograph of the markers after the lift-off process. Near the left edge of the sample, an Au bar was aligned parallel with the left edge of the sample, which guaranteed that cleaving lines in the final step would also be parallel to the crystallographic axis. The alignment for EBL is carried out automatically using the centre positions of the crosses and markers. The cross was used for coarse alignment while the small marker was used for fine alignment. The camera in the EBL machine would first find the centre position of the cross and then check the centre positions of the markers. The width of the cross branch was 50  $\mu\text{m}$  and the small marker was a square

with width of 20  $\mu\text{m}$ . Each step of alignment would require one cross and four markers at the four corners of the sample in total. The cross was used to help to find the small markers. Four markers were used for precise control of rotational and translational alignment. Because of damage, each cross or marker were only used once to ensure sharp contrast of the image taken by the e-beam machine. Therefore, it is always wise to put sufficient crosses and markers when designing the pattern at the start of the fabrication process.

### **3.4.4 Waveguide Isolation**

For complex designs of semiconductor lasers with multiple electrodes, electrical isolation is essential so that different electrodes can work independently. The DFB semiconductor lasers in this thesis were designed with at least two electrodes and waveguide isolation was carried out between two adjacent electrode pads. The basic solution is to remove the highly-doped contact layers on top of the wafer structure, shown in Fig. 3.2, which comprise InGaAs (200 nm) and InGaAsP (50 nm) in this case. Waveguide isolation was carried out before waveguide definition throughout this thesis so that the process could be monitored. Reactive Ion Etching (RIE) was used to remove the contact layers.

#### **3.4.4.1 Reactive Ion Etching**

After patterning resist masks, the process of etching was carried out to transfer patterns from resists to the surface of samples. Compared with wet etching, which employs liquid based etchants [171], dry etching has the advantages of being anisotropic, with less mask undercutting and greater reproducibility. Dry etching employs a chemically and physically reactive plasma to remove the desired material.

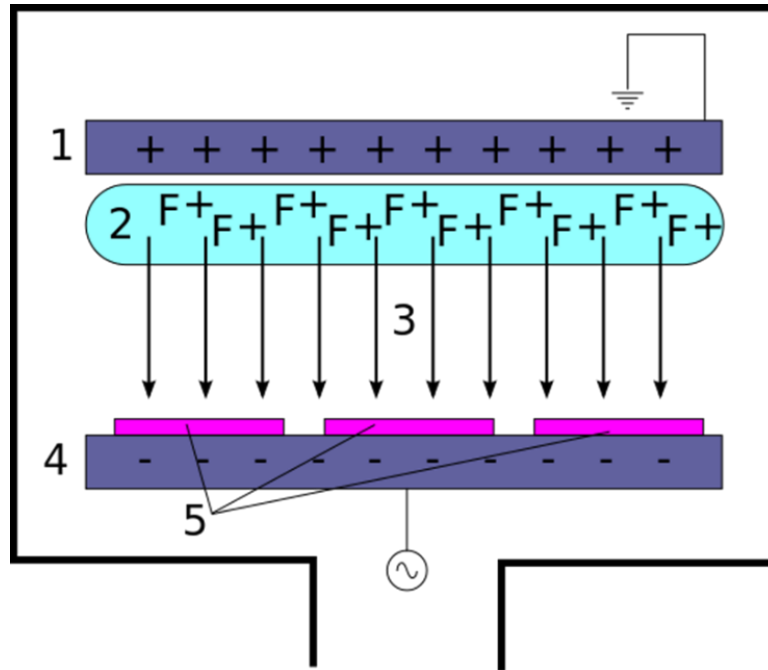


**Figure 3.16: A diagram of a common RIE set-up. A RIE consists of two electrodes (1 and 4) that create an electric field (3) that accelerates ions (2) toward the sample surface (5) [172].**

Figure 3.16 illustrates a typical RIE set-up, which takes place in a cylindrical chamber pumped to a high vacuum (a few  $10^{-3}$  mbar). A RIE system has two parallel electrodes. The upper one is grounded, while the lower one couples to a radio frequency (RF) power source and holds the samples to be etched. A gas or a combination of gases will be chosen according to the material to be etched, which will be struck into a plasma consisting of gases, electrons and ions. With the RF power applied, an electric field will be established that accelerates ions towards the surface of the samples, and material is removed by chemical reactions. The etch conditions in a RIE system depend on various parameters, such as RF power, gas composition, gas flows, chamber pressure and temperature. Parameters are adjusted to give an optimized etching recipe that achieves a good profile. A schematic of anisotropic etching is shown in Fig. 3.17(a). With the electric field present, ions will bombard the sample surface mainly in one direction, which prevents undercutting. During the etch process, not only the material will be etched, but also the resist masks will be consumed, as shown in Fig. 3.17(b). Masks are expected to be consumed more slowly than the material. Selectivity is defined as the ratio of the etch rate of material divided by the etch rate of resists. This value varies from 10:1 to  $\sim 1:1$  and in general should be as large as possible.

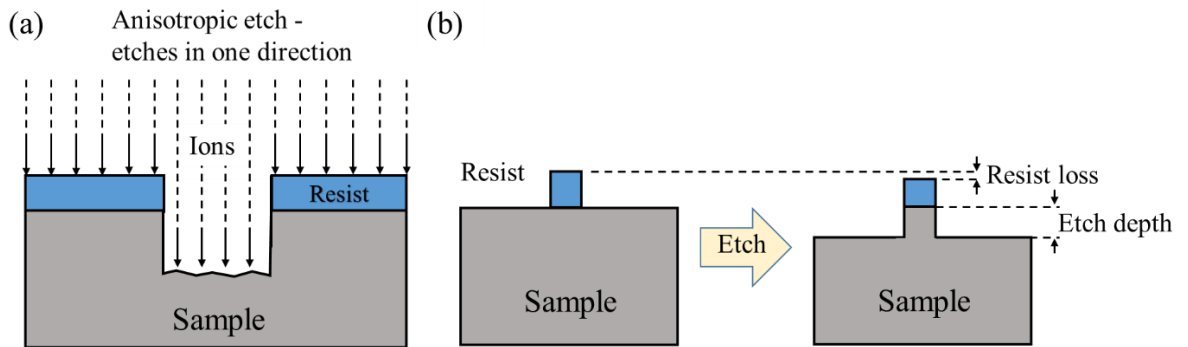


**Figure 3.17: (a) Schematic of anisotropic etch, and (b) resist loss and etch depth during the process of dry etching.**

### 3.4.4.2 Etching Process

Another type of RIE system, called inductively coupled plasma (ICP) RIE, was used for etching InP-based materials. In an ICP RIE system, the plasma is generated using a RF powered magnetic field, and as a result, very high plasma densities can be achieved. The machine used for InP dry etch is an Oxford Instruments PlasmaPro System 100 ICP180. There are two common dry etch recipes. One is based on *Chlorine* ( $\text{Cl}_2$ ) and the other is based on *Methane Hydrogen* ( $\text{CH}_4/\text{H}_2$ ) [173-177]. Which recipe will be chosen depends largely on the required etch rate and etch profile.  $\text{Cl}_2$  based chemistries have a fast etch rate, but a high substrate temperature ( $> 150\text{ }^\circ\text{C}$ ) is required to allow the etch products ( $\text{InCl}_x$ ) to volatilize, aiming to obtain a smooth surface after etch. The etch rate can reach as high as  $1\text{ }\mu\text{m}/\text{min}$ , suitable for deep etching. However, at such high temperatures, most resists cannot be used and so hard masks, such as  $\text{SiO}_2$ , are essential.

Methane hydrogen was chosen for dry etch here because it can be used at room temperature (set at  $20\text{ }^\circ\text{C}$  for the dry etch in this work), while providing good anisotropic profiles and smooth surfaces. It was first proposed for InP RIE processing in 1989 by Hayes et al. [178]. An issue with this recipe is the formation of hydrocarbon polymers on inert surfaces that may affect the etch rate and surface roughness. Since an  $\text{O}_2$  plasma can be used to remove hydrocarbon polymers, a small addition of  $\text{O}_2$  to the recipe is adopted to help to improve etch performance [179], which is also beneficial in producing more vertical etched sidewalls. The etch rate of this recipe is normally a few tens of  $\text{nm}/\text{min}$ .

For dry etch, a concern of resist consumption is always raised. Here, two layers of PMMA were spun on the surface of the sample, both of which are identical with each having a thickness of 1.2  $\mu\text{m}$ . The total thickness of 2.4  $\mu\text{m}$  was essential for long-time etching. The steps of resist baking and development were the same as the steps used for marker definition. Resist in the area of waveguide isolation was exposed by EBL and removed after development. To control the process during dry etch precisely, an interferometer was used to monitor the etch depth. The interferometer is a laser system which uses a laser beam of 675 nm to monitor the light reflectivity from the sample surface [180]. Since the sample material has different layers, the reflectivity will change as the material is etched. Hence, precise control of the dry etch depth can be realized. The chosen etch recipe,  $\text{CH}_4/\text{H}_2/\text{O}_2$  (6/50/0.2 sccm), had an etch rate of about 65 nm/min for InP. The ICP power and RF platen power of the machine were 200 and 100 W respectively, and the gas pressure in the chamber was 20 mTorr. However, for contact layers of InGaAs and InGaAsP, the etch rate was slower than normal. Figure 3.18 (a) shows a reflectivity trace from the etched areas, which displays light reflectivity changing with time. The lowest point of the reflectivity trace was the stop point, where the contact layers were removed completely. For a total 250 nm etched thickness, an average etch rate of 29 nm/min was calculated. A micrograph of the waveguide isolation patterns after dry etch is shown in Fig. 3.18(b) where the dark lines are etched slots for waveguide isolation.

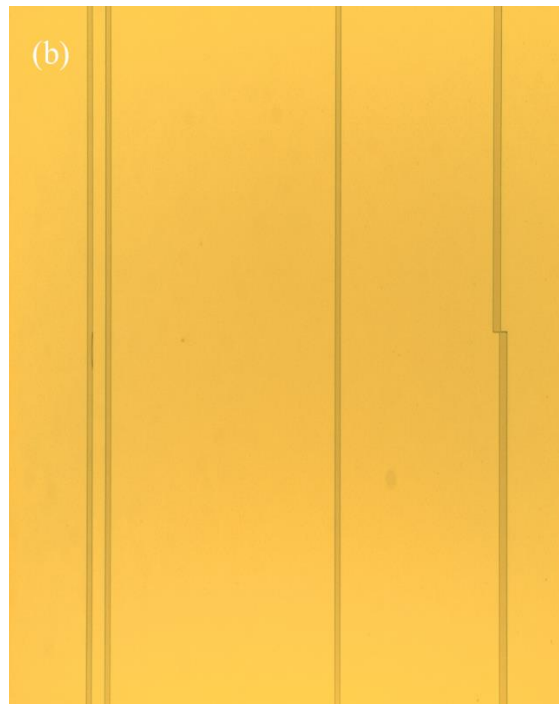
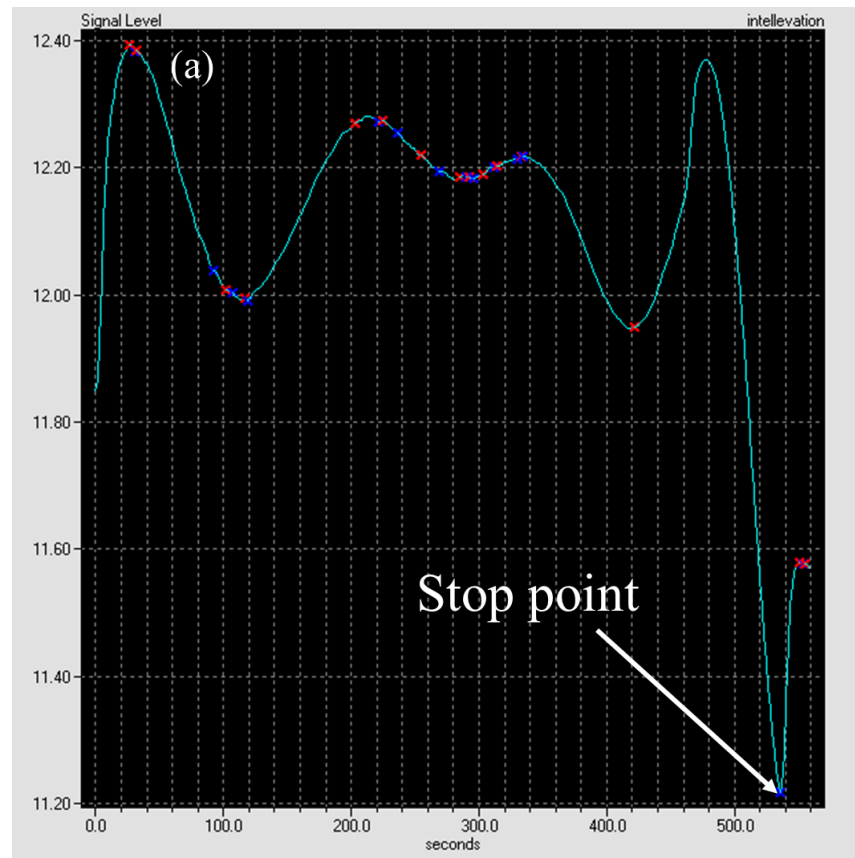


**Figure 3.18: (a) A reflectivity trace from the interferometer for waveguide isolation etch, and (b) a micrograph of waveguide isolation patterns after dry etch.**

### **3.4.5 Waveguide Definition**

#### **3.4.5.1 Side-wall Gratings**

Side-wall gratings are also called “laterally-coupled gratings”. For this type of grating, the Bragg gratings are introduced on the two sides of the ridge waveguide. Buried gratings are another type of grating, which are introduced in an additional layer just above or below the QWs. Compared with side-wall gratings, diode lasers based on buried gratings have the advantage of higher effective coupling coefficients, which will lead to a lower threshold current. Because buried gratings are normally fabricated with a thin layer of about tens of nanometres, the etching process is relatively easy to control by wet etch. Lower wider contrast associated with buried gratings also has a lower optical loss. However, for buried gratings, material regrowth by MOCVD or MBE is essential. Material regrowth requires high standards of the sample surface cleanliness after etching the gratings, and it is difficult to control this step of process. Compared with buried gratings, side-wall gratings are easy to fabricate, and no regrowth is required. In this thesis, side-wall gratings are chosen to make diode lasers. By introducing an etch stop layer in the wafer structure, shown in Fig. 3.2, the grating etch profiles could be well controlled. By optimising the grating profile and surface roughness, the optical loss could be reduced and higher effective coupling coefficients could be controlled. Lower threshold currents and higher output power are expected to be achieved.

#### **3.4.5.2 Dose Test**

As described above, the dose for EBL needs to be chosen properly. Dose tests were carried out firstly to find the optimum dose before the real run of EBL for the sample. This is especially essential for HSQ, since HSQ is very sensitive to the environmental temperature, moisture and contaminants. The dose of a small bottle of HSQ may change with usage time, and a dose test is required every time before using HSQ. HSQ is preferred for high precision applications, such as defining waveguides with gratings in this thesis, whose smallest feature size was only about 120 nm. Furthermore, after e-beam exposure, HSQ will be converted into SiO<sub>2</sub>, an excellent hard mask for dry etch.

The thickness of spun HSQ was 500-600 nm, which is thick enough for 1 hour dry etching for waveguide definition. The developer used for HSQ is a 25% solution of *Tetramethylammonium Hydroxide* (TMAH), giving excellent development performance [181, 182]. The development process is as follows: the sample is first dipped in TMAH (23 °C) for 30 seconds, then water for 1 minute followed by an IPA rinse for 30 seconds. An IPA rinse is good for high aspect ratio features, since IPA has a lower surface tension than water. The sample was then blown dry using a nitrogen gun.

Figure 3.19 shows typical results of a dose test for HSQ to define ridge waveguides with gratings. These ridge waveguides had a width of 2.5  $\mu\text{m}$  with grating recess of 0.6  $\mu\text{m}$ . The duty cycle of the gratings was designed as 50%. Since the gratings had very small feature sizes, a scanning electron microscope (SEM) was used to take images. Figure 3.19(a) shows the grating profile with a dose of 600  $\mu\text{C}/\text{cm}^2$ . It can be clearly seen that the duty cycle of the gratings was much smaller than 50%, showing a condition of under exposure, which means that the dose was not large enough. Figure 3.19(b) shows an SEM image of the gratings with a dose of 950  $\mu\text{C}/\text{cm}^2$ , in which the grating profile is good. In this circumstance, the EBL dose was chosen to obtain the duty cycle of 50%, with each grating tooth having a rectangular shape. Higher doses will also adversely affect the grating profile, a situation which is called over exposure. Figure 3.19(c) is an SEM image for gratings with a dose of 1200  $\mu\text{C}/\text{cm}^2$ . Over exposure means the region close to exposed areas would be affected by scattering electrons. In this SEM image, residual HSQ was found between grating teeth, which would affect the coupling coefficient after dry etch. From the three SEM images, we can see that it is very important to find the optimum dose for e-beam lithography, otherwise, the profiles of the pattern will not be optimum.

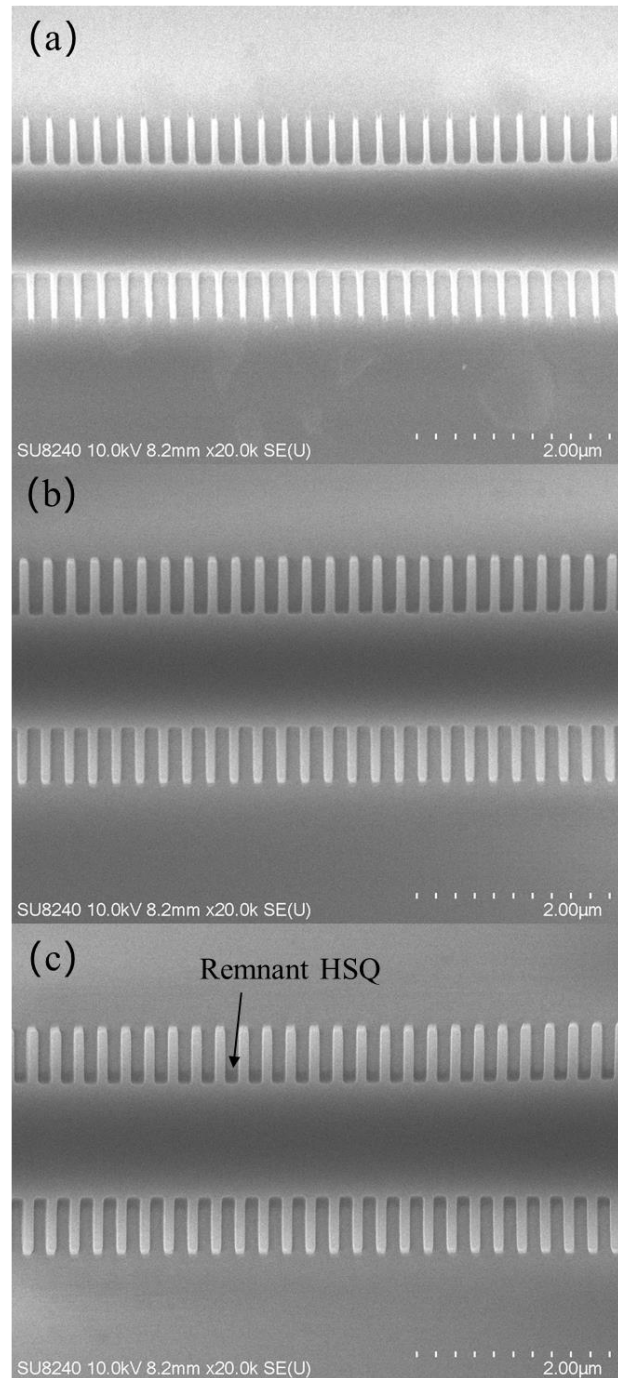
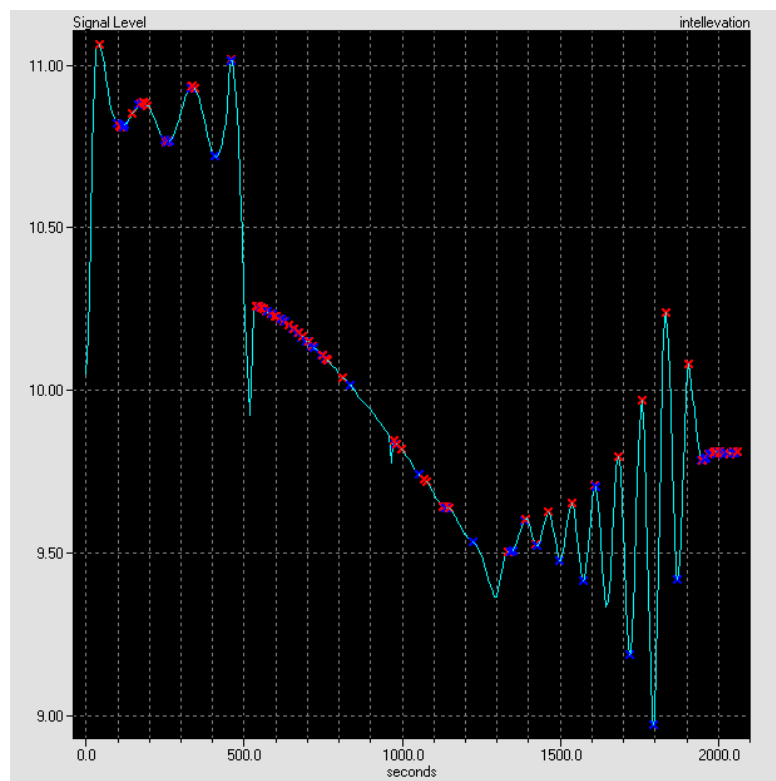


**Figure 3.19: SEM images of patterned HSQ for ridge waveguides with gratings, (a) under exposure, (b) right exposure, and (c) over exposure.**

The dose values shown here vary over a very wide range to show how under exposure and over exposure affect pattern profiles. In a practical dose test, the dose values are in a much narrower variation range. Once the optimum dose is found, this dose value can be used for real samples.

### 3.4.5.3 Undercut and RIE Lag Effects

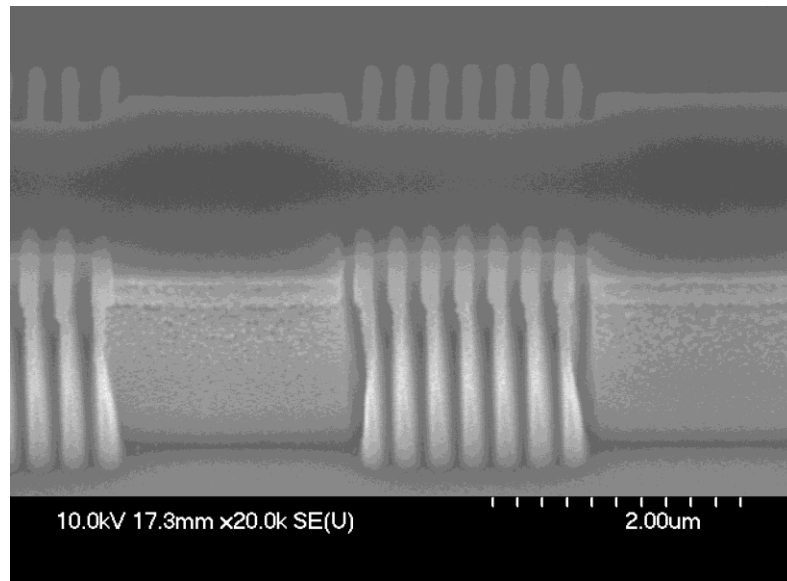
After defining the ridge waveguides, ICP dry etch was used for pattern transfer. The ICP180 system was also used for dry etching ridge waveguides. The etching recipe was the same as that used for waveguide isolation, gas composition of which was  $\text{CH}_4/\text{H}_2/\text{O}_2$  (6/50/0.2 sccm). The small amount of  $\text{O}_2$  in the recipe can turn aluminium into aluminium oxide, which is extremely resistant to etching. Hence, the upper AlGaInAs cladding layer shown in Fig. 3.2 can be utilised as the etch-stop layer. The total etch depth was 1920 nm for ridge waveguides. Figure 3.20 shows the reflectivity trace for ridge waveguide dry etch and an etching time period of 32 min was used. The etching rate was calculated as 60 nm/min. Because of the etch-stop layer, the reflectivity trace becomes flat at the end of the dry etch process.



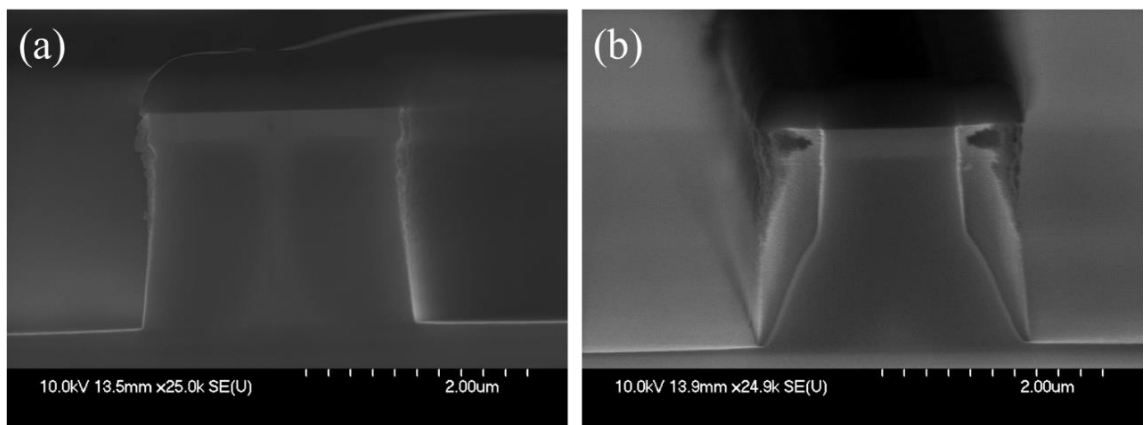
**Figure 3.20: The reflectivity trace for ridge waveguides dry etch.**

Figure 3.21 illustrates a side view of a laterally-coupled grating (SEM image), etched by  $\text{CH}_4/\text{H}_2/\text{O}_2$ . From this figure, we can see that the side-wall gratings were defined and the sampled Bragg grating structures are very clear. The SEM images of the cross-section view are also presented in Fig. 3.22. Figure 3.22(a) shows the cross-section of a straight ridge

waveguide without grating. The sidewall was not vertical and there was slight undercut. The undercut can be seen clearly in Fig. 3.22(b), where the material underneath the mask has been etched and the grating profile is not good. To produce devices with good performance, undercut needs to be avoided as much as possible.



**Figure 3.21: The side view of a laterally-coupled grating, etched by CH<sub>4</sub>/H<sub>2</sub>/O<sub>2</sub>.**



**Figure 3.22: The cross-section view of (a) a ridge waveguide, and (b) a laterally-coupled grating.**

One possible reason causing the undercut is the “loading effect”. A 6-inch silicon wafer was often used as the carrier wafer to hold samples. Silicon is a different material from the samples based on III-V materials. Although dry etch is material selective, the carrier wafer

will also be consumed during dry etch process. The “Loading effect” occurs in dry etching as the etchant is depleted by reaction with the substrate material [183]. To reduce the undercut, a 2-inch InP wafer was placed under the sample so that the sample would be in an etching atmosphere with similar materials. Although the InP wafer was still placed on the silicon wafer, it was expected that the undercut would be reduced. Figure 3.23 shows a side view of a laterally-coupled grating etched using the same recipe defined above, with a 2-inch InP wafer underneath the sample. Although the undercut can still be seen, this SEM image confirms that the undercut is reduced. However, because the InP wafer was also etched by the etchants and the wafer was much larger than the sample, the etching rate of the sample decreased. As a result, the required time to etch the sample to the same depth as before doubled. Long etching times can have deleterious effects on the profile of the patterns because of sample heating and accumulated undercut.

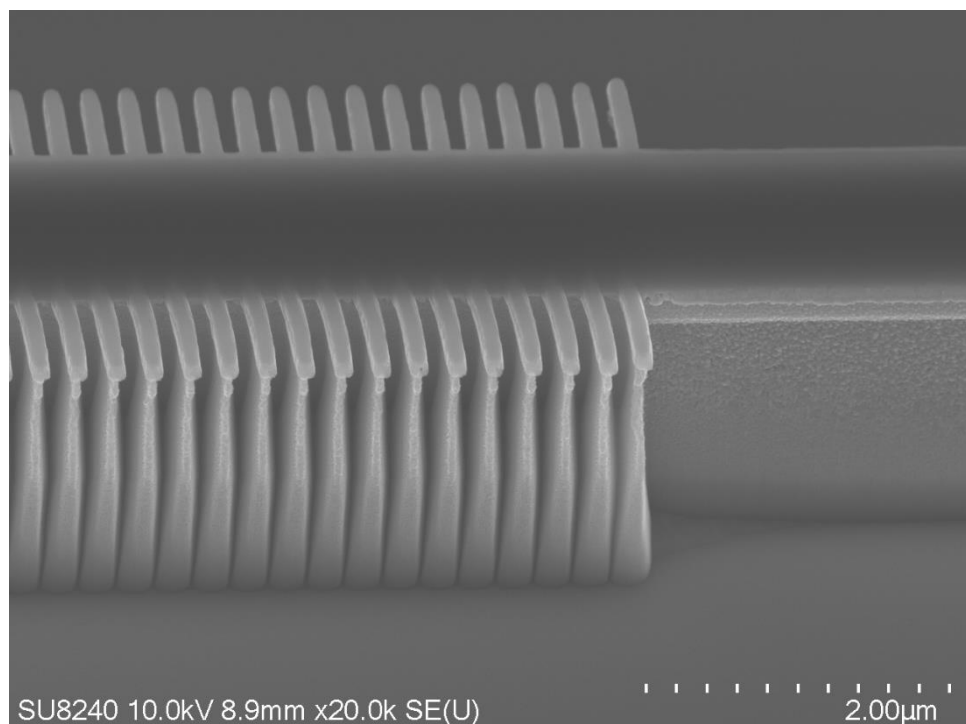


**Figure 3.23: The side view of a laterally-coupled grating etched by the same recipe with a 2-inch InP wafer underneath the sample.**

To reduce the etch time, two steps of dry etch were introduced. In the first step, the recipe based on  $\text{Cl}_2/\text{CH}_4/\text{H}_2$  at  $60^\circ\text{C}$  on ICP180 was used, which gave an etch rate of about 450 nm/min. The first step took 3.5 minutes. For the second step, the recipe based on  $\text{CH}_4/\text{H}_2/\text{O}_2$

was used and the sample was etched to the end of process. By this modification, the total etching time was reduced to a reasonable time (about 40 minutes) and the undercut was not severe. Figure 3.24 illustrates the SEM image of a laterally-coupled grating based on the two-step etching. We can see that the profile of the ridge waveguide with gratings is vertical and uniform.

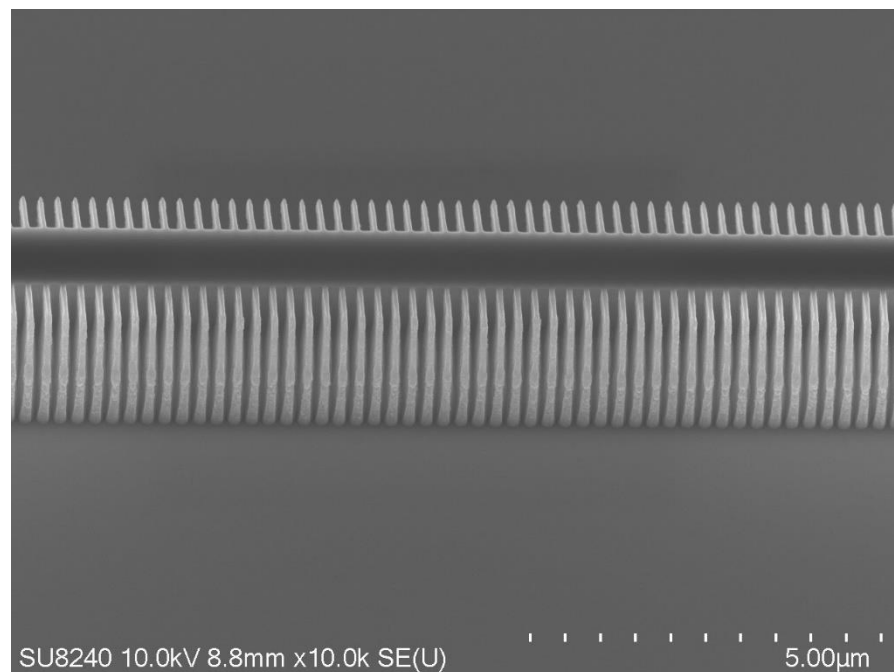


**Figure 3.24: The side view of a laterally-coupled ridge waveguide with gratings based on two-step etching.**

Figure 3.22(b) also shows another problem that occurs during dry etch, called the “RIE lag” effect. This effect occurs because etch rates have a dependence on the width of the slot and the aspect ratio of the feature sizes. The movement of ions is diffusion limited in the trench and the etch rate decreases as the aspect ratio increases [183-185]. This is especially a problem of deep-etched sidewall gratings with small feature sizes. Figure 3.22(b) shows an example of poor etching at the bottom in the gaps and the grating teeth are not clear. It is difficult for ions to diffuse into the gaps between the grating teeth. The etch-stop layer can be utilised to reduce the RIE lag effect. When the dry etch process reaches the etch-stop layer, the etching rate of the etch-stop layer is very low, only about 1-2 nm/min. At this point, if we keep etching, the material between the grating teeth will slowly be etched laterally while the etch-stop layer prevents etching downwards. As a result, the RIE lag effect

will be reduced. Usually, these added times for dry etch after reaching the etch-stop layer were 10 to 15 minutes.

### 3.4.6 Contact Window Opening

After defining the ridge waveguides, dielectric films were deposited on the sample for electrical isolation. Contact windows on the top of ridge waveguides were then opened by etching the dielectric films and metal deposition carried out to produce p-contact electrodes. This ensured electric currents were only injected into the top area of ridge waveguides.

Dielectric films of silicon dioxide ( $\text{SiO}_2$ ) were deposited as the insulator, performed by a *Plasma-Enhanced Chemical Vapour Deposition* (PECVD) process. Silicon dioxide is a good insulator and several hundred nanometres of silica were deposited on the sample surface. PECVD is a chemical vapour deposition process to deposit thin films based on chemical reactions in a plasma of reacting gases [186], and produces good quality thin dielectric films.

A first layer of 200 nm  $\text{SiO}_2$  was deposited on the sample by PECVD, followed by spinning a layer of about 400 nm HSQ to make the surface more uniform and smooth. After spinning HSQ, the sample was baked for 2 hours in the 180 °C oven. After baking, the HSQ becomes solid and can be used as liquid glass. A final layer of 100 nm PECVD  $\text{SiO}_2$  was deposited to ensure good insulation performance. The total  $\text{SiO}_2$  thickness was therefore ~ 700 nm. Because of the ridge waveguide high-mesa structure, the  $\text{SiO}_2$  films on top of the ridge waveguides were thinner than 700 nm, which was beneficial to reduce etching time.

Another RIE machine in the JWNC, an Oxford Instrument RIE80+, was used to etch the  $\text{SiO}_2$  films for contact window opening. In this step, PMMA was used as the mask. The sample was only exposed to electron beams on the top of ridge waveguides, where the PMMA was removed after development. Fluoroform ( $\text{CHF}_3$ ), with a gas flow of 30 sccm and pressure of 30 mTorr, was used for the  $\text{SiO}_2$  RIE dry etch. The RF power was set at 200 W with the working temperature at 20 °C. This etching recipe gave an etch rate of about 30 nm/min. Figure 3.25 shows a micrograph of a ridge waveguide before and after RIE etching for contact window opening. Before RIE  $\text{SiO}_2$  etching, as shown in Fig. 3.25(a), there was a layer of  $\text{SiO}_2$  on the top of the ridge waveguide, appearing as blue. After  $\text{SiO}_2$  etching,

illustrated in Fig. 3.25(b), the SiO<sub>2</sub> on top of the ridge waveguide was removed and a yellow metallic colour appears, which came from the InGaAs alloy. The colourful interference pattern in the micrograph came from HSQ, which acted as “liquid glass”.

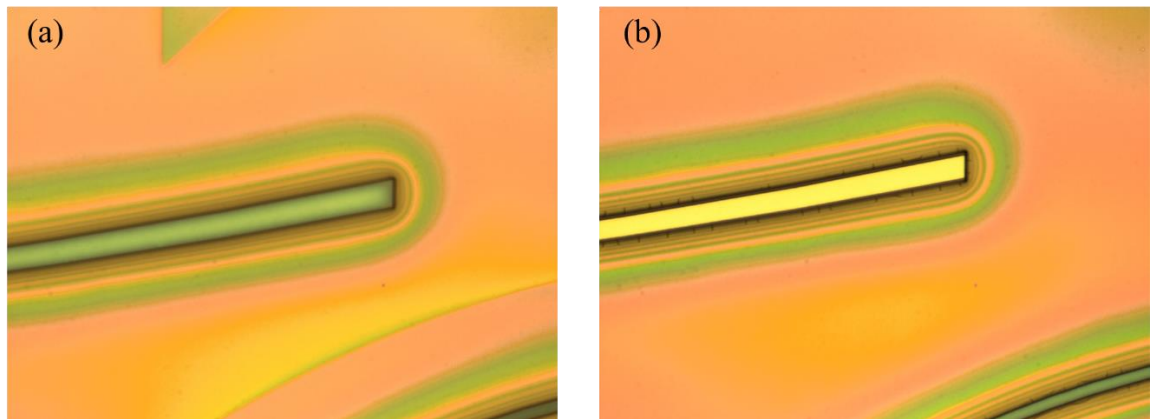


**Figure 3.25: The micrograph of a ridge waveguide (a) before and (b) after RIE etching for contact window opening.**

### 3.4.7 Metallisation for P-contact

After contact window opening, metal deposition on top of ridge waveguides for the anode electrodes (p-contact) was performed. This metallisation process was similar to that of producing markers, realized by lift-off process. The only difference was that a thicker layer of PMMA was required here because of the thicker p-contact metal. Metal layers of Titanium/Platinum/Gold (Ti/Pt/Au) with thickness of 33/33/240 nm respectively were deposited as the p-contact. The Ti is used as an adhesion layer as it is a reactive metal and oxidises easily. The Pt layer is adopted to prevent Au from diffusing into the semiconductor layer. The conductivity of Ti is not as good as that of Au so a final layer of 240 nm Au was deposited to ensure good electrical conductivity. The top 200 nm InGaAs layer of the wafer structure was highly-doped by Zn ( $1.5 \times 10^{19} \text{ cm}^{-3}$ ), enabling a good p-type ohmic contact with the Ti/Pt/Au layers. Figure 3.26 is a micrograph of Ti/Pt/Au p-contact electrodes after the lift-off process.



Figure 3.26: The micrograph of Ti/Pt/Au p-contact layer.

### 3.4.8 Thinning and Cleaving

The original thickness of the sample was about 360  $\mu\text{m}$ . To achieve good cleaving and lower resistance, the n-type substrate side of sample was thinned to about 180  $\mu\text{m}$ .  $\text{Al}_2\text{O}_3$  dispersoid in water was used for thinning and polishing by a Chemical Mechanical Polishing (CMP) process. First, a 9  $\mu\text{m}$   $\text{Al}_2\text{O}_3$  particles solution was used for thinning at a relatively fast thinning rate, then a 3  $\mu\text{m}$   $\text{Al}_2\text{O}_3$  solution was used to polish the sample surface and reduce sample surface roughness.

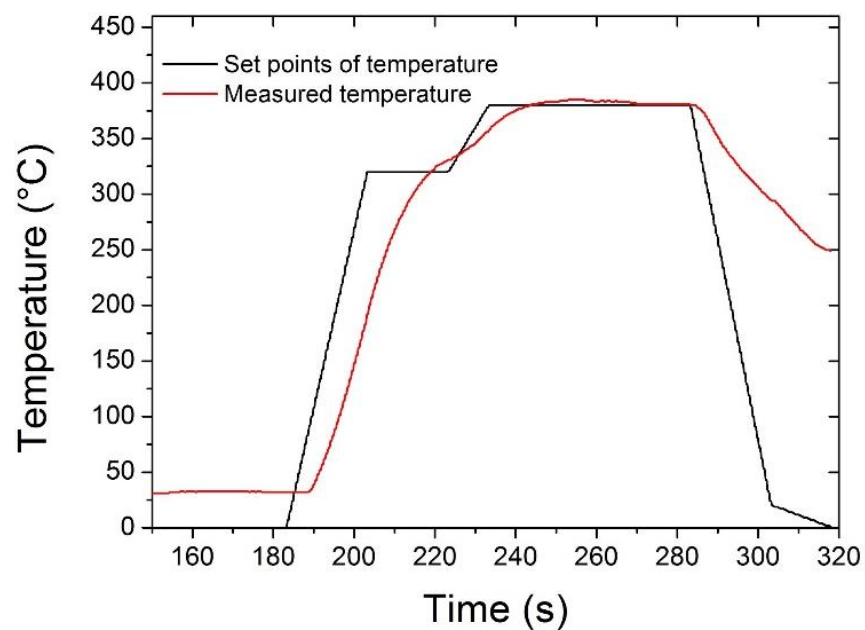


Figure 3.27: Annealing temperature changing with time.

After thinning and polishing, n-type metallisation was deposited on the backside of the sample surface. For the n-type contact, the InP was doped by Si to a level of  $3 \times 10^{18} \text{ cm}^{-3}$ , and a layer structure of Au/Ge/Au/Ni/Au of thicknesses 14/14/14/11/240nm was deposited by metal evaporation, a similar process to the p-contact. Annealing using a rapid thermal annealing (RTA) machine was then carried out to achieve a better ohmic contact for both the p-contact and the n-contact. The annealing condition was  $380 \text{ }^\circ\text{C}$  for 60 seconds, as shown in Fig. 3.27. The measured annealing temperature was very close to the set points. During the annealing process, Ge also diffuses into the semiconductor material under the n-contact and dopes the InP degenerately n-type, achieving a good ohmic contact.

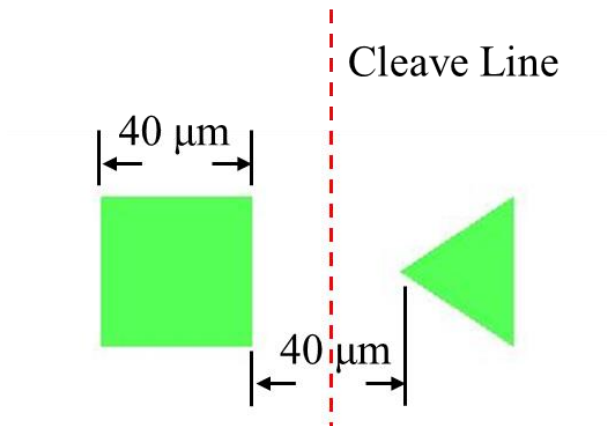


Figure 3.28: Design of the cleave sign.



Figure 3.29: An image of cleaved laser bars.

After annealing, the fabrication of the diode lasers was finally completed and the sample was ready to be cleaved into laser bars. Figure 3.28 shows the design of the cleave sign and the cleave line is in the middle between the square and the triangle. The square had a width of  $40\ \mu\text{m}$  and the distance between the square and the triangle was also  $40\ \mu\text{m}$ . A diamond tip was aligned to make a scratch on the sample surface at the edge and the sample was split by pressure according to the crystallographic axis along the cleave line. Figure 3.29 shows an image of three cleaved laser bars in a sample box. InP is very fragile and a little pressure is required for cleaving. After cleaving, the laser bars were ready for measurements.

### 3.5 Chapter Summary

In this chapter, semiconductor materials and diode laser fabrication were introduced. The fabricated DFB semiconductor diode lasers were based on multiple quantum well epitaxial wafers. To achieve good performance, the AlGaInAs/InP material system was adopted for semiconductor lasers. The basic structures of single mode ridge waveguides were then introduced. Ridge waveguides were bent at the facets to eliminate reflections, so, the stimulated optical modes would only depend on the Bragg gratings rather than the FP modes. Then the fabrication of semiconductor diode lasers was introduced in detail. Electron beam lithography was adopted to realise the small feature sizes of the Bragg gratings and was used for pattern transfer during the whole fabrication process. Eight main fabrication steps were described for fabricating diode lasers, including pattern design, sample preparation, marker definition, waveguide isolation, waveguide definition, contact window opening, metallisation for p-contact, thinning and cleaving. Among these steps, waveguide definition is the most critical. The process was optimised to achieve sidewall gratings with high aspect ratio and a small RIE lag effect. Reactive ion etching was employed to etch the III-V and dielectric materials, because dry etch has the advantages of etching anisotropy, less mask undercutting and greater reproducibility than wet etch. These fabrication processes were optimised and used to fabricate all of the semiconductor diode lasers in this thesis.

## Chapter 4

# Novel DFB Semiconductor Lasers and Laser Arrays

### 4.1 Introduction

DFB semiconductor lasers and laser arrays are of substantial interest in WDM networks for higher data capacity, especially for low-cost applications in data centres and access networks [29, 187]. According to equation (2.3), a DFB diode laser's lasing wavelength depends on the effective refractive index of the ridge waveguide and the corrugation pitch of the grating. To obtain different lasing wavelengths, it is easier to change the corrugation pitches, which are often defined by EBL, and in this way a wide range of wavelengths can be achieved [188]. However, the pattern unit of the EBL machine limits the resolution at which the corrugation pitch can be written; for example, to define a laser array with a wavelength spacing of 100 GHz, the resolution of the EBL machine needs to be about 0.125 nm, which is beyond the typical resolution limit of 0.5 nm of EBL machines.

There is therefore a need to improve the resolution for grating definition beyond the standard resolution of EBL systems. One such method is weighted-dose allocation variable-pitch EB-lithography [189]. But the associated algorithm makes the technique complex and ill-suited for volume manufacture. The REC technique based on SBGs mentioned in Chapter 2 has been applied to making semiconductor lasers successfully. Since the first DFB semiconductor laser diode with EPS was reported in 2007 [156], DFB semiconductor lasers based on the REC have continued to be developed with novel DFB semiconductor lasers and laser arrays based on this technique reported [190-193]. Recently, based on this technique, even a 60-wavelength DFB semiconductor laser array with a channel spacing of 100 GHz (about 0.8 nm around 1550 nm) was realized, which is a major feat [194]. These DFB semiconductor lasers were fabricated by holography combined with traditional contact photolithography, which is suitable for volume production. However, the effective coupling coefficient,  $\kappa$ , is reduced substantially compared to that of a continuous uniform Bragg

grating, which adversely affects the SLM performance of the laser. To increase the coupling coefficient, SBGs with phase-shifted sections were introduced, as mentioned in Section 2.4. This technique was firstly proposed and demonstrated in fibre lasers [159]. In these structures, the strength of the  $\pm 1^{\text{st}}$ -order reflections can be enhanced selectively, while suppressing the  $0^{\text{th}}$ -order reflection. Here, for the first time, we applied this technique to DFB semiconductor lasers by EBL.

## 4.2 Device Design and Fabrication

The structures for SBGs with phase-shifted sections are shown in Fig. 2.9, with grating structures of C-SBG, 2PS-SBG, 3PS-SBG and 4PS-SBG. For all of the SBGs,  $-1^{\text{st}}$ -order reflections were used as the working channels for the DFB semiconductor lasers and the duty cycles were all set as 0.5 for maximum effective coupling coefficients. The DFB lasers were based on ridge waveguides with sidewall gratings. The width of the ridge waveguide was  $2.5 \mu\text{m}$  and the recess of the gratings was  $0.6 \mu\text{m}$  on both sides.

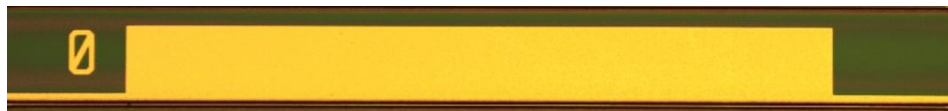


Figure 4.1: The micrograph of a single DFB semiconductor laser diode.

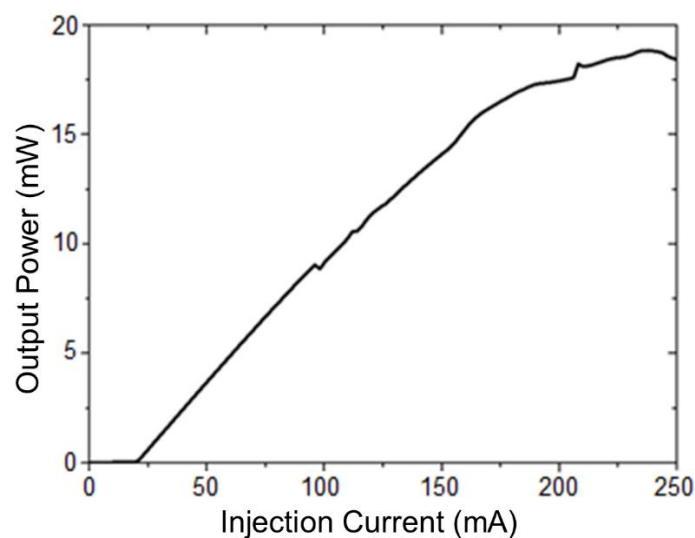
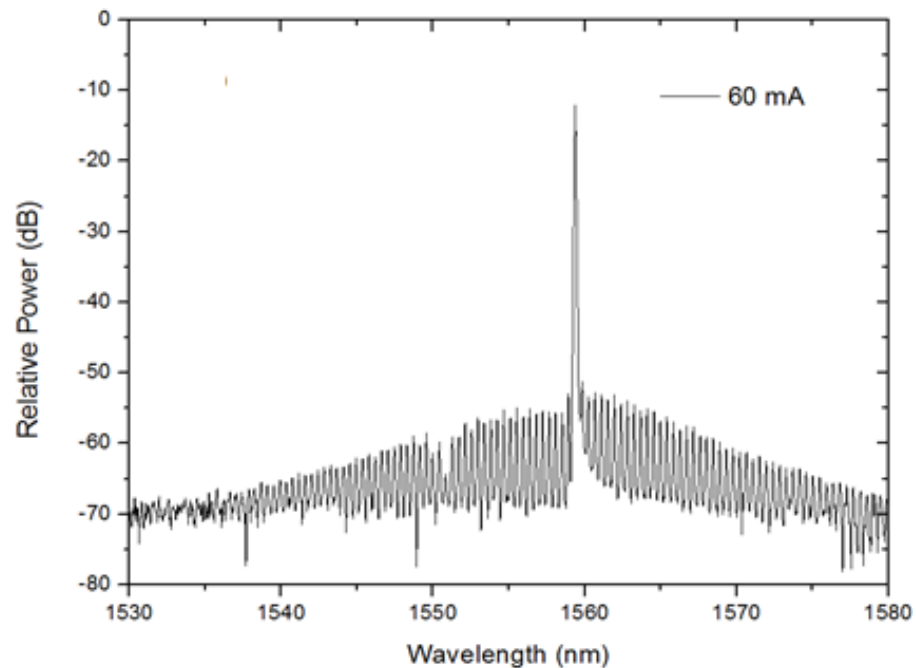


Figure 4.2: The *L/I* curve of the DFB laser diode.



**Figure 4.3: The output optical spectrum of the DFB laser diode @ 60 mA.**

Figure 4.1 shows the micrograph of the original design of a single DFB semiconductor laser diode. The DFB laser diode had a cavity length of  $1200\ \mu\text{m}$  with a straight ridge waveguide. Since it was tested as-cleaved, it had optical reflections from both output facets, which means that it would have severe FP modes. Figure 4.2 illustrates the light-current ( $LI$ ) curve of the DFB laser diode and the curve is not smooth. Figure 4.3 shows the output optical spectrum at an injection current of 60 mA. Although the side mode suppression ratio (SMSR) is  $> 40\ \text{dB}$ , the FP modes are really severe.

To make improvements, bend ridge waveguides integrated with a semiconductor optical amplifier (SOA) were introduced on both sides to eliminate the optical reflections from output facets, as shown in Fig. 4.4(a). The cavity length  $L$  of the DFB section was still  $1200\ \mu\text{m}$  and the SOA had a length of  $300\ \mu\text{m}$ , separated by an isolation gap of  $20\ \mu\text{m}$ . The SOA had a curved waveguide with radius of  $1724.1\ \mu\text{m}$  making an angle of  $10^\circ$  at the output facet. To avoid back reflections from the other side of the laser diode, a waveguide, of length  $125\ \mu\text{m}$  with a radius of  $233.3\ \mu\text{m}$  and an angle of  $32^\circ$  at the facet, absorbs the light. Figure 4.4(b) shows the micrograph of the fabricated DFB laser diode. The curved waveguides minimize back reflections from the output facets, so the lasing wavelength only depends on the

gratings in the DFB section. Figure 4.5 shows the SEM image of the bend ridge waveguides of fabricated DFB semiconductor laser diodes.



Figure 4.4: (a) The design of a DFB laser diode with bend ridge waveguides on both sides, and (b) the micrograph of the fabricated DFB laser diode [160].

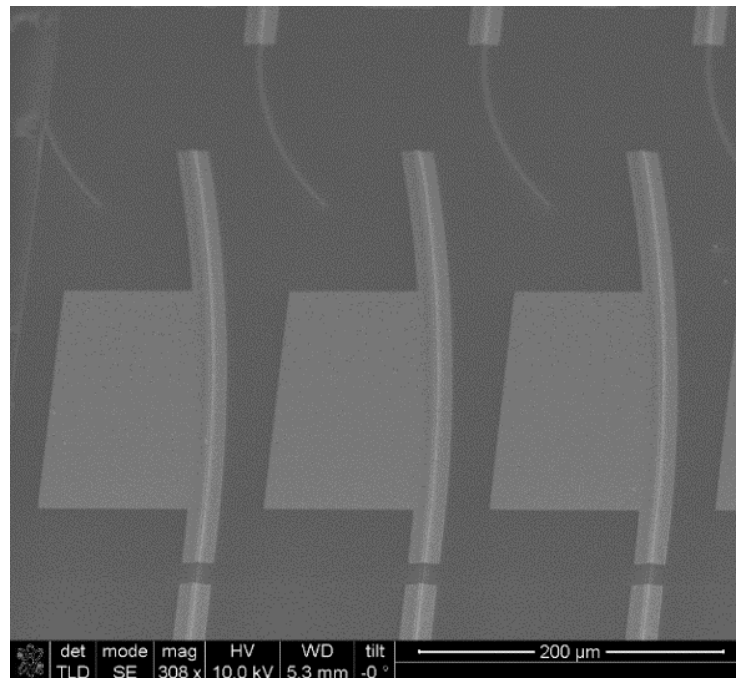


Figure 4.5: The SEM image of the bend waveguides of fabricated DFB laser diodes.

For all of the SBGs (including C-SBG, 2PS-SBG, 3PS-SBG, and 4PS-SBG), the grating period of the seed Bragg grating was set at 260 nm and the sampling period was 3.712  $\mu\text{m}$ ,

which would lead to lasing at wavelengths around 1550 nm. Here, as mentioned before, we choose the  $-1^{\text{st}}$ -order reflections as the working channels, so the appropriate phase shifts of adjacent sections for the 3PS-SBG and 4PS-SBG designs are  $-2\pi/3$  and  $-2\pi/4$  respectively, as shown in Fig. 2.10. To achieve SLM operation, the equivalent  $\pi$ -phase shift can be introduced in the middle of the sampling structures by shifting the sampling structures by half of the sampling period, which is  $1.856 \mu\text{m}$  in this circumstance. Figure 4.6 shows the micrograph of the equivalent  $\pi$ -phase shift introduced in the middle of ridge waveguides of C-SBG and 2PS-SBG respectively and the equivalent  $\pi$ -phase shift can be seen under a microscope.

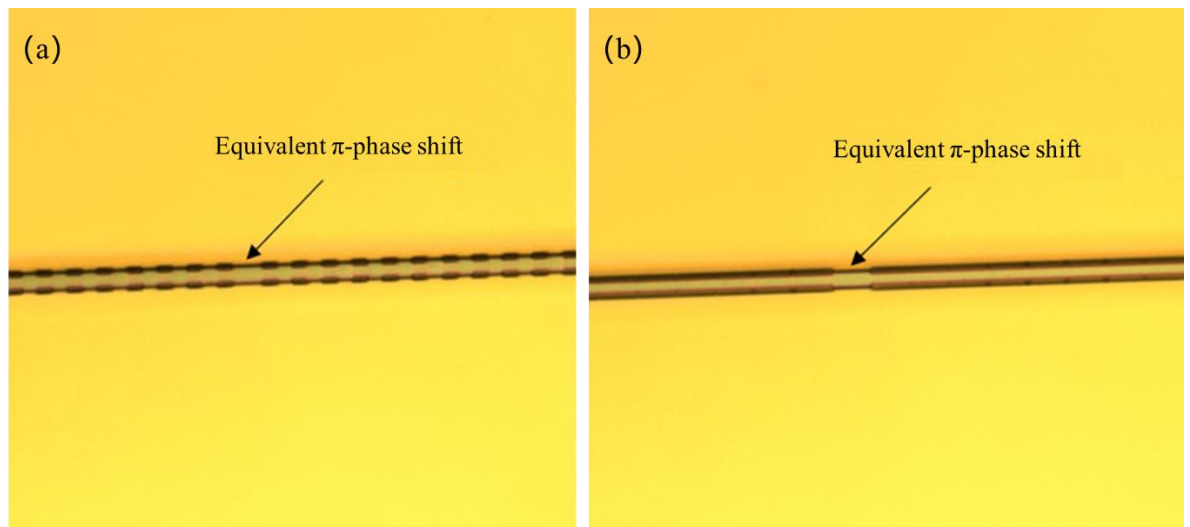


Figure 4.6: The micrograph of the equivalent  $\pi$ -phase shift introduced in the middle of ridge waveguides of (a) C-SBG, and (b) 2PS-SBG.

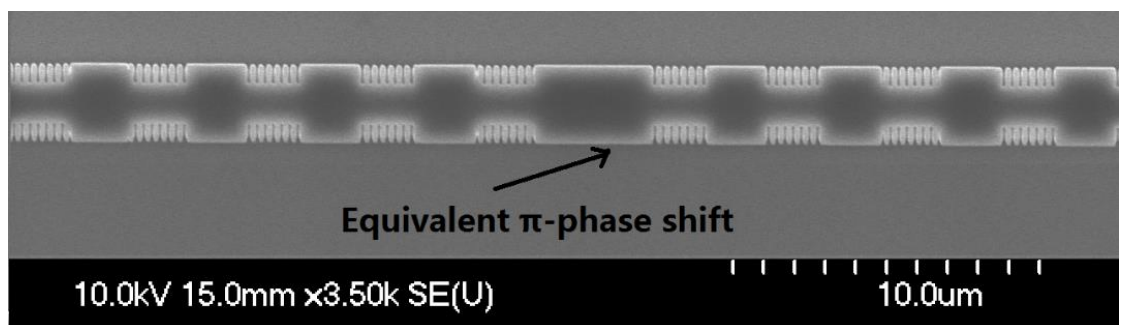
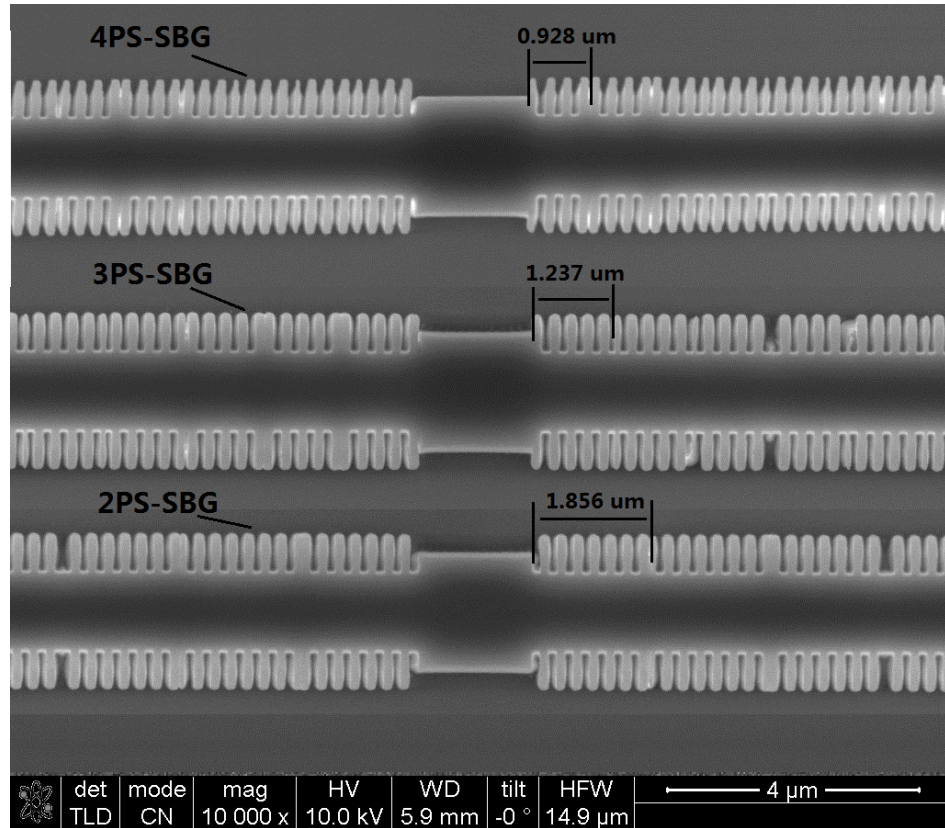


Figure 4.7: The SEM image of a C-SBG with an equivalent  $\pi$ -phase shift.



**Figure 4.8: The SEM image of 2PS-SBG, 3PS-SBG and 4PS-SBG structures with equivalent  $\pi$ -phase shifts.**

All of the SBGs were defined by EBL using HSQ. Figure 4.7 shows the SEM image of a C-SBG with an equivalent  $\pi$ -phase shift and Fig. 4.8 illustrates the SEM image of 2PS-SBG, 3PS-SBG and 4PS-SBG structures with equivalent  $\pi$ -phase shifts. All of the equivalent phase shifts can be seen clearly. Since for 2PS-SBG, 3PS-SBG and 4PS-SBG structures, one sampling period was divided into two, three and four sections respectively, the length for each sub-section was 1.856  $\mu\text{m}$ , 1.237  $\mu\text{m}$  and 0.928  $\mu\text{m}$  respectively, as shown in Fig. 4.8.

### 4.3 Set-up for Measurements

To measure devices shown in Fig. 4.4, two probes are needed, one for the DFB section and the other for the SOA section. Figure 4.9 shows the schematic of the set-up to measure the DFB laser diode integrated with an SOA. The laser bar is mounted on a copper sheet, under which there is a thermoelectric cooler (TEC) used for temperature control (set at 20 °C). A current driver is used to control the injection currents and the TEC at the same time. The

output light is coupled into a lensed fibre and then detected by an optical power meter or an optical spectrum analyser. The optical power meter is used to measure the output optical power and the optical spectrum analyser is used to measure the optical spectra. Utilising the General-Purpose Interface Bus (GPIB) interface, automated control can be realised by *Labview*. The current driver is controlled automatically by a computer and generated data can be collected and saved automatically, reducing the measuring time dramatically.

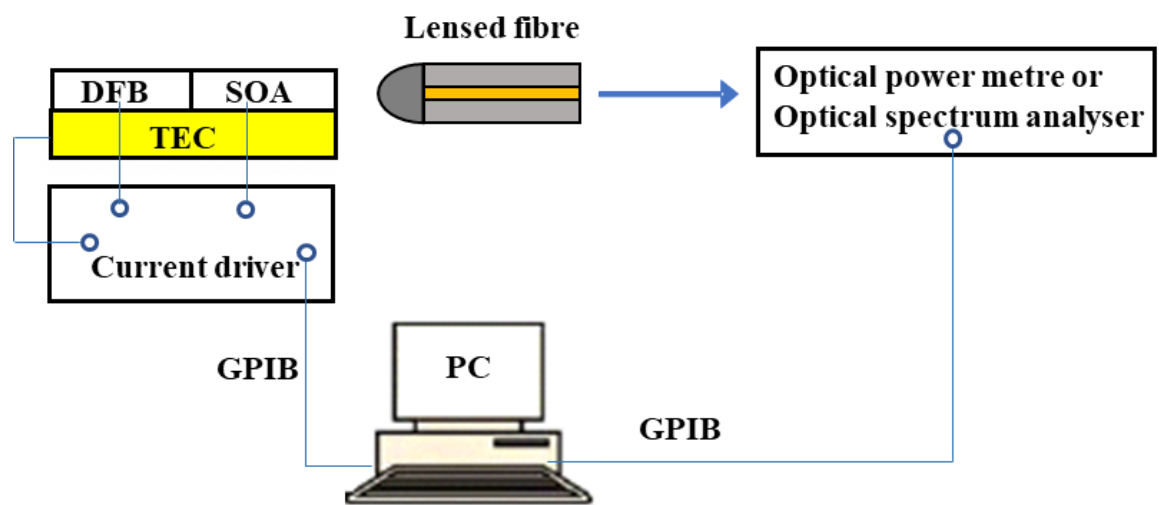


**Figure 4.9: Schematic of the set-up to measure a DFB laser diode integrated with an SOA.**

Figure 4.10 (a) shows the photograph of the set-up, two probes were used for independent current injection and a lensed fibre was mounted on a three-dimensional stage to adjust the position for coupling the output light. On top of the system, a microscope was used for checking the alignment. Figure 4.10(b) shows the micrograph of the two touched probes and the lensed fibre. Because of curved ridge waveguides, the lensed fibre was tilted at a specific angle of  $32^\circ$  to achieve the largest coupling efficient.

The modular controller used was a Model 8000 from *Newport Company*, as shown in Fig. 4.11. It can control the setting of the two injection currents independently at the same time, and can also control the TEC to achieve a stable temperature.



**Figure 4.10: (a) The photograph of the set-up, and (b) the micrograph of the two touched probes and the lensed fibre.**



**Figure 4.11: Model 8000 from Newport Company.**

During the measurements, the software *Labview* is used to control the equipment. Once the equipment is set up properly, measurements will be carried out automatically by *Labview*, which is beneficial to save time for measurements. The basic measurements include measuring output optical power and optical spectra.

## 4.4 Enhancement of Effective Coupling Coefficients Based on SBGs with Phase-shifted Sections

In Section 2.4.1, SBGs with phase-shifted sections are introduced for gaining higher effective coupling coefficients. Based on these grating structures, single-wavelength DFB semiconductor diode lasers were designed and fabricated. Demonstration of the enhancement of effective coupling coefficients was carried out by comparing the stop-bands of these DFB lasers at injection currents just below threshold. All of the results in this thesis were measured at a temperature of 20 °C controlled by the TEC.

### 4.4.1 Comparison of Stopbands

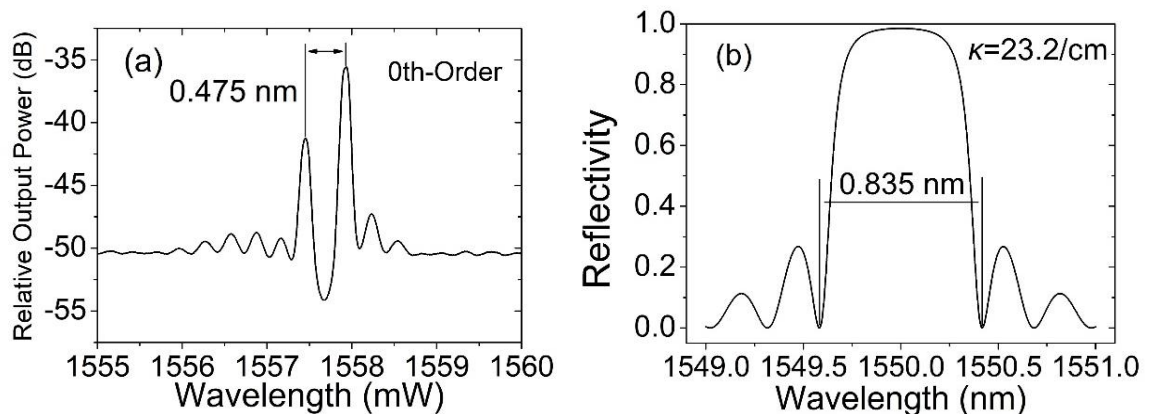


**Figure 4.12: (a) The optical spectrum of a laser diode just below threshold (50 mA) with uniform seed grating, and (b) the reflectivity spectrum of a passive waveguide of the corresponding uniform seed grating [160].**

Firstly, a DFB laser diode based on a uniform seed grating (0<sup>th</sup>-order reflection) with a grating period of 243 nm without sampling was fabricated as the reference laser, which would lase at around 1550 nm. This DFB diode laser's optical spectrum was measured at the injection currents of the DFB section and the SOA set just below threshold (50 mA) and at 5 mA respectively, as shown in Fig. 4.12(a). The measured stopband between the two main modes is 0.475 nm, from which  $\kappa$  is calculated to be 23.2 cm<sup>-1</sup>. The corresponding reflectivity spectrum of a passive waveguide with the same uniform grating parameters was simulated using the TMM, and, as shown in Fig. 4.12(b), the stopband is 0.835 nm. It is well

known that the measured stopband of a DFB grating in the presence of gain is significantly smaller than that of the equivalent passive waveguide [195], which accounts for the difference.

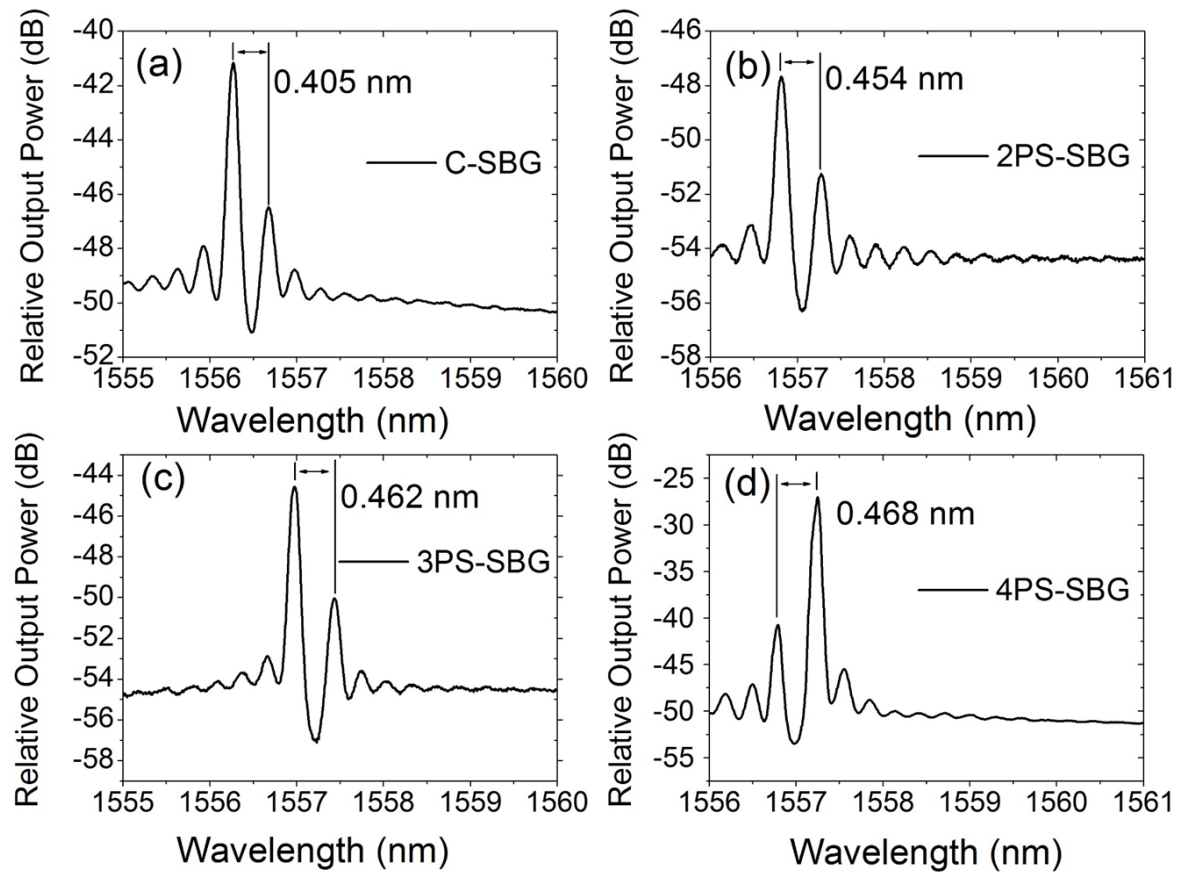


**Figure 4.13: Optical spectra measured just below threshold (50 mA) of (a) C-SBG, (b) 2PS-SBG, (c) 3PS-SBG and (d) 4PS-SBG [160].**

DFB semiconductor lasers based on SBGs with phase-shifted sections were firstly fabricated without equivalent phase shift corresponding to the four designs (C-SBG, 2PS-SBG, 3PS-SBG, and 4PS-SBG). According to the design, the same operating wavelengths were obtained as the reference laser. At the same injection currents as for the reference laser, the optical spectra of these grating structures were measured just below threshold, as shown in Fig. 4.13. The measured stopbands of the C-SBG, 2PS-SBG, 3PS-SBG and 4PS-SBG lasers are 0.405 nm, 0.454 nm, 0.462 nm and 0.468 nm respectively. Since the theoretical ratios of the effective  $\kappa$  of the  $-1^{\text{st}}$ -order channels to that of the  $0^{\text{th}}$ -order channel are about 0.32, 0.64, 0.83 and 0.90 respectively, the effective  $\kappa$  of  $-1^{\text{st}}$ -order channels are estimated as  $7.4 \text{ cm}^{-1}$ ,

14.8  $\text{cm}^{-1}$ , 19.3  $\text{cm}^{-1}$  and 20.9  $\text{cm}^{-1}$  for C-SBG, 2PS-SBG, 3PS-SBG and 4PS-SBG respectively. The reflectivity spectra of passive waveguides were simulated based on these estimated values of effective  $\kappa$ , as shown in Fig. 4.14. From the simulation, the corresponding stopbands are measured to be 0.645 nm, 0.719 nm, 0.777 nm and 0.805 nm respectively.

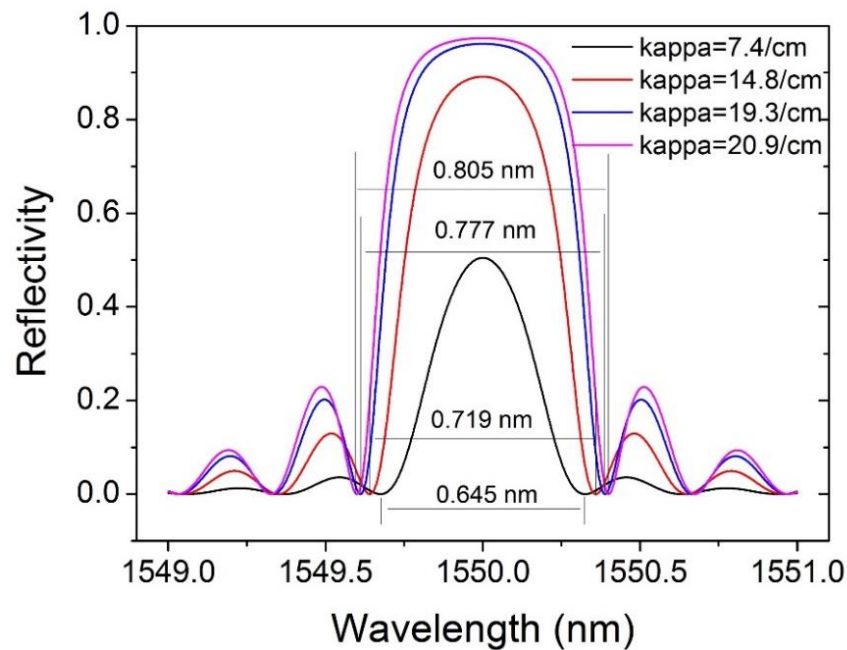


**Figure 4.14: Simulated reflectivity spectra of passive waveguides with different values of  $\kappa$  (smaller  $\kappa$  having narrower stopband) [160].**

**Table 4.1 Properties of modelled and measured gratings [160]**

Grating types	C-SBG	2PS-SBG	3PS-SBG	4PS-SBG	Uniform 0 <sup>th</sup> -order grating
Measured stopband / nm	0.405	0.454	0.462	0.468	0.475
Uniform grating Equivalent $\kappa$ / $\text{cm}^{-1}$	7.4	14.8	19.3	20.9	23.2
Uniform grating Passive stopband / nm	0.645	0.719	0.777	0.805	0.835
Ratio of {measured/passive stopband}	0.63	0.63	0.59	0.58	0.57

All these data are summarized in Table 4.1, where the calculated ratios of the stopbands of active waveguides and stopbands of passive waveguides are also presented. Since the ratios

are almost constant ( $0.6 \pm 0.03$ ), the effective coupling coefficients are approximately the same as the theoretical values. The reflection strengths of the  $-1^{\text{st}}$ -order channels are indeed enhanced as expected.

#### 4.4.2 Single-mode Lasers with Equivalent $\pi$ -phase shift

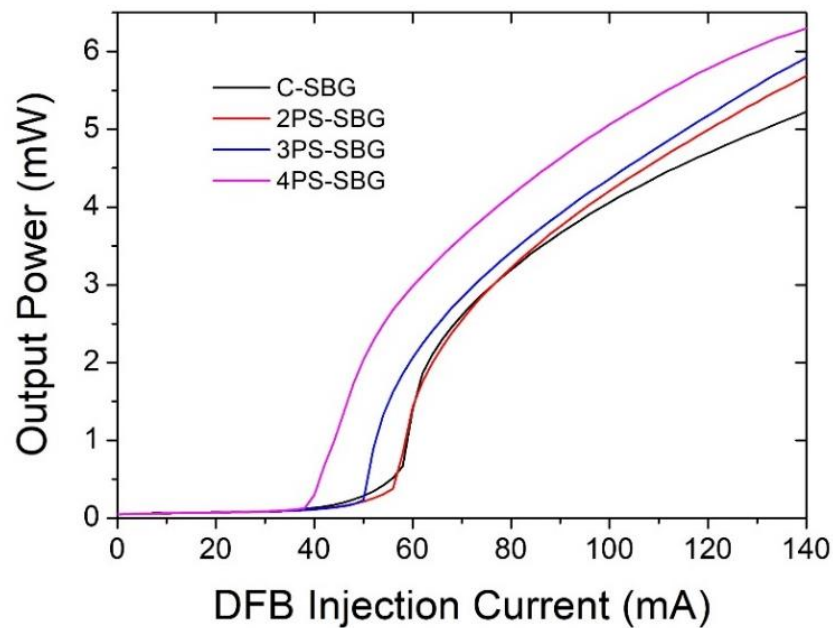


**Figure 4.15:** *LI* curves of the fabricated DFB laser diodes for the four SBGs, at the SOA's injection currents of 20 mA.

With equivalent  $\pi$ -phase shifts introduced as Fig. 4.7 and Fig. 4.8, single-mode lasing for the four SBGs (C-SBG, 2PS-SBG, 3PS-SBG and 4PS-SBG) can be realized. Figure 4.15 illustrates the light-current (*LI*) curves of the fabricated single-mode DFB laser diodes for the four SBGs, at the SOA injection currents of 20 mA. Since the effective  $\kappa$  was not very high, the threshold currents were about 40 to 50 mA. Because there was no reflection from either facet of the laser diode, the output optical power was not very high and we could obtain about 4 mW when the DFB injection current was 100 mA. If the high reflection coating is deposited on one facet in the future, the output power will be doubled. We can see the trends that, with more divided sections in one sampling period, more output optical power as well as lower threshold currents, were obtained, trends which are consistent with these of the effective coupling coefficients.

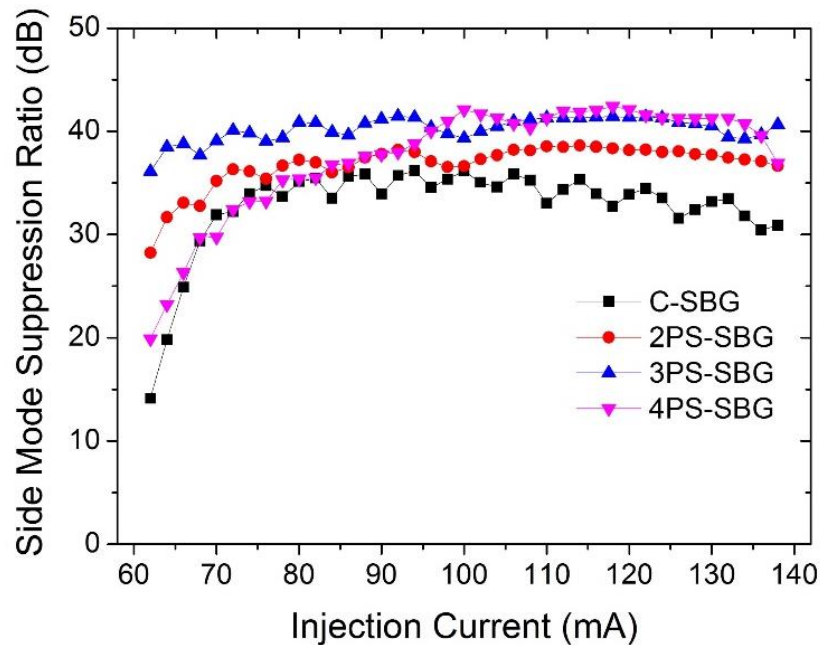


**Figure 4.16: SMSRs of the lasers at different DFB injection currents when the SOA injection current was 20 mA [160].**

The SMSRs of the various kinds of single-mode DFB lasers are shown in Fig. 4.16 at different DFB injection currents when the SOA injection current was 20 mA. Stable SLM operation was observed when the DFB injection current was more than 70 mA. Apart from the C-SBG, the SMSRs of the other three kinds of SBGs were all above 35 dB. Poor SMSRs of the C-SBG were obtained because of the relatively low coupling coefficient ( $\sim 7.4 \text{ cm}^{-1}$ ). An increase in the SMSR with the number of phase-shifted sections in one sampling period reflects the increase in the effective coupling coefficient.

Figure 4.17 shows the optical spectra from the DFB lasers based on the four SBGs when the injection currents of the DFB and SOA sections were set at 100 mA and 20 mA respectively. The FP modes are barely visible in the spectra, implying that the facet reflection and the reflection from the shallow etched isolation slot between the DFB and SOA were negligible. At these injection currents, the SMSRs were all above 36 dB. Meanwhile, the lasing wavelengths were nearly the same among the four SBGs (the wavelength of C-SBG was a little different because of a slight difference in the profile of the grating structure compared with the other three SBGs), which demonstrates the high precision that can be obtained by using the sampling technique with EBL.

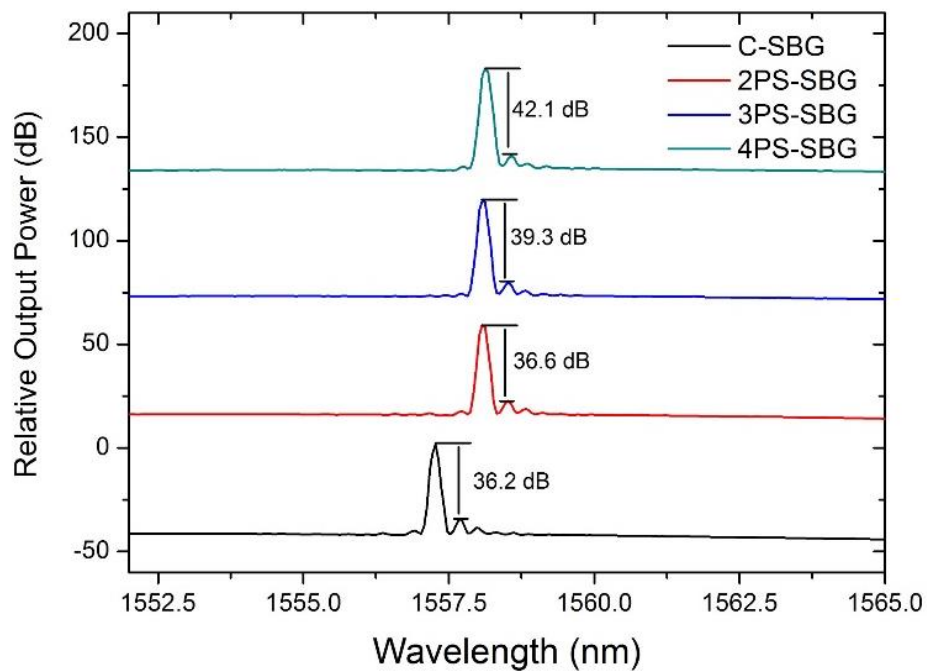


Figure 4.17: Optical spectra of the four SBGs at 100 mA [160].

## 4.5 An Eight-wavelength DFB Laser Array

DFB laser arrays have promising applications for WDM systems aimed at access networks and data centres. They are also key components for PICs for future applications. For traditional DFB lasers based on uniform Bragg gratings, we could achieve different lasing wavelengths by changing the grating periods, but the precision would be limited, as described in section 4.1. However, for DFB lasers based on the SBGs, different wavelengths can be realized easily by changing only the sampling periods. Unlike the seed grating periods, which have the feature sizes of about 200 to 300 nm, the sampling periods have much larger feature sizes, from several microns to dozens of microns. Larger feature sizes imply a relaxation in fabrication tolerance. As mentioned before, laser arrays based on the REC technique have been produced with high precision. According to reference [196], the error tolerance can be relaxed by several hundred times by applying sampling structures.

Here, an eight-wavelength DFB laser array with high wavelength precision has been demonstrated, based on the 2PS-SBG design shown in Fig. 2.9(b). The seed grating period was chosen to be 250 nm, and the sampling periods varied from 7.979  $\mu\text{m}$  to 9.206  $\mu\text{m}$ , to

give a wavelength spacing of 100 GHz, corresponding to  $\sim 0.8$  nm at 1550 nm. To ensure SLM operation of the DFB lasers, the central section contained the equivalent  $\pi$ -phase shift shown in Fig. 4.7 and Fig. 4.8. Figure 4.18 shows the micrograph of the fabricated eight-wavelength DFB laser array, with the lasers numbered from 1 to 8. For each laser diode, the total length was 1645  $\mu\text{m}$  and the width was 150  $\mu\text{m}$ .

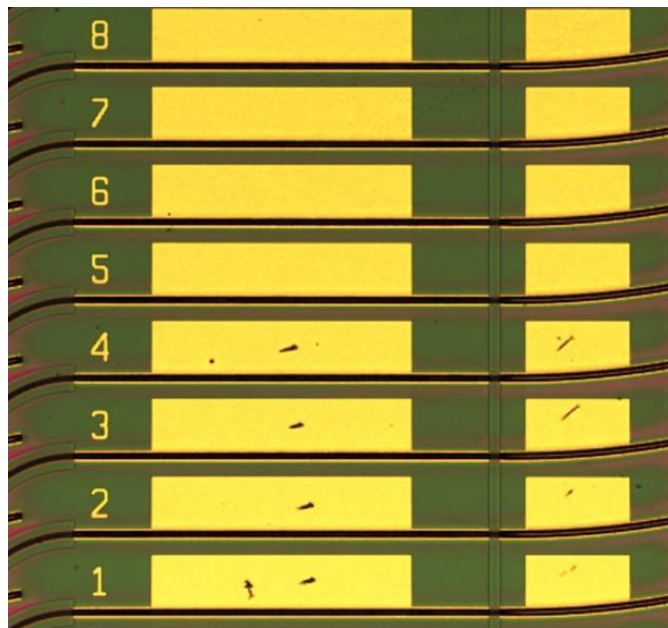


**Figure 4.18:** The micrograph of the fabricated eight-wavelength DFB laser array.

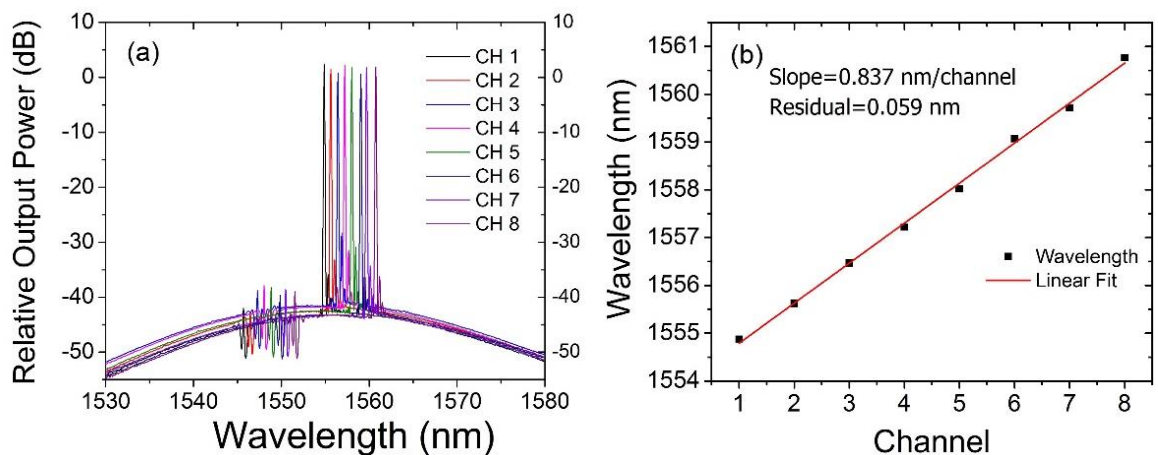


**Figure 4.19:** (a) Optical spectra of the laser array at injection currents of 100 mA (channels 1 to 8, left to right), and (b) linear fitting of the wavelengths [160].

The laser array was measured with the injection currents of the DFB and SOA sections set at 100 mA and 20 mA respectively. The lasing spectra are shown in Fig. 4.19(a). The difference in peak power between the lasers is not significant, and reflects variations in coupling the light from the SOAs into the single mode fibre used to feed the optical spectrum analyser. The SMSRs are all over 30 dB, which can be optimised further by improving the fabrication process by increasing the coupling coefficients. By linear fitting of the wavelengths, a slope of 0.837 nm per channel (104 GHz) was obtained, with a residual of 0.059 nm (Fig. 4.19(b)), which is very close to the design value. These results demonstrate the excellent wavelength precision that can be achieved with this technique.

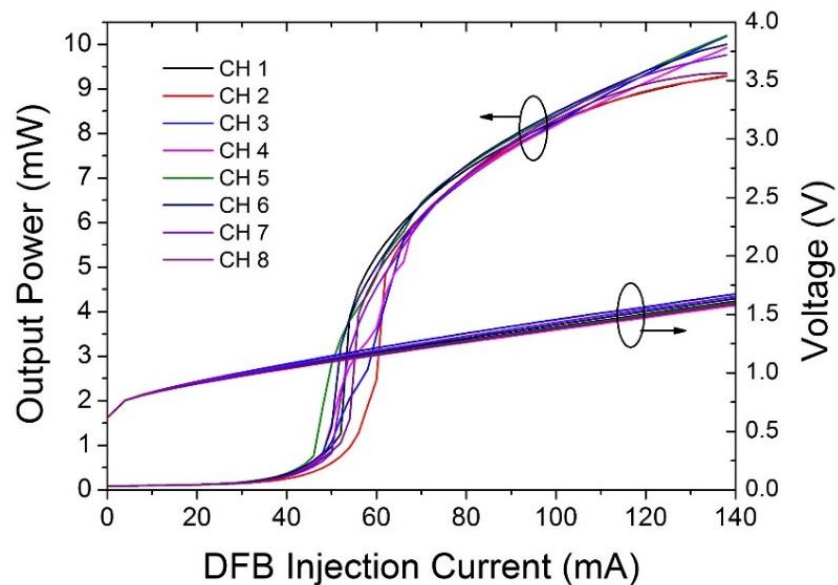


**Figure 4.20: LIV characteristics of the fabricated eight-wavelength laser array with SOA drive currents set at 40 mA [160].**

Figure 4.20 shows the light-current-voltage (*LIV*) curves of the lasers. The devices were measured with drive currents of 40 mA applied to the appropriate SOAs. Given each of the *LI* characteristics reflects the performance of a laser/SOA combination, the uniformity of optical output power is acceptable. The threshold currents are about 50 mA for all of the laser diodes. The lasers reported here were designed with relatively long cavities (1200  $\mu\text{m}$ ) because of low effective coupling coefficients. Figure 4.20 also shows almost 10 dBm (10 mW) output power with the DFB section driven at 140 mA. The voltages are about 1.25 V when the injection currents are set at 60 mA. By calculation, the resistance can be obtained

as about  $5.7 \Omega$  when the diodes are lasing, which is a normal value. Electro-absorption modulators will be integrated within future iterations of the DFB laser array to make an optical transmitter, suitable for use in PONs and data centres. From the lasing wavelengths and  $LIV$  curves of the eight different diode lasers, we can see that the lasing performance of different lasers is uniform. These diode lasers have similar effective coupling coefficients, which shows that the dry etch process of the gratings is in good control. This uniformity benefits from the etch-stop layer used to fabricate during the dry etch process.

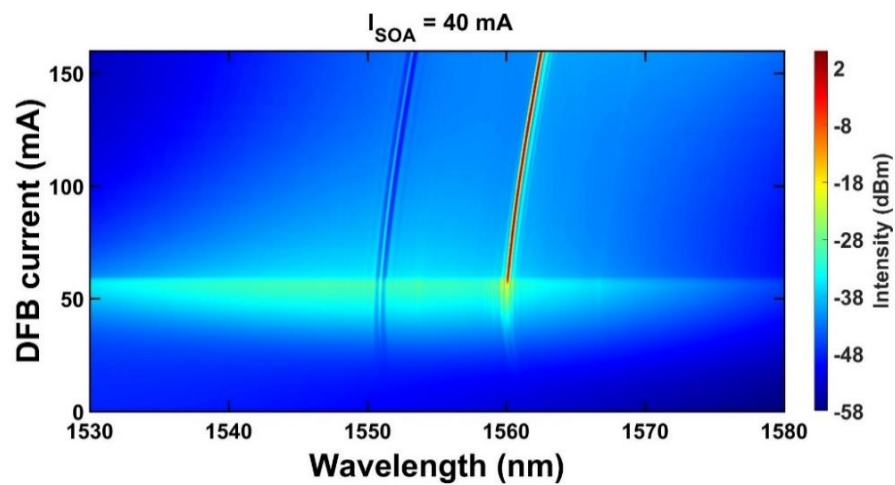


Figure 4.21: The 2D optical spectrum mapping of one of the DFB laser diodes.

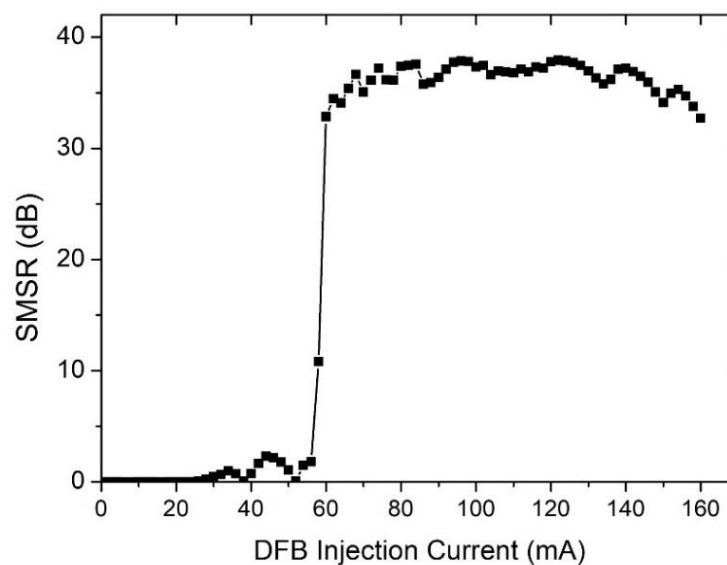


Figure 4.22: The SMSR changing with the DFB injection current.

The eight laser diodes are similar and one was chosen for further study. Figure 4.21 shows the 2D optical spectrum mapping of one of the DFB laser diodes at SOA current of 40 mA, which shows stable single-mode lasing at injection currents of DFB section from threshold to 160 mA. The change in SMSR with the DFB injection current is shown in Fig. 4.22, from which we can see that the SMSR is stable at about 36 dB for currents above threshold.

Lasing wavelength has also been measured as a function of DFB injection current (SOA current fixed at 40 mA), as shown in Fig. 4.23. This diagram shows that the relation between lasing wavelength and DFB injection current is relatively linear. Due to the thermal shift, the wavelength shift is about 2.35 nm at injection currents changing from 60 mA to 160 mA and a wavelength tuning of 23.5 pm/mA can be calculated.

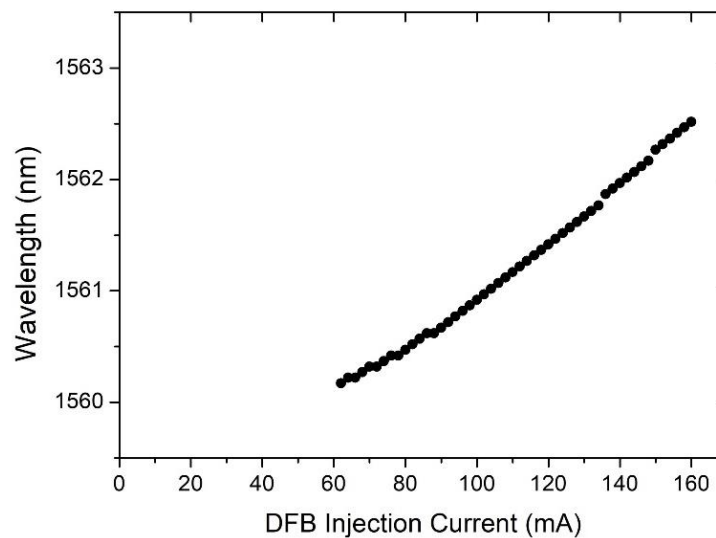


Figure 4.23: The lasing wavelength changing with DFB injection currents.

## 4.6 Measurements of Far-field Patterns

The far-field patterns of the semiconductor diode lasers were also measured. From this characteristic, the far-field pattern can reveal the quality of the laser beam and show that whether the laser beam is a good TE fundamental mode. Divergence angles of the laser beam can also be calculated. The schematic of the set-up to measure far-field patterns is shown in Fig. 4.24. As for the set-up that shown in Fig. 4.9, the diode lasers are mounted on a copper sheet with a TEC underneath for temperature control. The temperature is set at 20 °C and

probes are aligned to touch the electrode pads for current injection. The output light beam is then coupled into a goniometric radiometer for measurements. Figure 4.25 is a photograph of the set-up used to measure far-field patterns of diode lasers. After applying injection currents, the laser beam was sent into the goniometric radiometer directly. Controlled by a computer, a Goniometric Radiometer Model LD 8900R™ from Photon Inc. was used for measurement in this work and the associated software was used to collect the data automatically.

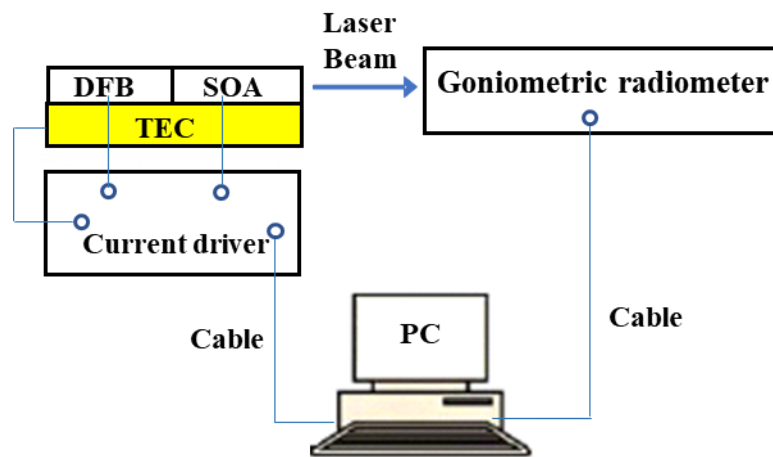


Figure 4.24: Schematic of the set-up to measure far-field patterns.

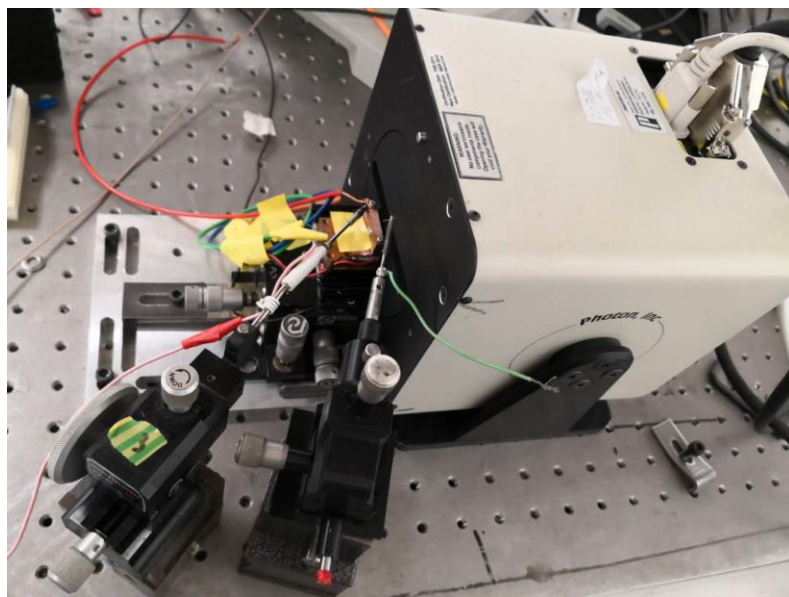
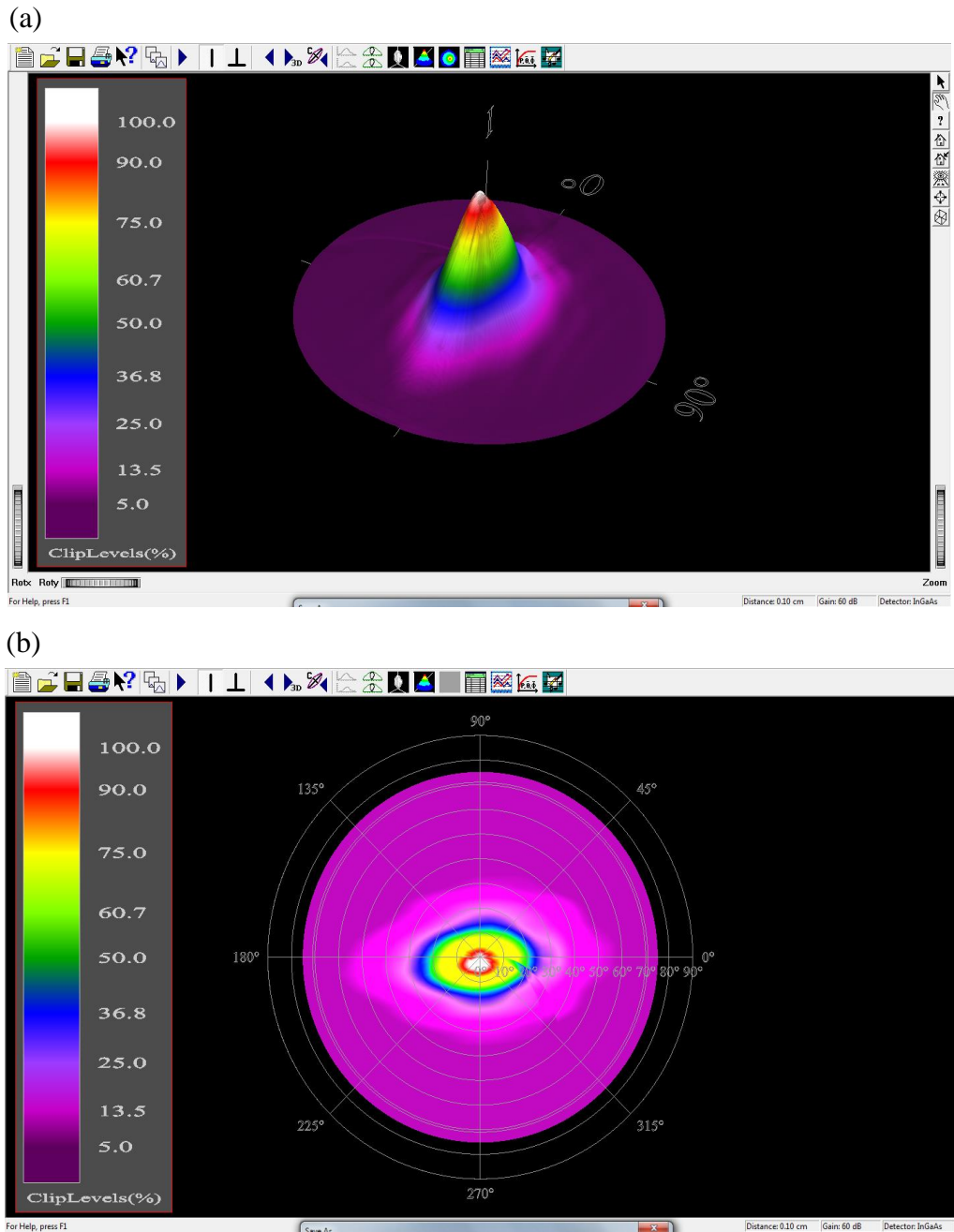


Figure 4.25: The photograph of the set-up to measure far-field patterns of diode lasers.

The far-field pattern of a diode laser based on a straight ridge waveguide, as shown in Fig. 4.1, was firstly measured. Figure 4.26(a) shows the 3D intensity profile of the output light beam in cylindrical coordinates, and Figure 4.26(b) shows the 2D display in polar coordinates from the 3D acquisition with the perspective view looking from the source. These two images illustrate that the output light beam has a Gaussian shape profile, confirming the good quality of TE fundamental mode lasing.



**Figure 4.26: (a) 3D and (b) 2D light beam intensity profiles for a diode laser based on the straight ridge waveguide.**

The light intensity distribution as a function of divergence angle is illustrated for the vertical and horizontal directions in Fig. 4.27. The divergence angles at the half-power points were calculated from the graphs. The divergence angles in the vertical and horizontal directions were  $40.9^\circ$  and  $23.5^\circ$  respectively. The laser beam is more divergent in the vertical direction, which is determined by the epitaxial wafer structure and the ridge waveguide design.

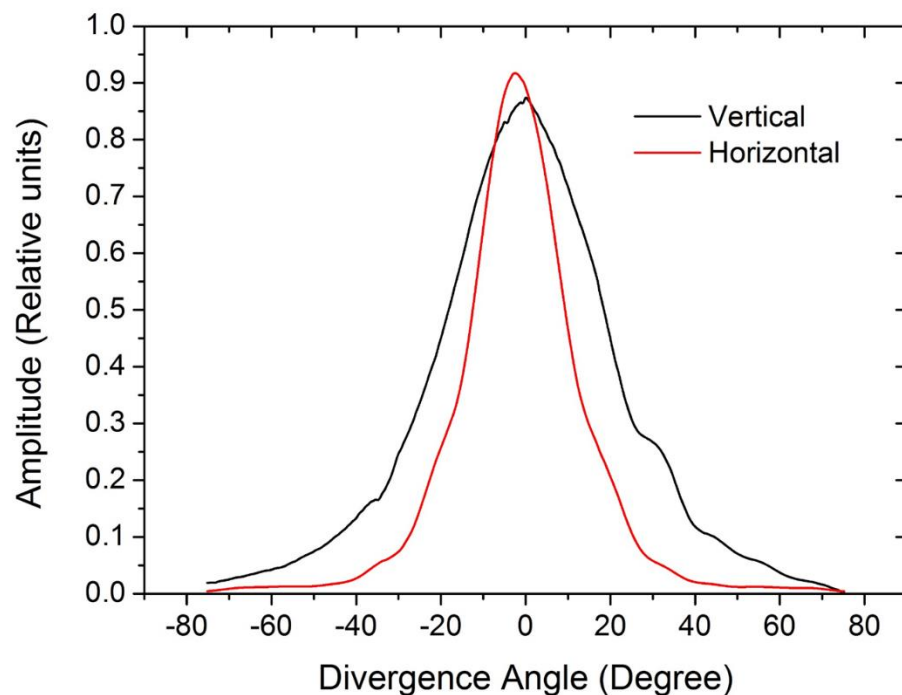


**Figure 4.27: Vertical and horizontal profiles of light intensity for a diode laser based on the straight ridge waveguide.**

The far-field pattern of a diode laser based on a bend ridge waveguide was also measured. The DFB diode laser structure with bend waveguides is shown in Fig. 4.4 where the SOA was tilted by  $10^\circ$  at the output facet. The corresponding 3D and 2D light beam intensity profiles are shown in Fig. 4.28. Because of the tilt, the peak of the beam intensity profile is not in the centre of the coordinates. However, the laser beam intensity profile still has a Gaussian shape. This means that the bend ridge waveguides in the design have no influence on the diode lasers' single-mode lasing performance.

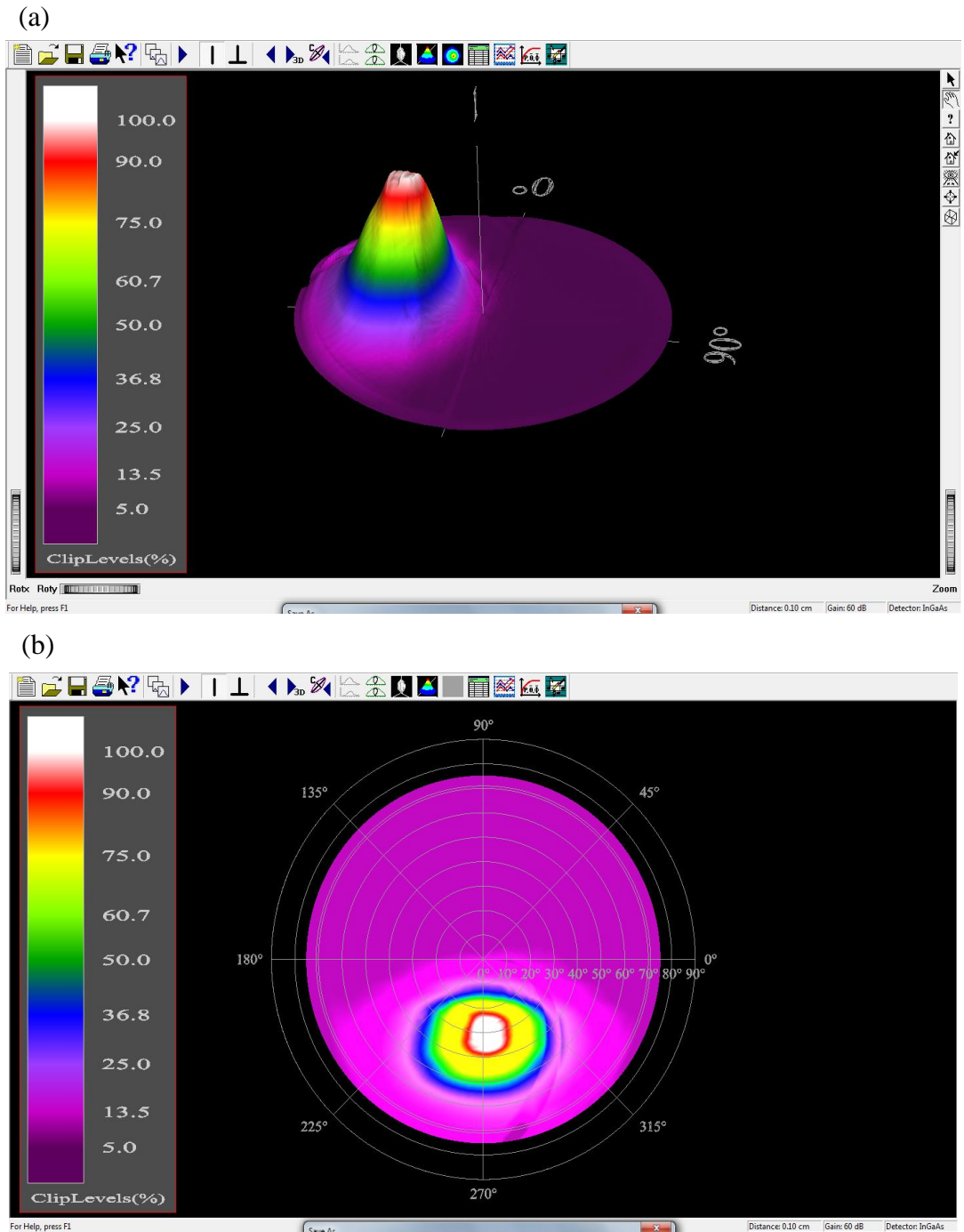


**Figure 4.28: (a) 3D and (b) 2D light beam intensity profiles for a diode laser based on a bend ridge waveguide.**

The horizontal profile of light intensity for the diode laser based on a bend ridge waveguide was derived, as shown in Fig. 4.29. From this graph, we can see that the transmission angle is exactly the design value of  $33^\circ$  for the bend ridge waveguide shown in Fig. 3.7.

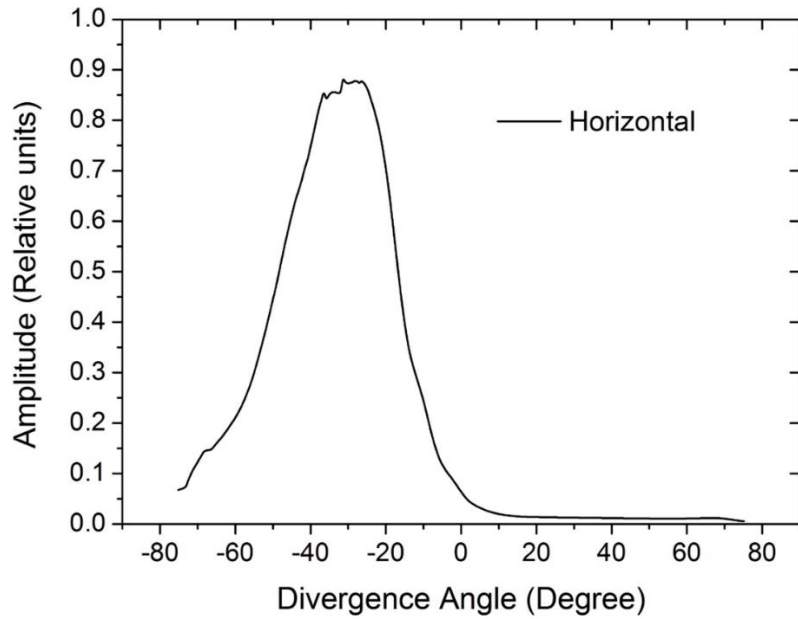


**Figure 4.29: The horizontal profile of light intensity for a diode laser based on a bend ridge waveguide.**

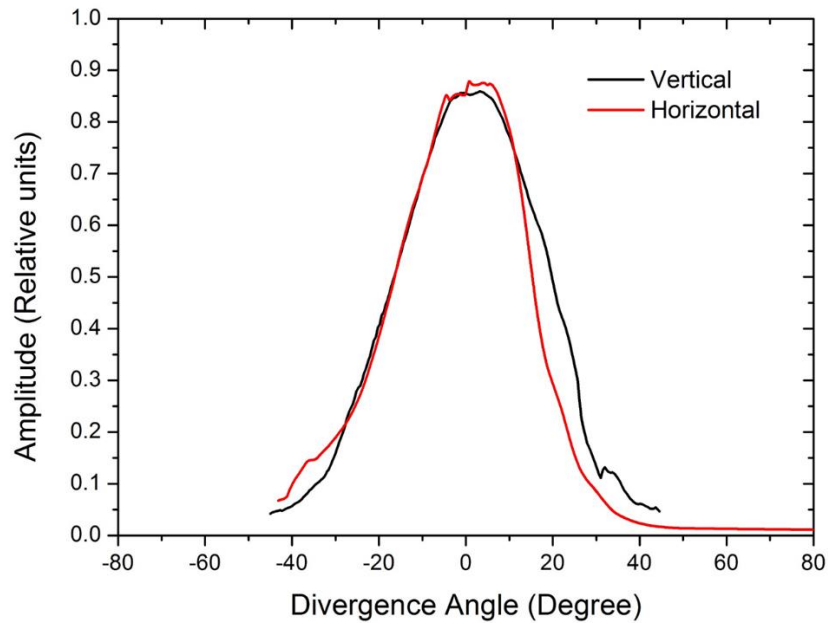


**Figure 4.30: Vertical and horizontal profiles of light intensity based on the bend ridge waveguide centered at the peak of intensity.**

Figure 4.30 illustrates vertical and horizontal profiles of the light intensity from the bend ridge waveguide centered at the peak of intensity. The vertical divergence angle was still

about  $40.9^\circ$ . However, the horizontal divergence angle was about  $34^\circ$ , larger than that of a straight ridge waveguide. The structure difference of the bend ridge waveguide in the horizontal direction will lead to an increase of the divergence angle.

The Gaussian-shaped laser beam profiles prove that these DFB diode lasers have good single-mode lasing performance, even with bend ridge waveguides. It is beneficial to introduce the bend ridge waveguides into the lasers to eliminate facet reflections, maintaining single-mode lasing at the same time.

## 4.7 Chapter Summary

In this chapter, novel DFB semiconductor lasers and laser arrays were designed and demonstrated. The design of the DFB semiconductor diode lasers were introduced first. Compared to conventional straight ridge waveguides, bend ridge waveguides were introduced to eliminate facet reflections. This is beneficial for single longitudinal mode operation of DFB diode lasers. Then the design parameters of four SBGs (C-SBG, 2PS-SBG, 3PS-SBG, and 4PS-SBG) were presented to produce novel DFB diode lasers. The set-up to measure these diode lasers was described, with automated measurements realized by Labview. Enhancement of the effective coupling coefficients for the four SBGs was demonstrated by comparison of the stopbands of DFB lasers just below threshold. DFB lasers based on the four SBGs with equivalent phase shifts were also realized and good single longitudinal mode operation was achieved. The increase of SMSRs of the DFB lasers based on the four SBGs also demonstrated an increase of effective coupling coefficients. Based on the 2PS-SBG structure, by simply changing the sampling periods, an eight-wavelength DFB laser array was realized. This laser array had a high wavelength spacing precision of 100 GHz and the grating design overcame the resolution limit of EBL machines. Characterisation showed that the laser array had good single longitudinal mode lasing performance and relatively high output power. Finally, far-field patterns of DFB diode lasers were measured, showing that bend ridge waveguides have no influence on the spatial longitudinal mode lasing of DFB diode lasers. The work in this chapter has shown that good performance of novel DFB diode lasers has been achieved. These DFB lasers and laser arrays have promising applications in the WDM systems.

## Chapter 5

# Terahertz Frequency Generation Based on Dual-mode Semiconductor Lasers

### 5.1 Introduction

THz frequency sources have attracted much attention in scientific research and are already used in the fields of environmental monitoring, security, agriculture and medicine [43]. Many different techniques have been developed to generate THz signals [45]. One of the promising methods is called photomixing. A combined optical beam including two spectral components with different frequencies can generate optical beating signals. Photomixing is a method to generate the corresponding beating signals by using photoconductive antennas. Two optical fields with angular frequencies  $\omega_1$  and  $\omega_2$  can be expressed as

$$\tilde{E}_1(t) = E_1(z) \exp(i\omega_1 t + \varphi) + c. c. \quad (5.1)$$

$$\tilde{E}_2(t) = E_2(z) \exp(i\omega_2 t) + c. c., \quad (5.2)$$

where c.c. is the complex conjugate and  $\varphi$  is the relative phase between two optical fields. The intensity  $I$  of the total field can then be defined as the square of the sum of the two optical waves:

$$\begin{aligned} \tilde{I}(t) &= E_1^2 \cos^2(\omega_1 t + \varphi) + E_2^2 \cos^2(\omega_2 t) + 2 E_1 E_2 \cos(\omega_1 t + \varphi) \cos(\omega_2 t) \\ &= \frac{E_1^2}{2} + \frac{E_2^2}{2} + E_1^2 \frac{\cos(2\omega_1 t + 2\varphi)}{2} + E_2^2 \frac{\cos(2\omega_2 t)}{2} \\ &\quad + E_1 E_2 \cos\{(\omega_1 + \omega_2)t + \varphi\} + E_1 E_2 \cos\{(\omega_1 - \omega_2)t + \varphi\}, \end{aligned} \quad (5.3)$$

where the final difference frequency term is of interest. When the frequency difference of the two wavelengths ( $\omega_1 - \omega_2$ ) is located in the THz frequency range, THz signals can be generated by photomixing in a high-speed detector connected to an antenna. Because of the

limited bandwidth of the detector, the sum frequencies of other frequency harmonics are ignored and only THz frequencies are detected and generated.

A wide variety of two-colour laser sources could be used to generate THz waves. However, photomixing based on semiconductor lasers has the advantages of compactness and low cost [197]. In particular, if the wavelengths of the semiconductor lasers are in the optical communications wavelength range, the wavelengths can be transmitted conveniently through an optical fibre and the THz signals can be generated long distance away from the laser sources. This feature could lead to various applications like remote THz sensing.

Here, novel dual-mode DFB semiconductor diode lasers based on sampled Bragg gratings (SBGs) have been designed and fabricated. Both lasing wavelengths were generated simultaneously in one cavity in the C-band wavelength range (1530-1565 nm) and a terahertz signal of 560 GHz was generated by photomixing based on mode beating effects.

## 5.2 Design of Dual-mode Lasers

The design concept of dual-mode lasers has been introduced in Section 2.4.2. The grating structure of the dual-mode laser was based on a 2PS-SBG structure, as shown in Fig. 5.1, the same as Fig. 2.9(b). The duty-cycle of the sampling periods in a 2PS-SBG is set as 0.5 to achieve the highest coupling coefficients in  $\pm 1^{\text{st}}$ -order channels. For a 2PS-SBG,  $\pi$  phase-shifted gratings are inserted into the blank half of each sampling period in a conventional SBG. As a result, the  $0^{\text{th}}$ -order channel is eliminated and the  $\pm 1^{\text{st}}$ -order channels are enhanced. By introducing an equivalent phase shift (EPS) in the sampling structure, single-mode lasing of the  $\pm 1^{\text{st}}$ -order channels is expected to be achieved.

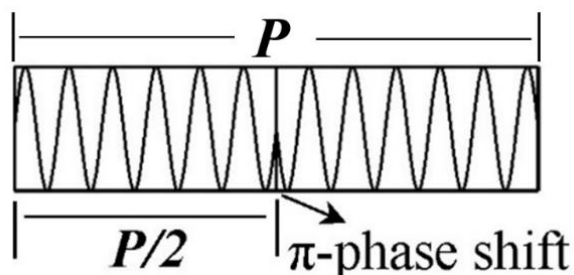


Figure 5.1: The grating structure of 2PS-SBG.

For the single-mode DFB lasers realized in Chapter 4, the sampling periods were of the order of several micrometres and the  $-1^{\text{st}}$ -order channel was used as the working channel. In this case, the  $0^{\text{th}}$ -order channel and the  $1^{\text{st}}$ -order channel were moved out of the gain spectrum so that only the  $-1^{\text{st}}$ -order channel experienced enough gain to lase and so single-mode lasing performance could be guaranteed. However, for dual-mode lasers, both of the  $\pm 1^{\text{st}}$ -order channels are required to lase stably and so both of the channels should be located in the gain spectrum range. So that the  $\pm 1^{\text{st}}$ -order channels experience similar gain values, the seed grating period should be chosen carefully. The value of the seed grating period was designed to locate the  $0^{\text{th}}$ -order channel at the peak of gain spectrum, so that the  $\pm 1^{\text{st}}$ -order channels located on both sides of the gain peak would have similar gain values. To generate THz signals by photomixing, the wavelength spacing of the two wavelengths should be several nanometres. According to equation (2.29), the sampling periods are calculated to be about dozens of micrometres.

The layout of the dual-mode laser was the same as that of a single-mode DFB laser, as shown in Fig. 4.4, with bend ridge waveguides on both sides, and the quantum well wafer structure was identical to the structure shown in Fig. 3.2. Shallow etching was adopted to fabricate ridge waveguides, the same as that shown in Fig. 3.4(a).

To achieve specific THz frequencies, the wavelength spacing needs to be designed precisely. The dispersion of the effective refractive index at different wavelengths needs to be taken into consideration. By carrying out several runs of fabricating DFB single-mode lasers, the value of the effective refractive index for the fundamental TE mode at 1550 nm was calculated as 3.1934, and the dispersion coefficient around 1550 nm was estimated as  $-0.00021 \text{ nm}^{-1}$ . Hence, for wavelengths around 1550 nm, the corresponding effective refractive index  $n_{\text{eff}}(\lambda)$  could be estimated as:

$$n_{\text{eff}}(\lambda) = -0.00021 * (\lambda - 1550) + 3.1934. \quad (5.4)$$

For an SBG with seed grating period  $\Lambda_0$  and sampling period  $P$ , according to equations (2.3) and (2.27), the wavelengths of the  $\pm 1^{\text{st}}$ -order channels,  $\lambda_{\pm 1}$ , can be expressed as:

$$\lambda_{+1} = 2n_{eff}(\lambda_{+1}) * \Lambda_{+1} = 2n_{eff}(\lambda_{+1}) * \frac{P\Lambda_0}{P-\Lambda_0}, \quad (5.5)$$

$$\lambda_{-1} = 2n_{eff}(\lambda_{-1}) * \Lambda_{-1} = 2n_{eff}(\lambda_{-1}) * \frac{P\Lambda_0}{P+\Lambda_0}. \quad (5.6)$$

From these equations, the values of  $\lambda_{\pm 1}$  can be derived and the wavelength spacing of  $\pm 1^{\text{st}}$ -order channels can be calculated.

## 5.3 Characteristics of Dual-mode Lasers

### 5.3.1 Optical Power and Spectra

For the design of dual-mode lasers based on a 2PS-SBG, the seed grating period was chosen to be 244 nm and the sampling period was 134.67  $\mu\text{m}$ . Since the dual-mode lasers had the same schematic as that of the single-mode DFB lasers shown in Chapter 4, the set-up for measurements was the same as that shown in Fig. 4.9 and Fig. 4.10. All the data were obtained automatically by software *Labview*.

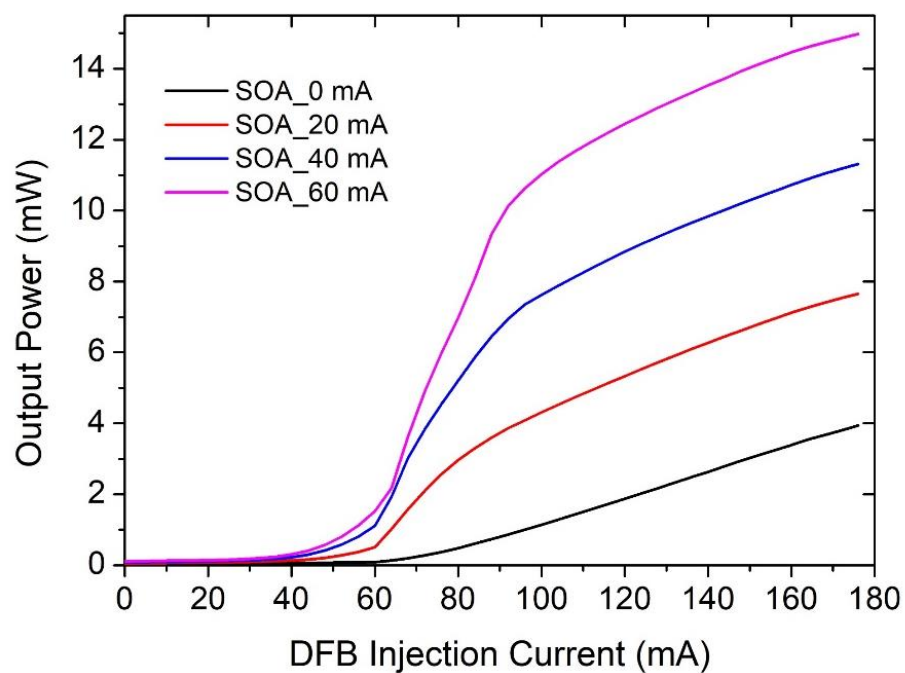
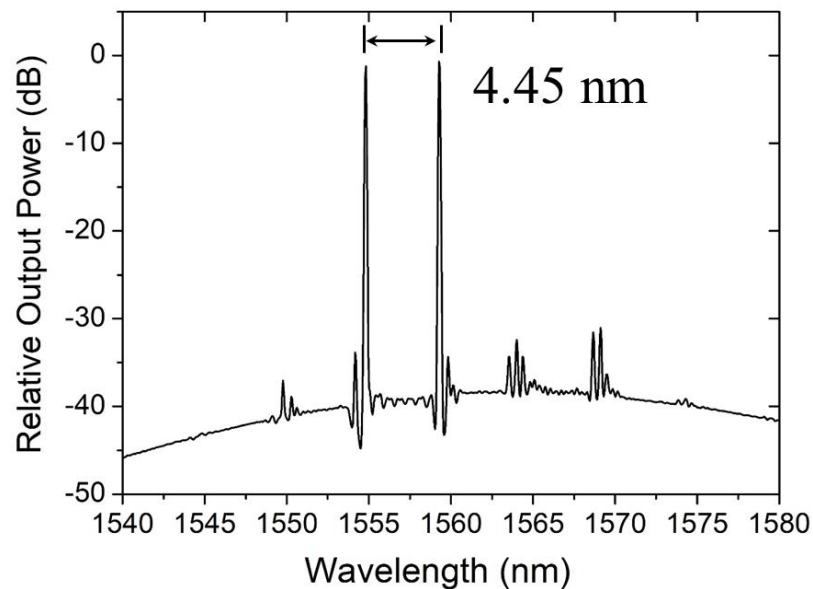


Figure 5.2: *LI* curves of a dual-mode laser.

Figure 5.2 illustrates typical  $LI$  curves of a dual-mode diode laser for different injection currents in the DFB and SOA sections. The DFB injection current was scanned from 0 to 180 mA and the SOA currents were set at 0, 20, 40 and 60 mA respectively. From these curves we can see that the threshold current was about 50 mA, a similar value to that of a single-mode DFB laser. The output optical power increases dramatically with the SOA current. When the injection currents of the DFB and SOA section were 110 mA and 40 mA respectively, a relatively high output optical power of 8 mW was achieved.



**Figure 5.3: The optical spectrum at an SOA current of 40 mA and DFB current of 120 mA [198].**

Optical spectra were also measured for the dual-mode lasers. Figure 5.3 shows a typical optical spectrum of a dual-mode laser with the injection currents of the SOA and DFB sections set at 40 mA and 120 mA respectively. The wavelength spacing of the two lasing wavelengths was measured as 4.45 nm, corresponding to a THz frequency of 560 GHz. The power difference between the two wavelengths was less than 0.5 dB and the SMSR of the two modes was larger than 30 dB, which is important for obtaining a large photomixing efficiency. A 2D-wavelength mapping at an SOA current of 40 mA is also illustrated, as shown in Fig. 5.4. This 2D-wavelength mapping is generated with the data acquired by the automated measurement system. During the long-time task to acquire all the measurements, the optical coupling between the fibre tip and the ridge waveguide may change because of

the influence of the environment, which will lead to a power change. From this figure, we can see a rise and fall in the ASE background. However, small changes in the power coupling will not influence the lasing wavelengths. This figure shows that the two modes were lasing stably over a wide range of DFB injection currents. The threshold current was about 50 mA and the two wavelengths lased stably above 80 mA.

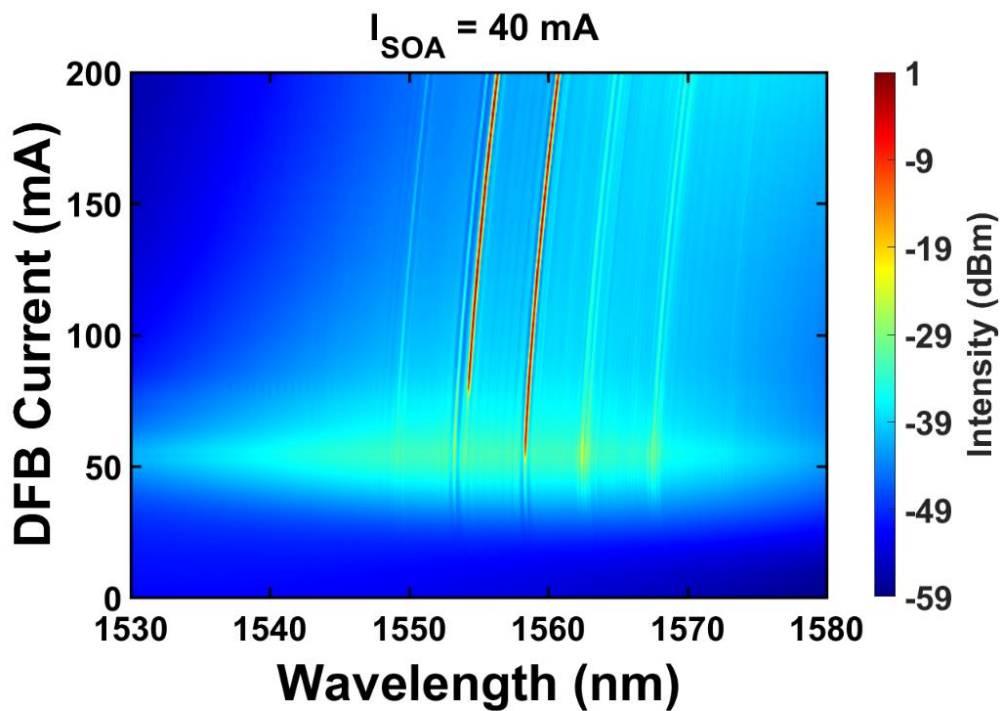


Figure 5.4: A 2D-wavelength mapping at an SOA current of 40 mA [198].

### 5.3.2 Autocorrelation Traces

Autocorrelation traces were also measured to check the generated THz frequency. Figure 5.5 shows the schematic of the set-up to measure autocorrelation traces. The dual-mode laser diode was mounted on a TEC for temperature control at 20 °C. A current driver was used to control the injection currents and the TEC at the same time. The output light was coupled into a lensed fibre and amplified by an EDFA. An optical isolator was placed between the laser and the EDFA to prevent unwanted light reflection, then the amplified light was transmitted through a polarization controller and sent into an autocorrelator. The polarization controller was used to control the polarization of the light to achieve the best performance. The autocorrelator was used to examine the autocorrelation of the light intensity and the

generated electrical signals were observed by an oscilloscope in real time. Utilising the GPIB interface, automated control was realised by *Labview*. The current driver was controlled automatically by a computer, and data from the oscilloscope were collected and saved automatically, reducing the measuring time. Figure 5.6 shows the equipment used for measuring autocorrelation traces. In this image, from top to bottom, the equipment is listed as Tektronix Oscilloscope TDS 210, Optical Fibre Amplifier from PriTel. Inc., and the autocorrelator from Femtochrome Research Inc.

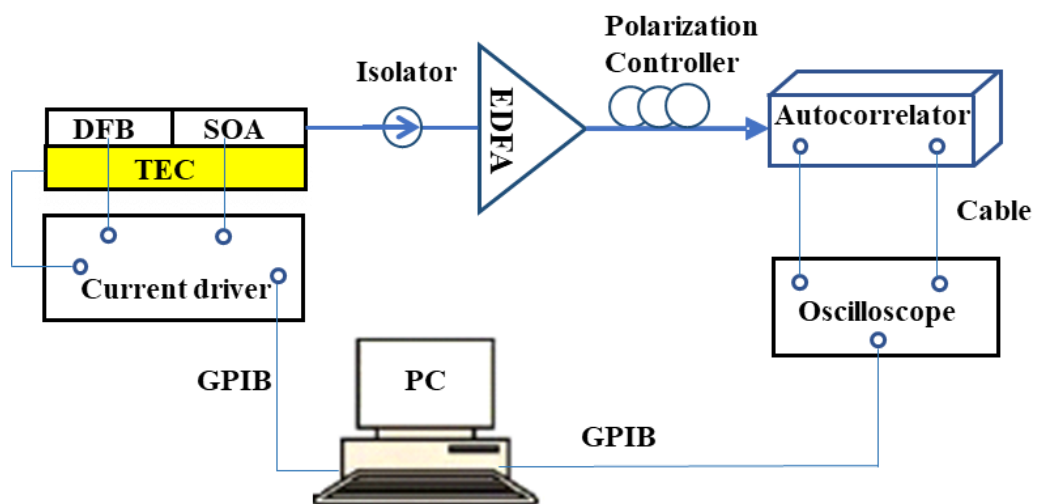
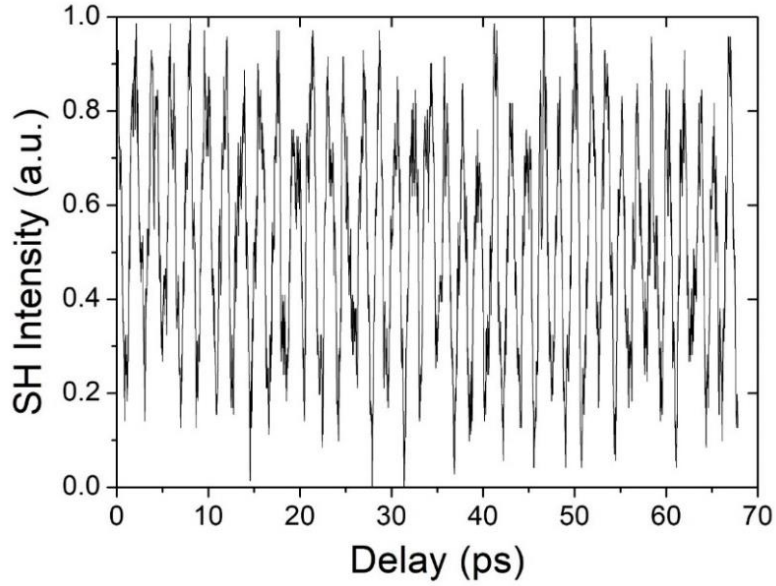


Figure 5.5: Schematic of the set-up to measure autocorrelation traces.



Figure 5.6: Equipment used for measuring autocorrelation traces.



**Figure 5.7: A measured autocorrelation trace [198].**

A measured second harmonic (SH) autocorrelation trace (AC) is shown in Fig. 5.7. The average period of the emitted pulse train, dividing the delay duration time by total peak cycle counts, was calculated as 1.8 ps, which corresponds to a beating frequency of 560 GHz. This is consistent with the optical spectrum, as shown in Fig. 5.3. Hence, the dual-mode laser was expected to generate the THz signal frequency of 560 GHz.

### 5.4 Measurement of THz Frequency Generation

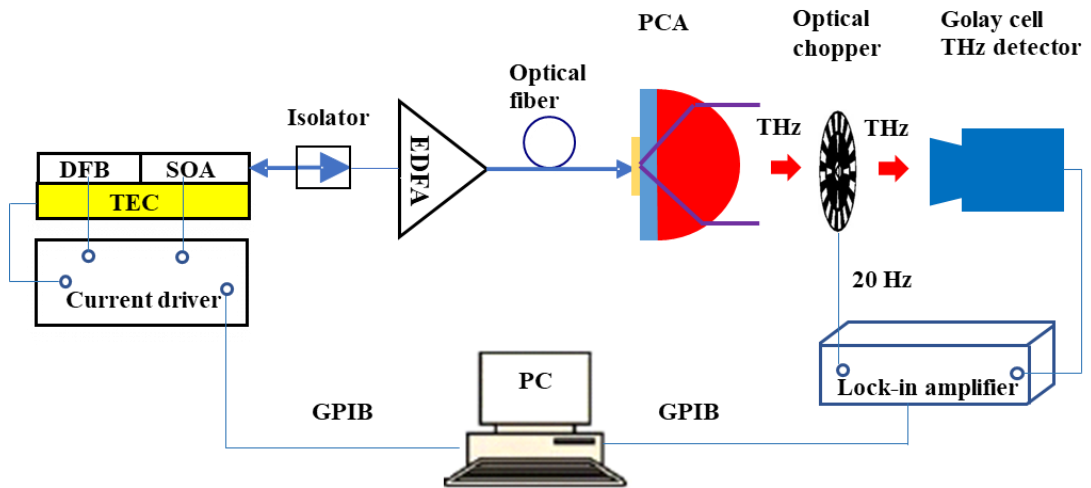


**Figure 5.8: Schematic of the set-up for generating and detecting THz waves.**

A set-up for generating and detecting THz waves was built based on the fabricated dual-mode lasers. The schematic of the set-up is shown in Fig. 5.8. The dual-mode diode lasers were mounted, driven, and coupled the same as that in Fig. 5.5. After being amplified by the EDFA, the coupled laser light was imaged on a photoconductive antenna (PCA) via a standard single-mode fibre, with the optical power set at about 25 mW after amplification by the EDFA. The core diameter of the single-mode fibre is about 10  $\mu\text{m}$  and the antenna gap of the PCA is 5  $\mu\text{m}$ . With careful alignment, the light spot could cover the antenna gap properly. The PCA was mounted on hyperhemispherical silicon substrate lens: PCA-180-05-10-1550-h. It has a diameter of 12 mm and a virtual focus length of 26.4 mm. The collection angle is  $57^\circ$  and the half divergence angle is  $15^\circ$ . The PCA was reverse biased at 10 V and THz waves were generated by photomixing the two wavelengths. After transmission through an optical chopper, the free-space THz waves were detected by a Golay cell. The Golay cell is a type of opto-acoustic detector mainly used for infrared spectroscopy [199]. It is filled with an infrared absorbing material and a flexible membrane. Light is reflected by the membrane and detected by a photodiode. When infrared radiation is absorbed, the gas will be heated and expand, resulting in pressure-induced deformation of the membrane. The deformation of the membrane deflects the light beam and produces a signal change in the detector. Thus the power of the incident radiation can be detected. The Golay cell has a high sensitivity and a broad frequency range of flat response. The frequency range can be extended to the Golay THz frequency range.

A lock-in amplifier was utilised to exact THz signals from the noisy environment, with the optical chopper frequency set at 20 Hz. The lock-in amplifier was controlled by a computer using *Matlab* programs through the GPIB interface. The THz power data were collected and saved automatically.

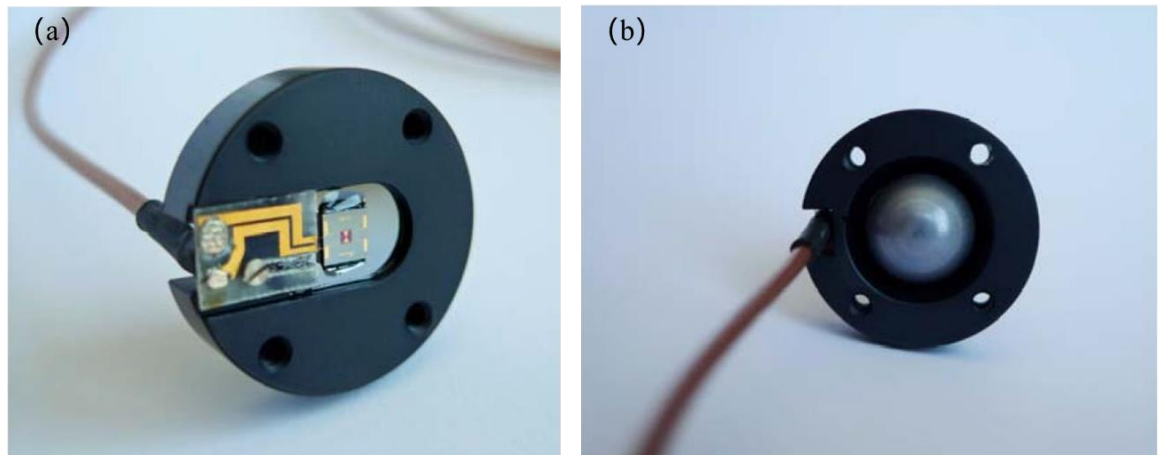


**Figure 5.9: (a) The front view and (b) the back view of the PCA.**

The PCA was based on semi-insulating GaAs from *BATOP Optoelectronics* (serial number: PCA-180-05-10-1550-a) with excitation wavelength of 1550 nm. The chip area is 4 mm × 4 mm, and mounted on hyperhemispherical silicon substrate lens. The focus length of the silicon lens is 50 mm. Figure 5.9 (a) shows the front view of the PCA and the laser beam transmitted out of the fibre needs to be aligned with the detector. Figure 5.9(b) shows the back view of the PCA. The hyperhemispherical silicon substrate lens is used to partially collimate the THz waves. The PCA has a response frequency region from 0.1 to 5 THz. In this work, the highest pump light power was set at 25 mW, the normal specific working point of the PCA. The PCA is expected to be linear before the saturation point [200]. However, whether the generated THz signal is linear to the pump light power depends on several aspects. One is the power difference of the two lasing modes, which would change with the injection currents. Another is whether the EDFA or the SOA would saturate during the measurements. However, from the results we could see that the THz signal power increases with the pump light power.

Figure 5.10 illustrates the Golay cell optoacoustic detector from *TYDEX Company*, model number GC-1P. The design of a Golay cell was first proposed by Dr. M.J.E. Golay in 1947 [201]. This detector can operate at room temperature and has a small size, a high sensitivity, and a broad operating wavelength range. The diameter of the entrance cone is 11 mm, and the material of the entrance window is high-density polyethylene. The optimal operating wavelength range is 15 μm ~ 2 mm. The wavelengths of the THz signals are usually several

hundred microns, which can be detected by the Golay cell. The optical responsivity @ 20 Hz was calibrated from the software with Golay cell as  $1.5 \times 10^{-5}$  W/V. An optical chopper and a narrow-band THz frequency filter were used together to extract the THz signals from the noisy environment.



**Figure 5.10: The Golay cell optoacoustic detector from TYDEX Company.**

The power of the generated THz signals was measured with the set-up shown in Fig. 5.8. Absolute power was calculated using the optical responsivity of  $1.5 \times 10^{-5}$  W/V. Figure 5.11 shows the 2D power intensity mapping of THz signals with changing of DFB and SOA injection currents. The injection currents of the DFB and SOA section were scanned from 0 mA to 200 mA and 100 mA respectively. From this image, we can see that THz signal power was detected above the threshold current of the DFB laser, which was consistent with lasing of the dual-mode laser. Above threshold current, THz signals were widely detected and stable THz signal generation was achieved. This confirmed stable lasing of the laser at two wavelengths simultaneously. The highest detected THz power is about 30 nW. There are two main factors which lead to the relatively low detected THz power. One is the poor optical-to-THz conversion efficiency at room temperature of the PCA, which is around  $10^{-5}$  [202]. The other reason is that only about 10% of the THz signal was collected by the Golay cell due to  $30^\circ$  divergence angle of radiation from the PCA, the distance (140 mm) between

the PCA and the entrance of the detector, and the limited diameter of the entrance cone of the detector. Considering the half divergence angle  $15^\circ$  of THz beam, the distance from the PCA to the detector, and window diameter of the detector, the total THz output power is estimated to be around  $1.4 \mu\text{W}$ . The conversion efficiency was calculated to be about  $5.6 \times 10^{-5}$ .

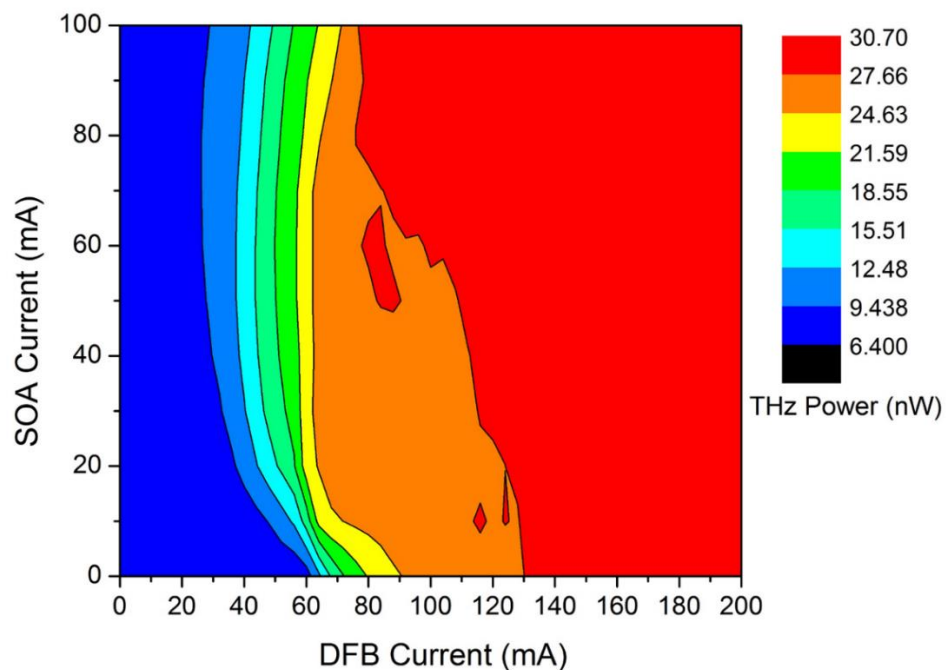


**Figure 5.11: 2D power intensity mapping of THz signals.**

Since the Golay cell is a wide-band detector, other sources of light would affect the detected power. Here, the residual 1550 nm light from the pump laser and the blackbody radiation from the heated PCA are the two main aspects to be taken into consideration. The residual 1550 nm light was first considered. The maximum pump light power was 25 mW. The 1550 nm light transmissivity through the PCA was measured to be 2%. The half divergence angle of a single-mode fibre is about  $7^\circ$ . Transmitted through the silicon lens, the half divergence angle becomes  $8.6^\circ$ . 1550 nm light has a transmissivity of about 45% for the high-density polyethylene window material of the Golay cell. Considering about the working distance of 140 mm from the PCA to the Golay cell window and 11 mm window cone diameter, the power at 1550 nm transmitted through the windows is estimated to be about  $7.6 \mu\text{W}$ . For the blackbody radiation, the laser spot size on the PCA was about  $10 \mu\text{m} \times 10 \mu\text{m}$ , and the

temperature at the laser spot was assumed 70 °C. Then the generated blackbody radiation into the Golay cell could be estimated to be about 0.03 nW. Compared to the detected power of 30 nW, the blackbody radiation could be ignored. The residual 1550 nm pump light into the Golay cell was high. However, the 1550 nm light was not in the operating wavelength range of the Golay cell. The detected highest power was only about 30 nW, much lower than the estimated residual 1550 nm light. To further demonstrate THz signal generation, we introduced a piece of paper into the system to see the power change from the detector.

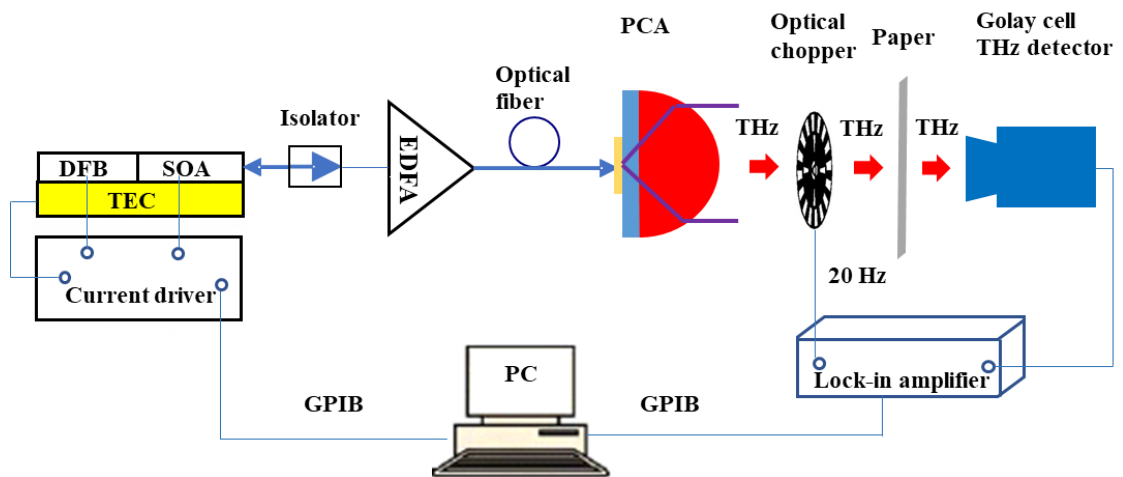


**Figure 5.12: Schematic of the set-up for generating and detecting THz waves transmitted through a piece of paper.**

Figure 5.12 shows the schematic of the experiment, where the paper was inserted between the optical chopper and the Golay cell. The rest of the experiment was the same as that shown in Fig. 5.8. The THz signal power was generated using the same dual-mode diode laser, with the injection currents of the DFB and SOA section scanned from 0 mA to 200 mA and 100 mA respectively, as shown in Fig. 5.13. Compared to Fig. 5.11, the detected relative power was reduced by about 24.5% at the highest power point of 23.15 nW. The piece of paper was nearly transparent for THz signals. However, the transmission of 1550 nm light through the paper was measured to be about 10%. Since the measured power drop was about 25%, we can conclude the detected signal was not dominated by the 1550 nm light. What is more, without amplifying any laser light, the background power of EDFA was measured to be 5 mW, which would contribute a residual light power of 1.5  $\mu$ W. The background noise of the Golay cell was only about 9 nW, which also showed that 1550 nm light did not contribute

to the detected power of the Golay cell. THz signals were detected. To further demonstrate specific frequency generated, the most direct way is to measure the frequency peak generated. This work will be carried out in future by using a Michelson interferometer setup [203].

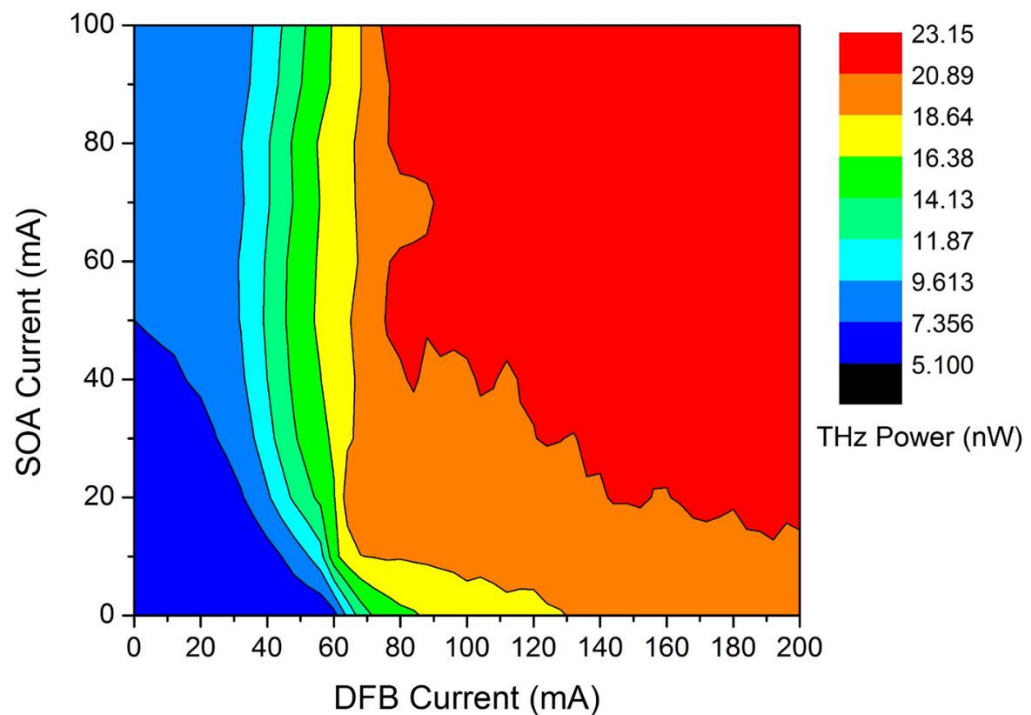


Figure 5.13: 2D power intensity mapping of THz signals transmitted through a piece of paper.

## 5.5 Chapter Summary

This chapter has introduced THz waves generation using dual-mode DFB semiconductor lasers. The design principals were first introduced and precisely-controlled wavelength spacing of the dual-mode laser's two wavelengths could be achieved by taken the dispersion of effective refractive index into consideration. Dual-mode DFB semiconductor lasers were successfully designed and fabricated. Characteristics of the dual-mode laser were measured, including the output optical power, the optical spectra and autocorrelation traces. The average period of the emitted pulse train of the autocorrelation trace was demonstrated to be

consistent with the dual wavelengths' spacing. A set-up for THz waves generation and detection was built based on the fabricated dual-mode lasers. THz signals were generated by a photoconductive antenna and detected by a Golay optoacoustic detector. An optical chopper and a lock-in amplifier operating at the frequency of 20 Hz were used to extract THz signals from the noisy environment. THz signals were successfully detected and confirmed stable lasing of the dual-mode lasers. It is concluded that the fabricated dual-mode lasers can be used to generate stable continuous-wave THz waves.

## Chapter 6

# Mode-locked Semiconductor Lasers Based on SGDBR Structures

### 6.1 Introduction

Ultrafast mode-locked laser diodes (MLLDs) operating at THz repetition frequency provide exciting opportunities in future telecom systems, terahertz spectroscopy, imaging, and sensing, as described in Section 1.3. MLLDs have the advantages of compactness, robustness and low-cost for manufacturing. They can also be integrated flexibly with other semiconductor elements, such as SOAs.

Mode-locking is a well-established route to generate short optical pulses. For a basic mode-locked semiconductor diode laser based on an FP cavity with a length of at least a few hundred microns, the repetition frequency cannot exceed 100-150 GHz for the III-V material platform [204-206], which can be estimated from equations 1.3 and 1.4. The repetition frequency of optical pulses is inverse to the cavity round-trip time: the shorter the cavity length, the higher the repetition frequency.

To generate pulse streams with higher repetition frequency, harmonic mode-locking can be utilised. This technique produces an optical pulse stream at a harmonic of the fundamental round-trip frequency of the device. Using this technique, repetition frequencies of several hundred gigahertz can be achieved. Harmonic mode-locking has been realized by several methods, including sub-harmonic optical injection [207], colliding pulse mode-locking (CPM) [208, 209], and compound-cavity mode-locking (CCM) [210, 211]. For sub-harmonic optical injection, optical pulses from an external oscillator are injected into a harmonic oscillator and phase synchronisation is achieved between the two oscillators. This is a technique for reducing time jitter and achieving synchronisation, but the harmonic oscillator has to exist.

The CPM laser was first realized to generate ultra-short pulses in dye lasers [212]. CPM exploits the interaction of two counter-propagating pulses in the SA. Figure 6.1 shows the schematic of a typical CPM semiconductor laser. In the CPM laser cavity, two gain sections and an SA section are required. The SA is placed in the centre of the laser cavity to achieve maximum coupling between two colliding pulses. Given this device configuration, two sub-cavities are formed, and the fundamental repetition frequency of the CPM laser is twice that of the whole cavity. Utilising this technique, a wide range of repetition frequencies from tens of GHz to 350 GHz have been realized at 1550 nm [208]. More complex structures of CPM have also been realized by dividing the laser cavity into more sections to achieve higher-order harmonic oscillation, introducing more Gain and SA segments [209, 213]. Although CPM laser has the advantage of achieving higher repetition frequencies, the mode-locking performance is poor over CCM lasers.

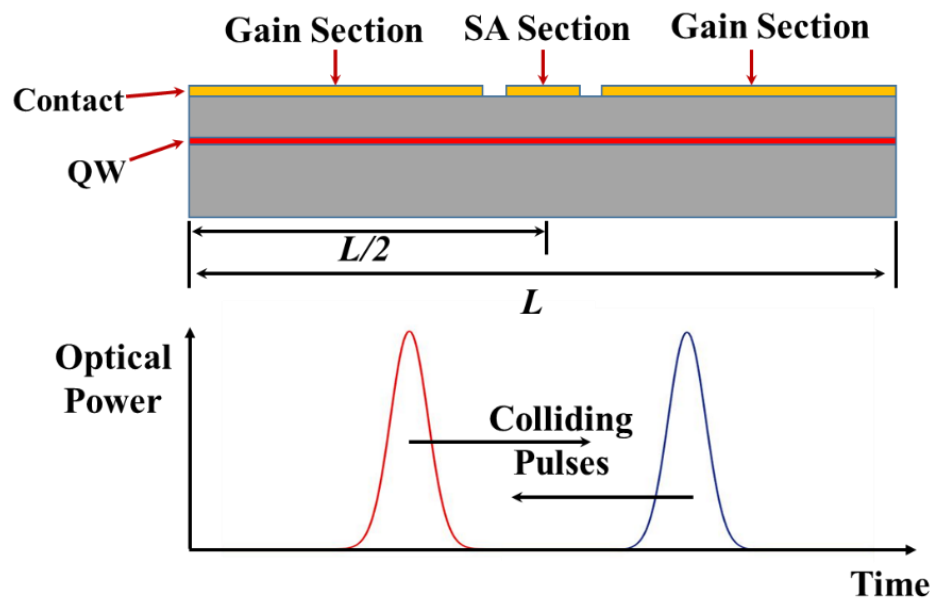


**Figure 6.1: Schematic of a typical CPM laser: two optical pulses colliding in the SA, which is placed in the cavity centre.**

The CCM effect was first demonstrated by introducing an intra-cavity DBR reflector in the laser cavity [211]. In this circumstance, a coupled sub-cavity was created in the main resonator, and the DBR reflector works as a frequency filter. For low pumping currents, the laser was mode-locked at the fundamental repetition frequency of the entire cavity.

However, when the pumping currents were high, optical pulses at the repetition frequency of the sub-cavity were generated. By choosing the length of the DBR section so that there is an integer ratio between the DBR section and the entire cavity, repetition frequencies at harmonic mode-locking will be generated. The repetition frequency as high as 1.54 THz was realized by introducing the DBR section as a sub-cavity [214]. To increase the range of operation conditions and reproducibility, a CCM laser based on an etched slot reflector was proposed, reaching a repetition frequency up to 2.1 THz at 860 nm [215]. In this device configuration, an additional FP sub-cavity was created, which can be considered as an alternative to the DBR section. Figure 6.2 shows the schematic of a monolithic CCM laser, which contains an SA section and two gain sections. The etched slot divides the laser cavity into two segments, with a length ratio  $L_1/L_2 = 1/(M-1)$ .  $L_1$  and  $L_2$  are the lengths of the two segments, as shown in Fig. 6.2, and  $M$  is an integer. Harmonic mode locking can be realized by spectral selectivity of the compound cavity and  $M^{\text{th}}$ -order mode-locking frequency can then be generated.

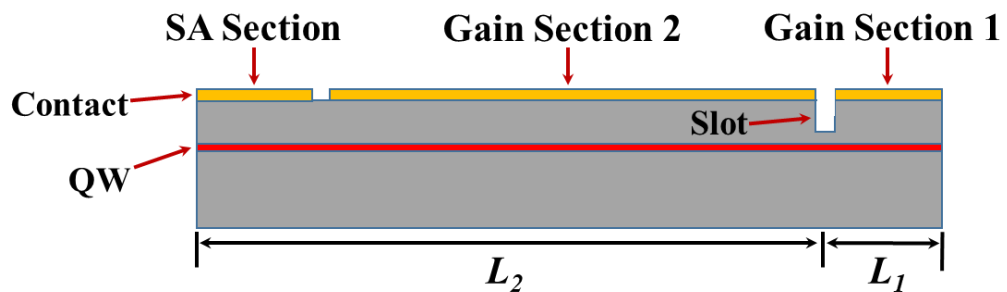


**Figure 6.2: Schematic of a monolithic CCM device with an etched slot reflector.**

In the THz repetition frequency range, the CPM laser suffers from poor performance. The CCM laser is very sensitive to the laser cavity length and operation at high repetition frequencies is limited by the resolution of conventional scribing tools. To overcome these disadvantages, MLLDs based on sampled grating distributed Bragg reflector (SGDBR) structures have been introduced to generate THz repetition frequencies that are determined by the grating periods, as well as achieving good mode-locking performance. Research on MLLDs based on novel SGDBR structures is the main topic for this chapter.

## 6.2 Device Design

### 6.2.1 Mode-locked Laser Diodes based on C-SGDBR

The use of SGDBR lasers to fabricate MLLDs with THz repetition frequencies was first proposed by my colleague, Dr. Lianping Hou. These reported DBR lasers were based on conventional SGDBR (C-SGDBR) structures, with grating sections spaced apart by sections of waveguide without gratings [216]. Compared to previously reported MLLDs, these MLLDs based on C-SGDBRs have shown the advantages of reproducibility, controllability and a higher frequency operation range, up to 1.3 THz.

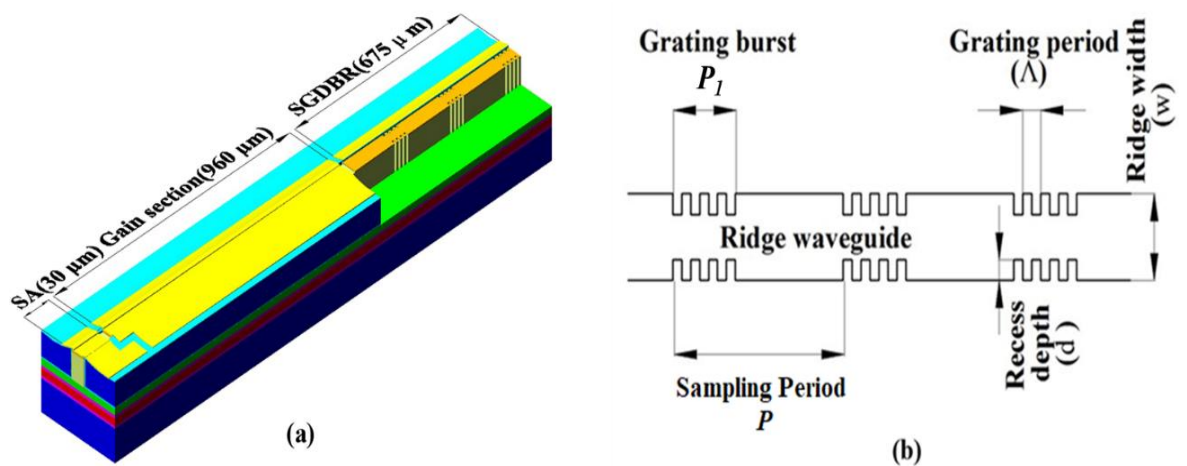


**Figure 6.3: (a) Schematic of the MLLD based on C-SGDBR, (b) configuration of the sidewall C-SGDBR [216].**

Figure 6.3 illustrates the design of a MLLD based on a C-SGDBR from reference [216]. The schematic of a MLLD based on C-SGDBR is shown in Fig. 6.3(a), which contains a 30 μm saturable absorber (SA), a 960 μm gain section and a 675 μm C-SGDBR reflector. The design of the C-SGDBR reflector is shown in Fig. 6.3(b). In this design, the width of the ridge waveguide for the C-SGDBR reflector was designed as 2.5 μm and the grating recess was 0.6 μm. The 0<sup>th</sup>-order grating period  $\Lambda$  (246 nm) and the sampling period  $P$  (67.5 μm) together determined the reflectivity spectrum of the C-SGDBR, which determined the oscillating frequencies for mode-locking. The grating burst in each sampling period was 10 μm, which offered a duty cycle of about 0.148 ( $P_1/P$ ). To achieve a relatively uniform

reflectivity spectrum of the C-SGDBR, the duty cycle cannot be very high. A low duty cycle will lead to a low coupling coefficient and a longer sampled Bragg grating is then required to provide sufficient light reflection to support lasing.

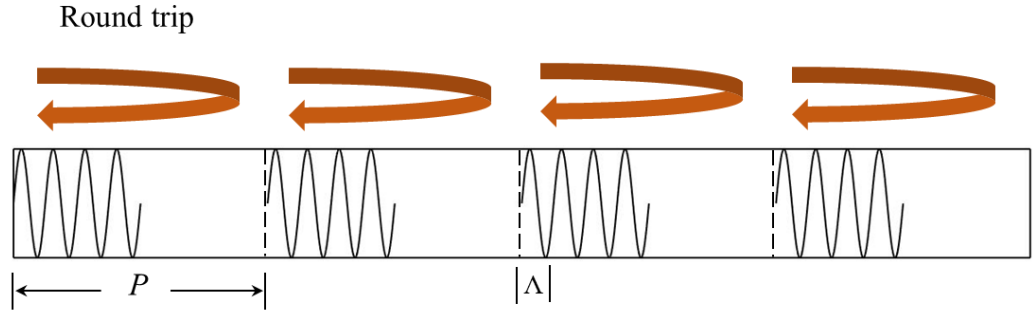


**Figure 6.4: Schematic of round trips generated in C-SGDBR.**

The principle of C-SGDBR for mode-locking is shown in Fig. 6.4. In the C-SGDBR, each sampling period can be regarded as a sub-cavity and a round trip is formed in each sampling period. Hence, the round trip time  $\tau$  is directly determined by the sampling period  $P$ , which can be given as:

$$\tau = 2n_g P / c, \quad (6.1)$$

where  $n_g$  ( $\approx 3.4889$ ) is the group index of the ridge waveguide and  $c$  is the velocity of light in free space. The repetition frequency  $F_r$  is inverse to the round trip time, which is:

$$F_r = 1/\tau = c/2n_g P. \quad (6.2)$$

To generate optical pulses with THz repetition frequencies, the sampling period  $P$  can be calculated as dozens of microns. The SGDBR acts as a filter and accurately determine the oscillating frequencies. From equation 6.1, we can see that the round trip time here is only related to the sampling period and is not affected by the cavity length. This device configuration relieves the stringent fabrication and cleaving tolerances of the CCM laser. The MLLD shown in Fig. 6.3(a) had an as-cleaved configuration and FP modes still existed. To further eliminate the influences from the FP modes, bend ridge waveguides at the output facets have been introduced in the novel design of SGDBR-based MLLDs in this work.

## 6.2.2 Mode-locked Laser Diodes based on PPS-SGDBR

The C-SGDBR has the significant disadvantage that the effective coupling coefficient,  $\kappa$ , is reduced significantly from that of a uniform Bragg grating because of the relatively small duty cycle. To overcome this limitation, the  $\pi$  phase-shifted SGDBR (PPS-SGDBR) structure was proposed and was applied to produce MLLDs successfully. The design of MLLDs based on PPS-SGDBR will be introduced in this section and the design of MLLDs based on C-SGDBR will be used for comparison. Compared with C-SGDBRs, the PPS-SGDBR has a significantly larger effective coupling coefficient so the number of sampling periods can be reduced to make more compact devices, while achieving better mode-locking performance at the same time.

The basic principle of introducing  $\pi$  phase-shifted gratings into sampling periods has been described in detail in Chapter 2. The sampled Bragg grating design for MLLDs was described in Section 2.4.3 and according to the simulation, the duty cycle for a uniform 0<sup>th</sup>-order grating was optimised to be 0.25, as shown in Fig. 2.18. Figure 6.5(a) shows the sampled Bragg grating structure of a C-SGDBR. The sampling period  $P$  is  $67.5 \mu\text{m}$  and the length of the 0<sup>th</sup>-order grating is  $P_1 = 10 \mu\text{m}$ . The corresponding duty cycle is calculated as 0.148. Figure 6.5(b) illustrates the sampled Bragg grating structure of a PPS-SGDBR, with the same sampling period and the same 0<sup>th</sup>-order grating period. When the duty cycle of the 0<sup>th</sup>-order grating is set as  $P_1/P = 0.25$ , the length of 0<sup>th</sup>-order grating  $P_1$  is calculated to be  $17 \mu\text{m}$  in each sampling period. The other blank part of each sampling period is filled by the 0<sup>th</sup>-order gratings with  $\pi$ -phase shifts. In this circumstance, the effective  $\kappa$  of the 0<sup>th</sup>-order reflection of the PPS-SBG is expected to be more than three times ( $(67.5 - 2 \times 17) \mu\text{m} / 10 \mu\text{m} = 3.35$ ) that of a C-SGDBR and half that of a uniform Bragg grating. Choosing the 0<sup>th</sup>-order grating period  $\Lambda = 246 \text{ nm}$  and sampling periods  $N_s = 10$  for both of the structures, the reflectivity spectra of the two structures were calculated by the transfer matrix method, as shown in Fig. 6.5(c). The effective  $\kappa$  for 0<sup>th</sup>-order grating was chosen as  $23.2 \text{ cm}^{-1}$ , which was calculated from the measured stop band of fabricated devices, as shown in Fig. 4.12. From the reflectivity spectra, the light reflection peaks of PPS-SGDBR are much higher than those of the C-SGDBR, which shows that the PPS-SGDBR indeed contributes a much larger effective coupling coefficient.

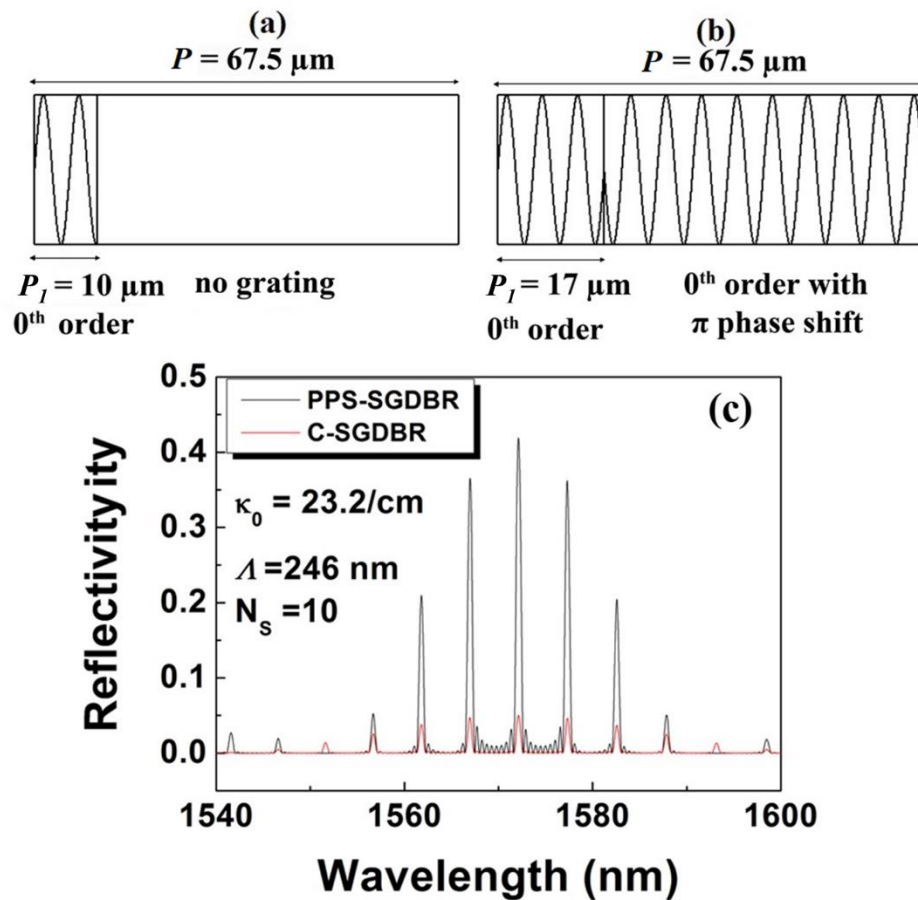


**Figure 6.5: Sampled Bragg grating structures of (a) C-SGDBR, and (b) PPS-SGDBR; (c) simulated reflectivity spectra for the two grating structures [217].**

Here, the C-SGDBR will only be used as a comparison. The work will be focused on the MLLDs based on PPS-SGDBRs while a deeper discussion of MLLDs based on C-SGDBRs can be found in references [206] and [217].

Based on the sampled Bragg grating design shown in Fig. 6.5, the configuration of MLLDs based on SGDBR structures is illustrated in Fig. 6.6(a), which contains different sections. The two kinds of MLLDs had similar device structures and the only difference was the grating design. Both had a 20  $\mu\text{m}$  saturable absorber (SA), a 960  $\mu\text{m}$  gain section, a 675  $\mu\text{m}$  SGDBR section and a 600  $\mu\text{m}$  SOA section with bent ridge waveguide. The isolation gap between adjacent electrode pads was designed as 30  $\mu\text{m}$ . Ten sampling periods of 67.5  $\mu\text{m}$  were used in the SGDBR section. Figure 6.6(b) shows SEM images of the sidewall gratings of the C-SGDBR and PPS-SGDBR. The ridge waveguide still had a width of 2.5  $\mu\text{m}$  and a

recess of  $0.6\ \mu\text{m}$ . We can see clearly from the image that part of the ridge waveguide of C-SGDBR did not have sidewall gratings, while the PPS-SGDBR was filled with  $\pi$  phase-shifted gratings. The  $\pi$ -phase shift in one sampling period has been highlighted in the image.

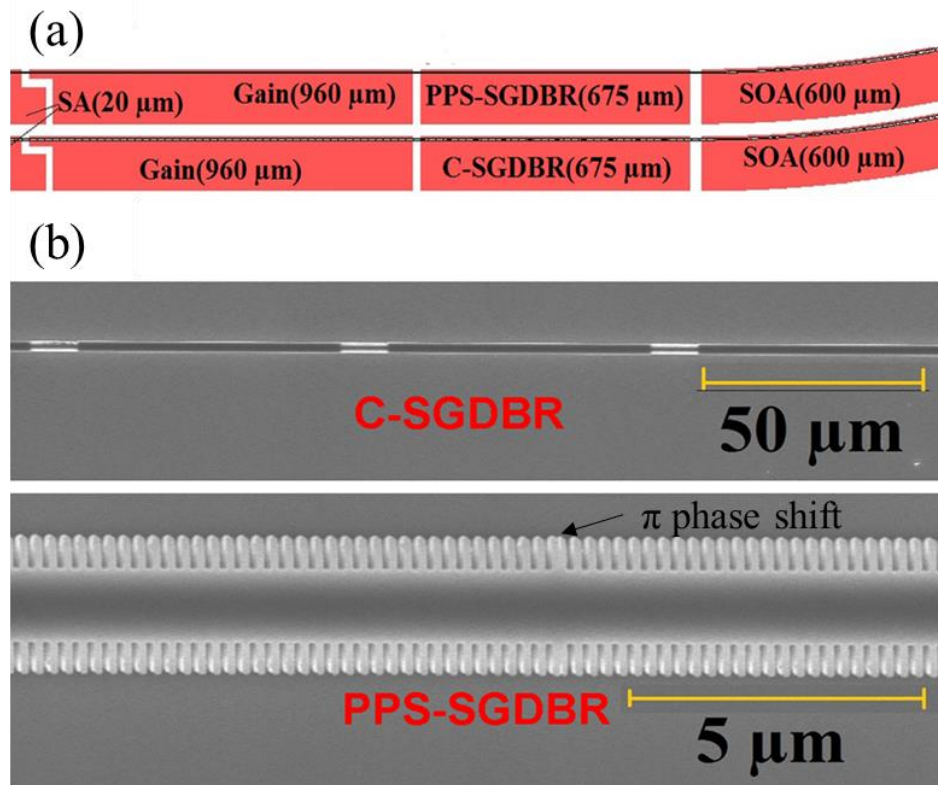


Figure 6.6: (a) Device structures based on C-SGDBR and PPS-SGDBR, (b) SEM images of the sidewall gratings of both of SGDBRs [217].

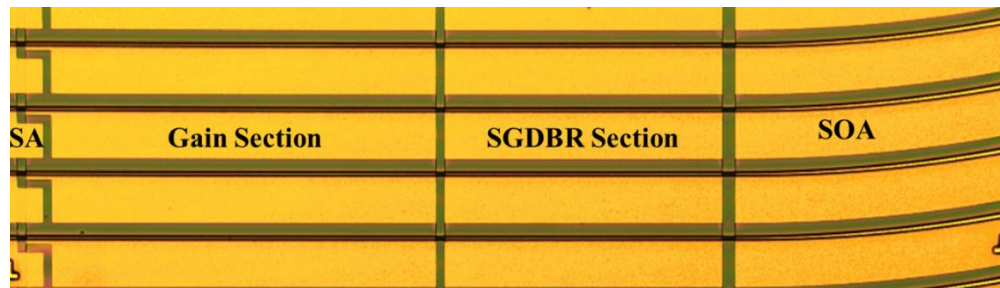


Figure 6.7: Micrograph of the fabricated MLLDs.

Figure 6.7 shows the corresponding micrograph of the fabricated MLLDs after depositing p-contact electrodes.

## 6.3 Characteristics of Mode-locked Lasers

### 6.3.1 640 GHz MLLDs Based on PPS-SGDBR

After the fabrication of the MLLDs was completed, the lasers were cleaved into bars for measurements.

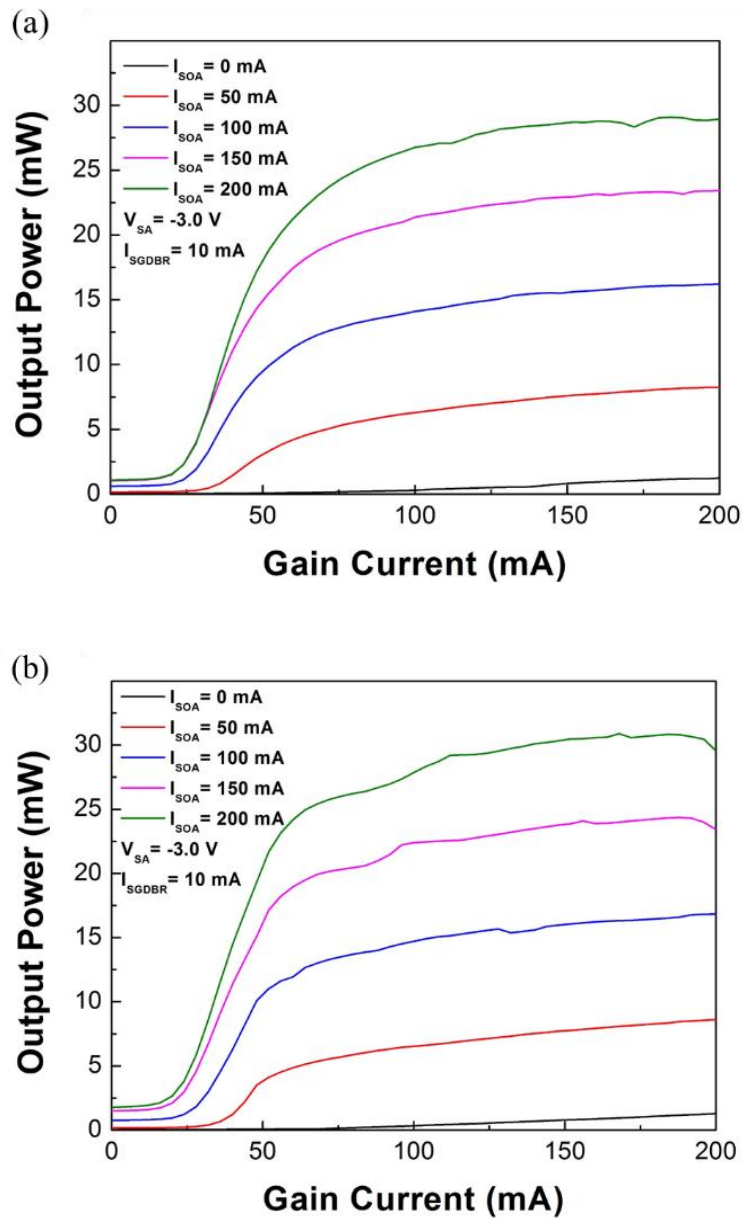
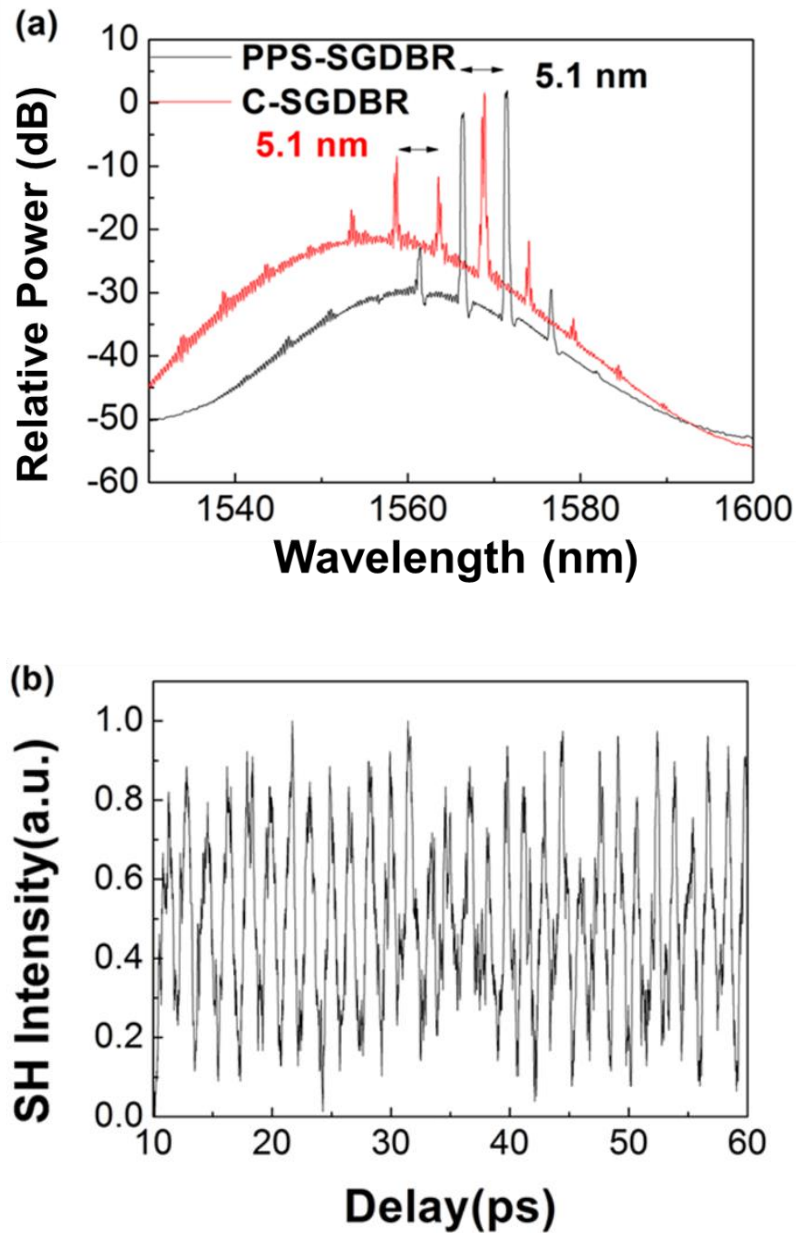


Figure 6.8: Typical output power from the SOA side of the 640 GHz (a) C-SGDBR, and (b) PPS-SGDBR laser versus the gain current with different SOA currents, when the  $V_{SA} = -3.0$  V and  $I_{SGDBR} = 10$  mA.



**Figure 6.9: (a) The optical spectra of 640 GHz C-SGDBR and PPS-SGDBR MLLDs measured at  $V_{SA} = -3.0$  V,  $I_{Gain} = 144$  mA,  $I_{SGDBR} = 10$  mA and  $I_{SOA} = 150$  mA, (b) the corresponding autocorrelation trace for PPS-SGDBR [217].**

Figure 6.8 shows the typical output power from the SOA side of the C-SGDBR and PPS-SGDBR lasers versus the gain current (injection current of the gain section) at different injection currents of the SOA section ( $I_{SOA}$ ), with the voltage of the SA section  $V_{SA} = -3.0$  V and the injection current of the SGDBR section  $I_{SGDBR} = 10$  mA. The SGDBR section was set at the transparency current to reduce optical loss as well as achieve stability without

optical gain. The  $I_{SOA}$  was scanned from 0 mA to 200 mA in steps of 50 mA. From these two graphs, we can see that the  $LI$  curves of the C-SGDBR and PPS-SGDBR lasers were similar. Both of the lasers had a threshold of about 25 mA and saturated at an output power of about 15 mW when the injection current of the SOA section was 100 mA. The threshold currents of the two types of lasers are similar. With the increase of SOA current, the threshold current was observed to decrease. This may be caused by the current leakage, since the resistance between adjacent electrode pads was only about tens of  $k\Omega$ . Ion implantation technique like helium bombardment could be applied in the future to make a highly resistive region in the ridge waveguide [218]. It would be ideal if the resistance could reach  $M\Omega$ .

For comparison, the optical spectra of the C-SGDBR and PPS-SGDBR lasers were measured under the same operating conditions, as shown in Fig. 6.9(a). The lasing spectra were measured at  $V_{SA} = -3$  V,  $I_{Gain} = 144$  mA,  $I_{SGDBR} = 10$  mA, and  $I_{SOA} = 150$  mA. As was pointed out previously, for these devices, the effective  $\kappa$  for the 0<sup>th</sup>-order grating was about  $23.2$   $cm^{-1}$ . Because of the low effective coupling coefficient, the SMSRs of the spectra are not very high and the amplified spontaneous emission (ASE) was strong, giving a broad spectrum background emission. The ASE indicates the gain spectrum of the material, which is centred at about 1560 nm in this case and would move to longer wavelengths with an increase of gain current. However, because the PPS-SGDBR has a higher effective coupling coefficient, the relative ASE level of the PPS-SGDBR laser is lower than that of the C-SGDBR laser. The suppression of the ASE confirms the enhancement of the effective coupling coefficient of the PPS-SGDBR structure. Since the two types of lasers were designed with the same sampling period and 0<sup>th</sup>-order grating, the lasers operated at similar wavelengths. The small difference of lasing wavelengths comes from the difference of ridge waveguide profiles of different SGDBR structures. According to equation 6.2, since the mode spacing is accurately determined by the sampling period  $P$ , both of the spectra had peaks separated by 5.1 nm. The longitudinal mode spacing is essentially independent of  $I_{SGDBR}$  and temperature. Because of higher effective coupling coefficient, the optical spectrum of PPS-SGDBR laser was clearer and sharper than that of C-SGDBR laser.

The autocorrelation of the pulse train from the PPS-SGDBR laser was also measured, using the method described in Section 5.3.2. Figure 6.9(b) shows the autocorrelation trace, which was measured under the same operating conditions as these utilised to measure the optical

spectrum shown in Figure 6.9(a). The SA section was reverse-biased at 3 V, which led to mode locking of the optical comb. To achieve good mode-locking performance, the voltage of the SA section is set between 2-3 V. The average period of the pulse train was 1.6 ps, corresponding to a repetition frequency of 620 GHz, and the pulse width was 0.8 ps. The repetition frequency was consistent with the longitudinal mode spacing of 5.1 nm. The design value of the repetition frequency was 640 GHz and the measurement result was very close, within 3.2%. Precise control of repetition frequency of optical pulses was achieved for MLLDs by using the sampling technique. Under high injection currents, additional lasing peaks were observed. Since there were reflections between the as-cleaved facet and the DBR mirrors, FP modes may exist. Under high injection currents, there is more gain, and these FP modes may lase, which would lead to additional lasing modes. This phenomenon need to be avoided and therefore the injection current should not be too high.

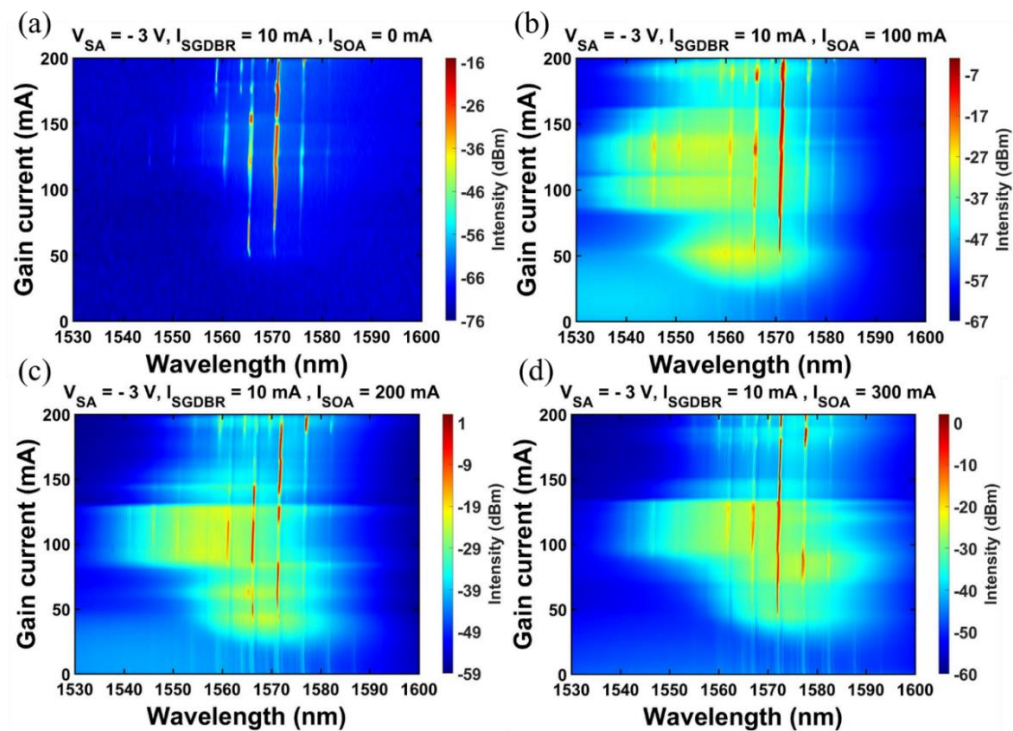


**Figure 6.10: 2D optical spectrum mapping of a 640 GHz PPS-SGDBR MLLD measured at  $V_{SA} = -3.0$  V,  $I_{SGDBR} = 10$  mA and (a)  $I_{SOA} = 0$  mA, (b)  $I_{SOA} = 100$  mA, (c)  $I_{SOA} = 200$  mA, (d)  $I_{SOA} = 300$  mA.**

The stability of lasing in the longitudinal modes is important. 2D optical spectrum mapping of a PPS-SGDBR MLLD was measured for a range of  $I_{Gain}$  from 0 mA to 200 mA in steps

of 4 mA and  $I_{SOA}$  from 0 mA to 300 mA in steps of 100 mA. These results were also measured with  $V_{SA} = -3.0$  V and  $I_{SGDBR} = 10$  mA, and are shown in Fig. 6.10. These figures show lasing in four main longitudinal modes and one longitudinal mode took the dominant role. With changes of the SOA current ( $I_{SOA}$ ), the 2D optical spectrum mapping also changed. The influence on the longitudinal modes by the SOA current may be because the electrical isolation between the SGDBR section and SOA section was not good, and the SOA current may have a leakage path to the SGDBR section. The electric isolation could be improved in the future by ion implantation-based isolation, using  $H^+$ ,  $He^+$ , etc. [219, 220]. This influence may also result from the accumulated heat due to the increase of SOA injection current. Better cooling for the diode lasers are required in the future.

The 2D optical spectrum mapping of a PPS-SGDBR MLLD was also measured for a range of  $I_{Gain}$  from 0 mA to 200 mA in steps of 4 mA and  $V_{SA}$  from  $-2.4$  V to  $-3.0$  V in steps of  $-0.2$  V. These results were measured when  $I_{SGDBR} = 10$  mA and  $I_{SOA} = 100$  mA, and are shown in Fig. 6.11. From these figures, we can see that the voltage applied to the SA section ( $V_{SA}$ ) had little influence on the multiple longitudinal modes.

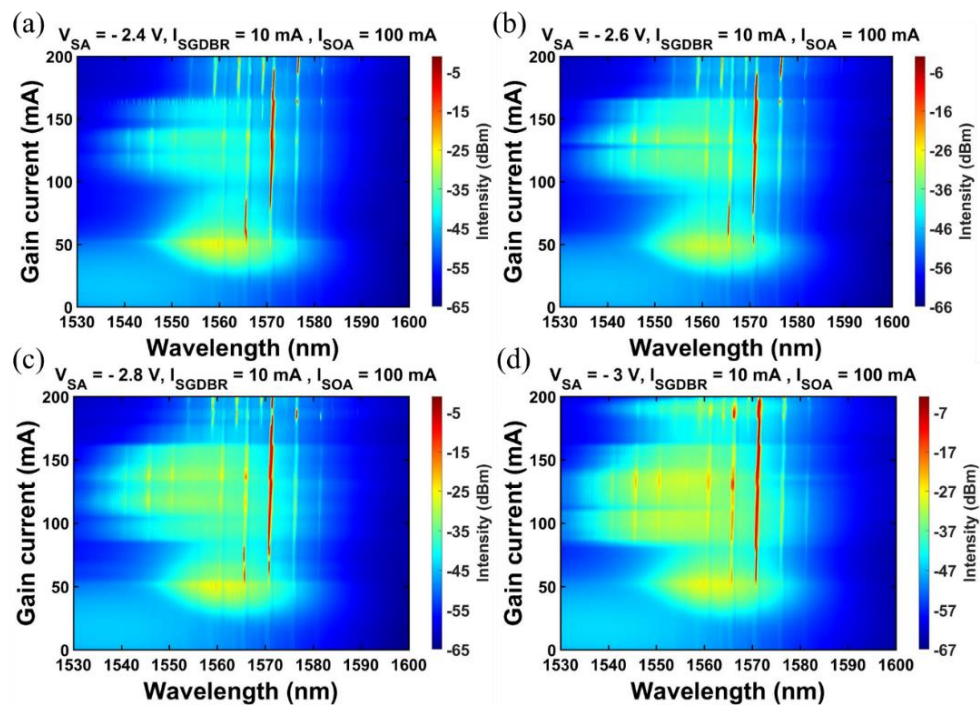


Figure 6.11: 2D optical spectrum mapping of a 640 GHz PPS-SGDBR MLLD at  $I_{SOA} = 100$  mA,  $I_{SGDBR} = 10$  mA and (a)  $V_{SA} = -2.4$  V, (b)  $V_{SA} = -2.6$  V, (c)  $V_{SA} = -2.8$  V, (d)  $V_{SA} = -3.0$  V.

### 6.3.2 1 THz MLLDs Based on PPS-SGDBR

According to equation 6.2, the repetition frequency  $F_r$  can be changed easily by changing the sampling period  $P$ . MLLDs with a repetition frequency of 1THz were also designed and fabricated.

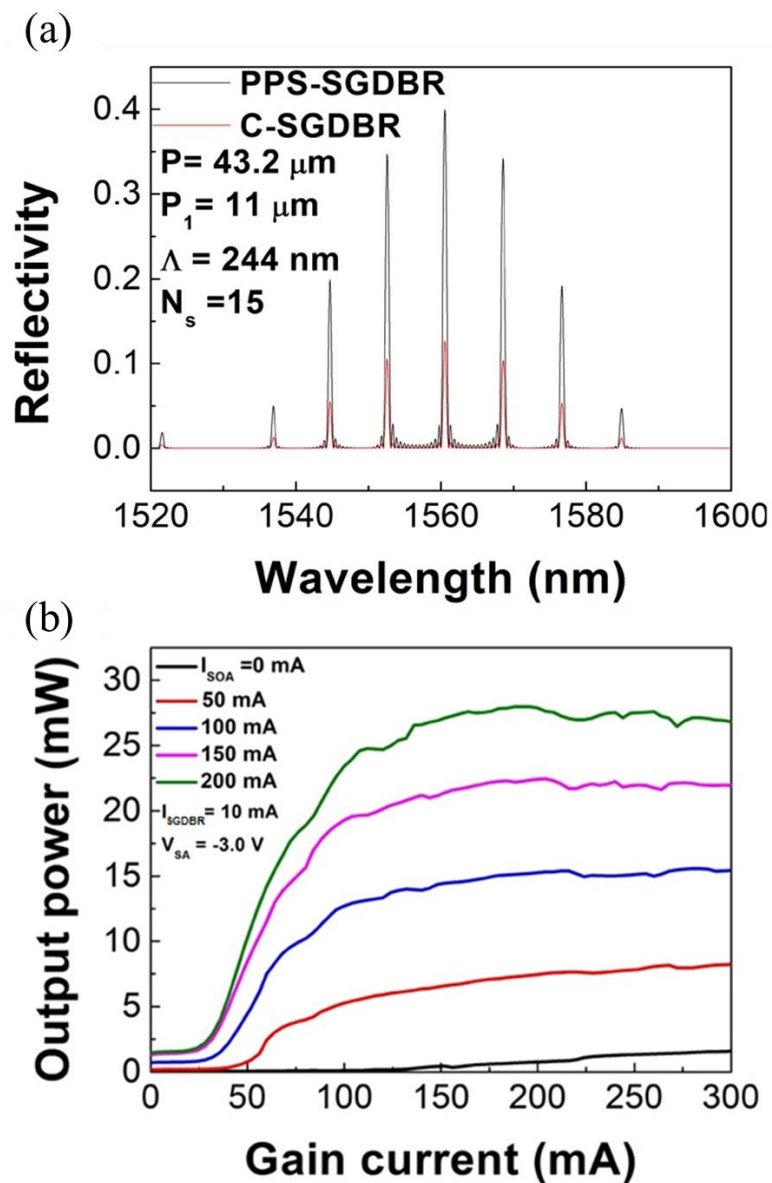
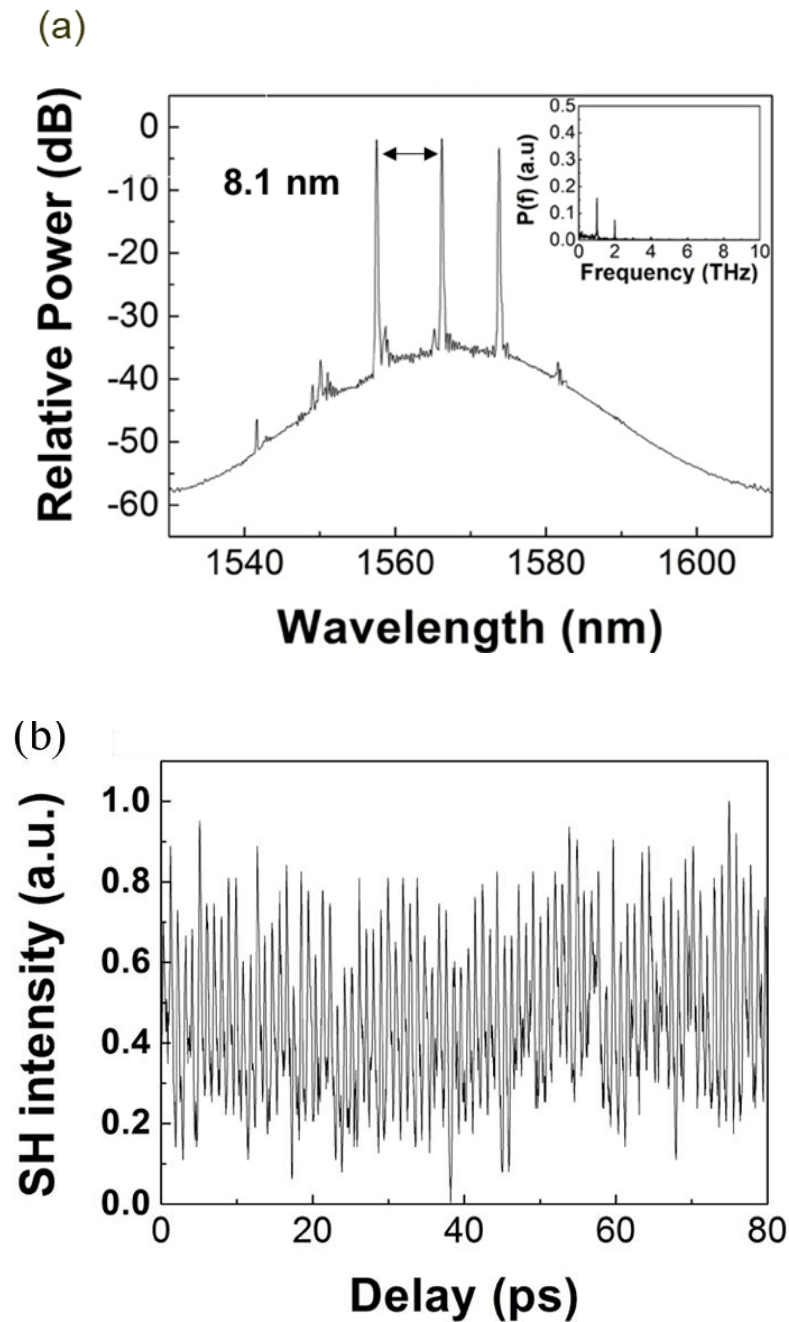


Figure 6.12: (a) Simulated reflectivity spectra of the 1THz PPS-SGDBR and its counterpart C-SGDBR, (b) typical output power from the SOA side for 1THz PPS-SGDBR MLLD when the  $V_{\text{SA}} = -3.0\text{V}$  and  $I_{\text{PPS-SGDBR}} = 10 \text{ mA}$  [217].

The device configuration was similar to the PPS-SGDBR integrated with an SOA shown in Fig. 6.6 (a), with an only difference being the design of the PPS-SGDBR section. The 0<sup>th</sup>-order grating period  $\Lambda$  was designed as 244 nm and the length of the PPS-SGDBR section was 648  $\mu\text{m}$ . The duty cycle of the PPS-SGDBR was still chosen to be  $P_I/P = 0.25$  and the parameters are listed as:  $P = 43.2 \mu\text{m}$ ,  $P_I = 11 \mu\text{m}$ ,  $N_s = 15$ . The effective  $\kappa$  of the PPS-SGDBR is expected to be around twice  $((43.2 - 2 \times 11)/11 = 1.93)$  that of a C-SGDBR and nearly half  $((43.2 - 2 \times 11)/43.2 = 0.49)$  that of a uniform grating. The reflectivity spectra of the PPS-SGDBR and the corresponding C-SGDBR were simulated by the TMM and are shown in Fig. 6.12(a), which confirms the above analysis. The designed central peak wavelength is 1560.5 nm and the wavelength spacing between adjacent modes is about 8.1 nm, which corresponds to about 1 THz around 1550 nm. Figure 6.12(b) shows the output power versus the gain current for different  $I_{\text{SOA}}$  with  $V_{\text{SA}} = -3.0 \text{ V}$  and  $I_{\text{SGDBR}} = 10 \text{ mA}$ . In this circumstance, the PPS-SGDBR laser was mode-locked at 1 THz. Other than the mode-locking frequency, this figure is similar to that of the 640 GHz mode-locked lasers shown in Fig. 6.8. A maximum output power of about 15 mW was achieved when  $I_{\text{SOA}} = 100 \text{ mA}$ .

A sharp and clear optical spectrum was measured for the 1 THz PPS-SGDBR MLLD at  $V_{\text{SA}} = -3.0 \text{ V}$ ,  $I_{\text{Gain}} = 232 \text{ mA}$ ,  $I_{\text{PPS-SGDBR}} = 10 \text{ mA}$ , and  $I_{\text{SOA}} = 100 \text{ mA}$ , as shown in Fig. 6.13(a). The wavelength spacing between adjacent longitudinal modes was measured as about 8.1 nm, which is the same as the design value. The main wavelength peak of the optical spectrum is also very close to the design value, as shown in Fig. 6.12(a). The wavelength spacings of the three wavelengths are not uniform because of wavelength dispersion in the laser cavity. In the frequency domain, the frequency separations are the same. Figure 6.13(b) illustrates the corresponding autocorrelation trace, with the same bias conditions as those used for measuring the optical spectrum. Although the pedestal of the autocorrelation trace is high, optical pulse signals can be clearly observed. The average period of the pulse train was measured to be about 1.0 ps, corresponding to an  $F_r$  of 1 THz. The fast Fourier transform (FFT) of the AC trace is also given as an inset in Fig. 6.13(a), which shows both the fundamental mode-locking frequency of 1 THz and the second harmonic. The width of an isolated pulse was 0.5 ps, half of the time period of the pulse train, assuming a sinusoidal pulse shape.



**Figure 6.13: (a) The optical spectrum and FFT of AC trace (inset) measured at  $V_{SA} = -3.0$  V,  $I_{Gain} = 232$  mA,  $I_{PPS-SGDBR} = 10$  mA, and  $I_{SOA} = 100$  mA, (b) corresponding AC trace for the 1 THz PPS-SGDBR MLLD [217].**

The 2D optical spectrum mapping of a 1 THz PPS-SGDBR MLLD for a range of  $I_{Gain}$  from 0 mA to 300 mA in steps of 4 mA is given in Fig. 6.14, measured at  $V_{SA} = -3.0$  V,  $I_{SGDBR} = 10$  mA, and  $I_{SOA} = 100$  mA. When the gain current was set at 232 mA, three longitudinal modes were observed, as shown in Fig. 6.13(a). Figure 6.14 shows the 2D mapping of the

lasing wavelength with injection current. For the three longitudinal modes, mode competition is strong, and the two main longitudinal modes were lasing in a wide injection current range. For each longitudinal mode, there appears to be two sub modes with mode hopping occurring in each channel. This mode instability was caused by the low coupling coefficient of the gratings. Longitudinal mode stability would be improved by increasing the coupling coefficient. In future, the device fabrication process is expected to be optimised to achieve stable multiple longitudinal modes stimulation. The gain spectrum is also expected to be broadened by modifying wafer structures to reduce gain differences between different wavelength modes in the future, so that more wavelength modes can be supported.

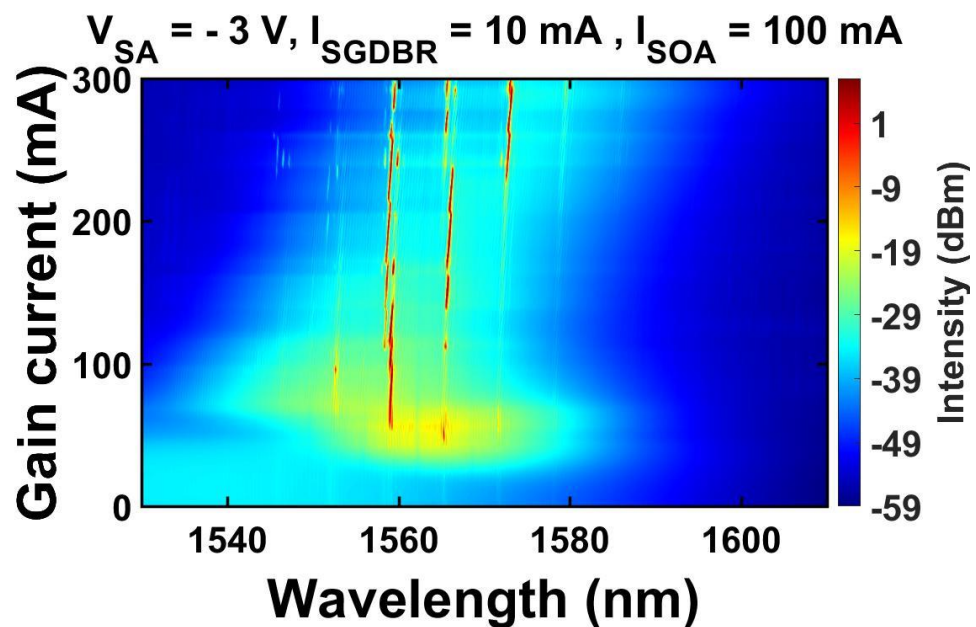


Figure 6.14: 2D optical spectrum mapping of a 1 THz PPS-SGDBR MLLD measured at  $V_{SA} = -3.0 \text{ V}$ ,  $I_{SGDBR} = 10 \text{ mA}$ , and  $I_{SOA} = 100 \text{ mA}$ .

## 6.4 Chapter Summary

In this chapter, ultrafast mode-locked laser diodes (MLLDs) operating at THz repetition frequencies have been introduced based on novel SGDBR structures. The MLLD based on conventional SGDBR (C-SGDBR) structure was introduced first. The C-SGDBR MLLD was designed at a repetition frequency of 640 GHz and its configuration was described in detail. The round trip time of the SGDBR laser was directly determined by the sampling

period of the gratings, hence, the repetition frequency is set precisely by changing only the sampling period, relieving the stringent fabrication and cleaving tolerances associated with other laser structures. By introducing  $\pi$ -phase shift gratings into each sampling period, MLLDs based on PPS-SGDBR using the 0<sup>th</sup>-order grating with a duty cycle of 0.25 were designed and fabricated. The duty cycle of 0.25 was optimised to give a uniform reflectivity spectrum that would support an optical comb. For comparison, C-SGDBR and PPS-SGDBR MLLDs with similar configurations were designed with the same sampling period and 0<sup>th</sup>-order grating period. The two types of MLLDs were demonstrated to have similar *LI* characteristics and close lasing wavelengths. The lower relative ASE level in the optical spectrum of the PPS-SGDBR MLLD has shown that the effective coupling coefficient of the PPS-SGDBR MLLD was significantly higher than that of the C-SGDBR MLLD. The behaviour was consistent with the simulation that showed the effective coupling coefficient of the PPS-SGDBR structure was about three times higher than that of the C-SGDBR structure with the same design of 0<sup>th</sup>-order grating period, sampling period and the number of sampling periods. The autocorrelation trace of the PPS-SGDBR MLLD has shown that the average period of the pulse train corresponded to a repetition frequency of 620 GHz, which was within 3.2% of the design value of 640 GHz. 2D optical spectrum mapping of the PPS-SGDBR MLLD at different SOA injection currents and SA bias voltages was also presented. By simply changing the sampling period, a MLLD based on a PPS-SGDBR structure with a repetition frequency of 1 THz was also designed and fabricated, which shows the flexibility and precision of sampling structures in realizing MLLDs with different repetition frequencies. Device characteristics, including *LI* curves, the output optical spectrum, the autocorrelation trace and the 2D optical spectrum mapping were all presented. It is concluded that MLLDs with compact design operating at THz repetition frequencies are promising components for use within THz sources.

## Chapter 7

### Conclusions and Future Work

#### 7.1 Research Summary

In this research work, novel designs of sampled Bragg gratings and their applications in DFB semiconductor lasers and mode-locked lasers were investigated. The research work was carried out in three main parts: design, fabrication and measurements.

To design a sampled Bragg grating with a specific functionality, the transfer matrix method (TMM) was utilised to simulate reflectivity spectra of the Bragg gratings. The TMM is capable of simulating sampled Bragg gratings with complex structures. From the basic theory of sampled Bragg gratings, sampled Bragg gratings with phase-shifted sections were introduced. By introducing phase-shifted sections into sampling periods, higher effective coupling coefficients and various new functionalities could be realized. Based on sampled Bragg gratings with multiple phase-shifted sections, the Bragg grating design for a single-mode DFB semiconductor laser array was simulated using the TMM. DFB semiconductor laser arrays using these sampled Bragg grating structures can achieve precise wavelength separation, with a smaller reduction of the effective coupling coefficient, compared to DFB semiconductor lasers with uniform Bragg gratings. Sampled Bragg grating structures for dual-mode lasers and mode-locked lasers were also introduced. These multi-longitudinal mode semiconductor lasers were designed to have a wavelength spacing corresponding to the THz frequency range. The optical reflectivity spectra of sampled Bragg gratings were optimised according to the simulation by the TMM.

The semiconductor diode lasers were fabricated in the AlGaInAs/InP material system with five quantum-wells and the fabrication was carried out in the JWNC at the University of Glasgow. These semiconductor lasers had ridge waveguides with side-wall gratings, which did not require material regrowth and so were easier to be fabricated. Electron beam lithography was utilised for pattern transfer during the whole fabrication process to achieve high precision. Electron beam lithography was especially essential for Bragg grating

definition, since the 0<sup>th</sup>-order grating period was only about 240 nm. Dry etch was chosen for etching III-V materials to take advantage of etching anisotropy, small mask undercutting and good repeatability. Mask definition and dry etch of ridge waveguides with side-wall gratings were the key steps in the fabrication process. Dose tests were carried out to obtain good profiles of the masks for side-wall gratings and dry etch processes were optimised to reduce the undercut and “RIE lag” effect. In the final step of device fabrication, the sample was cleaved into bars for measurements.

Measurements on fabricated semiconductor diode lasers were also carried out. The characteristics included *LI* curves, output optical spectra and far-field patterns. For dual-mode lasers and mode-locked lasers, the autocorrelation traces were also measured.

## 7.2 Main Achievements

Semiconductor diode lasers based on novel design of sampled Bragg grating structures were designed and fabricated successfully. The highlights of the research work and main achievements are as follows:

- An eight-wavelength DFB semiconductor laser array, aimed at WDM networks, was realised. The laser array was designed around 1550 nm and to have a wavelength spacing of 100 GHz. These DFB diode lasers had much higher effective coupling coefficients than those of DFB diode lasers based on a conventional sampled Bragg grating structure. The achieved average wavelength spacing was 104 GHz, which was nearly the same as the design value. The findings were reported in [160, 221, 222].
- A novel dual-mode semiconductor diode laser was realised with a wavelength spacing of 4.45 nm, which corresponds to the THz frequency of 560 GHz. This dual-mode laser had a single-cavity design based on the 2PS-SBG structure. Lasing in two longitudinal modes of the diode laser was stable. A demonstration of THz waves generation based on this dual-mode laser was also carried out. The related results were published in [198].

- Mode-locked laser diodes (MLLDs) based on optimised PPS-SGDBR structures were fabricated. Compared to a MLLD based on the conventional SGDBR structure, these MLLDs had higher effective coupling coefficients, which could contribute to shorter cavity lengths and more compact device configurations. MLLDs with repetition frequencies of 640 GHz and 1 THz were designed, fabricated and measured. The repetition frequency of the MLLD could be changed easily and precisely by changing the sampling periods. Autocorrelation traces have shown that the MLLDs were operated properly at the designed frequencies. The findings were published in [217, 223, 224].

### 7.3 Future Work

Improvements of the fabricated semiconductor lasers are worthy to be investigated. Although several novel designs of sampled Bragg gratings have been proposed, further new designs of sampled Bragg gratings are expected to be developed in the future. My suggestions for future work can be described as follows:

- Although the dry etch process of ridge waveguides with side-wall gratings has been optimised, the undercut and “RIE lag” effects are still present. The effective coupling coefficient is expected to be increased by further improving the dry etch process. Simulations show such semiconductor lasers are expected to have larger effective coupling coefficients, which can reach about  $80 \text{ cm}^{-1}$ . Semiconductor diode lasers with shorter cavity lengths but better performances, e.g. lower threshold currents, higher SMSRs, higher output power and larger modulation bandwidths, are expected to be produced.
- The eight-wavelength laser array was achieved with a wavelength spacing of 100 GHz. A narrower wavelength spacing, e.g. 50 GHz, could be investigated in the future. The laser array could be applied to DWDM systems, such as PONs, to assess the performance of the laser array in a transceiver and to study its cost-effectiveness in such an application. An investigation of integration with silicon-based devices is to be carried out to realize large-scale photonic integrated circuits. An array of FP

etalons could be hybrid integrated at the back of diode lasers to lock wavelengths to the WDM grid [225]. Benefiting from the precisely-controlled wavelengths, injection currents could be adjusted to lock the wavelengths to WDM grid. The integrated chip diode could share one TEC for temperature control, no need to adjust the temperature for each DFB diode laser.

- For the dual-mode lasers, different wavelength spacings could be achieved by designing grating structures with different sampling periods. Further applications in THz wave generation are expected to be investigated, covering a broad range of the THz spectrum.
- Mode-locked laser diodes with different repetition frequencies could be realised through sampled Bragg grating design with different sampling periods. Currently, competition between lasing modes is very strong. Stable lasing of multiple wavelengths in a single cavity would improve mode-locking performance at different injection currents. If more lasing wavelengths can be supported, the optical pulses will have a shorter duration time. Broadening the gain spectrum of the laser may be advantageous, e.g. by using quantum dots as the gain medium. Phase sections are also expected to be integrated into the mode-locked lasers. With phase tuning by injection currents, more stable multi-mode lasing and higher SMSR are expected to be achieved.
- It is not easy to evaluate mode locking performance, especially for THz repetition frequency optical pulses. In the future, linewidth of individual lasing line could be measured for both dual-mode lasers and mode-locked lasers. The linewidth reduction could indicate mode locking [197].
- It is also essential to measure the generated THz frequency. Current spectrum analyser can only detect the THz signals up to about 300 GHz. By using a harmonic mixer, the frequency range can be extended to 500 GHz [226]. To measure higher THz frequencies, a method based on the interferometer would be applied [203]. Then the emission THz frequency could be determined using a Michelson interferometer

setup. By detecting the interference patterns of THz radiation from the interferometer, the THz frequency could be calculated.

Novel semiconductor diode lasers including laser arrays, dual-mode lasers and mode-locked lasers have been introduced in this thesis. In the future, more and more new semiconductor lasers with different functionalities are expected to be produced, broadening the application areas of optoelectronic devices.

## Bibliography

- [1] R. Dupuis, "An introduction to the development of the semiconductor laser," *IEEE Journal of Quantum Electronics*, vol. 23, pp. 651-657, 1987.
- [2] L. A. Coldren, S. W. Corzine, and M. L. Mashanovitch, *Diode lasers and photonic integrated circuits* vol. 218: John Wiley & Sons, 2012.
- [3] P. Werle, "A review of recent advances in semiconductor laser based gas monitors," *Spectrochimica Acta Part A: Molecular and Biomolecular Spectroscopy*, vol. 54, pp. 197-236, 1998.
- [4] A. Pelman, A. I. Sander, and G. Yahav, "Gated 3D camera," ed: Google Patents, 2017.
- [5] W. Whitehouse, E. Foxlin, T. Calloway, and J. Popoolapade, "Dual-mode illuminator for imaging under different lighting conditions," ed: Google Patents, 2016.
- [6] B. Schwarz, "LIDAR: Mapping the world in 3D," *Nature Photonics*, vol. 4, pp. 429-430, 2010.
- [7] E. Selcuk, *Guided and deterministic self organization of quantum dots*, 2009.
- [8] R. Kazarinov and G. Belenky, "Novel design of AlGaInAs-InP lasers operating at 1.3/spl mu/m," *IEEE journal of quantum electronics*, vol. 31, pp. 423-426, 1995.
- [9] P. F. Liao and P. Kelley, *Quantum well lasers*: Elsevier, 2012.
- [10] X. Li, *Optoelectronic devices: design, modeling, and simulation*: Cambridge University Press, 2009.
- [11] K. Sekartedjo, N. Eda, K. Furuya, Y. Suematsu, F. Koyama, and T. Tanbun-Ek, "1.5  $\mu\text{m}$  phase-shifted DFB lasers for single-mode operation," *Electronics Letters*, vol. 20, pp. 80-81, 1984.
- [12] G. Sarlet, G. Morthier, and R. Baets, "Control of widely tunable SSG-DBR lasers for dense wavelength division multiplexing," *Journal of lightwave technology*, vol. 18, pp. 1128, 2000.
- [13] G. E. Keiser, "A review of WDM technology and applications," *Optical Fiber Technology*, vol. 5, pp. 3-39, 1999.

- [14] G. L. Wojcik, D. Yin, A. R. Kovsh, A. E. Gubenko, I. L. Krestnikov, S. S. Mikhlin, *et al.*, "A single comb laser source for short reach WDM interconnects," pp. 72300M-72300M-12, 2009.
- [15] A. J. Lowery, L. Du, and J. Armstrong, "Orthogonal frequency division multiplexing for adaptive dispersion compensation in long haul WDM systems," in *Optical fiber communication conference*, p. PDP39, 2006.
- [16] K.-I. Suzuki, H. Masuda, S. Kawai, K. Aida, and K. Nakagawa, "Bidirectional 10-channel 2.5 Gbit/s WDM transmission over 250 km using 76 nm (1531-1607 nm) gain-band bidirectional erbium-doped fibre amplifiers," *Electronics Letters*, vol. 33, pp. 1967-1968, 1997.
- [17] J. Cho, X. Chen, S. Chandrasekhar, G. Raybon, R. Dar, L. Schmalen, *et al.*, "Transatlantic field trial using high spectral efficiency probabilistically shaped 64-QAM and single-carrier real-time 250-Gb/s 16-QAM," *Journal of Lightwave Technology*, vol. 36, pp. 103-113, 2018.
- [18] T. Zami, B. Lavigne, O. B. Pardo, S. Weisser, J. David, M. Le Monnier, *et al.*, "31.2-Tb/s Real Time Bidirectional Transmission of 78× 400 Gb/s Interleaved Channels over C Band of One 90-km SMF Span," in *Optical Fiber Communications Conference and Exposition (OFC)*, pp. 1-3, 2018.
- [19] D. Qian, M.-F. Huang, E. Ip, Y.-K. Huang, Y. Shao, J. Hu, *et al.*, "101.7-Tb/s (370× 294-Gb/s) PDM-128QAM-OFDM transmission over 3× 55-km SSMF using pilot-based phase noise mitigation," in *National Fiber Optic Engineers Conference*, p. PDPB5, 2011.
- [20] J. Renaudier, A. C. Meseguer, A. Ghazisaeidi, P. Tran, R. R. Muller, R. Brenot, *et al.*, "First 100-nm continuous-band WDM transmission system with 115Tb/s transport over 100km using novel ultra-wideband semiconductor optical amplifiers," in *European Conference on Optical Communication (ECOC)*, pp. 1-3, 2017.
- [21] P. J. Winzer, D. T. Neilson, and A. R. Chraplyvy, "Fiber-optic transmission and networking: the previous 20 and the next 20 years," *Optics express*, vol. 26, pp. 24190-24239, 2018.
- [22] G. Shen and R. S. Tucker, "Energy-Minimized Design for IP Over WDM Networks," *Journal of Optical Communications and Networking*, vol. 1, pp. 176-186, 2009.
- [23] R. Nagarajan, C. H. Joyner, R. P. Schneider, J. S. Bostak, T. Butrie, A. G. Dentai, *et al.*, "Large-scale photonic integrated circuits," *IEEE Journal of Selected Topics in Quantum Electronics*, vol. 11, pp. 50-65, 2005.

- [24] C. Cole, B. Huebner, and J. E. Johnson, "Photonic integration for high-volume, low-cost applications," *Communications Magazine, IEEE*, vol. 47, pp. S16-S22, 2009.
- [25] J. L. Pleumeekers, P. W. Evans, W. Chen, R. P. Schneider Jr, and R. Nagarajan, "A new era in optical integration," *Optics and Photonics News*, vol. 20, pp. 20-25, 2009.
- [26] M. K. Smit, X. Leijtens, E. Bente, J. van der Tol, H. Ambrosius, D. Robbins, *et al.*, "A generic foundry model for InP-based photonic ICs," in *Optical Fiber Communication Conference*, p. OM3E. 3, 2012.
- [27] M. N. Sysak, J. W. Raring, J. S. Barton, M. Dummer, D. J. Blumenthal, and L. A. Coldren, "A single regrowth integration platform for photonic circuits incorporating tunable SGDBR lasers and quantum-well EAMs," *IEEE photonics technology letters*, vol. 18, 2006.
- [28] Y. Barbarin, E. Bente, T. de Vries, J. den Besten, P. van Veldhoven, M. Sander-Jochem, *et al.*, "Butt-joint interfaces in InP/InGaAsP waveguides with very low reflectivity and low loss," *Proc. IEEE/LEOS Benelux Chapter. ISBN*, pp. 2-960022645, 2005.
- [29] O. K. Kwon, Y. A. Leem, Y. T. Han, C. W. Lee, K. S. Kim, and S. H. Oh, "A 10×10 Gb/s DFB laser diode array fabricated using a SAG technique," *Optics express*, vol. 22, pp. 9073-9080, 2014.
- [30] J. H. Marsh, "Quantum well intermixing," *Semiconductor science and technology*, vol. 8, p. 1136, 1993.
- [31] R. Nagarajan, M. Kato, D. Lambert, P. Evans, S. Corzine, V. Lal, *et al.*, "Terabit/s class InP photonic integrated circuits," *Semiconductor Science and Technology*, vol. 27, p. 094003, 2012.
- [32] D. J. Moss, R. Morandotti, A. L. Gaeta, and M. Lipson, "New CMOS-compatible platforms based on silicon nitride and Hydex for nonlinear optics," *Nature Photonics*, vol. 7, pp. 597-607, 2013.
- [33] T. Goh, H. Yamazaki, T. Kominato, and S. Mino, "Novel flexible-format optical modulator with selectable combinations of carrier numbers and modulation levels based on silica-PLC and LiNbO<sub>3</sub> hybrid integration," in *Optical Fiber Communication Conference and Exposition (OFC/NFOEC) and the National Fiber Optic Engineers Conference*, pp. 1-3, 2011.

- [34] Z. Zhang, N. Mettbach, C. Zawadzki, J. Wang, D. Schmidt, W. Brinker, *et al.*, "Polymer-based photonic toolbox: passive components, hybrid integration and polarisation control," *IET optoelectronics*, vol. 5, pp. 226-232, 2011.
- [35] T. Mitze, M. Schnarrenberger, L. Zimmermann, J. Bruns, F. Fidorra, J. Kreissl, *et al.*, "Hybrid integration of III/V lasers on a silicon-on-insulator (SOI) optical board," in *2nd IEEE International Conference on Group IV Photonics*, pp. 210-212, 2005.
- [36] K. Kato and Y. Tohmori, "PLC hybrid integration technology and its application to photonic components," *IEEE Journal of Selected Topics in Quantum Electronics*, vol. 6, pp. 4-13, 2000.
- [37] M. J. Heck, J. F. Bauters, M. L. Davenport, J. K. Doylend, S. Jain, G. Kurczveil, *et al.*, "Hybrid silicon photonic integrated circuit technology," *IEEE Journal of Selected Topics in Quantum Electronics*, vol. 19, pp. 6100117-6100117, 2013.
- [38] D. Dai, J. Bauters, and J. E. Bowers, "Passive technologies for future large-scale photonic integrated circuits on silicon: polarization handling, light non-reciprocity and loss reduction," *Light: Science & Applications*, vol. 1, p. e1, 2012.
- [39] A. Mekis, S. Gloeckner, G. Masini, A. Narasimha, T. Pinguet, S. Sahni, *et al.*, "A Grating-Coupler-Enabled CMOS Photonics Platform," *IEEE Journal of Selected Topics in Quantum Electronics*, vol. 17, pp. 597-608, 2011.
- [40] D. Liang, J. Bowers, D. Oakley, A. Napoleone, D. Chapman, C.-L. Chen, *et al.*, "High-quality 150 nm InP-to-silicon epitaxial transfer for silicon photonic integrated circuits," *Electrochemical and solid-state letters*, vol. 12, pp. H101-H104, 2009.
- [41] Z. Wang, B. Tian, M. Pantouvaki, W. Guo, P. Absil, J. Van Campenhout, *et al.*, "Room-temperature InP distributed feedback laser array directly grown on silicon," *Nature Photonics*, vol. 9, pp. 837-842, 2015.
- [42] E. Palen, "Low cost optical interconnects," in *Photonics Packaging, Integration, and Interconnects VII*, p. 647804, 2007.
- [43] I. Hosako, N. Sekine, M. Patrashin, S. Saito, K. Fukunaga, Y. Kasai, *et al.*, "At the dawn of a new era in terahertz technology," *Proceedings of the IEEE*, vol. 95, pp. 1611-1623, 2007.
- [44] D. Mittleman, *Sensing with terahertz radiation* vol. 85: Springer, 2013.
- [45] B. Ferguson and X.-C. Zhang, "Materials for terahertz science and technology," *Nature materials*, vol. 1, p. 26, 2002.

- [46] P. de Maagt, "Terahertz technology for space and earth applications," in *First European Conference on Antennas and Propagation (EuCAP)*, pp. 1-4, 2006.
- [47] R. Guesten, I. Camara, P. Hartogh, H.-W. Huebers, U. U. Graf, K. Jacobs, *et al.*, "GREAT: the German receiver for astronomy at terahertz frequencies," in *Airborne Telescope Systems II*, 2003, pp. 56-62.
- [48] A. Smirnov, A. Baryshev, S. Pilipenko, N. Myshonkova, V. Bulanov, M. Arkhipov, *et al.*, "Space mission Millimetron for terahertz astronomy," in *Space Telescopes and Instrumentation 2012: Optical, Infrared, and Millimeter Wave*, p. 84424C, 2012.
- [49] C. Kulesa, "Terahertz spectroscopy for astronomy: From comets to cosmology," *IEEE Transactions on Terahertz Science and Technology*, vol. 1, pp. 232-240, 2011.
- [50] H. Harde, N. Katzenellenbogen, and D. Grischkowsky, "Line-shape transition of collision broadened lines," *Physical review letters*, vol. 74, p. 1307, 1995.
- [51] I. I. Sobel'Man, L. A. Vainshtein, and E. A. Yukov, *Excitation of atoms and broadening of spectral lines* vol. 15: Springer Science & Business Media, 2012.
- [52] C. K. Walker and C. A. Kulesa, "Terahertz astronomy from the coldest place on earth," in *The Joint 30th International Conference on Infrared and Millimeter Waves and 13th International Conference on Terahertz Electronics, IRMMW-THz*, pp. 3-4, 2005.
- [53] P. H. Siegel, "Terahertz technology," *IEEE Transactions on microwave theory and techniques*, vol. 50, pp. 910-928, 2002.
- [54] M. Tonouchi, "Cutting-edge terahertz technology," *Nature photonics*, vol. 1, p. 97, 2007.
- [55] D. Grischkowsky, S. Keiding, M. Van Exter, and C. Fattinger, "Far-infrared time-domain spectroscopy with terahertz beams of dielectrics and semiconductors," *JOSA B*, vol. 7, pp. 2006-2015, 1990.
- [56] D. M. Mittleman, R. H. Jacobsen, and M. C. Nuss, "T-ray imaging," *IEEE Journal of selected topics in quantum electronics*, vol. 2, pp. 679-692, 1996.
- [57] L. Thrane, R. H. Jacobsen, P. U. Jepsen, and S. Keiding, "THz reflection spectroscopy of liquid water," *Chemical Physics Letters*, vol. 240, pp. 330-333, 1995.

- [58] J. Kindt and C. Schmuttenmaer, "Far-infrared dielectric properties of polar liquids probed by femtosecond terahertz pulse spectroscopy," *The Journal of Physical Chemistry*, vol. 100, pp. 10373-10379, 1996.
- [59] P. Han, G. Cho, and X.-C. Zhang, "Time-domain transillumination of biological tissues with terahertz pulses," *Optics Letters*, vol. 25, pp. 242-244, 2000.
- [60] A. Markelz, S. Whitmire, J. Hillebrecht, and R. Birge, "THz time domain spectroscopy of biomolecular conformational modes," *Physics in Medicine & Biology*, vol. 47, p. 3797, 2002.
- [61] P. H. Bolivar, M. Brucherseifer, M. Nagel, H. Kurz, A. Bosserhoff, and R. Büttner, "Label-free probing of genes by time-domain terahertz sensing," *Physics in Medicine & Biology*, vol. 47, p. 3815, 2002.
- [62] M. C. Kemp, P. Taday, B. E. Cole, J. Cluff, A. J. Fitzgerald, and W. R. Tribe, "Security applications of terahertz technology," in *Terahertz for Military and Security Applications*, pp. 44-53, 2003.
- [63] I. Chih-Lin, C. Rowell, S. Han, Z. Xu, G. Li, and Z. Pan, "Toward green and soft: a 5G perspective," *IEEE Communications Magazine*, vol. 52, pp. 66-73, 2014.
- [64] A. Kim, Y. H. Joo, and Y. Kim, "60 GHz wireless communication systems with radio-over-fiber links for indoor wireless LANs," *IEEE Transactions on Consumer Electronics*, vol. 50, pp. 517-520, 2004.
- [65] R. C. Daniels and R. W. Heath Jr, "60 GHz wireless communications: Emerging requirements and design recommendations," *IEEE Vehicular technology magazine*, vol. 2, 2007.
- [66] J. Federici and L. Moeller, "Review of terahertz and subterahertz wireless communications," *Journal of Applied Physics*, vol. 107, p. 6, 2010.
- [67] T. Kleine-Ostmann and T. Nagatsuma, "A review on terahertz communications research," *Journal of Infrared, Millimeter, and Terahertz Waves*, vol. 32, pp. 143-171, 2011.
- [68] R. Piesiewicz, T. Kleine-Ostmann, N. Krumbholz, D. Mittleman, M. Koch, J. Schoebei, *et al.*, "Short-range ultra-broadband terahertz communications: Concepts and perspectives," *IEEE Antennas and Propagation Magazine*, vol. 49, pp. 24-39, 2007.
- [69] H.-J. Song and T. Nagatsuma, "Present and future of terahertz communications," *IEEE transactions on terahertz science and technology*, vol. 1, pp. 256-263, 2011.

- [70] D. H. Auston, K. Cheung, J. Valdmanis, and D. Kleinman, "Cherenkov radiation from femtosecond optical pulses in electro-optic media," *Physical Review Letters*, vol. 53, p. 1555, 1984.
- [71] C. Fattinger and D. Grischkowsky, "Point source terahertz optics," *Applied Physics Letters*, vol. 53, pp. 1480-1482, 1988.
- [72] M. van Exter, C. Fattinger, and D. Grischkowsky, "Terahertz time-domain spectroscopy of water vapor," *Optics Letters*, vol. 14, pp. 1128-1130, 1989.
- [73] D. M. Mittleman, R. Jacobsen, R. Neelamani, R. G. Baraniuk, and M. C. Nuss, "Gas sensing using terahertz time-domain spectroscopy," *Applied Physics B: Lasers and Optics*, vol. 67, pp. 379-390, 1998.
- [74] B. Fischer, M. Walther, and P. U. Jepsen, "Far-infrared vibrational modes of DNA components studied by terahertz time-domain spectroscopy," *Physics in Medicine & Biology*, vol. 47, p. 3807, 2002.
- [75] M. M. Nazarov, A. P. Shkurinov, E. Kuleshov, and V. V. Tuchin, "Terahertz time-domain spectroscopy of biological tissues," *Quantum Electronics*, vol. 38, p. 647, 2008.
- [76] W. L. Chan, J. Deibel, and D. M. Mittleman, "Imaging with terahertz radiation," *Reports on progress in physics*, vol. 70, p. 1325, 2007.
- [77] D. Hashimshony, A. Zigler, and K. Papadopoulos, "Conversion of electrostatic to electromagnetic waves by superluminous ionization fronts," *Physical review letters*, vol. 86, p. 2806, 2001.
- [78] D. W. Van der Weide, J. Murakowski, and F. Keilmann, "Gas-absorption spectroscopy with electronic terahertz techniques," *IEEE Transactions on Microwave theory and Techniques*, vol. 48, pp. 740-743, 2000.
- [79] A. Nahata, A. S. Weling, and T. F. Heinz, "A wideband coherent terahertz spectroscopy system using optical rectification and electro - optic sampling," *Applied physics letters*, vol. 69, pp. 2321-2323, 1996.
- [80] J. Faist, F. Capasso, D. L. Sivco, C. Sirtori, A. L. Hutchinson, and A. Y. Cho, "Quantum cascade laser," *Science-AAAS-Weekly Paper Edition-including Guide to Scientific Information*, vol. 264, pp. 553-555, 1994.
- [81] R. Köhler, A. Tredicucci, F. Beltram, H. E. Beere, E. H. Linfield, A. G. Davies, *et al.*, "Terahertz semiconductor-heterostructure laser," *Nature*, vol. 417, p. 156, 2002.

- [82] S. Kumar, B. S. Williams, S. Kohen, Q. Hu, and J. L. Reno, "Continuous-wave operation of terahertz quantum-cascade lasers above liquid-nitrogen temperature," *Applied physics letters*, vol. 84, pp. 2494-2496, 2004.
- [83] C. Worrall, J. Alton, M. Houghton, S. Barbieri, H. E. Beere, D. Ritchie, *et al.*, "Continuous wave operation of a superlattice quantum cascade laser emitting at 2 THz," *Optics Express*, vol. 14, pp. 171-181, 2006.
- [84] C. Walther, M. Fischer, G. Scalari, R. Terazzi, N. Hoyler, and J. Faist, "Quantum cascade lasers operating from 1.2 to 1.6 THz," *Applied Physics Letters*, vol. 91, p. 131122, 2007.
- [85] B. S. Williams, S. Kumar, Q. Hu, and J. L. Reno, "High-power terahertz quantum-cascade lasers," *Electronics letters*, vol. 42, pp. 89-91, 2006.
- [86] S. Fatholouloumi, E. Dupont, C. Chan, Z. Wasilewski, S. Laframboise, D. Ban, *et al.*, "Terahertz quantum cascade lasers operating up to ~ 200 K with optimized oscillator strength and improved injection tunneling," *Optics express*, vol. 20, pp. 3866-3876, 2012.
- [87] Q. Lu, N. Bandyopadhyay, S. Slivken, Y. Bai, and M. Razeghi, "Room temperature single-mode terahertz sources based on intracavity difference-frequency generation in quantum cascade lasers," *Applied physics letters*, vol. 99, p. 131106, 2011.
- [88] L. A. Samoska, "An Overview of Solid-State Integrated Circuit Amplifiers in the Submillimeter-Wave and THz Regime," *IEEE Transactions on Terahertz Science and Technology*, vol. 1, pp. 9-24, 2011.
- [89] M. Seo, M. Urteaga, J. Hacker, A. Young, Z. Griffith, V. Jain, *et al.*, "InP HBT IC Technology for Terahertz Frequencies: Fundamental Oscillators Up to 0.57 THz," *IEEE Journal of Solid-State Circuits*, vol. 46, pp. 2203-2214, 2011.
- [90] O. Momeni and E. Afshari, "High Power Terahertz and Millimeter-Wave Oscillator Design: A Systematic Approach," *IEEE Journal of Solid-State Circuits*, vol. 46, pp. 583-597, 2011.
- [91] W. Steyaert and P. Reynaert, "A 0.54 THz Signal Generator in 40 nm Bulk CMOS With 22 GHz Tuning Range and Integrated Planar Antenna," *IEEE Journal of Solid-State Circuits*, vol. 49, pp. 1617-1626, 2014.
- [92] U. R. Pfeiffer, Y. Zhao, J. Grzyb, R. Al Hadi, N. Sarmah, W. Forster, *et al.*, "14.5 A 0.53 THz reconfigurable source array with up to 1mW radiated power for terahertz imaging applications in 0.13  $\mu\text{m}$  SiGe BiCMOS," in *IEEE International Solid-State Circuits Conference Digest of Technical Papers (ISSCC)*, pp. 256-257, 2014.

- [93] T. Sollner, W. Goodhue, P. Tannenwald, C. Parker, and D. Peck, "Resonant tunneling through quantum wells at frequencies up to 2.5 THz," *Applied Physics Letters*, vol. 43, pp. 588-590, 1983.
- [94] T. Maekawa, H. Kanaya, S. Suzuki, and M. Asada, "Oscillation up to 1.92 THz in resonant tunneling diode by reduced conduction loss," *Applied Physics Express*, vol. 9, p. 024101, 2016.
- [95] S. Suzuki, A. Teranishi, K. Hinata, M. Asada, H. Sugiyama, and H. Yokoyama, "Fundamental oscillation of up to 831 GHz in GaInAs/AlAs resonant tunneling diode," *Applied Physics Express*, vol. 2, p. 054501, 2009.
- [96] M. Feiginov, H. Kanaya, S. Suzuki, and M. Asada, "Operation of resonant-tunneling diodes with strong back injection from the collector at frequencies up to 1.46 THz," *Applied Physics Letters*, vol. 104, p. 243509, 2014.
- [97] E. Brown, T. Sollner, C. Parker, W. Goodhue, and C. Chen, "Oscillations up to 420 GHz in GaAs/AlAs resonant tunneling diodes," *Applied Physics Letters*, vol. 55, pp. 1777-1779, 1989.
- [98] E. Brown, J. Söderström, C. Parker, L. Mahoney, K. Molvar, and T. McGill, "Oscillations up to 712 GHz in InAs/AlSb resonant - tunneling diodes," *Applied Physics Letters*, vol. 58, pp. 2291-2293, 1991.
- [99] M. Asada, S. Suzuki, and N. Kishimoto, "Resonant tunneling diodes for sub-terahertz and terahertz oscillators," *Japanese Journal of Applied Physics*, vol. 47, p. 4375, 2008.
- [100] T. Maekawa, H. Kanaya, S. Suzuki, and M. Asada, "Frequency increase in terahertz oscillation of resonant tunnelling diode up to 1.55 THz by reduced slot-antenna length," *Electronics Letters*, vol. 50, pp. 1214-1216, 2014.
- [101] S. Suzuki, M. Asada, A. Teranishi, H. Sugiyama, and H. Yokoyama, "Fundamental oscillation of resonant tunneling diodes above 1 THz at room temperature," *Applied Physics Letters*, vol. 97, p. 242102, 2010.
- [102] H. Kanaya, R. Sogabe, T. Maekawa, S. Suzuki, and M. Asada, "Fundamental oscillation up to 1.42 THz in resonant tunneling diodes by optimized collector spacer thickness," *Journal of Infrared, Millimeter, and Terahertz Waves*, vol. 35, pp. 425-431, 2014.
- [103] H. Kanaya, H. Shibayama, R. Sogabe, S. Suzuki, and M. Asada, "Fundamental oscillation up to 1.31 THz in resonant tunneling diodes with thin well and barriers," *Applied Physics Express*, vol. 5, p. 124101, 2012.

- [104] S. Suzuki, M. Shiraishi, H. Shibayama, and M. Asada, "High-power operation of terahertz oscillators with resonant tunneling diodes using impedance-matched antennas and array configuration," *IEEE Journal of Selected Topics in Quantum Electronics*, vol. 19, pp. 8500108-8500108, 2013.
- [105] M. Asada and S. Suzuki, "Theoretical analysis of coupled oscillator array using resonant tunneling diodes in subterahertz and terahertz range," *Journal of Applied Physics*, vol. 103, p. 124514, 2008.
- [106] K. J. Siebert, H. Quast, R. Leonhardt, T. Löffler, M. Thomson, T. Bauer, *et al.*, "Continuous-wave all-optoelectronic terahertz imaging," *Applied Physics Letters*, vol. 80, pp. 3003-3005, 2002.
- [107] S. Verghese, K. McIntosh, S. Calawa, W. Dinatale, E. Duerr, and K. Molvar, "Generation and detection of coherent terahertz waves using two photomixers," *Applied Physics Letters*, vol. 73, pp. 3824-3826, 1998.
- [108] I. S. Gregory, W. Tribe, C. Baker, B. Cole, M. Evans, L. Spencer, *et al.*, "Continuous-wave terahertz system with a 60 dB dynamic range," *Applied Physics Letters*, vol. 86, p. 204104, 2005.
- [109] S. Matsuura, M. Tani, and K. Sakai, "Generation of coherent terahertz radiation by photomixing in dipole photoconductive antennas," *Applied Physics Letters*, vol. 70, pp. 559-561, 1997.
- [110] G. Mouret, S. Matton, R. Bocquet, F. Hindle, E. Peytavit, J. Lampin, *et al.*, "Far-infrared cw difference-frequency generation using vertically integrated and planar low temperature grown GaAs photomixers: application to H<sub>2</sub>S rotational spectrum up to 3 THz," *Applied Physics B*, vol. 79, pp. 725-729, 2004.
- [111] P. R. Smith, D. H. Auston, and M. C. Nuss, "Subpicosecond photoconducting dipole antennas," *IEEE Journal of Quantum Electronics*, vol. 24, pp. 255-260, 1988.
- [112] N. Li, X. Li, S. Demiguel, X. Zheng, J. C. Campbell, D. A. Tulchinsky, *et al.*, "High-saturation-current charge-compensated InGaAs-InP uni-traveling-carrier photodiode," *IEEE Photonics Technology Letters*, vol. 16, pp. 864-866, 2004.
- [113] N. Shimizu, N. Watanabe, T. Furuta, and T. Ishibashi, "InP-InGaAs uni-traveling-carrier photodiode with improved 3-dB bandwidth of over 150 GHz," *IEEE Photonics Technology Letters*, vol. 10, pp. 412-414, 1998.
- [114] K. S. Giboney, J. Rodwell, and J. E. Bowers, "Traveling-wave photodetector theory," *IEEE transactions on microwave theory and techniques*, vol. 45, pp. 1310-1319, 1997.

- [115] H. Ito, S. Kodama, Y. Muramoto, T. Furuta, T. Nagatsuma, and T. Ishibashi, "High-speed and high-output InP-InGaAs untraveling-carrier photodiodes," *IEEE Journal of selected topics in quantum electronics*, vol. 10, pp. 709-727, 2004.
- [116] E. Rouvalis, C. C. Renaud, D. G. Moodie, M. J. Robertson, and A. J. Seeds, "Traveling-wave uni-traveling carrier photodiodes for continuous wave THz generation," *Optics Express*, vol. 18, pp. 11105-11110, 2010.
- [117] *Mode-locking*. Available: <https://en.wikipedia.org/wiki/Mode-locking>
- [118] E. Rafailov, M. Cataluna, and W. Sibbett, "Mode-locked quantum-dot lasers," *Nature photonics*, vol. 1, p. 395, 2007.
- [119] A. H. Quarterman, K. G. Wilcox, V. Apostolopoulos, Z. Mihoubi, S. P. Elsmere, I. Farrer, *et al.*, "A passively mode-locked external-cavity semiconductor laser emitting 60-fs pulses," *Nature Photonics*, vol. 3, p. 729, 2009.
- [120] L. Hou, M. Haji, J. H. Marsh, and A. C. Bryce, "490 fs pulse generation from a passive C-band AlGaInAs/InP quantum well mode-locked laser," *Optics letters*, vol. 37, pp. 773-775, 2012.
- [121] R. Tucker, U. Koren, G. Raybon, C. Burrus, B. Miller, T. Koch, *et al.*, "40 GHz active mode-locking in a 1.5  $\mu$ m monolithic extended-cavity laser," *Electronics letters*, vol. 25, pp. 621-622, 1989.
- [122] K. Sato, K. Wakita, I. Kotaka, Y. Kondo, M. Yamamoto, and A. Takada, "Monolithic strained - InGaAsP multiple - quantum - well lasers with integrated electroabsorption modulators for active mode locking," *Applied physics letters*, vol. 65, pp. 1-3, 1994.
- [123] Y. Silberberg, P. Smith, D. Eilenberger, D. Miller, A. Gossard, and W. Wiegmann, "Passive mode locking of a semiconductor diode laser," *Optics Letters*, vol. 9, pp. 507-509, 1984.
- [124] X. Huang, A. Stintz, H. Li, L. Lester, J. Cheng, and K. Malloy, "Passive mode-locking in 1.3  $\mu$ m two-section InAs quantum dot lasers," *Applied Physics Letters*, vol. 78, pp. 2825-2827, 2001.
- [125] H. A. Haus, "Mode-locking of lasers," *IEEE Journal of Selected Topics in Quantum Electronics*, vol. 6, pp. 1173-1185, 2000.
- [126] M. Haiml, R. Grange, and U. Keller, "Optical characterization of semiconductor saturable absorbers," *Applied Physics B*, vol. 79, pp. 331-339, 2004.

- [127] E. Avrutin, J. Marsh, and E. Portnoi, "Monolithic and multi-gigahertz mode-locked semiconductor lasers: constructions, experiments, models and applications," *IEEE Proceedings-Optoelectronics*, vol. 147, pp. 251-278, 2000.
- [128] A. V. Uskov, J. Karin, R. Nagarajan, and J. Bowers, "Dynamics of carrier heating and sweepout in waveguide saturable absorbers," *IEEE Journal of Selected Topics in Quantum Electronics*, vol. 1, pp. 552-561, 1995.
- [129] K. Merghem, A. Akrouf, A. Martinez, G. Moreau, J.-P. Turrenc, F. Lelarge, *et al.*, "Short pulse generation using a passively mode locked single InGaAsP/InP quantum well laser," *Optics express*, vol. 16, pp. 10675-10683, 2008.
- [130] L. Hou, P. Stolarz, J. Javaloyes, R. P. Green, C. N. Ironside, M. Sorel, *et al.*, "Subpicosecond Pulse Generation at Quasi-40-GHz Using a Passively Mode-Locked AlGaInAs-InP 1.55  $\mu\text{m}$  Strained Quantum-Well Laser," *IEEE Photonics Technology Letters*, vol. 21, pp. 1731-1733, 2009.
- [131] T. Erdogan, "Fiber grating spectra," *Journal of lightwave technology*, vol. 15, pp. 1277-1294, 1997.
- [132] H. Kogelnik and C. Shank, "Coupled - wave theory of distributed feedback lasers," *Journal of applied physics*, vol. 43, pp. 2327-2335, 1972.
- [133] J. Buus, M.-C. Amann, and D. J. Blumenthal, *Tunable laser diodes and related optical sources*: Wiley-Interscience New York, 2005.
- [134] H. Ghafouri-Shiraz, *Distributed feedback laser diodes and optical tunable filters*: John Wiley & Sons, 2004.
- [135] M. Ibsen, M. K. Durkin, M. J. Cole, and R. I. Laming, "Sinc-sampled fiber Bragg gratings for identical multiple wavelength operation," *IEEE Photonics Technology Letters*, vol. 10, pp. 842-844, 1998.
- [136] F. Ouellette, P. Krug, T. Stephens, G. Dhosi, and B. Eggleton, "Broadband and WDM dispersion compensation using chirped sampled fibre Bragg gratings," *Electronics Letters*, vol. 31, pp. 899-901, 1995.
- [137] H. Haus and C. Shank, "Antisymmetric taper of distributed feedback lasers," *IEEE Journal of Quantum Electronics*, vol. 12, pp. 532-539, 1976.
- [138] N. R. Broderick and C. M. de Sterke, "Theory of grating superstructures," *Physical review E*, vol. 55, p. 3634, 1997.
- [139] B. Eggleton, P. Krug, L. Poladian, and F. Ouellette, "Long periodic superstructure Bragg gratings in optical fibres," *Electronics letters*, vol. 30, pp. 1620-1622, 1994.

- [140] B.-O. Guan, H.-Y. Tam, X.-M. Tao, and X.-Y. Dong, "Simultaneous strain and temperature measurement using a superstructure fiber Bragg grating," *IEEE Photonics Technology Letters*, vol. 12, pp. 675-677, 2000.
- [141] Y. Tohmori, F. Kano, H. Ishii, Y. Yoshikuni, and Y. Kondo, "Wide tuning with narrow linewidth in DFB lasers with superstructure grating (SSG)," *Electronics letters*, vol. 29, pp. 1350-1352, 1993.
- [142] Y. Tohmori, Y. Yoshikuni, H. Ishii, F. Kano, T. Tamamura, Y. Kondo, *et al.*, "Broad-range wavelength-tunable superstructure grating (SSG) DBR lasers," *IEEE journal of quantum electronics*, vol. 29, pp. 1817-1823, 1993.
- [143] H. Ishii, Y. Tohmori, M. Yamamoto, T. Tamamura, and Y. Yoshikuni, "Modified multiple-phase-shift superstructure-grating DBR lasers for broad wavelength tuning," *Electronics Letters*, vol. 30, pp. 1141-1142, 1994.
- [144] X.-f. Chen, Y. Luo, C.-c. Fan, T. Wu, and S.-z. Xie, "Analytical expression of sampled Bragg gratings with chirp in the sampling period and its application in dispersion management design in a WDM system," *IEEE Photonics Technology Letters*, vol. 12, pp. 1013-1015, 2000.
- [145] Y. Dai, X. Chen, D. Jiang, S. Xie, and C. Fan, "Equivalent phase shift in a fiber Bragg grating achieved by changing the sampling period," *IEEE Photonics Technology Letters*, vol. 16, pp. 2284-2286, 2004.
- [146] Y. Dai, X. Chen, L. Xia, Y. Zhang, and S. Xie, "Sampled Bragg grating with desired response in one channel by use of a reconstruction algorithm and equivalent chirp," *Optics letters*, vol. 29, pp. 1333-1335, 2004.
- [147] J. Sun, Y. Dai, X. Chen, Y. Zhang, and S. Xie, "Thermally tunable dispersion compensator in 40-Gb/s system using FBG fabricated with linearly chirped phase mask," *Optics express*, vol. 14, pp. 44-49, 2006.
- [148] Y. Dai, X. Chen, J. Sun, Y. Yao, and S. Xie, "Dispersion compensation based on sampled fiber Bragg gratings fabricated with reconstruction equivalent-chirp method," *IEEE photonics technology letters*, vol. 18, pp. 941-943, 2006.
- [149] Y. Dai, X. Chen, Y. Shi, M. Chen, M. Zou, and S. Xie, "Tunable dispersion compensator for 40-Gb/s optical transmission systems fabricated by reconstruction and equivalent chirp method," in *Conference on Lasers and Electro-Optics (CLEO)*, pp. 1420-1422, 2005.
- [150] Y. Dai, X. Chen, J. Sun, Y. Yao, and S. Xie, "High-performance, high-chip-count optical code division multiple access encoders-decoders based on a reconstruction equivalent-chirp technique," *Optics Letters*, vol. 31, pp. 1618-1620, 2006.

- [151] Y. Dai, X. Chen, Y. Yao, J. Sun, and S. Xie, "511-chip, 500-chip/s OCDMA en/decoders based on equivalent phase-shift method," in *Optical Fiber Communication Conference, 2006 and the 2006 National Fiber Optic Engineers Conference*, p. 3 pp, 2006.
- [152] Y. Dai, X. Chen, X. Xu, C. Fan, and S. Xie, "High channel-count comb filter based on chirped sampled fiber Bragg grating and phase shift," *IEEE photonics technology letters*, vol. 17, pp. 1040-1042, 2005.
- [153] J. Sun, Y. Dai, Y. Zhang, X. Chen, and S. Xie, "Dual-Wavelength DFB Fiber Laser Based on Unequalized Phase Shifts," *IEEE Photonics Technology Letters*, vol. 18, pp. 2493-2495, 2006.
- [154] J. Dianjie, C. Xiangfei, D. Yitang, L. Haitao, and X. Shizhong, "A novel distributed feedback fiber laser based on equivalent phase shift," *IEEE Photonics Technology Letters*, vol. 16, pp. 2598-2600, 2004.
- [155] X. Chen, D. Jiang, Y. Dai, H. Liu, Y. Zhang, S. Xie, *et al.*, "Distributed feedback fiber laser with a novel structure," in *Optical Fiber Communication Conference (OFC)*, vol. 1, p. 3, 2005.
- [156] Y. Dai and X. Chen, "DFB semiconductor lasers based on reconstruction-equivalent-chirp technology," *Optics Express*, vol. 15, pp. 2348-2353, 2007.
- [157] J. Li, H. Wang, X. Chen, Z. Yin, Y. Shi, Y. Lu, *et al.*, "Experimental demonstration of distributed feedback semiconductor lasers based on reconstruction-equivalent-chirp technology," *Optics Express*, vol. 17, pp. 5240-5245, 2009.
- [158] Y. Dai and J. Yao, "Numerical study of a DFB semiconductor laser and laser array with chirped structure based on the equivalent chirp technology," *IEEE journal of quantum electronics*, vol. 44, pp. 938-945, 2008.
- [159] J. Li, Y. Cheng, Z. Yin, L. Jia, X. Chen, S. Liu, *et al.*, "A multiexposure technology for sampled Bragg gratings and its applications in dual-wavelength lasing generation and OCDMA en/decoding," *IEEE Photonics Technology Letters*, vol. 21, pp. 1639-1641, 2009.
- [160] S. Tang, L. Hou, X. Chen, and J. H. Marsh, "Multiple-wavelength distributed-feedback laser arrays with high coupling coefficients and precise channel spacing," *Optics Letters*, vol. 42, pp. 1800-1803, 2017.
- [161] J. S. Barton, E. J. Skogen, M. L. Masanovic, S. P. DenBaars, and L. A. Coldren, "A widely tunable high-speed transmitter using an integrated SGDBR laser-semiconductor optical amplifier and Mach-Zehnder modulator," *IEEE Journal of selected topics in quantum electronics*, vol. 9, pp. 1113-1117, 2003.

- [162] L. A. Coldren, G. A. Fish, Y. Akulova, J. S. Barton, L. Johansson, and C. W. Coldren, "Tunable Semiconductor Lasers: A Tutorial," *Journal of Lightwave Technology*, vol. 22, p. 193, 2004.
- [163] JWNC. Available: <http://www.jwnc.gla.ac.uk/>
- [164] H. Yamazaki, T. Sasaki, N. Kida, M. Kitamura, and I. Mito, "250kHz Linewidth Operation in Long Cavity 1.5  $\mu\text{m}$  Multiple Quantum Well DFB-LDs with Reduced Linewidth Enhancement Factor," in *Optical Fiber Communication Conference*, p. PD33, 1990.
- [165] S. Adachi, "Refractive indices of III–V compounds: Key properties of InGaAsP relevant to device design," *Journal of Applied Physics*, vol. 53, pp. 5863-5869, 1982.
- [166] M. Mondry, D. I. Babic, J. Bowers, and L. Coldren, "Refractive indexes of (Al, Ga, In) As epilayers on InP for optoelectronic applications," *IEEE Photonics Technology Letters*, vol. 4, pp. 627-630, 1992.
- [167] M. Quillec, "Material for future InP-based optoelectronics: InGaAsP versus InGaAlAs," in *Physical Concepts of Materials for Novel Optoelectronic Device Applications I: Materials Growth and Characterization*, pp. 34-47, 1991.
- [168] K. Takemasa, T. Munakata, M. Kobayashi, H. Wada, and T. Kamijoh, "High-temperature operation of 1.3  $\mu\text{m}$  AlGaInAs strained multiple quantum well lasers," *Electronics Letters*, vol. 34, pp. 1231-1233, 1998.
- [169] K. Williams, E. Bente, D. Heiss, Y. Jiao, K. Ławniczuk, X. Leijtens, *et al.*, "InP photonic circuits using generic integration," *Photonics Research*, vol. 3, pp. B60-B68, 2015.
- [170] *Fresnel equations*. Available: [https://en.wikipedia.org/wiki/Fresnel\\_equations](https://en.wikipedia.org/wiki/Fresnel_equations)
- [171] R. E. Williams, *Modern GaAs processing methods*: Artech House Publishers, 1990.
- [172] *Reactive-ion etching*. Available: [https://en.wikipedia.org/wiki/Reactive-ion\\_etching](https://en.wikipedia.org/wiki/Reactive-ion_etching)
- [173] N. Furuhashi, H. Miyamoto, A. Okamoto, and K. Ohata, "Chemical dry etching of GaAs and InP by  $\text{Cl}_2$  using a new ultrahigh - vacuum dry - etching molecular - beam - epitaxy system," *Journal of Applied Physics*, vol. 65, pp. 168-171, 1989.
- [174] J. Lin, A. Leven, N. Weimann, Y. Yang, R. Kopf, R. Reyes, *et al.*, "Smooth and vertical-sidewall InP etching using  $\text{Cl}_2/\text{N}_2$  inductively coupled plasma," *Journal*

*of Vacuum Science & Technology B: Microelectronics and Nanometer Structures Processing, Measurement, and Phenomena*, vol. 22, pp. 510-512, 2004.

- [175] M. Bösch, L. Coldren, and E. Good, "Reactive ion beam etching of InP with Cl<sub>2</sub>," *Applied Physics Letters*, vol. 38, pp. 264-266, 1981.
- [176] C. Cremer and M. Schienle, "RIE etching of deep Bragg grating filters in GaInAsP/InP," *Electronics Letters*, vol. 25, pp. 1177-1178, 1989.
- [177] K. Shinoda, K. Nakahara, and H. Uchiyama, "InGaAlAs/InP ridge-waveguide lasers fabricated by highly selective dry etching in CH<sub>4</sub>/H<sub>2</sub>/O<sub>2</sub>/plasma," in *International Conference on Indium Phosphide and Related Materials*, pp. 550-553, 2003.
- [178] T. Hayes, M. Dreisbach, P. Thomas, W. Dautremont - Smith, and L. Heimbrook, "Reactive ion etching of InP using CH<sub>4</sub>/H<sub>2</sub> mixtures: Mechanisms of etching and anisotropy," *Journal of Vacuum Science & Technology B: Microelectronics Processing and Phenomena*, vol. 7, pp. 1130-1140, 1989.
- [179] J. E. Schramm, D. I. Babić, E. L. Hu, J. E. Bowers, and J. L. Merz, "Fabrication of high-aspect-ratio InP-based vertical-cavity laser mirrors using CH<sub>4</sub>/H<sub>2</sub>/O<sub>2</sub>/Ar reactive ion etching," *Journal of Vacuum Science & Technology B: Microelectronics and Nanometer Structures Processing, Measurement, and Phenomena*, vol. 15, pp. 2031-2036, 1997.
- [180] P. Collot, T. Diallo, and J. Canteloup, "Dry - etch monitoring of III - V heterostructures using laser reflectometry and optical emission spectroscopy," *Journal of Vacuum Science & Technology B: Microelectronics and Nanometer Structures Processing, Measurement, and Phenomena*, vol. 9, pp. 2497-2502, 1991.
- [181] M. G. Wood, L. Chen, J. R. Burr, and R. M. Reano, "Optimization of electron beam patterned hydrogen silsesquioxane mask edge roughness for low-loss silicon waveguides," *Journal of Nanophotonics*, vol. 8, p. 083098, 2014.
- [182] D.-H. Kim, S.-K. Kang, G.-Y. Yeom, and J.-H. Jang, "Nanometer-Scale Fabrication of Hydrogen Silsesquioxane (HSQ) Films with Post Exposure Baking," *Journal of nanoscience and nanotechnology*, vol. 13, pp. 1918-1922, 2013.
- [183] M. J. Madou, *Manufacturing techniques for microfabrication and nanotechnology* vol. 2: CRC press, 2011.
- [184] H. Jansen, M. de Boer, R. Wiegerink, N. Tas, E. Smulders, C. Neagu, *et al.*, "RIE lag in high aspect ratio trench etching of silicon," *Microelectronic Engineering*, vol. 35, pp. 45-50, 1997.

- [185] J. Arnold and H. H. Sawin, "Charging of pattern features during plasma etching," *Journal of Applied Physics*, vol. 70, pp. 5314-5317, 1991.
- [186] PECVD. Available: [https://en.wikipedia.org/wiki/Plasma-enhanced\\_chemical\\_vapor\\_deposition](https://en.wikipedia.org/wiki/Plasma-enhanced_chemical_vapor_deposition)
- [187] L. Schares, Y. H. Lee, D. Kuchta, U. Koren, and L. Ketelsen, "An 8-Wavelength Laser Array with High Back Reflection Tolerance for High-Speed Silicon Photonic Transmitters," in *Optical Fiber Communication Conference*, p. Th1C.3, 2014.
- [188] T. Kurobe, T. Kimoto, K. Muranushi, Y. Nakagawa, H. Nasu, S. Yoshimi, *et al.* "High fibre coupled output power 37 nm tunable laser module using matrix DFB laser," *Electronics Letters*, vol 39(15), pp.1125-1126, 2003.
- [189] Y. Muroya, T. Nakamura, H. Yamada, and T. Torikai, "Precise wavelength control for DFB laser diodes by novel corrugation delineation method," *IEEE Photonics Technology Letters*, vol. 9, pp. 288-290, 1997.
- [190] Y. Shi, X. Chen, Y. Zhou, S. Li, L. Li, and Y. Feng, "Experimental demonstration of the three phase shifted DFB semiconductor laser based on Reconstruction-Equivalent-Chirp technique," *Optics express*, vol. 20, pp. 17374-17379, 2012.
- [191] Y. Shi, S. Li, J. Li, L. Jia, S. Liu, and X. Chen, "An apodized DFB semiconductor laser realized by varying duty cycle of sampling Bragg grating and reconstruction-equivalent-chirp technology," *Optics Communications*, vol. 283, pp. 1840-1844, 2010.
- [192] J. Li, X. Chen, N. Zhou, J. Zhang, X. Huang, L. Li, *et al.*, "Monolithically integrated 30-wavelength DFB laser array," in *Asia Communications and Photonics Conference and Exhibition (ACP)*, pp. 1-6, 2009.
- [193] Y. Shi, S. Li, L. Li, R. Guo, T. Zhang, L. Rui, *et al.*, "Study of the multiwavelength DFB semiconductor laser array based on the reconstruction-equivalent-chirp technique," *Lightwave Technology, Journal of*, vol. 31, pp. 3243-3250, 2013.
- [194] Y. Shi, S. Li, X. Chen, L. Li, J. Li, T. Zhang, *et al.*, "High channel count and high precision channel spacing multi-wavelength laser array for future PICs," *Scientific reports*, vol. 4, 2014.
- [195] G. Barwood, P. Gill, and W. Rowley, "Longitudinal mode control in laser diodes," *Measurement Science and Technology*, vol. 3, p. 406, 1992.
- [196] Y. Shi, X. Chen, Y. Zhou, S. Li, L. Lu, R. Liu, *et al.*, "Experimental demonstration of eight-wavelength distributed feedback semiconductor laser array using equivalent phase shift," *Optics letters*, vol. 37, pp. 3315-3317, 2012.

- [197] L. Hou, M. Haji, I. Eddie, H. Zhu, and J. H. Marsh, "Laterally coupled dual-grating distributed feedback lasers for generating mode-beat terahertz signals," *Optics letters*, vol. 40, pp. 182-185, 2015.
- [198] S. Liang, B. Hou, D. Chen, L. Hou, and J. H. Marsh, "Terahertz Signal Generation Based on a Dual-Mode 1.5  $\mu\text{m}$  DFB Semiconductor Laser," 2018.
- [199] *Golay cell*. Available: [https://en.wikipedia.org/wiki/Golay\\_cell](https://en.wikipedia.org/wiki/Golay_cell)
- [200] M. Tani, S. Matsuura, K. Sakai, and S.-i. Nakashima, "Emission characteristics of photoconductive antennas based on low-temperature-grown GaAs and semi-insulating GaAs," *Applied optics*, vol. 36, pp. 7853-7859, 1997.
- [201] M. J. Golay, "A pneumatic infra - red detector," *Review of Scientific Instruments*, vol. 18, pp. 357-362, 1947.
- [202] A. Gupta, G. Rana, A. Bhattacharya, A. Singh, R. Jain, R. D. Bapat, *et al.*, "Enhanced optical-to-THz conversion efficiency of photoconductive antenna using dielectric nano-layer encapsulation," *APL Photonics*, vol. 3, p. 051706, 2018.
- [203] F. Turkoglu, H. Koseoglu, Y. Demirhan, L. Ozyuzer, S. Preu, S. Malzer, *et al.*, "Interferometer measurements of terahertz waves from Bi<sub>2</sub>Sr<sub>2</sub>CaCu<sub>2</sub>O<sub>8</sub>+ d mesas," *Superconductor Science and Technology*, vol. 25, p. 125004, 2012.
- [204] L. Hou, M. Haji, C. Li, B. Qiu, and A. Bryce, "80-GHz AlGaInAs/InP 1.55  $\mu\text{m}$  colliding-pulse mode-locked laser with low divergence angle and timing jitter," *Laser Physics Letters*, vol. 8, p. 535, 2011.
- [205] J. Renaudier, R. Brenot, B. Dagens, F. Lelarge, B. Rousseau, F. Poingt, *et al.*, "45 GHz self-pulsation with narrow linewidth in quantum dot Fabry-Perot semiconductor lasers at 1.5  $\mu\text{m}$ ," *Electronics Letters*, vol. 41, pp. 1007-1008, 2005.
- [206] J. H. Marsh and L. Hou, "Mode-locked laser diodes and their monolithic integration," *IEEE Journal of Selected Topics in Quantum Electronics*, vol. 23, pp. 1-11, 2017.
- [207] Y. J. Wen, D. Novak, H. F. Liu, and A. Nirmalathas, "Generation of 140GHz optical pulses with suppressed amplitude modulation by subharmonic synchronous modelocking of Fabry-Perot semiconductor laser," *Electronics Letters*, vol. 37, p. 1, 2001.
- [208] Y. Chen, M. Wu, T. Tanbun - Ek, R. Logan, and M. Chin, "Subpicosecond monolithic colliding - pulse mode - locked multiple quantum well lasers," *Applied Physics Letters*, vol. 58, pp. 1253-1255, 1991.

- [209] Y. Katagiri and A. Takada, "A harmonic colliding-pulse mode-locked semiconductor laser for stable subterahertz pulse generation," *IEEE Photonics Technology Letters*, vol. 9, pp. 1442-1444, 1997.
- [210] D. A. Yanson, M. W. Street, S. D. McDougall, L. Thayne, J. H. Marsh, and E. A. Avrutin, "Ultrafast harmonic mode-locking of monolithic compound-cavity laser diodes incorporating photonic-bandgap reflectors," *IEEE Journal of Quantum Electronics*, vol. 38, pp. 1-11, 2002.
- [211] S. Arahira, S. Oshiba, Y. Matsui, T. Kunii, and Y. Ogawa, "500 GHz optical short pulse generation from a monolithic passively mode - locked distributed Bragg reflector laser diode," *Applied physics letters*, vol. 64, pp. 1917-1919, 1994.
- [212] R. Fork, B. Greene, and C. V. Shank, "Generation of optical pulses shorter than 0.1 psec by colliding pulse mode locking," *Applied Physics Letters*, vol. 38, pp. 671-672, 1981.
- [213] Y.-K. Chen and M. C. Wu, "Monolithic colliding-pulse mode-locked quantum-well lasers," *IEEE Journal of Quantum Electronics*, vol. 28, pp. 2176-2185, 1992.
- [214] S. Arahira, S. Oshiba, Y. Matsui, T. Kunii, and Y. Ogawa, "Terahertz-rate optical pulse generation from a passively mode-locked semiconductor laser diode," *Optics letters*, vol. 19, pp. 834-836, 1994.
- [215] D. Yanson, M. Street, S. McDougall, I. Thayne, J. Marsh, and E. Avrutin, "Terahertz repetition frequencies from harmonic mode-locked monolithic compound-cavity laser diodes," *Applied Physics Letters*, vol. 78, pp. 3571-3573, 2001.
- [216] L. Hou, M. Haji, and J. H. Marsh, "Mode locking at terahertz frequencies using a distributed Bragg reflector laser with a sampled grating," *Optics letters*, vol. 38, pp. 1113-1115, 2013.
- [217] L. Hou, S. Tang, B. Hou, S. Liang, and J. H. Marsh, "1.55- $\mu\text{m}$  AlGaInAs/InP Sampled Grating Laser Diodes for Mode Locking at Terahertz Frequencies," *IEEE Journal of Selected Topics in Quantum Electronics*, vol. 24, pp. 1-8, 2018.
- [218] M. Focht, A. Macrander, B. Schwartz, and L. C. Feldman, "High resistivity in InP by helium bombardment," *Journal of applied physics*, vol. 55, pp. 3859-3862, 1984.
- [219] S. Pearton, "Ion implantation for isolation of III-V semiconductors," *Materials science reports*, vol. 4, pp. 313-363, 1990.

- [220] S. Pearton, C. Abernathy, J. Lee, F. Ren, and C. Wu, "Comparison of H<sup>+</sup> and He<sup>+</sup> implant isolation of GaAs - based heterojunction bipolar transistors," *Journal of Vacuum Science & Technology B: Microelectronics and Nanometer Structures Processing, Measurement, and Phenomena*, vol. 13, pp. 15-18, 1995.
- [221] S. Tang, L. Hou, I. Eddie, X. Chen, and J. H. Marsh, "Novel Sampled Grating Design for High Precision, Multiple Wavelength DFB Laser Arrays," 2017.
- [222] S. Tang, L. Hou, X. Chen, and J. H. Marsh, "DFB laser arrays with precise channel separation and high coupling coefficient," in *The European Conference on Lasers and Electro-Optics*, p. CB\_6\_5, 2017.
- [223] L. Hou, S. Tang, and J. H. Marsh, "THz repetition frequency mode-locked laser using novel sampled gratings," in *The European Conference on Lasers and Electro-Optics*, p. CB\_8\_5, 2017.
- [224] L. Hou, S. Tang, B. Hou, and J. H. Marsh, "Mode Locking at THz Repetition Frequencies using Lasers with Phase Shifted Sampled Gratings," in *CLEO: Science and Innovations*, p. SW4Q. 7, 2018.
- [225] C.-L. Yang and S.-L. Lee, "Wavelength monitoring of tunable DWDM sources using a FP etalon and a FP laser diode," in *Optical Fiber Communication Conference and Exhibit*, pp. 393-395, 2002.
- [226] *Harmonic Mixer 325-500 GHz*. Available: <https://www.radiometer-physics.de/products/mmwave-and-terahertz-products/mixers/mixers-subharmonic-and-harmonic-mixers/harmonic-mixers/harmonic-mixer-325-500-ghz/>